Max-Planck-Institut
für Meteorologie

MAX-PLANCK-GESELLSCHAFT

The HOAPS Climatology
Evaluation and Applications

Axel Andersson

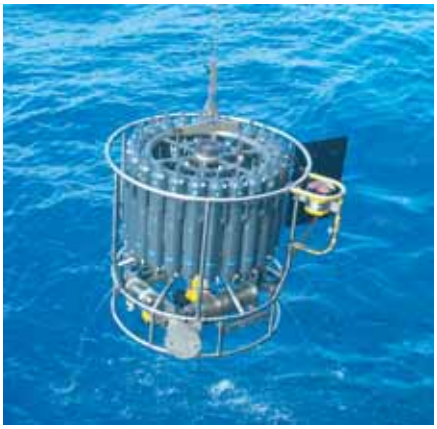

Berichte zur Erdsystemforschung 72/2009

Reports on Earth System Science

Hinweis

Die Berichte zur Erdsystemforschung werden vom Max-Planck-Institut für Meteorologie in Hamburg in unregelmäßiger Abfolge herausgegeben.

Sie enthalten wissenschaftliche und technische Beiträge, inklusive Dissertationen.

Die Beiträge geben nicht notwendigerweise die Auffassung des Instituts wieder.

Die "Berichte zur Erdsystemforschung" führen die vorherigen Reihen "Reports" und "Examensarbeiten" weiter.

Notice

The Reports on Earth System Science are published by the Max Planck Institute for Meteorology in Hamburg. They appear in irregular intervals.

They contain scientific and technical contributions, including Ph. D. theses.

The Reports do not necessarily reflect the opinion of the Institute.

The "Reports on Earth System Science" continue the former "Reports" and "Examensarbeiten" of the Max Planck Institute.

Anschrift / Address

Max-Planck-Institut für Meteorologie
Bundesstrasse 53
20146 Hamburg
Deutschland

Tel.: +49-(0)40-4 11 73-0
Fax: +49-(0)40-4 11 73-298
Web: www.mpimet.mpg.de

Layout:

Bettina Diallo, PR & Grafik

Titelfotos:
vorne:
Christian Klepp - Jochem Marotzke - Christian Klepp
hinten:
Clotilde Dubois - Christian Klepp - Katsumasa Tanaka

Berichte zur Erdsystemforschung 72/2009

The HOAPS Climatology
Evaluation and Applications

Axel Andersson

aus Hamburg

Hamburg 2009

Reports on Earth System Science 72/2009

ISSN 1614-1199

Axel Andersson
Max-Planck-Institut für Meteorologie
Bundesstrasse 53
20146 Hamburg
Germany

Als Dissertation angenommen
vom Department Geowissenschaften der Universität Hamburg

auf Grund der Gutachten von
Prof. Dr. Hartmut Graßl
und
Dr. Stephan Bakan

Hamburg, den 13. Juli 2009
Prof. Dr. Jürgen Oßenbrügge
Leiter des Departments für Geowissenschaften

ISSN 1614-1199

The HOAPS Climatology
Evaluation and Applications

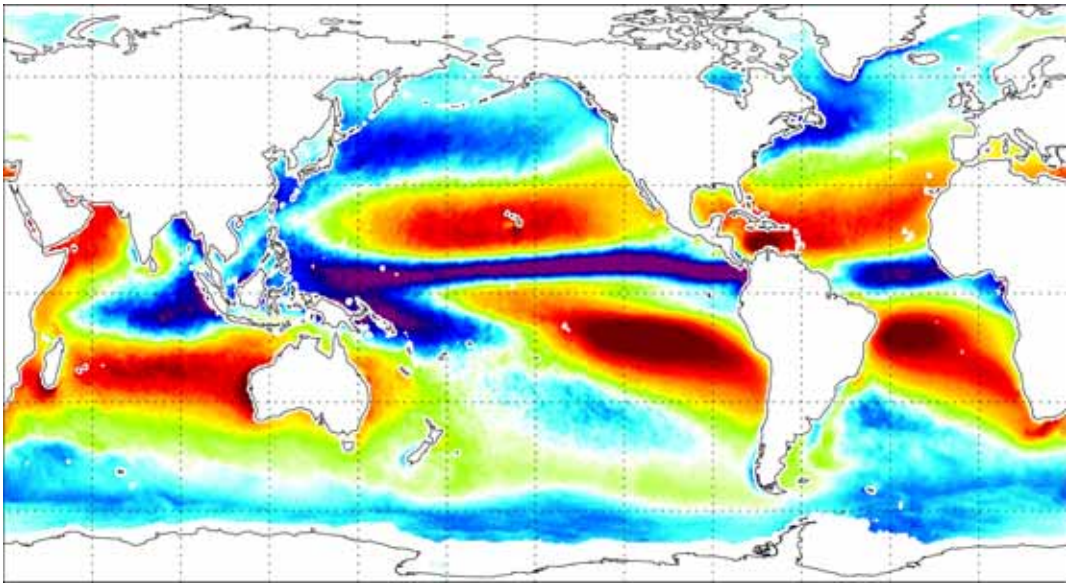

Axel Andersson

Hamburg 2009

Contents

Abstract

To facilitate a better understanding and modeling of climate processes a proper knowledge of the components of the global water cycle components is essential. For the assessment of the freshwater flux at the ocean surface on global scale, exchange processes at the air-sea interface play a key role. With the ability to derive ocean latent heat flux and precipitation from satellite data with acceptable accuracy, and frequent global coverage, a climatological assessment of the crucial processes has become possible.

HOAPS - the Hamburg Ocean Atmosphere Parameters and fluxes from Satellite data - is a satellite derived climatology of evaporation, precipitation, hence freshwater flux, and of all basic state variables needed to retrieve these fluxes over the global ice-free oceans. Exclusively based upon satellite data, HOAPS now covers more than 18 years from July 1987 to December 2005. Except for the NODC/RSMAS AVHRR Pathfinder SST data set, all HOAPS variables are derived from brightness temperatures of the SSM/I radiometers on polar orbiting DMSP satellites. The use of all available SSM/I instruments after careful intersensor calibration, results in homogeneous and reliable spatial and temporal coverage.

In this thesis, the third version of the HOAPS climatology will be presented and evaluated. Besides a description of the data set and methodological aspects, evaluation and application issues of HOAPS-3 data on different temporal and spatial scales will be investigated.

High resolution HOAPS-3 data is used in a case study of the extratropical transition of a hurricane demonstrating the ability of HOAPS-3 to derive geophysical parameters in extreme synoptic conditions and to give valuable insight into the transformation process. Furthermore, the variability of North Atlantic precipitation and freshwater flux with respect to the North Atlantic Oscillation will be assessed. This includes a novel combination of HOAPS-3 and over land rain gauge based precipitation fields. On climatological scale, an assessment of systematic differences and consistencies of HOAPS-3 parameters compared to other comparable data sets will be carried out.

The Evaluation and application of HOAPS-3 data on different temporal and spatial scales presented in this work indicates a consistent and homogeneous time series, which is valuable for regional and case studies as well as, with some limitation regarding trend analyses, for climatological investigations.

Kurzfassung

Für das Verständnis und die Modellierung von Prozessen im Klimasystem der Erde ist es unabdingbar, die Komponenten des globalen Frischwasserkreislaufs zu erkennen und zu erfassen. Hierbei spielen Austauschprozesse an der Grenzfläche zwischen Ozean und Atmosphäre eine zentrale Rolle. Mit satellitengestützten Fernerkundungsverfahren besteht heutzutage die Möglichkeit, den latenten Wärmefluss sowie den Niederschlag über dem Ozean mit ausreichender Genauigkeit und regelmäßiger globaler Abdeckung zu erfassen und klimatologisch auszuwerten.

Die Satellitenklimatologie HOAPS - Hamburg Ocean Atmosphere Parameters and fluxes from Satellite data - leitet die Verdunstung, der Niederschlag und somit der Frischwasserfluss, sowie die zur Bestimmung dieser Variablen benötigten Parameter über dem eisfreien Ozean ausschließlich aus Satellitendaten ab. Derzeit ist HOAPS für den Zeitraum von Juli 1987 bis Ende Dezember 2005 verfügbar. Abgesehen vom NODC/RSMAS AVHRR Pathfinder SST Datensatz werden alle Parameter in HOAPS von Helligkeitstemperaturen des SSM/I Radiometers abgeleitet, welches sich auf den polarumlaufenden DMSP-Satelliten befindet. Die gleichzeitige Nutzung aller verfügbaren SSM/I und einer sorgfältigen Inter-Sensor Kalibration gewährleistet eine homogene und zuverlässige Zeitreihe.

In der vorliegenden Arbeit wird die mittlerweile dritte Version der HOAPS Klimatologie vorgestellt und ausgewertet. Neben einer Beschreibung der methodischen Aspekte liegt der Schwerpunkt auf der Evaluation und Anwendung von HOAPS-3 Daten auf unterschiedlichen räumlichen sowie zeitlichen Skalen. In einer Fallstudie wird die Transition eines Hurrikans in eine extratropische Zyklone mittels hochaufgelöster HOAPS-3 Daten untersucht und Einblicke in den Transformationprozess gewonnen. Des Weiteren wird die Variabilität des Niederschlags sowie des Frischwasserflusses im nordatlantischen Raum im Zusammenhang mit der Nordatlantischen Oszillation untersucht. Hierzu wurde die Niederschlagszeitreihe um landgestützte Regenmesserdaten ergänzt und ein neuartiger kombinierter Datensatz erstellt. Auf klimatologischer Skala werden systematische Unterschiede und Gemeinsamkeiten mit zu HOAPS-3 vergleichbaren Datensätzen herausgearbeitet.

Die Evaluation und Anwendung der HOAPS-3 Daten auf unterschiedlichen Zeit- und Raumskalen bestätigen die Konsistenz der Zeitreihen, sowie die Anwendbarkeit von HOAPS-3 nicht nur in Fallstudien, sondern, mit Einschränkungen bezüglich der Trendanalyse, auch in der Erfassung klimarelevanter Prozesse.

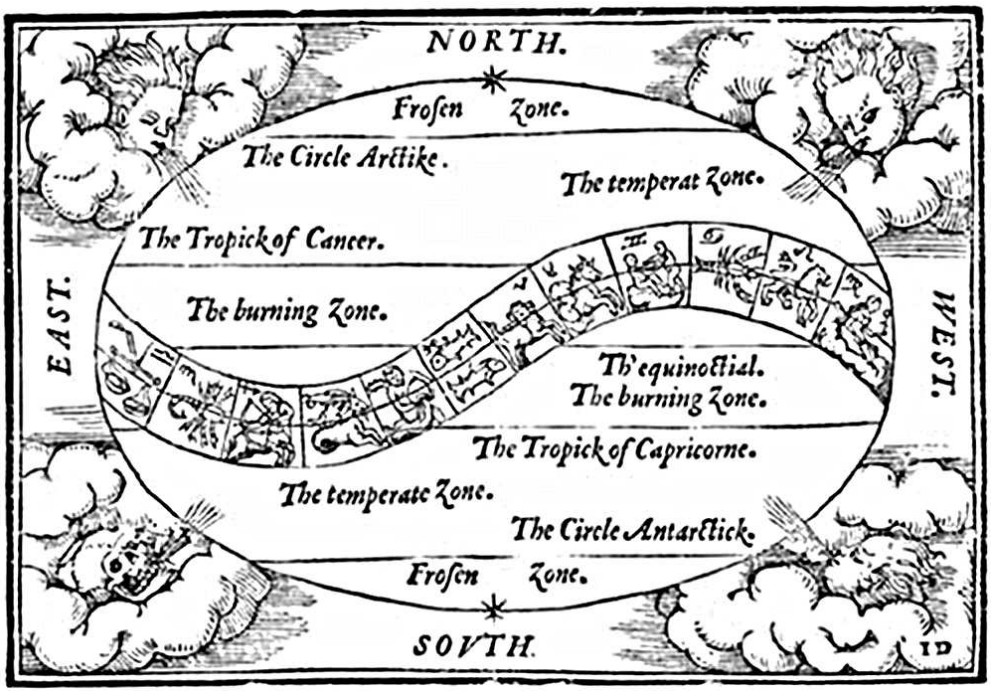

Map showing the Earth's climate zones together with the signs of the zodiac as published in "The Cosmographical Glasse, conteinyng the pleasant Principles of Cosmographie, Geographie, Hydrographie, or Nauigation" by William Cuningham (London, 1559).

1 Introduction

As shown by the contemporary impression from William Cuningham's "Cosmographical Glasse" on the previous page, the basic knowledge about different climatic zones on our planet was already present in the middle of the 16$^{\text{th}}$ century. Seafarers had traveled the oceans of the world and brought home observations from distant regions by that time. From this mosaic of information, people were able to form a rudimentary idea of the Earth's climatic zones. For a long time, ground based sparsely distributed observations were the only source of regular information about the weather and, when aggregated, the climate. In the first half of the 20$^{\text{th}}$ century technical progress allowed the use of instruments on airplanes and weather balloons to observe the Earth and gain more detailed information about the atmosphere. With the availability of radar, a certain region could be continuously sampled. The era of satellites in weather observations began with the *Television and InfraRed Observation Satellite* (TIROS) 1, which was launched into orbit in 1960. From that time on it was possible to monitor the Earth constantly and for a great domain. Meanwhile the computer technology was sophisticated enough to calculate with first models of the atmosphere meteorological phenomena, and to predict weather. Today, a variety of satellites carrying all kinds of instruments constantly monitor the Earth from space and computer systems are used to calculate climate processes with highly complex coupled ocean–atmosphere models. However, the exact observation and modeling of the Earth's climate system still remains a challenging task.

The main driving force of the Earth's climate system is the asymmetric distribution of incoming solar and outgoing long wave radiation at the top of the atmosphere. The tropical regions of the globe take up most of the incoming so-

lar energy. This surplus of energy is redistributed through the oceans and the atmosphere to higher latitudes, where a net loss of energy back to space in the form of long wave radiation exists, thus balancing the globally incoming and outgoing radiation. The transport of energy through the climate system takes place in various forms, such as internal heat, potential energy, latent heat, and kinetic energy (*Trenberth and Stepaniak*, 2004). Processes on different temporal and spatial scales are involved in the redistribution of energy, and the interaction of these mechanisms in the ocean and atmosphere determine the local weather as well as processes on the climatological scale.

A key role in the climate system is taken by the oceans which cover more than two thirds of the Earth's surface. Exchange processes at the air–sea interface are an important source of energy for large scale circulations such as the Hadley cell as well as individual midlatitude synoptic systems. About 85 % of global evaporation stems from the oceans and almost 80 % of global precipitation occurs over the oceans, hence representing the governing part of the Earth's hydrological cycle and a key part in the global energy cycle. The global energy and hydrological cycles are linked through the radiative properties and phase changes of water. Energy is extracted from the oceans via evaporative cooling, which occurs mainly in the tropical and subtropical regions. The latent energy contained in water vapor may be transported over large distances, before it returns to the surface as liquid or solid precipitation, thus releasing the latent energy. The surplus of evaporation from the oceans is transported over land from where the water is transported back into the oceans for example via continental runoff, as groundwater flow, and from calving glaciers. Moreover, the ocean circulation may be influenced by freshwater influx or deficit, which modifies the salinity of the upper ocean layers and hence creates density gradients in the ocean. Attributing the utterly importance of the hydrological cycle for the Earth system, *Rasmusson and Arkin* (1993) termed the Earth a "water driven planet".

Hence, a thorough knowledge of the global water cycle and its components is an indispensable prerequisite for the understanding and successful modeling of the global climate system. Measuring the relevant quantities is however a notoriously difficult task, especially over the global ocean with the generally insufficient spatial and temporal coverage by ships or buoys. The advent of satellite platforms provided the opportunity to retrieve global data sets with an equally dense spatial distribution over sea and over land. Especially since the availability of passive microwave detectors in space, the derivation of several essential water cycle components over the global ocean with acceptable accuracy became possible.

Due to the inherent physical properties of long-wave electromagnetic radiative transfer through the atmosphere, the microwave spectral range is well suited for the derivation of atmospheric gaseous and particulate water content and the fresh-

water flux components at the ocean surface. In contrast to visible and infrared measurements, microwave remote sensing adds the ability to penetrate through clouds, even in light rain conditions. Especially over open water, the surface emissivity in the microwave spectral ranges leads to a higher sensitivity of the measured radiances to atmospheric parameters (*Schlüssel and Emery*, 1990).

After early experience with experimental microwave sensors the availability of the *Special Sensor Microwave Imager* (SSM/I) on the *Defense Meteorological Satellites Program* (DMSP) satellites since 1987 motivated several international research groups to derive and provide long term global fields of some of these quantities. Depending on the main application purpose, data from various additional sources are blended with the SSM/I satellite data in these climatologies. Generally these data sets fall into two categories, on one hand providing surface fluxes, and on the other hand precipitation estimates.

A number of satellite derived climatological precipitation data sets with different temporal and spatial resolutions exist. The *Global Precipitation Climatology Project* (GPCP, *Huffman et al.*, 1997; *Adler et al.*, 2003), utilizes SSM/I and additional infrared data from geostationary and polar orbiting satellites over the global oceans since 1979 to derive global precipitation fields. Over the continents, rain gauge data from the *Global Precipitation Climatology Center* (GPCC, *Rudolf and Schneider*, 2005) are added into the GPCP product. A comparable product is the *CPC Merged Analysis of Precipitation* (CMAP, *Xie and Arkin*, 1997), which also uses reanalysis data to complement the satellite retrieved precipitation. *Remote Sensing Systems* (RSS) supplies operational global ocean fields of precipitable water (vertically integrated water vapor), cloud liquid water, surface wind speed, and precipitation based on passive microwave data from the SSM/I, the *Tropical Rainfall Measuring Mission* (TRMM), and the *Advanced Microwave Scanning Radiometer for Earth Observing System* (AMSR-E) (*Wentz*, 1997; *Wentz and Spencer*, 1998). These sensors are also used in the improved passive microwave rain products from the *Unified Microwave Ocean Retrieval Algorithm* (UMORA, *Hilburn and Wentz*, 2008). The TRMM satellite platform, which was launched in cooperation of the *National Aeronautics and Space Administration* (NASA) and the *Japan Aerospace Exploration Agency* (JAXA) carries a passive microwave radiometer, the *TRMM Microwave Imager* (TMI) and the active *Precipitation Radar* (PR). TRMM serves as the reference in a variety of precipitation products, such as the *TRMM multisatellite precipitation analysis* (TMPA, *Huffman et al.*, 2007) and the *Global Satellite Mapping of Precipitation* (GSMaP, *Kubota et al.*, 2007). In order to achieve high temporal coverage, techniques based on additional use of information from geostationary satellites have been developed, such as the *CPC Morphing Technique* (CMORPH, *Joyce et al.*, 2004) and *Precipitation Estimation from Remotely Sensed Information using Artificial Neural Networks* (PERSIANN, *Hsu et al.*, 1997).

On the other hand, several prominent surface flux products exist, which are mainly derived incorporating passive microwave data. The *Japanese Ocean Flux data sets with the Use of Remote sensing Observations* (J-OFURO 2, *Kubota and Tomita*, 2007) derives turbulent heat fluxes, momentum flux, short- and longwave radiation from SSM/I and additional microwave and infrared satellite data. The *Goddard Satellite based Surface Turbulent Fluxes version 2* (GSSTF2, *Chou et al.*, 2003), produced by the surface turbulent fluxes research group at NASA GSFC provides turbulent flux related products based on SSM/I and NCEP reanalysis data for the time period July 1987 to December 2000. The *Objectively Analyzed air-sea FLUXes* (OAFLUX, *Yu and Weller*, 2007; *Yu et al.*, 2008) synthesizes satellite data, in-situ and NWP products into an objectively analyzed flux product with improved resolution and quality between 1958 and 2006. Another multi-satellite flux product is the *Institut Français de Recherche pour l'Exploration de la Mer* (IFREMER) merged flux data set, that is derived over the global oceans using an objective method (*Bentamy et al.*, 2003). Bulk variables, wind stress, latent and sensible heat fluxes are estimated using SSM/I measurements, scatterometer wind speeds and NOAA sea surface temperature data.

Except from GSSTF2, all of the latent and sensible heat flux products mentioned here are based on the *Coupled Ocean-Atmosphere Response Experiment* (COARE) flux algorithms (*Fairall et al.*, 2003). However, significant differences between the data sets remain in the sources and handling of input data.

For validation purposes, a ship based data set from the *National Oceanographic Centre Southampton* (NOCS) provides fields of global ocean heat fluxes. The data sets is constructed using an optimum interpolation method and a bias adjustment procedure, and is widely used as a reference for the evaluation of model and satellite based data sets. An updated and extended version 2 of the NOCS Surface Flux Dataset, that is compiled using *Voluntary Observing Ships* (VOS) data from the *International Comprehensive Ocean-Atmosphere Data Set* (ICOADS, *Slutz et al.*, 1985) and the COARE flux algorithms is available since August 2008 (*Berry and Kent*, 2008).

An extensive overview of satellite retrieved sea flux data sets will be given in *Clayson et al.* (2009). Furthermore, *Levizzani et al.* (2007) provide a comprehensive introduction to current state of the art rainfall algorithms and products as well as validation and modeling aspects of precipitation.

Based on polar orbiting *Advanced Very High Resolution Radiometer* (AVHRR) and geostationary infrared satellite data, the *International Satellite Cloud Climatology* (ISCCP, *Rossow and Schiffer*, 1991) contains multiple cloud property parameters, i.e. cloud cover, cloud type, cloud top temperature, cloud top pressure and cloud optical thickness, as well as radiation budget data for the years 1983 to 2005.

Another approach to benefit from satellite data for long term data sets is assimilating these data into a retrospective-analysis (or reanalysis) procedure. By using a fixed assimilation system and a comprehensive quality control, reanalysis data sets incorporate a large number of observations, including satellite data. Together with the continuity of a numerical model, they provide a dynamically consistent time series. Currently several prominent reanalysis projects exist. A joint effort of the *National Centers for Environmental Prediction* (NCEP) and the *National Center for Atmospheric Research* (NCAR) provides the widely used NCEP/NCAR reanalysis (NCEP-R1) which is covers the time period from 1949 until present (*Kalnay et al.*, 1996). An improved version of NCEP-R1 was introduced by NCEP in collaboration with the *Department of Energy* (DOE) for the Atmospheric Model Intercomparison Project (AMIP-II). The NCEP/DOE reanalysis (NCEP-R2) uses an upgraded version of the NCEP-R1 general circulation model with data starting in 1979 (*Kanamitsu et al.*, 2002). From the *European Centre for Medium-Range Weather Forecast* (ECMWF) the *ECMWF Re-Analysis* (ERA) data sets are available. The ERA-40 *Uppala et al.* (2005) covers the period from 1957 to 2002. Currently an improved version, the ERA-interim *Simmons et al.* (2007) reanalysis, is produced starting with the data-rich period from 1989 onwards. The *Japanese 25-year ReAnalysis* (JRA-25, *Onogi et al.*, 2007) initially covered the period from 1979 to 2004. It is continued as the *JMA Climate Data Assimilation System* (JCDAS).

Under the international frameworks of the *World Climate Research Programme* (WCRP), its *Global Energy and Water Cycle Experiment* (GEWEX) Radiation Panel, and the *Coordination Group for Meteorological Satellites* (CGMS), several working groups dedicated to satellite remote sensing exist. In particular, the SEAFLUX project and the *International Precipitation Working Group* (IPWG) foster the development of satellite-based data sets of surface turbulent fluxes and precipitation.

In principle, the satellite retrieved data sets could be combined to estimate the global ocean freshwater flux. This would be a highly required but difficult task, as different data sources have to be combined while there is no comprehensive in-situ validation data available (*Schlosser and Houser*, 2007).

The *Hamburg Ocean Atmosphere Parameters and Fluxes from Satellite Data* (HOAPS) is hitherto the only generally available compilation of both precipitation and evaporation with the goal of estimating the freshwater flux from one consistently derived global satellite product that is retrieved independently of numerical weather prediction or other model data.

In combination with multi-satellite averages, inter-sensor calibration, and an efficient sea ice detection procedure, the SSM/I measurements are an appropriate base for a climatological data set. For the sake of long-term homogeneity, the

use of data from different satellite instruments has been avoided. All variables are derived from SSM/I passive microwave radiometers, except for the *sea surface temperature* (SST), which is obtained from AVHRR measurements. Since 1987, six SSM/I instruments have been launched into space which are considered to be stable measuring instruments (*Hollinger et al.*, 1990; *Jost*, 2000), thus providing a reliable basis for a climatological data set.

The latest version, HOAPS-3, was reprocessed as part of the present thesis work. Based on the previous version HOAPS II (*Fennig et al.*, 2006ab), it includes a prolonged time series, unpublished retrievals, and a newly developed procedure to synthesize the unusable 85 GHz channels of the SSM/I on the DMSP F08 satellite. Additionally, the *NOAA National Oceanographic Data Center* (NODC) and *Miami's Rosenstiel School of Marine and Atmospheric Science* (RSMAS) Oceans Pathfinder Version 5.0 SST was implemented into the HOAPS-3 data set. The HOAPS-3 data sets have been processed for the period 1987–2005 and are publicly available from the website *www.hoaps.org*.

Apart from the description of the methodological aspects involving the data processing and retrieval procedures, the main goal of this thesis is an evaluation of HOAPS-3 parameters and their application on different temporal and spatial scales. The focus is on the parameters related to the freshwater flux and the retrieval procedures of its components. Hitherto unpublished retrievals of precipitation and wind speed will be treated as well as the new SST data set, the evaporation and the freshwater flux itself. Wind speed and SST are needed to derive the evaporation through the bulk aerodynamic approach used in HOAPS-3.

At first a short introduction to the physical basis of satellite based remote sensing will be given in chapter 2. The key features and data subsets of HOAPS-3 along with the methodology involved in the data processing and the retrieval schemes of the individual parameters are introduced in chapter 3.

In chapter 4, HOAPS-3 parameters are evaluated against other data sets on climatological scale. The assessment of systematic differences and pattern consistency on global scale between HOAPS-3 and other data sets is the main aim of this chapter. Also, the long term evolution of the freshwater flux parameters will be addressed.

An application of HOAPS-3 data is presented in chapter 5 with the case study of the extratropical transition of the hurricane Maria in 2005. Pixel level data is used to get insight into the transformation process of a tropical cyclone into an extratropical cyclone and to evaluate HOAPS-3 parameters under extreme environmental conditions on the smallest spatial and temporal scales available from HOAPS.

In chapter 6, a novel approach will be used to asses the precipitation variabi-

lity of the North Atlantic with respect to the *North Atlantic Oscillation* (NAO). For this study, the HOAPS-3 oceanic precipitation was combined with the rain gauge based land precipitation product from the GPCC. This combined product provides a quasi global climatological data set, which is suitable to asses North Atlantic precipitation variability as well as to allow a mutual validation for the two independent precipitation data sets.

Finally, the evaluation and application studies are discussed in chapter 7 together with an outlook on the further development of the HOAPS climatology.

2

Physical Basis

All satellite based remote sensing systems are based on the measurement of energy transmitted as electromagnetic radiation, which can be characterized by its wavelength or frequency. Such instruments sample at distinct ranges of the spectrum, which are regarded as channels or bands. The detection ranges of common sensors within the spectrum of electromagnetic waves are shown in Fig. 2.1. The spectrum represents the continuum of electromagnetic energy, starting at extremely short wavelengths, the gamma and Roentgen radiation, followed by the ultraviolet range. Then, a relatively small part of visible light is located at wavelengths from 400 to 700 nm. The next region is regarded as the infra-red with wavelengths up to 1 mm. It is common to distinguish between near (0.7 μm – 3 μm), middle (3 μm – 15 μm), and far infrared (>15 μm). Wavelengths in the millimeter to meter range are regarded as the microwave part of the spectrum. For Radar applications the microwave spectrum is often subdivided into frequency intervals, the so called bands. Waves with wavelengths from meters to kilometers are regarded as radio waves.

Most systems rely on external sources to generate all the electromagnetic energy needed to sample the atmosphere and/or the surface of the Earth. These instruments are regarded as passive sensors as they record the energy, which is reflected or emitted by the underlying atmosphere and Earth's surface. Sensors which send out a signal by their own are called active sensors. Such instruments transmit a defined amount of energy in a certain direction and record the portion of the signal reflected back to the sensor. HOAPS-3 relies on measurements from passive sensors, microwave radiometer SSM/I and the infrared sensor AVHRR.

In all cases the signal recorded at the sensor is influenced by the underlying surface and features in the pathway through the atmosphere. Interactions with matter can change the direction, intensity, wavelength dependency, and polarization of electromagnetic radiation. The nature of these changes depends on the chemical composition and physical structure of the material. Knowledge about characteristic interactions of electromagnetic radiation with certain environments is the basis to derive retrievals of geophysical parameters.

2.1 Planck's Law

Any object emits electromagnetic radiation depending on its temperature, material, and structure of the surface. An object that absorbs all electromagnetic radiation falling on it is referred to as a "black body". Following Kirchhoff's law of thermal radiation, the radiation emitted by a black body equals the radiation absorbed by it. For instance, the universe nearly behaves like a black body. It absorbs radiation emitted to space almost completely and emits radiation with the power of an object at a very low temperature of about 2.7 K.

A black body emits energy at all wavelengths, according to the Planck's law. The spectral radiance, i.e. the power emitted at a specific wavelength λ, per unit time, per unit solid angle, and per unit area of emitting surface, is a function of the temperature:

$$B_\lambda(T) = \frac{2hc^2}{\lambda^5} \cdot \left(\frac{1}{e^{hc/\lambda kT} - 1} \right) \tag{2.1}$$

symbols are:

$B_\lambda(T)$	spectral radiance $[\frac{W}{m^2\ \mu m\ sr}]$
λ	wavelength
T	black body temperature
h	Planck constant
c	speed of light
k	Boltzmann constant

Planck functions for black bodies with different temperatures are depicted in the top panel of Fig. 2.1. Important for passive remote sensing are the window regions for which the atmosphere exhibits a high transmittance. For example the solar radiation reflected by the Earth's surface in the visible spectrum and radiation emitted in the thermal infrared and microwave spectrum is used to sample the Earth from space.

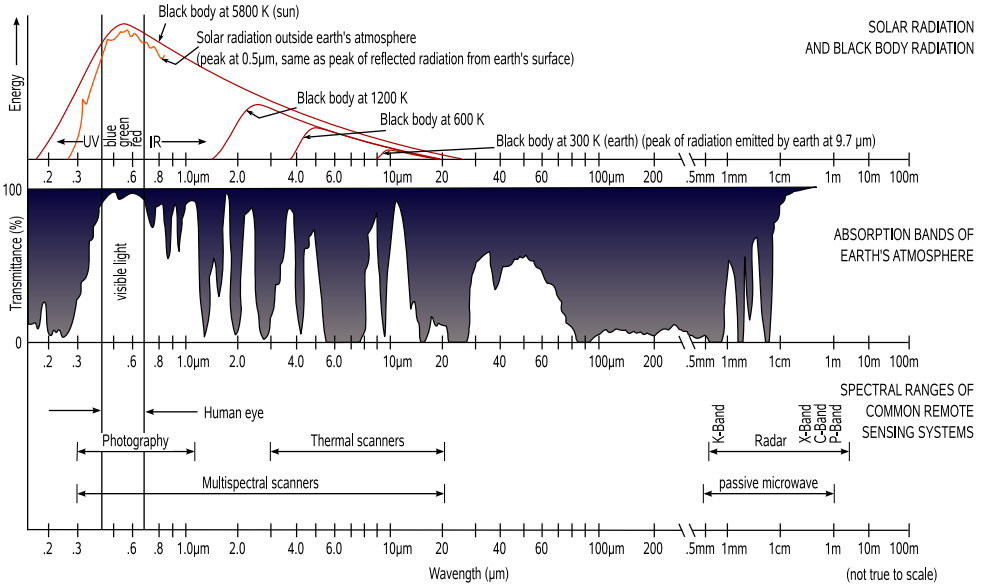

Figure 2.1: Energy radiated by a black body at different temperatures (top), atmospheric transmittance (middle), and spectral characteristics of some remote sensing systems (bottom). The wavelength scale is logarithmic. (adapted from *Kronberg*, 1985)

2.2 Stefan-Boltzmann Law

From the top panel of Fig. 2.1 it is evident that the radiation emitted from a black body increases strongly with its temperature.

This relation is described by the Stefan-Boltzmann law, which corresponds to the spectral flux density from a flat surface radiances from Eq. 2.1 integrated over all wavelengths:

$$B\left(T\right) = \sigma \cdot T^4 \tag{2.2}$$

where σ is the Boltzmann constant with a value of $5.67 \cdot 10^{-8} \frac{W}{m^2 K^4}$.

2.3 Wien's Displacement Law

With higher temperatures not only the total emitted energy of an object increases, but also the wavelength of the peak of the emission is displaced towards shorter wavelengths, as it is evident from Fig. 2.1, top panel. For example, the maximum of solar insolation is located in the visible spectrum, while the maximum of radiation emitted by the Earth is in the thermal infrared at 9.7 μm. This corresponds to a black body with a temperature of 300 K.

Wien's displacement law can be derived from Planck's law (Eq. 2.1) by differentiation and setting the derivative equal to zero. It describes the wavelength of the peak emission of a black body (λ_{max} at $dB_\lambda(T)/d\lambda = 0$) depending on its temperature:

$$\lambda_{max} \cdot T = 2897.7685 \mu m K \tag{2.3}$$

2.4 Emissivity and Brightness Temperature

For wavelengths in the microwave spectrum a valid assumption at atmospheric temperatures is $hc/\lambda \ll kT$. In this case Planck's law can be approximated with the Rayleigh-Jeans law. For the microwave spectrum, this is often written using frequencies instead of wavelengths :

$$B_\nu(T) \approx \frac{2k\nu^2}{c^2}T = \frac{2k}{\lambda^2}T \tag{2.4}$$

Hence, for a black body the radiance is related linearly to the temperature. The radiance measured by a radiometer at a fixed frequency can be assigned to an equivalent temperature, the *brightness temperature* (TB):

$$T_B = \frac{c^2}{2\nu^2 k}B_\nu(T) \tag{2.5}$$

The brightness temperature of a black body is equal to its physical temperature. A real object will not behave at all wavelengths like a black body. In this case, the spectral radiance is determined by the emissivity ϵ, which specifies the ratio of the maximum possible radiance of a black body with the same temperature that is actually emitted by the object:

$$T_B = \epsilon T \tag{2.6}$$

The emissivity depends on the emitting angle, frequency, and polarization of the radiation and can have values between zero and one. The T_B of any real object is smaller than its physical temperature.

In the microwave spectrum the emissivity is strongly affected by the surface properties of an object. Furthermore, microwave radiation has the ability to penetrate into a surface to a certain depth. This penetration depth depends on factors such as the moisture content of the surface, which, on the other hand, also affects the emissivity. So one can derive geophysical parameters from a modification in emissivity at constant temperature. In the infrared, this relationship is much less pronounced. Usually a change in the temperature at a nearly constant surface emissivity is measured at these wavelengths.

2.5 Influence of the Atmosphere

Radiation is influenced by different processes on its pathway through the atmosphere. The signal that is recorded by a sensor depends on the wavelength and the state of the underlying atmosphere. The spectral radiance measured by a radiometer in space can be described as follows:

$$L = L_S e^{-\tau} + L_A^{\uparrow} + (1 - \epsilon) L_A^{\downarrow} e^{-\tau} \tag{2.7}$$

where the terms on the right hand of the equation represent:

1. radiation emitted from the surface, attenuated by atmospheric extinction
2. upward directed atmospheric radiation
3. reflected downward atmospheric radiation, attenuated by atmospheric extinction

The atmospheric extinction is determined by two processes, absorption and scattering:

Absorption by atmospheric gases

At specific wavelengths, molecular absorption influences the transmittance properties of the atmosphere. In particular the atmospheric gases water vapor, carbondioxide, and ozone have pronounced absorbing properties. As depicted in the middle panel of Fig. 2.1 the penetrability of the atmosphere strongly varies within the electromagnetic spectrum. In some wavelength ranges the atmospheric transmittance is very high, the atmosphere is nearly transparent for radiation. These so called "atmospheric windows" are often used for remote sensing. On the other hand, absorption bands can also be used to directly detect the properties of atmospheric gases such as carbon dioxide.

Scattering

Another phenomenon that influences the detected signal is scattering, which occurs for example in combination with molecules, aerosols, and hydrometeors such as cloud water droplets, rain, and snow. Depending on the wavelength of radiation and the size of the scattering center, different types of scattering can be identified:

- $r \ll \lambda$, *Rayleigh-Scattering*: particle size is much smaller than the wavelength; common with atmospheric gases and strongly dependent on the wavelength
- $r \approx \lambda/2\pi$, *Mie-Scattering*: particle size is about the same as the wavelength; mostly involves aerosol particles and weakly dependent on the wavelength

- $r \gg \lambda$, *Nonselective Scattering*: particle size is much larger than the wavelength; not depending on the wavelength, can be observed with haze, clouds, and fog.

3

The HOAPS Climatology

The initial version of HOAPS (*Schulz et al.*, 1998; *Graßl et al.*, 2000; *Jost et al.*, 2002) mainly based on the algorithms of *Bauer and Schlüssel* (1993). One SSM/I instrument per time period was used without sensor inter-calibration, which resulted in fairly poor data coverage and fairly large systematic deviations of the derived parameters. Comparisons with similar data sets within the SEAFLUX project (*Kubota et al.*, 2003; *Chou et al.*, 2004; *Curry et al.*, 2004) indicated that the evaporation in the first HOAPS version was substantially low biased in the tropics.

The second version, HOAPS II (*Fennig et al.*, 2006ab), was available since mid 2004. It included major improvements, such as the concurrent use of all available SSM/I instruments up to December 2002 including inter-calibration and improved algorithms to derive sea surface flux parameters (*Klepp*, 2005). The tropical evaporation bias was removed by replacing the surface specific humidity algorithm with the one proposed by *Bentamy et al.* (2003) (see section 3.2.2) and using the neural net based wind speed algorithm described in section 3.2.1 of this paper. Sea surface heat fluxes were derived employing a parameterization scheme from *Fairall et al.* (1996b).

Further comparisons revealed however, that the global mean precipitation in HOAPS II was significantly lower compared to other climatologies, resulting in an implausibly large climatological global net ocean surface freshwater flux into the atmosphere. This and a few other issues led to the development of the most recent version HOAPS-3 (*Andersson et al.*, 2007abc).

HOAPS-3 includes a new neural network based precipitation algorithm (see

Table 3.1: Overview of HOAPS-3 parameters and algorithms.

parameter	source	HOAPS-code
wind speed at 10m	neural net algorithm	WIND
AVHRR Oceans Pathfinder SST	*Kenneth* (2004)	ASST
sea surf. satur. spec. humidity	Magnus formula	HSEA
near surf. spec. humidity	*Bentamy et al.* (2003)	HAIR
humidity difference	HSEA minus HAIR	DHUM
evaporation, latent heat flux	*Fairall et al.* (1996b 2003)	EVAP, LATE
sensible heat flux at sea surface	*Fairall et al.* (1996b 2003)	HEAT
latent heat transfer coefficient	*Fairall et al.* (1996b 2003)	TRCE
longwave net flux at sea surface	*Schlüssel* (1995)	FNET
vertically integrated liquid water	*Bauer* (1992)	LWPA
vertically integrated total water	*Bauer and Schlüssel* (1993)	TWPA
vertically integrated water vapor	*Schlüssel and Emery* (1990)	WVPA
precipitation	neural net algorithm	RAIN
freshwater flux	EVAP minus RAIN	BUDG

section 3.2.6), the NODC/RSMAS AVHRR Pathfinder Version 5 SST (see section 3.1.6), and a newly developed 85 GHz channel synthesis algorithm for the missing DMSP F08 data between 1988 and 1990 (see section 3.1.4). HOAPS-3 covers more than 18 years of data between July 1987 and December 2005. In total 15 parameters are available with spatial resolutions of up to 0.5 degree, ranging temporally from monthly and pentad averages to twice daily global ice-free ocean data. Tab. 3.1 gives an overview of all parameters. All data are also archived in native SSM/I resolution for detailed analyses. Homogeneous time-series over several generations of space-borne radiometers are required for the derivation of accurate statistics for climatological analyses. Towards this goal, great care was taken for continued attention to instrument stability and inter-sensor calibration (see section 3.1.3).

Three data subsets of HOAPS-3 are available, scan based pixel-level data and two types of gridded data products, allowing HOAPS to be used for a wide range of applications.

The HOAPS-S data subset contains all retrieved physical parameters in the original SSM/I pixel-level resolution for each individual satellite, providing the basis for the gridded data products HOAPS-G and HOAPS-C.

HOAPS-G climatological datasets contain globally gridded data with a resolution of 0.5 degree. Pentad and monthly means of all 15 parameters are available, consisting of multi-satellite averages including all SSM/I instruments available at the same time (*Andersson et al.*, 2007ca). The data fields are accompanied by basic statistical information about standard deviation and number of observations per grid cell. Climatological mean fields for each parameter along with the climatological monthly means and zonal mean annual cycle can be found in Appendix C.

HOAPS-C contains one-degree twice daily globally gridded multi-satellite composite fields of each parameter (*Andersson et al.*, 2007b). HOAPS-C was introduced to fulfill the need for a globally gridded data product with daily temporal resolution. Each grid cell contains the average of data from the specific satellite that passed this grid box closest to 12 and 24 UTC respectively. Since each grid cell contains data from only one satellite pass, there is no average from two or more satellites. This method provides more spatial consistency on a daily scale than just averaging all available data to daily mean fields. The fields are archived for 00-12 and 12-24 UTC. Time steps in the data files are 0 UTC (00-12 UTC overpasses) and 12 UTC (12-24 UTC overpasses).

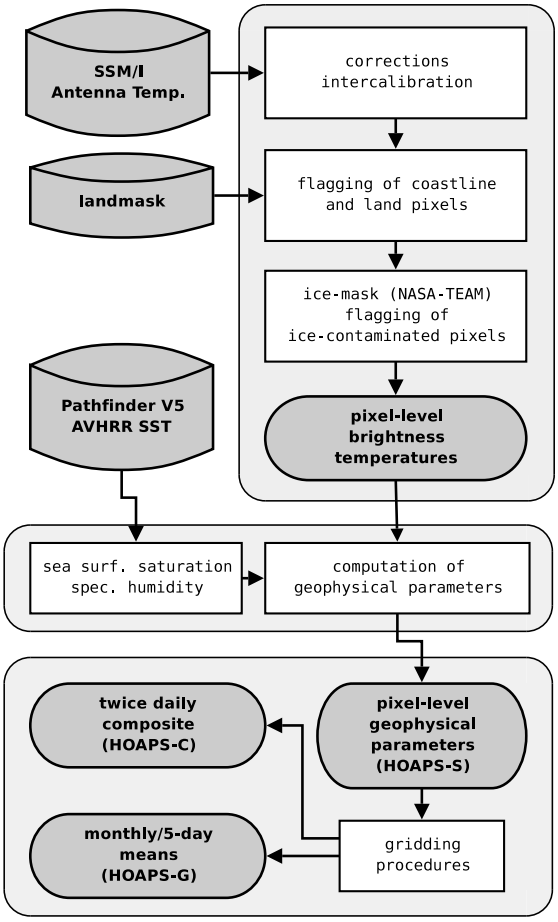

Figure 3.1: Flow chart for the data processing chain in HOAPS from SSM/I antenna temperatures to geophysical products.

3.1 Data Sources and Processing

Starting point in the data processing chain, as illustrated in Fig. 3.1, are SSM/I antenna temperatures. These are converted to an internal *brightness temperature* (TB) data set. This procedure includes several instrument-related corrections, inter-sensor calibration, and the flagging of land and sea-ice covered pixels. From the TB data set and the NODC/RSMAS AVHRR Pathfinder SST, geophysical parameters are calculated on SSM/I pixel level (HOAPS-S). Finally, the previously described gridded HOAPS products are generated from the scan-based HOAPS-S data. The handling of SSM/I raw data and SST data sets is described in the following, while the retrieval algorithms will be described in section 3.2.

3.1.1 The SSM/I Instrument

SSM/I sensors have been carried aboard the DMSP satellite family since 1987. As an extensive description of the instrument and satellite characteristics has been published by *Hollinger et al.* (1990) and *Wentz* (1991), only a very short summary of essential information is given here. The DMSP satellites fly in a near-circular, sun-synchronous orbit, with an inclination of 98.8°at an approximate altitude of 860 km. Each day, 14.1 orbits with a period of about 102 minutes are performed. Complete coverage of the Earth by one SSM/I is achieved within two to three days, except for a small circular sector around the poles.

The SSM/I is a conically scanning, seven channel radiometer measuring emitted microwave rediation at four frequency intervals centered at 19.35, 22.235, 37.0, and 85.5 GHz. The channels will be referred to as 19, 22, 37, and 85 GHz channels hereafter. All data is sampled at horizontal and vertical polarization, except for the 22 GHz channel, which measures only vertically polarized radiation. A fixed cold space reflector and a reference black body hot load are available for onboard calibration. Sampling of the Earth's surface is performed with a constant local zenith angle of 53.1° leading to a 1400 km wide swath. The spatial resolution varies from 69 km by 43 km with a sampling frequency of 25 km for the 19 GHz channel to 15 km by 13 km with 12.5 km sampling frequency for the 85 GHz channel.

To date, six SSM/I instruments have been successfully launched aboard the F08, F10, F11, F13, F14 and F15 spacecraft. All satellites have a local equator crossing time between 5 and 10 a.m./p.m. for the ascending/descending node. The F08 had a reversed orbit with the descending node in the morning. Also, the view direction of the SSM/I on this satellite is, differently from the others, to the aft. Data from all available SSM/I is used in HOAPS. Tab. 3.2 shows the time span of each instrument, as they are used in HOAPS-3.

Table 3.2: Time period of SSM/I instruments used in HOAPS-3.

satellite ID	start date	end date
F08	1987-07-09	1991-12-31
F10	1991-01-07	1996-12-31
F11	1992-01-01	1999-12-31
F13	1995-09-01	2005-12-31
F14	1997-06-01	2005-12-31
F15	2000-03-01	2005-12-31

3.1.2 Data Processing

Main input data for HOAPS are the *Antenna Temperature Tapes* (ATT) from *Remote Sensing Systems* (RSS) and *Temperature Data Records* (TDR) from the *National Environmental Satellite, Data, and Information System* (NESDIS). Either data source has been used during several intervals for various logistic reasons. An analysis of SSM/I data from different sources (*Ritchie et al.*, 1998), including NESDIS TDR and RSS ATT data, showed no systematic differences between these data sets.

In a first step the different input data sets are preprocessed to a common internal data format containing navigated and calibrated antenna temperatures. The antenna temperatures are then converted to TBs according to *Wentz* (1991). In addition, this procedure treats several known issues with the radiometer, including corrections for an along-scan bias (*Wentz*, 1991; *Colton and Poe*, 1999) and zenith angle variations (*Fuhrhop and Simmer*, 1996). Due to the higher resolution of the 85 GHz channels, the zenith angle correction method of *Fuhrhop and Simmer* (1996) is not applicable to these channels.

A single *field of view* (FOV) at 85 GHz covers only about 18% of the area sampled at 37 GHz. However, to correctly apply the retrieval algorithms it is important that about the same area is seen by all channels. To achieve this, a method to average nine neighboring 85 GHz FOVs (A and B scans) down to the resolution of the 37 GHz channel has been implemented. The pixels are weighted according to their distance from the 85 GHz center FOV, resembling a virtual antenna pattern analogue to the 37 GHz channel. TBs of each channel and polarization will be referred to as $TB_{19v/h}$, TB_{22v}, $TB_{37v/h}$, and $TB_{85v/h}$ hereafter.

3.1.3 Inter-sensor Calibration

In the next step, a relative inter-sensor calibration is applied to the TB data. The calibration reference for this procedure is the SSM/I instrument on DMSP F11. This radiometer showed good long-term stability in comparisons of wind speed algorithms with in-situ buoy data and has a temporal overlap with most of the other radiometers. Since the SSM/Is on F08 and F15 do not have a temporal overlap with F11, they are calibrated to the F10 and F13 radiometers, respectively.

In order to determine the calibration coefficients, rain-free oceanic TBs of each channel are binned into a global 1° by 1° grid and averaged for 10 days. These selection criteria increase the polarization ratio of the channels, filter highly variable events like precipitation, and minimize the influence of diurnal cycle variations. For each radiometer a match-up data set with the selected reference radiometer is compiled from the gridded 10-day mean TBs for at least one overlapping year. This match-up data set is randomized and histogram-equalized with a histogram bin size of 1 K for the range 100-300 K. The calibration coefficients are then calculated with a linear regression between the TBs of both radiometers. Due to the accurate and stable in-orbit calibration, the coefficients are considered to be constant during the lifetime of a radiometer. However, the unstable orbit of the F10 satellite platform, needed a recalibration for the radiometer aboard the DMSP F10. Calibration coefficients were determined for the two years 1992 and 1996 and then linearly interpolated to the respective year.

This kind of inter-sensor calibration ensures a homogeneous time series of successive radiometers.

As an example for the result from this procedure, Fig. 3.2 shows a comparison of global mean TB_{19v} for each SSM/I before and after application of the inter-sensor calibration coefficients. Only minor differences in the brightness temperature time series remain after the intercalibration has been applied, which can be mainly attributed to the different sampling and diurnal cycle of the individual satellites.

3.1.4 Synthesis of 85 GHz Channel Data

From April 1988 to the end of its lifetime, both 85 GHz channels on the DSMP F08 spacecraft were defective (*Wentz*, 1992). This failure affects all HOAPS parameters depending on these channels (i.e. precipitation, vertically integrated liquid and total water content, and longwave net flux at sea surface). A computationally efficient way of handling this problem is to synthesize approximate values of the missing 85 GHz information from the remaining channels. This allows the application of the same algorithms for all parameters throughout all analysis steps

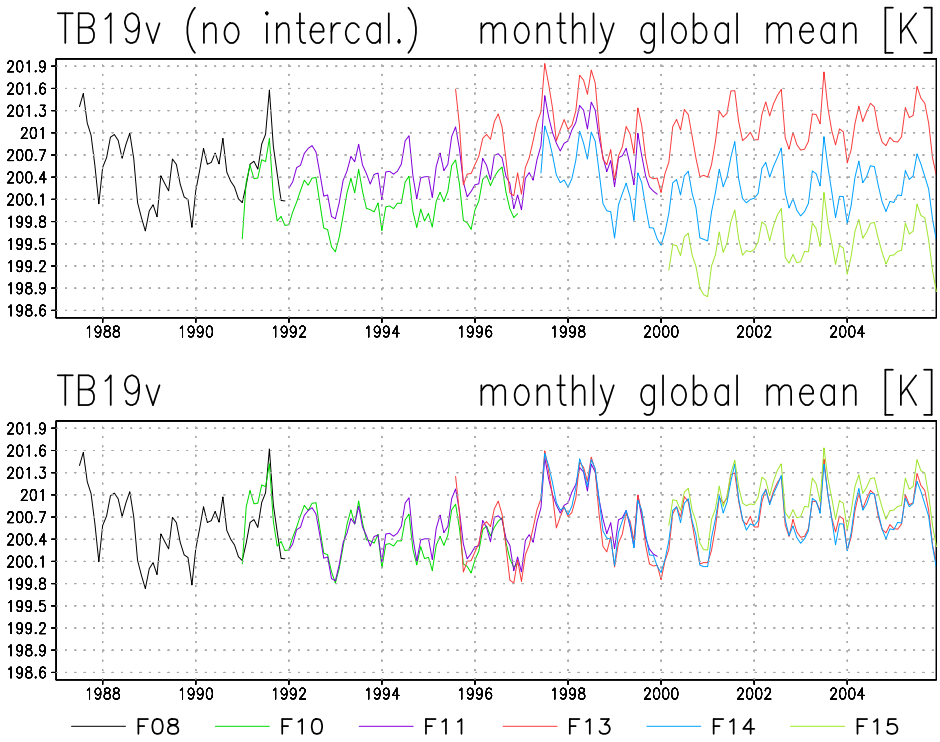

Figure 3.2: Example for SSM/I inter-sensor calibration as applied in the HOAPS processing chain. Time series of monthly global mean TB_{19v} of each SSM/I without (top) and with (bottom) inter-sensor calibration.

Table 3.3: Global mean error values for parameters calculated with synthesized brightness temperatures.

Parameter	mean $TB_{SSM/I}$	mean TB_{synth}	RMSE	bias
RAIN [mm/d]	2.97	3.09	0.16 (5.4%)	0.12 (4.0%)
LWPA [kg/m^2]	0.1351	0.1303	0.0053 (3.9%)	-0.0048 (3.6%)
TWPA [kg/m^2]	0.2013	0.1974	0.0045 (2.2%)	-0.0039 (1.9%)
FNET [W/m^2]	54.44	47.31	7.25 (13.3%)	-7.13 (13.1%)
TB_{85h} [K]	232.65	232.13	1.20 (0.5%)	-0.52 (0.2%)
TB_{85h} [K]	260.06	260.98	1.17 (0.4%)	0.92 (0.4%)

without individual replacement algorithms for each parameter. It has however to be kept in mind, that such a procedure cannot fully reconstruct the specific 85 GHz information but is only a computationally convenient way of handling the missing data by a plausible replacement.

The synthesis is based on a neural network approach, which is used to estimate $TB_{85v/h}$ of the 9-pixel averaged 85 GHz FOV (see section 3.1.2) from the other SSM/I channels ($TB_{19v/h}$, TB_{22v}, and $TB_{37v/h}$).

The training dataset for the neural network was compiled from randomly selected brightness temperatures of SSM/I radiometers on board DMSP F11, F13, and F14 from 1998. In this year the El Niño event generated extreme values, resulting in a wide distribution of TBs. Pixels containing high near surface wind speeds or precipitation generate a comparable signal in the 19 and 37 GHz channels. A good relationship to separate such situations proofed to be

$$TB_{37v} - TB_{37h} \gtrless 0.25 \cdot TB_{22v} + 104K \tag{3.1}$$

Based on this relationship two input data sets were constructed and the algorithm was divided into two parts. To ensure an equal distribution of the training data, the input values were binned in a two dimensional grid using TB_{22v} and the precipitation rate as x and y axis, yielding approximately 30 000 data samples for each training data set. Finally, the input values were normalized to the sample mean and standard deviation. These data sets were used to train, two fully connected feed forward networks consisting of six input neurons ($TB_{19v/h}$, TB_{22v}, $TB_{37v/h}$, TB_{22v}-TB_{19v}), two hidden layers, and two output neurons (TB_{85h} and TB_{85v}).

Tab. 3.3 summarizes the resulting values for all other parameters depending on the 85 GHz channels. The results for the precipitation rate, vertically integrated

liquid and total water content turn out to be very good. For the longwave net flux, the results are less convincing, but sufficient.

3.1.5 Land Mask and Sea Ice Detection

All SSM/I pixels within 50 km of any coastline and sea ice margin are neglected in HOAPS in order to avoid any contamination of the data caused by the abrupt change in surface emissivity between water, land or sea ice covered areas. The corresponding areas are flagged during the processing in the pixel-level data (see Fig. 3.1).

A static high resolution land-sea mask is derived from the Global Land One-km Base Elevation data base (*GLOBE Task Team*, 1999), however removing small islands and expanding the coastlines 50 km into the sea.

To account for the varying sea ice margins, a daily sea ice mask is generated from the HOAPS SSM/I TBs. In a first step the total sea ice covered fraction within a single SSM/I FOV is computed with the NASA Team sea ice algorithm of *Swift et al.* (1985). The resulting sea ice observations from all available SSM/I instruments are then gridded to common daily fields on a regular $0.5° \times 0.5°$ grid. In order to distinguish between strong rain events and sea ice, which are characterized by similar TB signatures, only grid boxes with an averaged sea ice fraction above 15 % for at least 5 consecutive days are accepted as ice covered. Daily sea ice maps are then derived from this reduced data set by re-expanding the reliably identified sea ice areas in time and space and filling remaining data gaps by spatial and temporal interpolation. Finally, the resulting sea ice margin is extended 50 km into the ocean to avoid any spurious sea ice contamination.

3.1.6 Sea Surface Temperature

To rely exclusively on satellite data for the computation of latent and sensible heat flux parameters, the *NOAA National Oceanographic Data Center* (NODC) and *Miami's Rosenstiel School of Marine and Atmospheric Science* (RSMAS) Oceans Pathfinder Version 5.0 SST product is used within HOAPS (*Kilpatrick et al.*, 2001; *Kenneth*, 2004; *NODC*, 2008). In the Pathfinder data set a quality flag with a value from 0 to 7 is assigned for each pixel, with 7 being the highest quality observation. For the further processing in HOAPS, only pixels with a minimum overall quality flag of four are accepted. This conforms with the Pathfinder Version 4 "best-SST" product and involves several quality checks including a cloud screening (c.f. *Kilpatrick et al.* (2001) for details).

Pathfinder AVHRR day and night-time observations data are averaged to daily SST maps. Data void regions are filled by spatial and temporal interpolation.

Table 3.4: NOAA satellite IDs for AVHRR instruments used in NODC/RSMAS Pathfinder V5. (i) denotes periods with interim coefficients.

Year	Satellite
1987–1988	NOAA-09
1989–1994	NOAA-11
1995–2000	NOAA-14
2001	NOAA-16
2002	NOAA-16 (i)
2003	NOAA-17
2004–2005	NOAA-17 (i)

Finally, the data is remapped to SSM/I pixel resolution. Tab. 3.4 shows the individual NOAA satellites and their temporal coverage in the NODC/RSMAS Pathfinder V5 as used for HOAPS-3. Periods denoted with (i) refer to a year of data where interim coefficients from the previous year are used to calculate empirical coefficients in the Pathfinder SST algorithm. At the time of the processing of HOAPS-3, Pathfinder SST data computed with regular coefficients were not available for these periods and data based on the interim coefficients is used. The regular coefficients are computed from a buoy match-up data set and are processed with a delay to the realtime data in order to maintain the long term stability of the data set (*NODC*, 2008). Consequently, the SST data computed using the interim coefficients may reveal a slight bias compared to the final values.

It should be mentioned here, that in the wake of the June 1991 eruption of Mt. Pinatubo, the high load of volcanic aerosol contaminated the AVHRR radiance measurements and the atmospheric correction of the SST retrieval had to be increased (*Kilpatrick et al.*, 2001). Consequently, undetected aerosol leads to a nighttime cold bias in the daily mean SST fields (*Reynolds*, 1993). During the first phase for about 6 months following the eruption, a significant bias is introduced in the SST. Hence, the retrievals of latent and sensible heat flux are impaired during this period. Overall, a cooling through the aerosol injected by Mt. Pinatubo is detectable in satellite derived SST data until 1993 (*Lawrence et al.*, 2004). A further evaluation of this issue will be given in chapter 4.3.

3.2 Retrieval Schemes and Parameterizations

In this section the algorithms and parameterizations to derive HOAPS parameters are described with a focus on previously unpublished algorithms. Latent and sensible heat fluxes are estimated with a bulk aerodynamic approach employing *Fairall et al.* (1996b 2003). This method requires the knowledge of near surface wind speed, SST and atmospheric near surface specific humidity. The retrieval of the longwave net flux also depends on SST data. All other parameters such as atmospheric water contents and precipitation are derived directly from SSM/I measurements.

3.2.1 Wind Speed

The near surface wind speed is dynamically coupled to short ripple waves and foam coverage of the ocean surface, which in turn influences the surface emissivity and hence the upwelling radiances. At satellite altitude, the SSM/I brightness temperatures (especially TB_{19h} and TB_{37h}) increase non-linearly with increasing wind speed. To retrieve the wind speed, also TB_{19v}, TB_{22v}, and TB_{37v} have to be considered in order to remove the atmospheric contribution to the radiometric signal, which would otherwise tamper the wind induced surface signatures. However, situations with high liquid water content or high rain water content are filtered, since the strong emission from atmospheric water is masking the surface signal.

Following a neural network approach after *Krasnopolsky et al.* (1995), the wind speed is estimated using a fully connected 3-layer feed forward neural network, composed of one input layer utilizing $TB_{19v/h}$, TB_{22v}, and $TB_{37v/h}$, a hidden layer with three neurons and an output layer with one neuron, the wind speed (Fennig, pers. comm). All three neurons in the hidden layer are non-linear with the sigmoid function *tanh* as the unit's activation function. The output neuron is linear in order to maximize the networks extrapolation capabilities (Fennig, pers. comm).

Two different data sets serve as input for the training data set, one derived from radiosonde profiles and radiative transfer simulations and a second one from collocated SSM/I and buoy observations. This approach ensures the representativeness of the input and output data of the neural network.

The radiosonde data set consists of about 2 000 globally distributed atmospheric profiles. These are subsampled in groups of equidistant surface wind speed steps of 2 m/s within a range from 2 to 30 m/s. The radiation emitted from the ocean surface is calculated with the surface emissivity model of *Bauer* (2001) and the top of the atmosphere radiance is calculated with the radiative transport scheme of *Schlüssel and Emery* (1990).

The buoy data set is compiled using match-ups between SSM/I F11 TBs with near-surface wind speed measurements from 20 buoys from the *National Data Buoy Center* (NDBC) and 59 buoys from the *Tropical Atmosphere/Ocean* (TAO) array for the years 1997 and 1998. The criterion of a maximum difference of 30 minutes and 50 km between satellite and buoy observations resulted in a match-up data set of about 470 000 samples.

Both data sets are then combined by collecting all data samples in 2 m/s wide wind speed bins, ensuring that all parts of the wind spectrum are equally weighted. The neural network's training data set is then compiled by taking an equal number of randomized samples from each of the wind speed bins. The resulting data set consists of about 15 000 samples. By taking randomized samples separately for each bin, the input TBs cover the whole possible range of atmospheric conditions including high water vapor observations from the TAO buoys. The smaller wind speed ranges are mixed with data samples from both data sets, while most samples larger than 15 m/s originate from the set of radiative transfer calculations.

Applied to the training data set, the wind speed algorithm has a retrieval rms error of 1.6 m/s with zero bias and a correlation coefficient of 0.98. Applying the algorithm to the entire buoy data set yields an overall bias of 0.08 m/s and an rms value of 1.65 m/s (r = 0.83) (Fennig, pers. comm).

3.2.2 Humidity Parameters

The algorithm for the specific air humidity at the reference level of 10 m above the sea surface is based on a two-step regression method after *Schulz et al.* (1993) and its refinement by *Schlüssel* (1996). *Bentamy et al.* (2003) showed that the chosen linear channel combination is sufficient for the estimation of the near surface specific humidity. Recalculating the regression coefficients with an improved training data set removed a bias of 2 g/kg in the inner tropics due to high precipitable water values (*Bentamy et al.*, 2003).

For the derivation of the evaporation through the bulk formula, the difference in humidity, i.e. sea surface specific humidity minus near surface specific humidity, is calculated. The sea surface saturation specific air humidity is calculated by applying the Magnus formula to SST. An approximate salinity correction is applied by scaling the value for pure water with a factor of 0.98.

3.2.3 Turbulent Heat Flux Parameterization and Evaporation

HOAPS-3 latent and sensible heat fluxes are parameterized using the *Coupled Ocean-Atmosphere Response Experiment* (COARE) bulk flux algorithm version 2.6a (*Bradley et al.*, 2000), which is an updated version of the COARE 2.5b algo-

rithm (*Fairall et al.*, 1996b), based on a flux database containing measurements from higher latitudes and under stronger wind conditions. With minor modifications of physics and parameterizations to the version 2.6a, the algorithm is published as COARE 3.0a by *Fairall et al.* (2003).

The COARE algorithm iteratively estimates stability dependent scaling parameters and wind gustiness to account for sub-scale variability. The latent and sensible heat fluxes Q_l and Q_s are calculated by:

$$Q_l = \rho L_E C_E u \left(q_s - q_a\right) \tag{3.2}$$

and

$$Q_s = \rho c_p C_T u \left(T_s - \Theta_a\right) \tag{3.3}$$

where ρ is air density, c_p is specific heat of the air at constant pressure, u is the wind speed at 10 meters height, L_E is the latent heat of evaporation (calculated SST-dependent), C_T is the Stanton number, C_E is the Dalton number, T_s is the SST, Θ_a is the potential air temperature, q_s is the saturation specific humidity at the sea surface, and, q_a is the specific humidity at the 10 m atmospheric measurement level. Apart from the air temperature and the transfer coefficients C_T and C_E, all parameters are derived from SSM/I measurements or from the SST as described above.

The air temperature is estimated using the mean of two simple bulk approaches:
a. The satellite derived near surface specific humidity is assumed to be at a constant relative humidity of 80 %.
b. A constant temperature difference of 1 K between sea surface and air temperature is assumed.

Under certain conditions, especially at strong stable stratification of the atmospheric surface layer, this will affect the quality of the sensible heat flux. On climatological scale, this error should not have a significant effect on the quality of the parameters.

Evaporation is calculated from the latent heat flux after *Fairall et al.* (1996b) by:

$$E = Q_l/(L_E \rho_0) \tag{3.4}$$

where ρ_0 is the freshwater density as a function of temperature.

3.2.4 Longwave Net Flux

The longwave net flux at the sea surface is computed following *Schlüssel* (1995) from the atmospheric back radiation and the SST utilizing the spectrally inte-

grated surface emissivity which is close to 0.89 (*Gardashov et al.*, 1988) and the Stefan-Boltzmann constant. The atmospheric back radiation is retrieved directly from SSM/I measurements with the algorithm of *Schlüssel* (1995) under clear and cloudy conditions using the TB_{22v}, $TB_{37v/h}$, and $TB_{85v/h}$ channels.

3.2.5 Water Content and Water Vapor Parameters

The liquid and ice phase in clouds and precipitation strongly change the radiative properties of the atmosphere within the microwave spectrum and directly influence the radiometer signal. To account for different atmospheric conditions, a threshold technique is used to distinguish between cloud-free, cloudy and rainy scenes. A different set of individual algorithms is used to derive liquid and total water paths for each situation. This approach is based on the internally calculated total water path and rain-rates as described in *Bauer and Schlüssel* (1993).

Nearly all of the water vapor variance is explained by the TB_{22v} channel, which is located within the 22.235 GHz water vapor absorption line. Hence allowing the derivation of quite robust algorithms to obtain the vertically integrated water vapor. In HOAPS, the vertically integrated water vapor is derived with the globally applicable retrieval scheme of *Schlüssel and Emery* (1990). Major information on the integrated water vapor is contained in the 22 GHz channel located in a water vapor absorption line. This algorithm additionally uses TB_{37v} to correct for undesirable effects of atmospheric liquid-water content or extreme near surface temperature gradients in TB_{22v}.

3.2.6 Precipitation

Microwave based retrievals of precipitation are based on the direct interaction of the radiation field and the hydrometeors (water droplets, ice particles). The emission from cloud and rain particles at small frequencies causes a strong increase of the brightness temperatures and results in a strong contrast to the radiometrically cold sea surface. In contrast to that, the brightness temperature at high frequencies decreases, with increasing precipitation due to the scattering of radiation by the precipitation elements.

The successful usage of a neural network for the near-surface wind speed retrieval also encouraged a similar approach for the precipitation algorithm. A fully connected 3-layer feed forward network was constructed that includes (Fennig, pers. comm):

- an input layer with six neurons at $TB_{19v/h}$, TB_{22v}, $TB_{37v/h}$, and TB_{85v}

Table 3.5: Accuracies of the neural net algorithm for precipitation. N = number of samples; mean, bias, and RMS are in mm/h. (see text)

Data set	N	mean	bias	RMS	r
verification data set	54850	0.255	-0.007	0.062	0.950
complete data file	2596899	0.158	-0.063	0.157	0.915
complete data file cutoff: 0.3 mm/h	357492	0.780	-0.166	0.342	0.907

- a hidden layer with three non-linear neurons using the tanh function as the activation function and
- an output layer with one linear neuron, the rain rate.
- additional direct linear connections from TB_{19v} and TB_{22v} to the output neuron

The training data set is based on radiative transfer calculations as described in *Bauer et al.* (2006ab). The data set contains one month (August 2004) of assimilated SSM/I TBs and the corresponding precipitation values of the *European Centre for Medium-Range Weather Forecast* (ECMWF) model. This data set covers a wide variety of globally distributed rainfall events including extreme rainfall in hurricanes. However, as it consists of more than 2.5 million data samples, it must be filtered in order to ensure good coverage and equal weight of all possible input TB combinations. Hence it was binned in a two-dimensional grid using TB_{22v} and the polarization difference TB_{19v}-TB_{19h} as x and y axis. The final training data set was then compiled by randomly taking an equal number of samples from each bin, which makes about 110 000 data samples in total of which only 50 % were actually used for training. In order to avoid an inappropriately high influence of the larger uncertainties at higher precipitation rates, the training values were scaled non-linearly by the following transformation, with R^* representing the transformed precipitation rate (Fennig, pers. comm):

$$R^* = \sqrt{log10\,(R+1)} \tag{3.5}$$

A lower threshold value is put to the algorithm, below which the precipitation signal is considered to be zero. From experience with the formerly used algorithm, a value of 0.3 mm/h turned out to be an appropriate limit for distinguishing between a real precipitation signal and background noise.

The results of this training procedure are depicted in Tab. 3.5. The first line shows the quality of the derived algorithm compared to the unused second half of the training data set. Due to the strong peak of the distribution at cases of small precipitation, the mean precipitation rate is only about 0.25 mm/h. The derived algorithm reproduces the test cases with a correlation of r=0.95, a very small bias and a RMS of about 0.006 mm/h, which represents the theoretical algorithm accuracy. Testing the algorithm against the complete ECMWF data yields a lower mean value of 0.16 mm/h, which is due to the larger sample size compared to the verification data, a bias of -0.06 mm/h, and a RMS of 0.16 mm/h. When a lower cutoff of 0.3 mm/h is applied to the ECMWF data set as it is done in the HOAPS retrieval, the mean precipitation rate increases to 0.78 mm/h. Bias and RMS are also very low with values of -0.17 mm/d and 0.34 mm/h, respectively. The correlation is in the range of two previous cases with r=0.91.

The detection rates of the algorithm compared to the ECMWF training data set are 93.4 % correctness for the raining and rain-free cases, with a probability of rain detection of 70.5 % and a false alarm rate of 20.4 % (Fennig, pers. comm).

3.2.7 Freshwater Flux

The freshwater flux in mm/d of each grid box is computed as the difference between the spatially and temporally averaged evaporation and the averaged precipitation. Hence no statistical variables like the number of observations or standard deviation are available.

4

Global Evaluation of HOAPS Parameters

In this chapter HOAPS parameters are evaluated at climatological scale. The assessment of systematic differences and pattern consistency between HOAPS-3 and other data sets is the main aim of this chapter. Algorithm-specific uncertainties are described in chapter 3.2 and related publications. In particular, the focus is on wind (see chapter 3.2.1) and precipitation (see chapter 3.2.6) retrievals, which are newly introduced in HOAPS-3. Furthermore the SST, which is used from an external source in HOAPS, will be investigated with respect to the possible error due to the outbreak of Mt. Pinatubo in 1991. Finally, the evaporation and freshwater flux parameters are inspected at climatological scale.

First evaluations of HOAPS-3 have been presented by *Andersson et al.* (2007de), showing overall good long term stability and performance of HOAPS-3 precipitation and flux products.

4.1 Wind Speed

A previous study involving the HOAPS-3 wind speed, was carried out by *Winterfeldt et al.* (2009) who compared HOAPS-3, QuikSCAT/SeaWinds scatterometer, and NCEP-reanalysis wind speeds with North Sea and North Atlantic buoy data. In that study the HOAPS wind retrieval showed RMS values of 2 m/s, which is comparable to QuikSCAT's mission requirement and is regarded to be consistent with values from other studies. It is shown that HOAPS performs equally well in near coastal and remote regions. *Blechschmidt* (2008) and *Zahn et al.* (2008) successfully used HOAPS-3 wind speed data for the detection and model validation

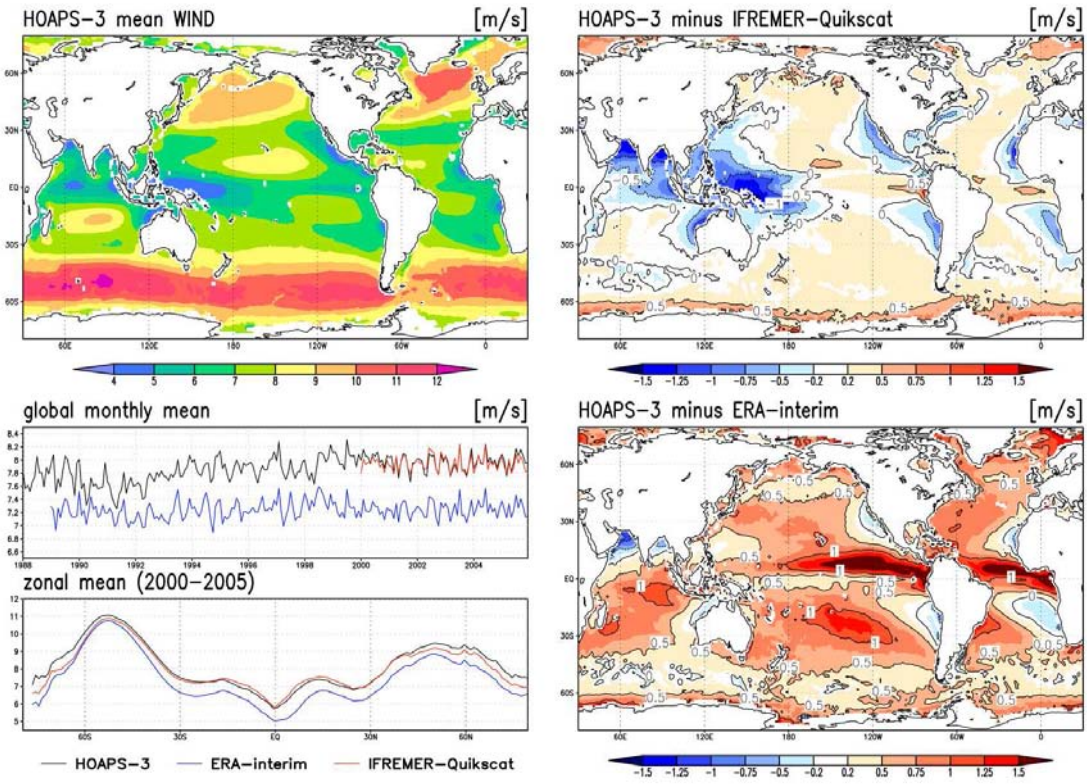

Figure 4.1: HOAPS-3 1988-2005 mean wind speed (top left) compared to IFREMER QuikSCAT (upper right) (1999-2005) and ERA-interim (lower right) (1988-2002). Lower left panel shows the global monthly mean wind speed of each data set and the zonal mean wind speed for the overlapping time period September 1999 to August 2002.

of Polar Low events in the North Atlantic.

HOAPS climatological mean wind speed for the years 1988 to 2005 is shown in the top left panel of Fig. 4.1. North Atlantic and Pacific storm track regions can be clearly identified as well as the Southern Ocean maxima in the "Roaring Forties" and "Furious Fifties". The characteristic minima of the subtropical Calms and the southeast Asian warm pool region are also clearly evident. Secondary local maxima exist in the tropical trade wind area.

In the following, HOAPS wind speed is compared with the QuikSCAT mean wind field (MWF) product (*IFREMER/CERSAT*, 2002) from IFREMER and with the analyzed monthly mean wind speeds of the new interim *ECMWF Re-Analysis* (ERA, *Simmons et al.*, 2007). The IFREMER product uses a kriging technique to construct globally gridded and gap-filled synoptic fields from individual observations of the SeaWinds scatterometer on the QuikSCAT satellite. For this comparison, data for the overlapping period with HOAPS-3 from 2000 to 2005 is used. The *ERA interim* (ERAint) reanalysis is a new and improved re-

analysis data set provided by the ECMWF. It uses an advanced data assimilation scheme and additional observations from various sources compared to ERA-40. At present date, the ERAint record starts at 1989. Hence the comparison will refer to the years 1989 to 2005.

The top right panel of Fig. 4.1 shows the difference between HOAPS and the IFREMER product. On the global scale, both data agree well with a bias below 0.2 m/s. Relevant deviations occur in the tropical warm pool and monsoon regions where HOAPS wind speeds are more than 1 m/s lower than the IFREMER product on average. Over the upwelling regions at the western continental boundaries differences are also evident. The reason for this may lie in the differences of the radiative transfer models used to derive the retrievals. Both products show very good agreement in magnitude and variability for the monthly global mean time series and zonal mean (Fig. 4.1, lower left panels), and have a high correlation of r=0.80. At high latitudes above 60° HOAPS wind speeds are systematically higher than the QuikSCAT winds by more than 0.5 m/s. Larger differences in these regions are presumably caused by residual errors introduced through different sea ice detection procedures.

The bottom right panel of Fig. 4.1 shows the difference of wind speed between HOAPS-3 and ERAint. HOAPS wind speeds are generally higher than ERAint, and a mean bias of 0.60 m/s is found on the global scale, with the highest local differences occurring in the tropical regions. A similar behavior in the comparison of satellite retrieved wind speeds in comparison with reanalysis data was found in earlier studies (*Meissner et al.*, 2001; *Kelly et al.*, 2001; *Monahan*, 2006). One reason for the systematic differences lies in the principle of the wind speed determination. Satellite observations measure the surface wind stress, which is then often recalculated to represent 10-m equivalent neutral-stability windspeed. In contrast to that, the reanalysis models simulate the actual winds at 10 m. Another general error source is, that the reanalyses implement a static sea surface, while satellite measurements are sensitive to surface currents and measure the wind speed relative to the underlying sea surface. Also, the regionally varying measurements acquired by rawinsondes and the radiative transfer calculations underlying the satellite retrieval algorithms and the reanalyses lead to locally different results in the wind speed.

Distinct local differences in the comparison of HOAPS and ERAint (Fig. 4.1, bottom right panel) occur in the *Inter-Tropical Convergence Zone* (ITCZ), where HOAPS exhibits systematically higher values compared to ERAint, while the largest negative bias is found in the Arabian Sea, and Bay of Bengal.

In regions with cold surface currents, such as the Antarctic Circumpolar Current and at the upwelling regions on the western continental boundaries HOAPS and ERAint show comparable values. HOAPS winds are partly lower than these

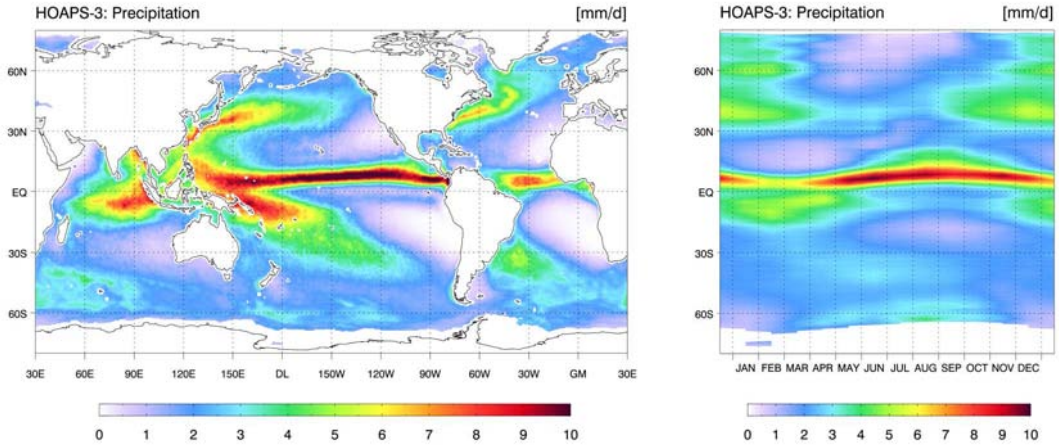

Figure 4.2: Climatological mean field (left) and zonal mean annual cycle (right) of HOAPS-3 precipitation for the years 1988-2005.

from ERAint and the patterns are comparable to the difference of HOAPS and the IFREMER QuikSCAT product.

The correlation coefficient of the HOAPS and ERAint time series (Fig. 4.1, bottom left panel) is r=0.66, which is considerably smaller than between HOAPS and the IFREMER QuikSCAT product. Apart from the constant bias, the zonal mean for ERAint compares well to the two other data sets. The location of the latitudinal maxima is very similar to the satellite products.

4.2 Precipitation

In this section, HOAPS precipitation is compared with the *Global Precipitation Climatology Project* (GPCP) version 2 combined product (*Adler et al.*, 2003) and the *Tropical Rainfall Measuring Mission* (TRMM) 3B43 data set (*Adler et al.*, 2000).

Over the ocean, these products use a combination of various data sources for their precipitation estimates. This includes passive microwave and infrared data from polar orbiting and geostationary satellites. The 3B43 estimate also integrates data from the *TRMM Microwave Imager* (TMI) and the *Precipitation Radar* (PR), operated on the TRMM satellite since 1997. GPCP covers the whole record of HOAPS-3, while the TRMM product is only available for a comparison during the period 1998 to 2005.

In the climatological mean precipitation from HOAPS-3 (Fig. 4.2, left panel), the well-known global precipitation distribution patterns are represented. Dominant features are the overall highest rain rates in the ITCZ, as well as the regional

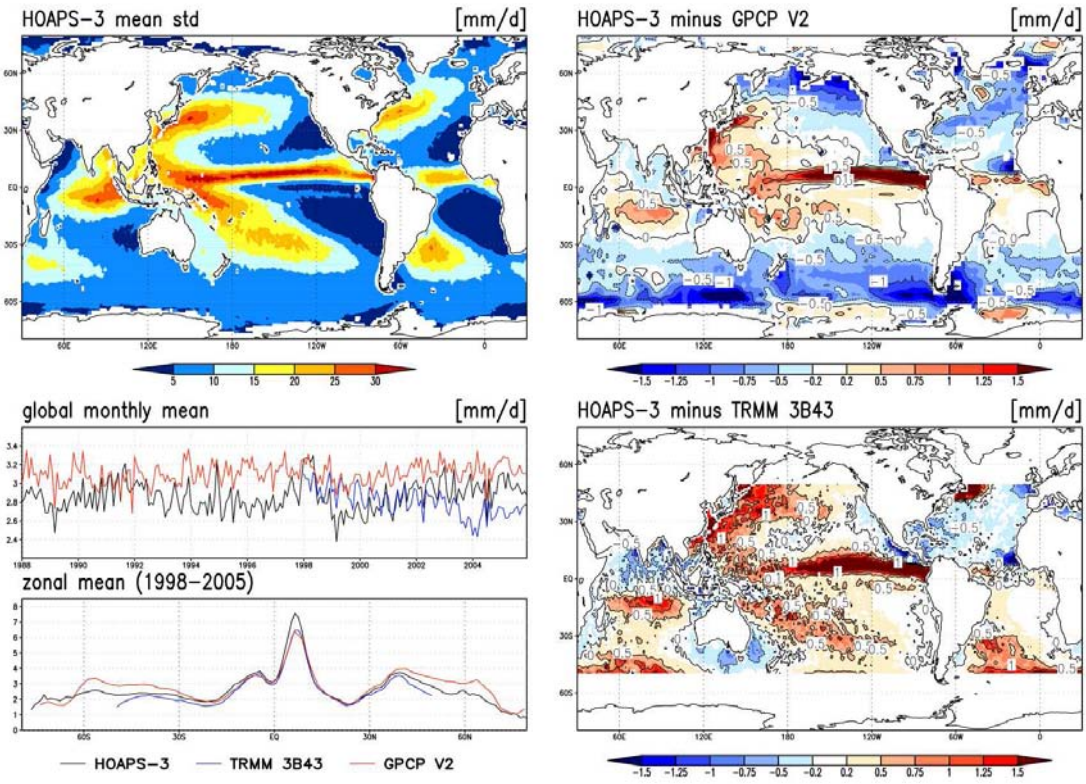

Figure 4.3: HOAPS-3 mean monthly standard deviation of precipitation (top left), HOAPS-3 minus TRMM 3B43 (1998-2005) precipitation rate (upper right), HOAPS-3 minus GPCP V2 (1988-2005) precipitation rate (lower right). The lower left panel shows the global monthly mean of each time series and the zonal mean for the overlapping time period from 1998 to 2005.

maxima over the Indian Ocean and the *South Pacific conversion zone* (SPCZ). North Atlantic and Pacific storm tracks are also clearly identifiable. Global precipitation minima can be observed in the so called subtropical oceanic deserts in the eastern Atlantic and Pacific. The zonal mean annual cycle is shown in the right panel of Fig. 4.2. Clearly evident is the northward and southward displacement of the ITCZ throughout the year, as well as high precipitation values induced by Northern Hemisphere autumn and winter storm tracks and the Southern Hemisphere subtropical maximum, which develops from January to April.

The mean monthly standard deviation of HOAPS-3 precipitation is shown in the top left panel of Fig. 4.3. Regions of strong variability coincide with domains of high precipitation values with the maximum located in the ITCZ and the southeast Asian monsoon regions.

The difference map between HOAPS-3 and TRMM 3B43 precipitation (Fig. 4.3 lower right panel) shows an overall good agreement between the data sets. In total, HOAPS precipitation is slightly higher with deviations below 0.5 mm/d for most

regions. This may be attributed to the introduction of the *Advanced Microwave Sounding Unit-B* (AMSU-B) data to the TRMM data set in 2001-2003, which gradually introduced a low bias of about 10 % (*GSFC*, 2007). The effect can also be identified in the global mean time-series in the lower left panel of Fig. 4.3. Regional differences can be observed coinciding with high variability over the western Pacific, the SPCZ, and the Indian Ocean. In these regions, HOAPS exceeds the TRMM product by up to 1 mm/d. However, due to the high mean values of precipitation the relative deviation is less than 15-20 %. The largest absolute difference can be found in the central Pacific ITCZ where HOAPS-3 exceeds TRMM by more than 1.5 mm/d. Only in the North Atlantic, HOAPS precipitation is systematically lower compared to the TRMM 3B43 data.

The comparison of HOAPS-3 with GPCP V2 exhibits similar differences for the tropical regions. HOAPS precipitation is slightly higher with the maximum deviation of about 1.5 mm/d located at the Pacific ITCZ. In the mid and high latitudes between 40° and 70° GPCP precipitation is systematically higher than HOAPS, while above 70° HOAPS mostly exceeds GPCP. Poleward of 40° north and south GPCP utilizes *TIROS Operational Vertical Sounder* (TOVS) infrared data to compensate deficiencies in the GPCP high-latitude microwave based retrievals (*Adler et al.*, 2003). At mid-latitudes the TOVS data is adjusted to the large-scale bias of the SSM/I estimates, and at high latitudes beyond 70° the adjustment is done using rain gauge data. Aside from this, the consistency between all products is good between 40° north and south. The overall bias in this region is low and the tropical and subtropical minima and maxima agree in location and magnitude for all data sets, apart from the northern branch of the ITCZ, which is stronger in HOAPS.

On regional scale, the detection of cold season precipitation over the ocean at high latitudes and its validation in particular is a mostly unsolved issue. Detailed case study analyses on mid-latitude cyclones with intense post-frontal mesoscale convective mixed-phase precipitation were carried out by *Klepp et al.* (2003). Utilizing in-situ voluntary observing ship data it was shown that HOAPS, in contrast to other satellite products, recognizes all systems that lead to precipitation with reliable patterns and intensities. This type of precipitation is also mostly missing in a large sample of events investigated in the ECMWF numerical weather prediction and ERAint re-analysis data sets (*Klepp et al.*, 2005). To further validate these finding,s a cold season in-situ experiment for measuring quantitative precipitation using an optical disdrometer was carried out on a research vessel offshore the Lofoten Islands off Norway. This data set contains light to moderate snowfall along with cases of drizzle and a passage of a polar low. *Klepp* (2007) demonstrates the ability of HOAPS to detect even minor amounts of cold season precipitation with reasonable patterns and amounts.

4.3 SST

The SST is the only parameter in HOAPS which is not retrieved from SSM/I measurements, but taken from the ancillary NODC/RSMAS AVHRR Pathfinder V5 SST data set.

As mentioned in chapter 3.1.6, the Pathfinder V5 data set exhibits an anomaly following the eruption of Mt. Pinatubo in June 1991. In order to assess the effects of the eruption on the SST data and consequently the HOAPS-3 evaporation, the entire HOAPS-3 data set was reprocessed using an alternative AVHRR-based SST product. All reliable satellite derived global SST time series that are available for the entire HOAPS-3 record are based on AVHRR measurements. Thus an evaluation with a data set that is fully independent from the NODC/RSMAS Pathfinder SST is not possible for the time period of the Mt. Pinatubo eruption.

Moreover, an evaluation of the standard HOAPS-3 data against a time series that was reprocessed using the alternative SST data set may reveal systematic differences in the flux parameters. Especially the latent heat flux, i.e. evaporation, is of interest as being one component of the freshwater flux. However, the following results for the evaporation are mainly valid for the sensible heat flux parameter as well.

A suitable global data set to substitute the *NODC/RSMAS Pathfinder V5 SST* (PFSST) is the *Daily Optimum Interpolation (Daily OI) SST* (DOISST) which is based on the 1971-2000 Reynolds OI.v2 SST methodology (*Reynolds et al.*, 2002 2007). The DOISST data set contains daily mean SST fields and is based on the AVHRR Pathfinder time series. In situ data from buoys and ships are used for an additional bias adjustment of the satellite measurements and data gaps are filled by applying an optimum interpolation method. Due to the additional corrections applied, the DOISST product is expected to show distinct differences in a comparison with the PFSST.

Moreover, the DOISST data set provides a bulk SST representative for the SST at some meters depth from a well mixed layer, while the PFSST contains data which are more comparable to skin SST values, as it is required for the HOAPS-3 flux retrievals. The oceanic skin layer consists of the upper few micrometers of the ocean surface. Due to molecular transport processes from the upper ocean to the sea surface in this layer, it is typically some tenths of degrees cooler compared to the underlying water (*Graßl*, 1976; *Schluessel et al.*, 1990). The difference of skin and bulk SST varies between day and nighttime and depends on the wind speed and net heat flux (*Wick et al.*, 1996). In previous studies (e.g. *Graßl*, 1976; *Schluessel et al.*, 1990; *Fairall et al.*, 1996a; *Wick et al.*, 2002) mean values ranging from 0.1 to 0.35 °C were found for the skin–bulk difference at day and nighttime, respectively. Hence, a globally constant value of 0.2 °C is assumed as

an approximation for the daily mean cool skin effect and was subtracted from the DOISST before the processing, in order to obtain SST values comparable to the PFSST data set. In the following this skin corrected DOISST will be referred to as DOISST(skin).

Fig. 4.4 a shows the monthly global mean SST time series of the PFSST data set and the DOISST(skin) data set. The data sets are in good agreement on the global scale and the temporal developments of both time series are very similar. The difference between the global mean values are mostly below 0.1 °C. From mid 2000 to the end of 2003, the DOISST(skin) data set exhibits a noticeable constant low bias compared to the Pathfinder data of around 0.1 °C. The largest difference occurs after the Mt. Pinatubo eruption in June 1991, when the Pathfinder data drops to global mean values between 19.3 °C and 19.4 °C, while the DOISST(skin) data is on average 0.3 °C warmer. From January 1992 on, both data sets are back to the same level again. Apparently, the correction coefficients in both data sets have converged at that time. This is also evident from the anomaly plot for the global mean evaporation in Fig. 4.4 b. Shortly after the eruption, in August and September 1991, the largest negative anomaly is detectable in both time series. However, the negative peak is twice as strong for the Pathfinder based time series as it is for the data set processed using the DOISST(skin). During 1992 both time series persist on a level of about 0.2 mm/d below the mean.

The global mean SST anomaly (Fig. 4.4 c) seems to confirm the impact of the eruption on global scale. In addition to the PFSST and DOISST(skin), the SST anomaly of the *National Oceanography Centre Southampton* (NOCS) Flux Dataset V2.0 (*Berry and Kent*, 2008) which is based on ship observation is depicted in Fig. 4.4 c. All data sets exhibit a negative anomaly shortly after the eruption of Mt. Pinatubo, with PFSST showing the greatest deviation. By the end of 1991 the anomaly decreases, which is likely to be related to an El Niño event, which occurred at that time. Prior to the eruption, a decreasing tendency is already detectable in the global mean evaporation (Fig. 4.4 b), but not in the SST. Hence this decrease is due to other factors, such as the wind speed which exhibits a minimum at that time (Fig. 4.1).

If only the SST anomaly for the tropical regions is considered (Fig. 4.4 d), the comparison for the period after the eruption on Mt. Pinatubo is not consistent. Unlike the PFSST, the NOCS and DOISST data sets show only a minimal decrease of less than 0.2 °C (Fig. 4.4 d) in the second half of 1991. The PFSST exhibits a strong negative anomaly of almost 1 °C for in the tropics which, on the other hand, is likely to be too high due to a nighttime bias (*Reynolds*, 1993). Hence the response in the global mean data from NOCS and DOISST data sets must have its origin in the mid and high latitudes. However, the transport of volcanic aerosol into the extratropical regions lagged behind the distribution in the tropics

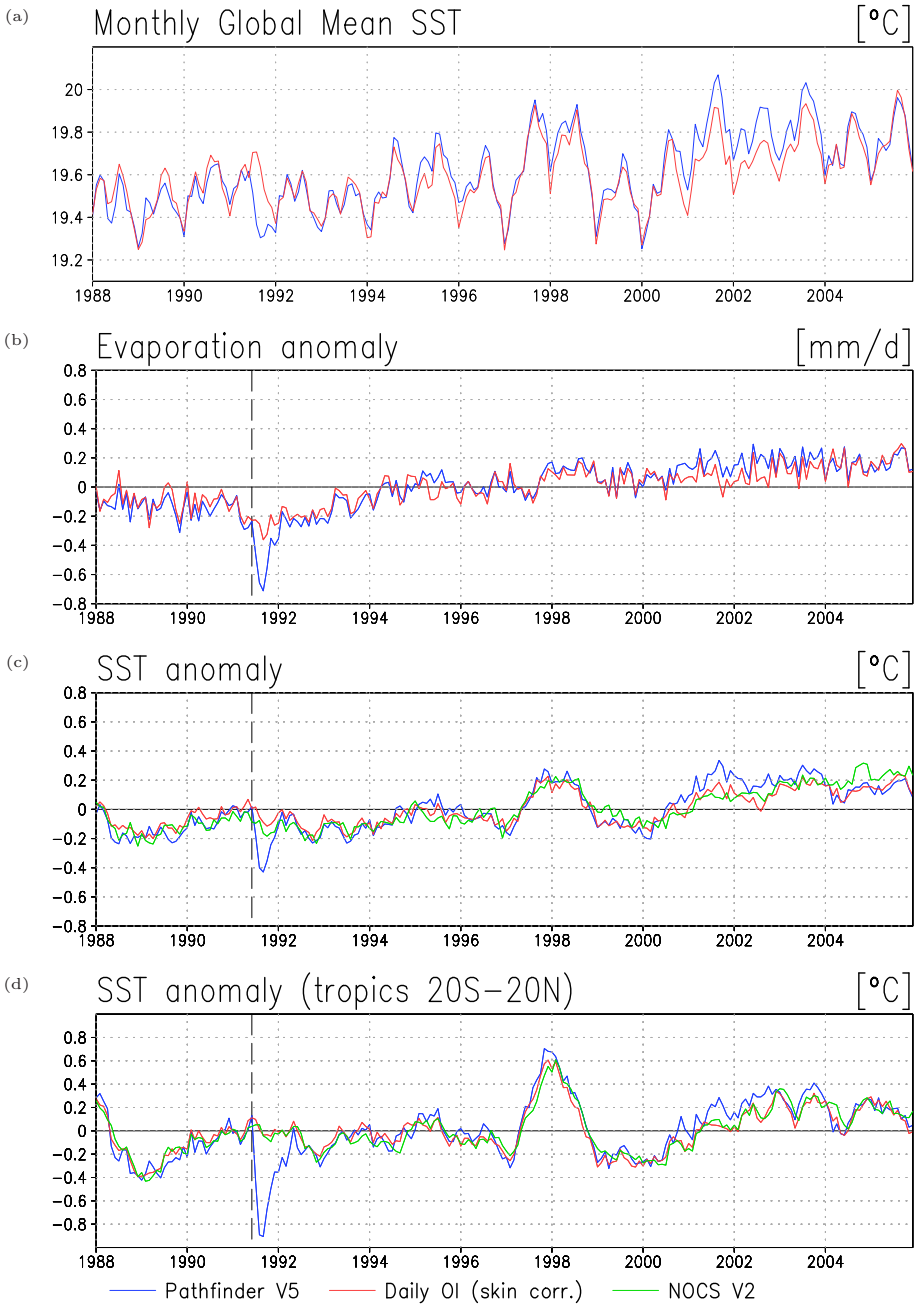

Figure 4.4: a): Global monthly mean of HOAPS SST remapping of the NODC/RSMAS Pathfinder V5 SST (blue line) and the Reynolds Daily OI SST (red line). A skin correction of -0.2 °C was applied to the Daily OI SST.
b): Global monthly mean evaporation time series calculated using either of the above data sets with the seasonal cycle removed.
c): Global monthly mean SST time series with the seasonal cycle removed. Additionally to the upper panels, the NOCS V2 SST is plotted.
d): Same as panel c, but restricted to the tropics (20°S–20°N).
The vertical line denotes the eruption of Mt. Pinatubo in June 1991.

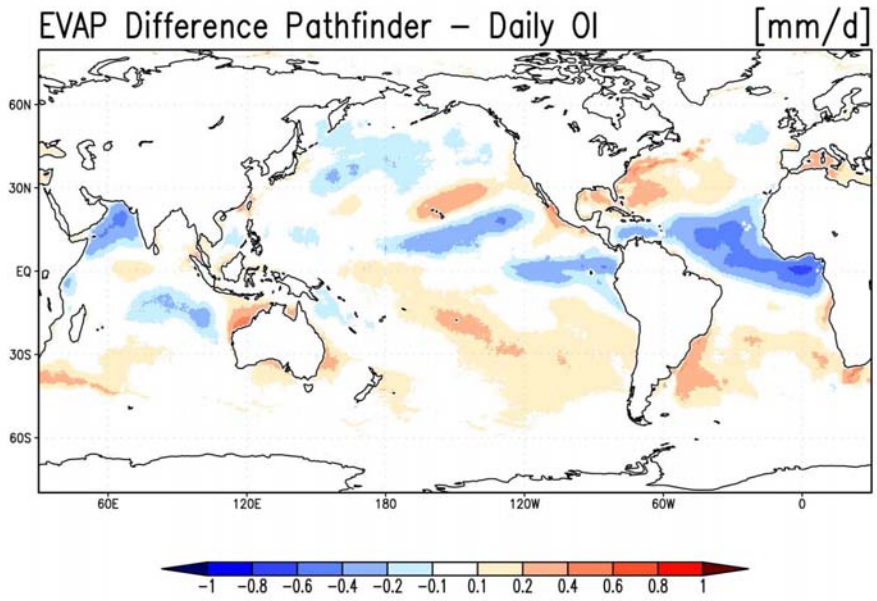

Figure 4.5: Difference map of HOAPS-3 climate mean (1988-2005) evaporation calculated with NODC/RSMAS Pathfinder V5 SST and Reynolds Daily-OI SST.

and led to a tropospheric warming in the winter and a cooling in the summer (*Parker et al.*, 1996; *Robock*, 2002; *Stenchikov et al.*, 2002). Moreover, the signal in the tropics is masked by the developing El Niño in late 1991. These factors complicate the quantitative assessment of the real impact of the Mt. Pinatubo eruption on the SST and consequently on the HOAPS-3 evaporation.

The impact of the different SST data sets on the HOAPS-3 evaporation parameter is depicted in Fig. 4.5. The figure shows the difference of the climate mean HOAPS-3 evaporation of the years 1988–2005 calculated by using either of the PFSST and DOISST(skin) data set. Positive (negative) values are related to a generally higher (lower) PFSST compared to the DOISST(skin) due to the increase (decrease) of specific saturation humidity at the sea surface with higher (lower) SST.

The systematic differences that occur in the HOAPS-3 evaporation product from the two SST datasets are smaller than 0.2 mm/d or a corresponding relative deviation of less than 5 % for most of the global oceans. However, in the tropical regions some larger biases are evident. The largest differences occur in the tropical Atlantic where the evaporation calculated with the PFSST is substantially lower than for the time series using the DOISST(skin). Here, the difference exceeds 0.6 mm/d (30 %). In this region the PFSST is known to exhibit biases caused by aerosol contamination from Saharan dust storms (*NODC*, 2008). A similar feature related to aerosol transport from deserts is located in the Arabian sea. Along the Gulf Stream in the western Atlantic strong positive values occur in the

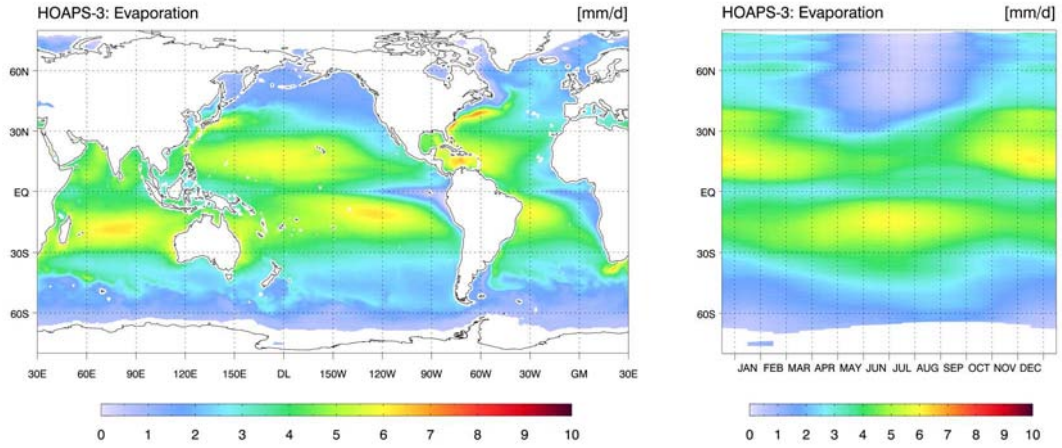

Figure 4.6: Climatological mean field (left) and zonal mean annual cycle (right) of HOAPS-3 evaporation for the years 1988-2005.

difference map. These differences may be caused by the different interpolation methods to fill data gaps due to persistent cloud coverage. In the tropical Pacific and Indian Ocean, the difference patterns are most pronounced in the eastern Pacific and the southeast Asian warm pool region, being related to El Niño.

4.4 Evaporation

Several comparison studies for global ocean evaporation and latent heat flux data sets have been carried out, such as *Bourras* (2006) and *Liu and Curry* (2006). These include HOAPS version 2 fluxes, which do not substantially differ from HOAPS-3 values as the flux parameterization scheme did not change and the used SST data sets are comparable.

The major part of the climatological mean global ocean evaporation (Fig. 4.6, left panel) originates from the trade wind belts in the subtropics, while the mid and high latitudes exhibit generally low values. Outside the tropics, the highest values are found over the warm boundary currents of the Kuroshio, the Gulf Stream, and the Agulhas current, with the Gulf Stream generating the highest values on the globe. A pronounced variability can be identified in the annual cycle zonal mean map (Fig. 4.6, right panel). Maximum evaporation is found during the winter season of each hemisphere.

The intercomparison of current turbulent heat flux data set is subject of the SEAFLUX project. A comprehensive evaluation study carried out within this international framework will be published in *Clayson et al.* (2009).

Here, HOAPS-3 evaporation data is compared to three climatological data

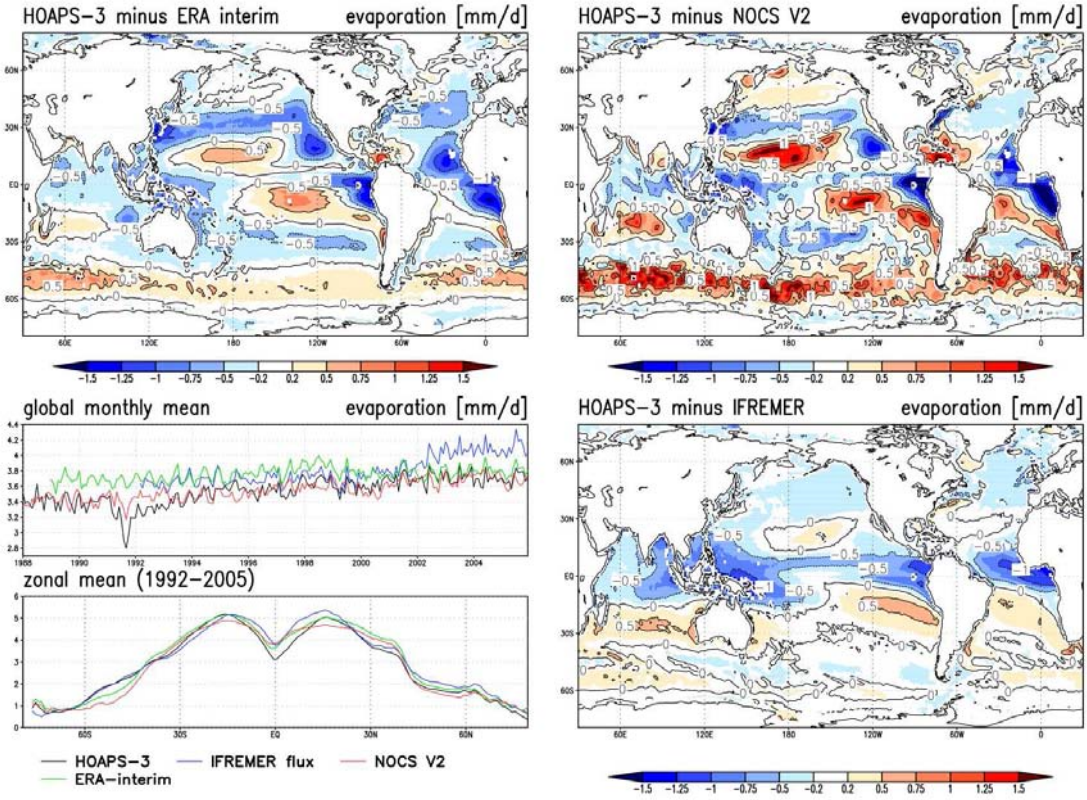

Figure 4.7: Difference of climate mean HOAPS-3 evaporation and ERA interim (1989–2005, top left), NOCS v2.0 (1988–2005, top right), and IFREMER (1992–2005, bottom right). The lower left panel shows the global monthly mean evaporation and the zonal mean evaporation for the overlapping time period 1992 to 2005.

sets of different origin: the evaporation estimate from the ERAint reanalysis, the NOCS v2.0 flux data set, and the IFREMER merged flux product.

NOCS (*Berry and Kent*, 2008) is compiled using *Voluntary Observing Ships* (VOS) data from the *International Comprehensive Ocean-Atmosphere Data Set* (ICOADS) (*Slutz et al.*, 1985). The NOCS data set provides fields of global ocean heat fluxes, which are constructed using an optimum interpolation method and a bias adjustment procedure. Due to the limitation to ship data, the data coverage for regions away from the common shipping routes is mostly poor. Especially the data-void Southern Hemisphere exhibits substantial uncertainties. Bentamy et al. (2003) developed at IFREMER a remotely sensed data set of wind stress and surface turbulent latent and sensible heat fluxes, that uses scatterometer retrieved wind fields, NOAA sea surface temperatures, and passive microwave based estimates of specific humidity to derive these parameters. Here the version 3.0 is used, which is currently available for the time range 03/1992–12/2007 (source: `ftp://ftp.ifremer.fr/ifremer/cersat/products/gridded/flux-merged`)

The IFREMER and NOCS data sets both rely on the COARE bulk flux algorithm of *Fairall et al.* (2003) to derive the turbulent latent and sensible heat fluxes, which is also used in HOAPS.

Fig. 4.7 shows the HOAPS-3 climatological mean of the evaporation compared to ERAint (1989-2005, top left), NOCS (1988-2005, top right), and IFREMER (1992-2005, bottom right) as difference maps. The bottom left plots in Fig. 4.7 show the global monthly mean time series of each of the products and the climatological zonal mean for the common time range from 1992 to 2005. The difference maps in Fig. 4.7 show in all cases distributions similar to the climatological mean field of HOAPS-3 evaporation (Fig. 4.6), giving in general higher difference values in regions of large evaporation and smaller values in regions with low values of evaporation. These difference patterns are more distinct in the comparison of HOAPS-3 with ERAint (Fig. 4.7, top left) and NOCS (Fig. 4.7, top right), while the difference map of HOAPS-3 and the IFREMER data set (Fig. 4.7, bottom right) shows similar tendencies, but with mostly smaller absolute values. The magnitude of deviations are regionally largest in the comparison with NOCS. Furthermore, the comparisons of HOAPS-3 with NOCS and ERAint exhibits quite strong regional similarities. The reason for this may be that the ICOADS data are also assimilated in the ERA reanalysis. Hence, these data sets may not be completely independent, albeit different methods are used to estimate the fluxes.

The most distinct differences between HOAPS-3 and the compared data sets occur in the tropical regions and over the southern midlatitudes. In the subtropical central pacific, HOAPS-3 values exceed ERAint by up to 1 mm/d and NOCS by partly more than 1.5 mm/d. This corresponds to a relative bias of 10 % to 20 %. In the comparison with IFREMER, these features are also evident, but overall

weaker with differences below 0.75 mm/d.

Along a band extending from the Kuroshio current over the North Pacific to the east HOAPS-3 is systematically lower compared to ERAint and NOCS by up to 1 mm/d. This pattern continues southward along the North American west coast. Also over the cold tong in the eastern equatorial Pacific and the southeast Asian warm pool HOAPS-3 evaporation is systematically lower compared to the other data sets. Due to the relatively low absolute values of evaporation (see Fig. 4.6), the relative error reaches more than 30 % in these regions and is most expressed in the comparison with IFREMER.

Another region with relatively high deviations of HOAPS-3 against the other compared data sets is the eastern tropical Atlantic, where differences of more than 1 mm/d occur. The low bias of HOAPS-3 evaporation in the Atlantic is likely to be caused by an apparent cooling of SST due to an inappropriate correction in the SST retrieval for aerosol from the Sahara (see section 4.3).

Over the North Atlantic midlatitudes, HOAPS-3 evaporation has a slightly low bias of up to 0.5 mm/d compared to NOCS and IFREMER and 0.75 mm/d compared to ERAint, which equals up to 20 % for the latter.

Over the southern mid to high latitudes, NOCS and HOAPS-3 exhibit the largest differences coinciding with the Southern Hemisphere's band of strong winds between 40° S and 60° S (see Fig. 4.1). The mean evaporation of HOAPS-3 is locally more than 1.5 mm/d above NOCS which is more than 50 % in these regions. However, due to the insufficient sampling, the error in the NOCS product is generally very high, hence a comparison has very limited validity in these regions.

Compared to ERAint, the HOAPS-3 evaporation is up to 0.75 mm/d (more than 30 %) higher for the southern midlatitudes. This is remarkable, since the comparison of HOAPS-3 and ERAint wind speed (Fig. 4.1, top left) agreed best for the midlatitudes of the Southern Hemisphere.

In the comparison of the climatological zonal means (Fig. 4.7, bottom left), all data sets show an overall agreement in the location and magnitude of the maxima and minima. In the southern midlatitudes HOAPS-3 and IFREMER agree almost perfectly, while ERAint and NOCS exhibit significantly lower values, as shown by the difference maps. In the tropical regions, the maxima in the NOCS data set are flatter than in the other data sets, while HOAPS-3 exhibits the lowest values of all data sets around the equator. The latter is mainly due to the low bias in the tropical Atlantic and southeast Asian warm pool.

While the zonal means (Fig. 4.7, bottom left) for all data sets agree quite well, general biases and a different temporal evolution of the individual data sets are evident from the global monthly mean time series shown in Fig. 4.7. HOAPS-3 and NOCS data are in good agreement for the entire time series, except for the

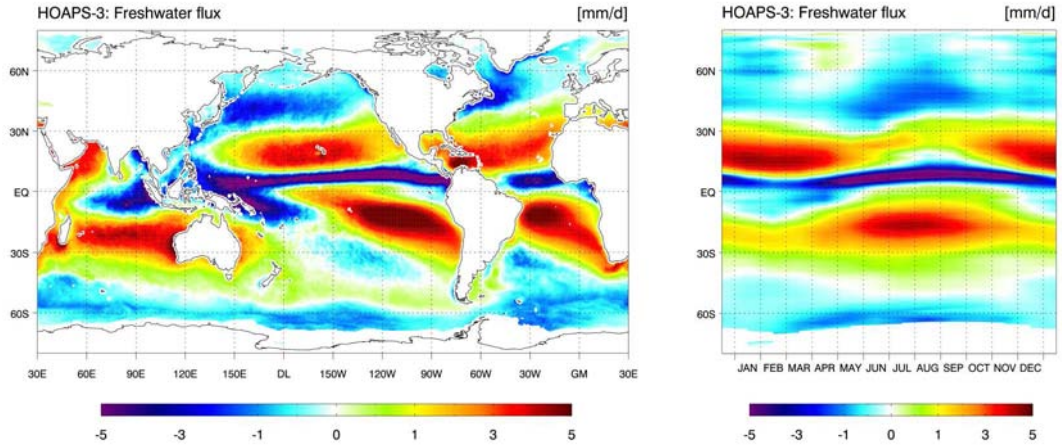

Figure 4.8: Climatological mean field (left) and zonal mean annual cycle (right) of the HOAPS-3 freshwater flux for the years 1988-2005.

period after the eruption of Mt. Pinatubo (see section 4.3). Both data sets show an increase from 3.4 mm/d global mean evaporation at the beginning of the record to a level of 3.7 mm/d at the end of the time series. ERAint evaporation is nearly constant with an increase of less than 0.1 mm/d between 1989 and 2005. The IFREMER time series is very similar to ERAint from 1992 until the end of 2001, but exhibits a sudden increase in 2002, which is likely to be an artifact from one of the input data sources.

From the SST time series used in HOAPS-3 a trend of 0.2 °C per decade can be derived. According to the Clausius Clapeyron relationship, latent energy exchange can increase by approximately 6.4 % per 1 °C temperature increase at a temperature of 20 °C. Translated to the evaporation using the observed trend of 0.2 °C, this would mean a trend of 1.3 % or 0.045 mm/d per decade. The observed trends of HOAPS-3 and NOCS are substantially larger and hence cannot be explained by the SST increase alone. For HOAPS-3, trends in the global mean wind speed (2.7 % per decade) and humidity difference (4.5 % per decade) are evident which contribute to the increase in evaporation. The different temporal behavior of the evaporation estimates has implications on the long term evaluation of the global freshwater budget which will be discussed in the next section.

4.5 Freshwater Flux

The difference between the precipitation and evaporation yields the oceanic freshwater flux into the atmosphere. Dominant features of either precipitation or evaporation fields determine the resulting global distribution of freshwater flux (Fig. 4.8). A net flux into the ocean is mainly found in regions of precipitation

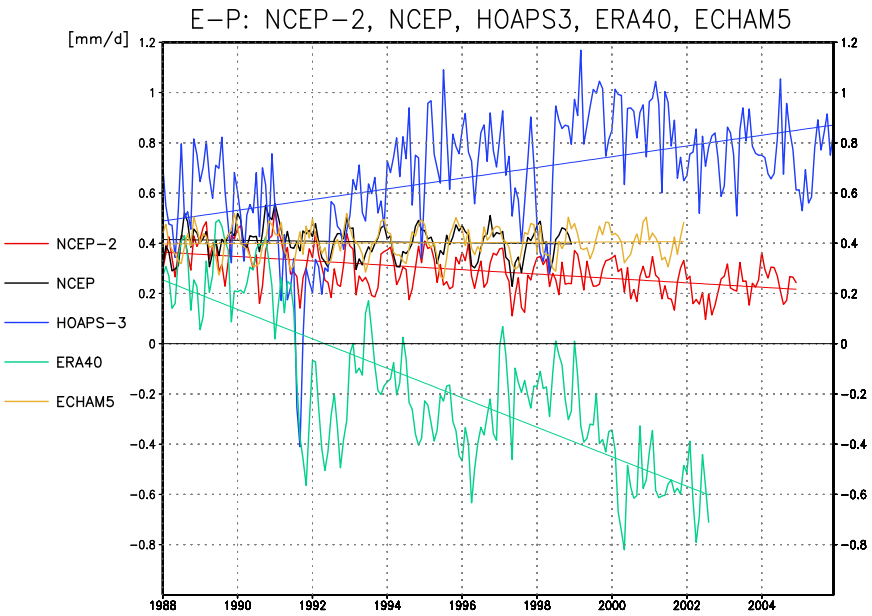

Figure 4.9: Monthly global mean values and regression lines of the oceanic freshwater flux from HOAPS-3, NCEP-R1 and R2, ERA-40, and ECHAM5 control run ensemble. (from *Klocke*, 2008)

maxima in the ITCZ, the midlatitude storm tracks and at high latitudes. In contrast, subtropical regions generate the major part of the freshwater flux into the atmosphere. In the annual cycle, the dominant features of the input parameters are reproduced.

Wentz et al. (2007) demonstrated that satellite data is in principle capable of estimating the global ocean freshwater cycle and that it may be used to evaluate coupled ocean-atmosphere models with respect to the response on global warming. A comparison of freshwater flux estimates from the GECCO-model, HOAPS-3 and NCEP (*Romanova et al.*, 2009) confirms these findings, although regional differences and uncertainties in the long term stability remain, that have to be further evaluated. *Schlosser and Houser* (2007) assessed current satellite based global water cycle estimates, and pointed out advances, but also deficiencies in the development of such products, such as inconsistencies in global trends as well as a general imbalance between precipitation and evaporation for various data sets. The latter also accounted for the previous version of HOAPS which was included in the study of *Schlosser and Houser* (2007). In HOAPS II a generally too low global precipitation compared to the evaporation, lead to a unrealistically large mean freshwater loss of the ocean into the atmosphere.

Klocke (2008) investigated the global ocean freshwater flux of HOAPS-3, NCEP-R1/2 and ERA40 reanalyses, and a climate model control run ensemble of the *European Centre Hamburg Model V5* (ECHAM5). Apart from an overall agreement

in spatial patterns between the data sets, large discrepancies in their temporal behavior were revealed as depicted in Fig. 4.9. For the NCEP and ECHAM5 data sets, the global ocean freshwater balance is internally nearly balanced. In the analysis of the freshwater flux components, the almost constant NCEP-R1/2 data result from a substantial continuous increase in global mean evaporation as and a nearly similarly strong increase of precipitation during the comparison time period. In contrast to that, the ECHAM5 freshwater flux remains constant as the result of almost constant precipitation and evaporation.

The freshwater flux from ERA40 in Fig. 4.9 exhibits an unrealistically strong negative trend due to an unreliable precipitation estimate. ECHAM5 and NCEP-R1 do not show a significant trend on global scale, while the NCEP-R2 freshwater flux decreases slightly with time. HOAPS-3 exhibits a positive trend in the global mean freshwater flux, which is due to a temporally constant precipitation, while the evaporation increases with time. However, the magnitude of the resulting trend in the HOAPS-3 freshwater flux appears to be too large to be compensated by an increased water vapor storage capability in the atmosphere. Furthermore, a significant global increase of precipitation over land and hence continental river runoff of that magnitude is not detected in other studies (*Dai et al.*, 1997; *Labat et al.*, 2004; *Legates et al.*, 2005; *Huntington*, 2006). As shown in section 4.2 the precipitation in other satellite based data sets does not exhibit significant trends, while for evaporation data sets a divergent development is observed (see section 4.4). From the different behavior of the examined data sets a consistent answer to the temporal development of the global ocean freshwater flux and its components still remains an open issue for all climate related data sets.

Notwithstanding the uncertainties in the long term evolution of the global mean freshwater flux, a major improvement for this parameter was achieved with HOAPS-3 compared to the former HOAPS version 2 that underestimated the global precipitation considerably. This issue has been addressed with the new precipitation algorithm in HOAPS-3. The globally averaged HOAPS-3 mean net freshwater flux into the atmosphere is 0.68 mm/d, which is equivalent to a liquid water volume of 84 000 km^3/a. For a closure of the global freshwater balance, this should be compensated by continental runoff. Data given by the *Global Runoff Data Center* (GRDC) and other sources add up to a mean value of approximately 0.32 mm/d (equiv. 40 000 km^3/a) (*GRDC*, 2009). However, uncertainties of 10 % to 20 % exist between different runoff estimates. Additionally, other runoff sources, such as annual ice melt and groundwater flow into the ocean are estimated to be up to 10% of the river discharge (*Burnett et al.*, 2001). Comparing these values to the HOAPS-3 global ocean freshwater flux leaves an imbalance of about 0.3 mm/d in the global freshwater balance. Hence, the global ocean freshwater balance is nearly closed in HOAPS-3 within a range of 10 % of the global mean evaporation and precipitation estimates.

4.6 Conclusions

In this chapter HOAPS-3 parameters were globally evaluated on the climatological scale. The focus lied on the previously unpublished wind speed and precipitation parameters as well as on the SST, for which a new version of the AVHRR Pathfinder product was used in HOAPS-3. Finally, the evaporation parameter and the freshwater flux were examined. On the climatological scale, all of the examined parameters exhibit reasonable global patterns. The comparison with other data sets reveals some systematic regional differences as well as convincing consistency with the HOAPS-3 retrievals.

The HOAPS-3 wind speed was compared with the IFREMER MWF QuikSCAT product and the ERAint reanalysis. ERAint exhibited nearly globally a low bias of 0.6 m/s compared to IFREMER and HOAPS-3, which is known from previous studies comparing satellite retrieved and reanalysis wind speeds. For HOAPS-3 and IFREMER, the difference of the global mean values is below 0.2 m/s and mostly below 0.5 m/s for the regional comparison of the climate mean fields.

The HOAPS-3 precipitation was compared with two satellite retrieved climatological products, GPCP V2 and TRMM 3B43. The largest absolute differences between the data sets occurred in regions with high variability. HOAPS-3 precipitation was significantly higher compared to the other data sets at the Pacific ITCZ, while the precipitation in subtropical regions agreed. At higher latitudes, GPCP exhibits a known high bias compared to HOAPS-3 poleward of 40° north and south. The global mean time series of all data sets is around 3 mm/d, with GPCP being generally slightly higher compared to the other data sets.

For the evaluation of the AVHRR Pathfinder SST V5 data set, the HOAPS-3 time series was reprocessed using the alternative Daily-OI SST data set. While the 1991 negative dip occurring in the PFSST during that time appears to be exaggerated, DOISST and NOCS SST show only a very small and nonuniform response. On the climatological scale, differences in the evaporation retrieval due to the substitution of PFSST through DOISST are evident in the tropical Atlantic and Arabian Sea, where desert aerosol influences the retrieval, as well as in the El Niño affected regions of the eastern Pacific.

The HOAPS-3 evaporation was evaluated with ERAint reanalysis data, the satellite based IFREMER merged flux product, and the NOCS version 2 flux data set, which is compiled from ship observations. Similar difference patterns appeared in the comparison of HOAPS-3 with all datasets with HOAPS-3 showing generally a positive bias in regions with high values of evaporation, and lower values of HOAPS-3 compared to the other data sets in regions with low evaporation. The deviations in the comparison with ERAint and NOCS were larger than for the IFREMER product, which appeared very similar to HOAPS-3. The global mean

evaporation from the compared data sets does not differ more than 10 % for most of the time series. However, differences in their temporal development are evident.

As HOAPS is the only satellite based product which derives the global ocean freshwater flux inherent in the data set, a direct comparison with other data sets for this parameter is not possible. However, previous studies, such as *Schlosser and Houser* (2007) and *Klocke* (2008), using model data and compound data sets revealed inconsistencies in the temporal development as well as in the mean global freshwater balance among the products. Thus, regarding the validity of the temporal development of the global ocean freshwater flux in HOAPS-3, a consistent answer could not be given using available data sets.

However, the imbalance in the global ocean freshwater flux compared to global river runoff data is approximately 10 % of the HOAPS-3 global mean precipitation and evaporation. Although regionally higher differences occur, this appears to be within the accuracy on global scale found in the evaluations of HOAPS-3 parameters with other data sets in this chapter. Overall, this value is a great improvement compared to earlier versions of HOAPS and points out the unique feature of HOAPS to derive the global ocean freshwater balance from satellite data consistently in one data set.

5

A Satellite View on the Extratropical Transition of Hurricane Maria

In this chapter the development of the hurricane "Maria" from the year 2005 and its *extratropical transition* (ET) is inspected by the synergetic use of HOAPS-3 and other satellite data. The purpose of this study is two fold. The first aim is to get insight into the transformation process of a *tropical cyclone* (TC) in an extratropical cyclone by the use of satellite retrieved data. On the other hand this study will give an evaluation of HOAPS-3 geophysical parameters under extreme environmental conditions, as they occur in a hurricane and during the ET.

5.1 Introduction

When a TC moves northward and leaves the tropics it encounters a substantially different environment that will impact the structure of the cyclone. Subsequently it may transform into an extratropical cyclone and persist in the extratropical environment. This process of ET takes place successively initiated from changes in the large scale environment instead of being a sudden change in the dynamics of the TC. The main changes triggering the ET are increased baroclinity, a pronounced decrease in the underlying *sea surface temperature* (SST), local humidity gradients as well as the increased Coriolis parameter (*Jones et al.*, 2003). During ET the TC undergoes structural changes in the transformation process, either leading to decay or re-intensification in its further development as an extratropical cyclone. In the transformation process visible changes of the cloud structure

occur such as a decrease in deep convection and disappearance of the high cloud canopy. The increased translation speed of the cyclone in the extratropical environment leads to a highly asymmetric wind field, which is associated with a higher radius of gale and hurricane force winds compared to a TC. Often, the TC loses its warm core and transforms to a cold core system. During and after ET a cyclone produces intense rainfall, vigorous winds and large waves. Hence it poses a thread to humans and nature on the land as well as on the sea. *Hart and Evans* (2001) showed that ET of tropical cyclones is a common phenomenon in the Atlantic. From their climatology of ET events resulted, that 46 % of the TCs in the North Atlantic transitioned to an extratropical phase and 50 % of these systems re-intensified after the transition.

Some of the structural changes such as the loss of the symmetric appearance of the TC core, the formation of a comma-shaped cloud pattern and/or frontal structures can be directly observed on *infrared* (IR) and *visible* (VIS) satellite imagery. Previous studies of ETs in the Pacific and Atlantic mostly relied on the VIS and IR data from geostationary satellites and the satellite observations were mostly limited to the detection of changes in the cloud structure of a TC (e.g. *Agusti-Panareda et al.*, 2004; *Evans et al.*, 1994; *Harr and Elsberry*, 2000; *Kitabatake*, 2008; *Klein et al.*, 2000; *Thorncroft and Jones*, 2000). Therefore, *Jones et al.* (2003) pointed out the need for more studies based on satellite observations. Especially data from active and passive microwave sensors is considered to give valuable additional information. Such studies are needed to improve the knowledge about real ET events and for the validation of model studies.

In this context, passive microwave sensors can provide valuable data for additional geophysical parameters with their ability to penetrate through clouds to retrieve information of atmospheric and surface parameters such as precipitation, water vapor, wind, and turbulent sea surface fluxes. In particular the SSM/I can be systematically used, as a twice daily quasi-global coverage is achieved in the configuration with up to three sensors simultaneously in space on the polar orbiting DMSP satellites. Additionally, SSM/I observations are not impaired at high latitudes by an unfavorable viewing geometry as it applies for instruments on geostationary satellites.

In the following the case of hurricane Maria from the year 2005 will be investigated. In contrast to many other TCs, Maria did not make landfall at the American coast, but moved over the open ocean until it reached northern Europe after its ET. Hence Maria is an ideal case for a detailed analysis using HOAPS-3 over ocean retrievals. Apart from a focus on the ET, the hurricane phase of Maria will also be inspected in the following.

At first an introduction to a conceptual model of ET and the data set which are used in this study will be given. This is followed by a synoptic overview of the

temporal development of Maria. Then two dates during the hurricane phase will be evaluated. This involves a comparison of coincident HOAPS-3 and QuikSCAT wind fields for the peak hurricane phase. For the ET of Maria, a stepwise analysis using HOAPS-3 and VIS/IR data will give a detailed insight into the transition process. Finally, a summary concludes this chapter.

5.2 A Conceptual Model of Extratropical Transition

Klein et al. (2000) developed a conceptual model for ET in the western North Pacific, which could basically also be applied to a TC in the North Atlantic. The scheme describes the typical changes that occur in a TC during the process of ET. However, the detailed evolution of a TC during and after the ET may vary and the further development, i.e. re-intensification or decay, depends on different environmental factors such as the interaction with a midlatitude trough (e.g. *Hart et al.*, 2006).

The scheme of *Klein et al.* (2000) is shown in Fig. 5.1. It distinguishes three steps in the transformation process, which are mainly based on the appearance of the cyclone on IR-satellite data. In the first step the cyclone begins to leave the tropics and starts to interact with the decreasing SSTs and the baroclinic zone. The outer circulation of the TC is affected at first by the changing environment. Advection of cold air masses (labeled with 1 in Fig. 5.1) from the north into the western sector cause decreased convection down to the southwestern quadrant. On the eastern side of the TC, northward flow of warm, moist tropical air masses (labeled with 3 in Fig. 5.1) persists and the deep convection is maintained. The overall appearance of the storm begins to become more asymmetric. In the northern sector of the cyclone, the air masses ascend on tilted isentropic surfaces in the baroclinic zone (labeled with 4 in Fig. 5.1), which is often associated with strong precipitation. In the upper levels, interaction with the jetstream may occur and cause enhanced vertical wind shear.

In the second phase of transformation, the position of core is just south of the border of the baroclinic zone. The shape of the cyclone becomes more asymmetric, as the advection of cool (warm) air masses in the west (east) persists and a dry slot is extending into the southern sector. The lifted air in the north begins to move cyclonically around the center of the cyclone to the western quadrant. While the deep convection in the inner core still persists, a cirrus shield from the warm upper-tropospheric outflow of the former TC forms in the north due to the vertical wind shear in the baroclinic zone (labeled with 6 in Fig. 5.1).

In the third step, the transformation of the TC is complete. The storm center is now within the baroclinic environment and the system experiences strong vertical

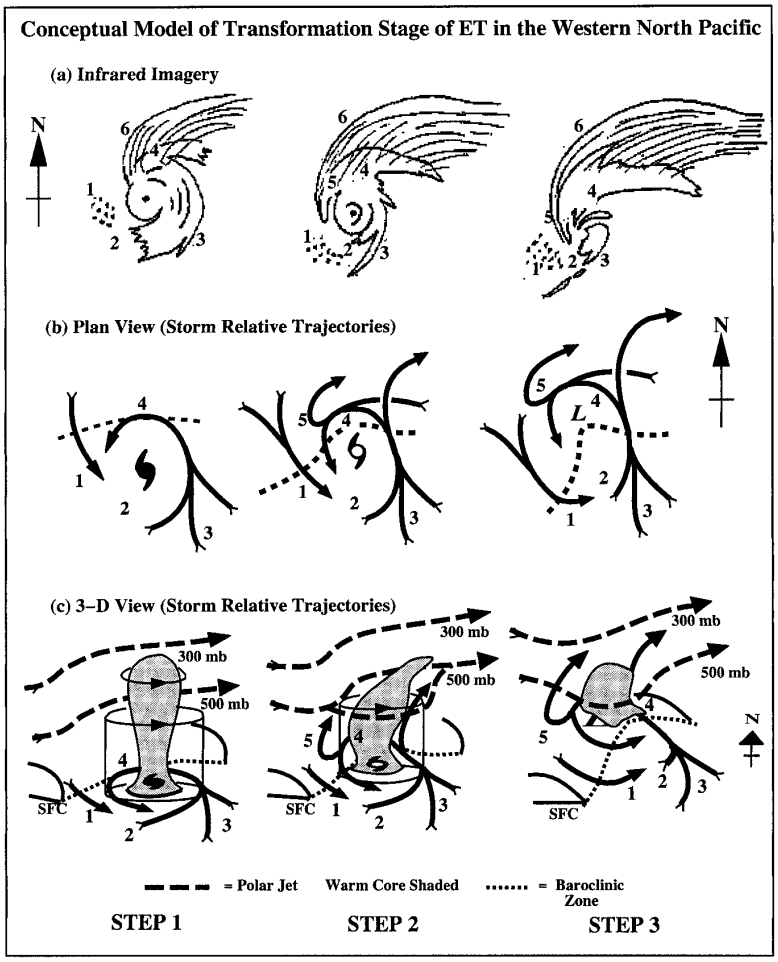

Figure 5.1: Conceptual model of transformation stage of ET, with labeled areas as follows:
1) environmental equatorward flow of cooler, drier air (with corresponding open cell cumulus);
2) decreased tropical cyclone convection in the western quadrant (with corresponding dry slot) in step 1, which extends throughout the southern quadrant in steps 2 and 3;
3) environmental poleward flow of warm, moist air is ingested into tropical cyclone circulation, which maintains convection in the eastern quadrant and results in an asymmetric distribution of clouds and precipitation in steps 1 and 2; steps 2 and 3 also feature a southerly jet that ascends tilted isentropic surfaces;
4) ascent of warm, moist inflow over tilted isentropic surfaces associated with baroclinic zone (dashed line) in middle and lower panels;
5) ascent (undercut by dry-adiabatic descent) that produces cloudbands wrapping westward and equatorward around the storm center; dry-adiabatic descent occurs close enough to the circulation center to produce erosion of eyewall convection in step 3;
6) cirrus shield with a sharp cloud edge if confluent with polar jet.
(from *Klein et al.*, 2000)

wind shear. The advection of warm (cold) air in the east (west) continues, with ascent to the north and descent in the west. Multi-layer clouds in the north are cyclonically moving around the center to the west of the transformed cyclone. A warm front evolves east of the core, and to the southeast develops a weaker cold front. In the core, dry adiabatic descent weakens convection and the remnants of the eyewall erode. The warm core of the cyclone is becoming weaker.

5.3 Data

5.3.1 NHC "best-track" Data Set

The individual positions of the hurricane are obtained from the "best-track" data set that is provided by the *National Hurricane Center* (NHC) of the US national Weather Service (*Jarvinen et al.*, 1984). This data set contains the position, maximum wind speed, and minimum pressure of North Atlantic TCs since 1851 at 6-hourly intervals. For the first half of the record, the values are estimated from ship and land based observations only. Since the mid of the 20^{th} century, also data from radiosondes, coastal radars and aircraft reconnaissance flight, which became successively available as well as satellite based estimates are included.

The NHC best track data set contains a flag that declares a TC as extratropical from a certain time step on. This point of ET for a TC is determined subjectively from the appearance of the storm on satellite images and the underlying SST. *Hart and Evans* (2001) regard this definition as early in the process of ET. It marks the point when the storm starts to interact with the extratropical environment and just begins to lose its tropical characteristics.

5.3.2 Satellite Data

In order to resolve as much detail as possible, the scan based HOAPS-S data set is used here, which has resolution of about 50 km per pixel (see chapter 3.1.1). In 2005 data from the radiometers aboard of the DMSP satellites F13, F14, and F15 are available, providing a twice daily near global coverage. In this study, the geophysical parameters precipitation (see chapter 3.2.6), wind (see chapter 3.2.1) and water vapor (see chapter 3.2.5) are examined.

Additionally L1B granule VIS images from the *Moderate Resolution Imaging Spectroradiometer* (MODIS) on NASA's Aqua and Terra satellites and IR images from the *Advanced Very High Resolution Radiometer* (AVHRR) aboard the *National Oceanic and Atmospheric Administration's* (NOAA) Polar Orbiting Environmental Satellite series are used to identify changes in the cloud structure of

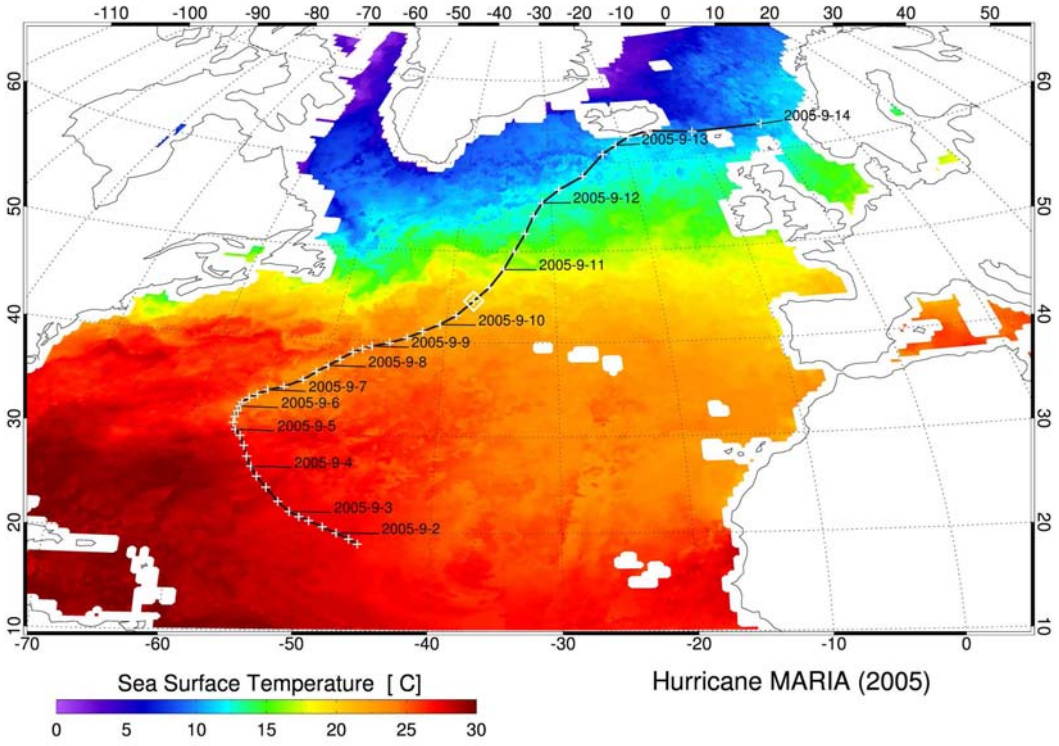

Figure 5.2: Track of hurricane Maria from the NHC best track data set. The date labels correspond to 0 UTC of each day. The point of ET from the best track data set on 10 September is marked with a white diamond on the track. The background field shows the SST from HOAPS-3 for 10 September.

the hurricane. The MODIS data is accessible via `http://modis-atmos.gsfc.nasa.gov/IMAGES/index.html`. The AVHRR quicklook images were obtained from the NERC Satellite Receiving Station of the Dundee University, Scotland (source: `http://www.sat.dundee.ac.uk/`).

For comparison with HOAPS-3, a QuikSCAT scatterometer wind field produced by the Jet Propulsion Laboratory of the NASA is used (source: `http://scp.byu.edu/data/QuikSCAT/HRStorms.html`).

5.3.3 NCEP-R2 Pressure Fields

Additionally, *mean sea level pressure* (MSLP) and 500 hPa geopotential height data from the NCEP/DOE reanalysis 2 (NCEP-R2, *Kanamitsu et al.*, 2002) complete the synoptic information.

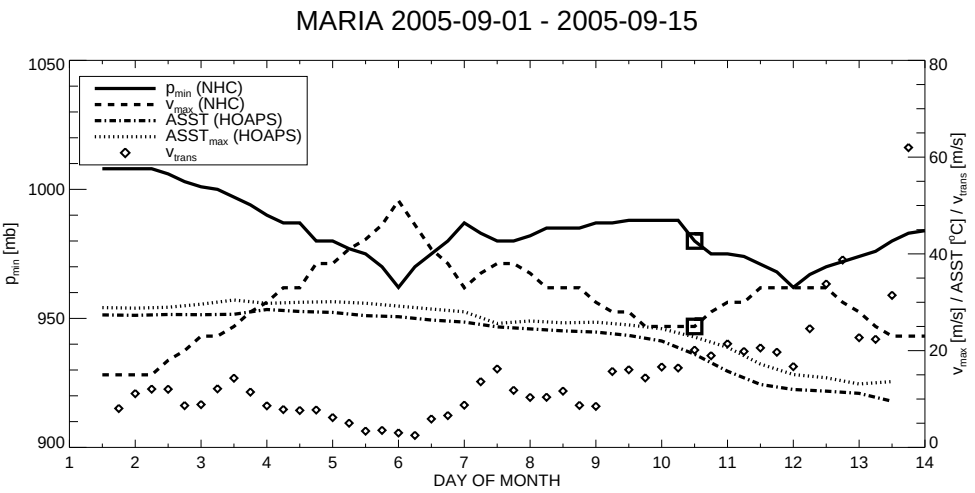

Figure 5.3: Temporal evolution of Maria from 1 September to 14 September. Minimum pressure (p_{min}, solid line), maximum wind speed (v_{max}, dashed line), and translation velocity (v_{trans}, diamonds) are taken from the 6-hourly NHC best track dataset. The square indicates the point, where the cyclone is declared extratropical in the NHC data set. The mean and maximum SST values (ASST, dashed-dotted and dotted line) are inferred from HOAPS-3 within a 500 km region around the center of the cyclone from 0-12 UTC and 12-24 UTC overpasses (see text).

5.4 Storm Overview

The track of hurricane Maria across the North Atlantic from the tropics to northern Europe is depicted in Fig. 5.2. Hurricane Maria developed from a tropical wave in the eastern tropical Atlantic by the end of August 2005. A system with persistent deep convection established on 1 September in the central subtropical North Atlantic. In the morning of 4 September Maria reached hurricane force and its peak intensity around 6 September 0 UTC, when it was a category 3 hurricane according to the Saffir-Simpson hurricane scale (*Simpson*, 1974). After 6 September the storm turned towards the northeast and gradually weakened to tropical storm strength on 9 September 0 UTC. On 10 September Maria was declared extratropical and subsequently began to re-intensify. It hit Iceland on 13 September with nearly hurricane force winds of more than 30 m/s. At the next day the remnants of Maria reached Norway, causing flooding and landslides from heavy precipitation and 1 death (*Pasch and Blake*, 2006).

Fig. 5.3 shows the 6-hourly values of minimum pressure, maximum wind speed, and translation velocity from the NHC best track data set. The translation velocity was calculated from the distance between the NHC track positions. Additionally, the mean and maximum SST values from HOAPS-3 are shown. Fig. 5.4 shows the NHC wind and pressure data, but plotted with the HOAPS-3 mean

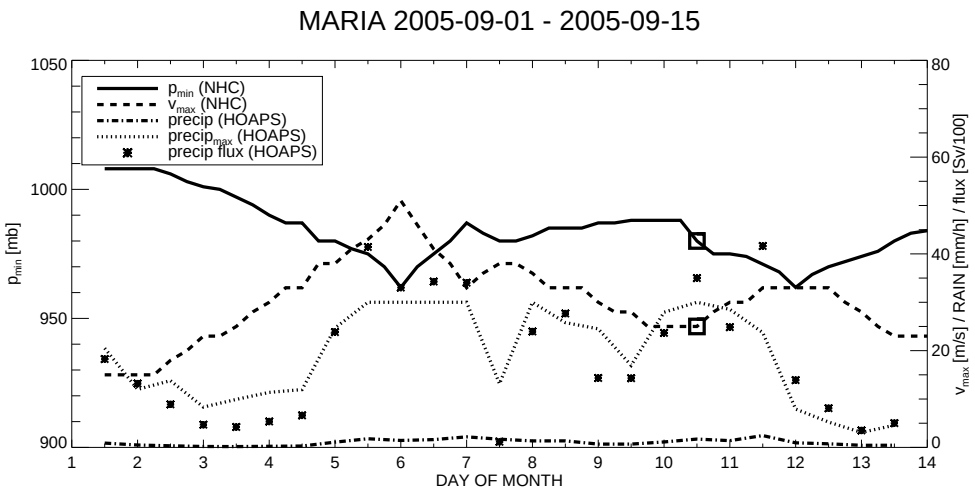

Figure 5.4: Same as Fig. 5.3, but HOAPS-3 values for mean (precip, dotted-dashed line) and maximum precipitation (precip$_{max}$, dotted line) and the total precipitation flux (precip flux, asterisks) within the 500 km region around the center of the cyclone. The unit for the precipitation flux is Sverdrup (1 Sv=10^6 m^3/s).

and maximum precipitation rate as well as the estimated total precipitation flux.

The HOAPS values in both diagrams are inferred from a rectangular region with an edge length of 1000 km which is centered over the storm. This area is considered to capture the center of the storm as well as the surrounding environment for both, the tropical and extratropical phase. The data from all available SSM/I overpasses within this area for 0-12 UTC and 12-24 UTC are binned into 0.5° gridboxes and then averaged for each grid box. The mean values in Fig. 5.3 and Fig. 5.4 are then calculated from the values of the regridded HOAPS-3 data. Accordingly, the maximum values do not represent the value of a single SSM/I pixel, but correspond to the highest value in one of the grid boxes for each date.

To estimate the rain flux in Fig. 5.4, the mean rain rate is scaled with the area that is covered by the rebinned data from the satellite overpasses in the depicted domain of 500 km around the storm center. Precipitation rates above 30 mm/h are masked out in the HOAPS-3 data, as the retrieval does not give reliable quantitative results for values greater than 30 mm/h (see chapter 3.2.6). To compensate for that, the missing values in the precipitation were set to 30 mm/h for the statistics in Fig. 5.3 and Fig. 5.4 if a liquid water path of more than 2 g/kg is detected in the corresponding pixel. This indicates that a substantial water content in the atmosphere is present and intense precipitation is expected. As not the whole domain may be covered by satellite overpasses, the values for the flux also vary with the satellite coverage of the storm. This can be observed in Fig. 5.4 on 7 September, where only a small outer part of the cyclone was captured.

During the formation phase, Maria successively deepened over warm water with temperatures between 25 °C and 30 °C as shown in Fig. 5.3. At the same time, the maximum wind speed increases constantly until a peak of 50 m/s was reached at a minimum pressure of 962 hPa on 6 September.

The translation velocity (Fig. 5.3) declines from about 10 m/s in the formation phase to a minimum around the peak intensity on 5 and 6 September, which lies within the range of 3 to 6 m/s. The latter range is known to be favorable for the development of an intense TC (*Wang and Wu*, 2004). At lower translation speeds vertical mixing of the upper ocean layers through wind stress causes a cooling of the ocean surface, while a faster movement will cause an asymmetric wind field. Both of these factors will hinder the further intensification of a TC (*Wang and Wu*, 2004).

After reaching the maximum intensity, Maria moved further north and accelerated during the ET to a velocity around 20 m/s, with peaks of 40 m/s within the extratropical environment.

Along the track of the storm, the mean underlying SST around the storm center dropped from 25 °C to 12 °C during the ET between 10 and 12 September. This strong gradient can also be observed in the SST field in Fig. 5.2 between 40° N and 50° N.

The highest values for the maximum precipitation (Fig. 5.4) are found near the time of peak intensity, where the value reaches the upper limit of the HOAPS-3 precipitation retrieval of 30 mm/h. During the intermediate weakening after Maria reached its peak intensity, the maximum precipitation rate decreases to values around 20 mm/h and increases again to nearly 30 mm/d as the storm approaches the extratropical environment and undergoes ET. The mean precipitation rate for the 500 km area around the storm center is below 5 mm/h for the whole record. Maximum values occur near the peak intensity and re-intensification stage. Accordingly, the estimate of the precipitation flux reaches a maximum during these phases with values of 0.4 Sv. During the extratropical re-intensification stage, the cyclone produces as much rainfall, as it did in its peak intensity tropical phase.

5.5 Hurricane Phase

Fig. 5.5 shows satellite images of Maria on 4 September, when it just was declared a category 1 hurricane. HOAPS-3 precipitation (Fig. 5.5, top right panel) and wind speed (Fig. 5.5, bottom panel) exhibit a well defined spiral structure. The MODIS image from the afternoon overflight at 17:00 UTC (Fig. 5.5, top left panel) does not fully cover the storm, but clearly shows the cloud band in the southeastern quadrant and the convective cloud cover around the core. Both are

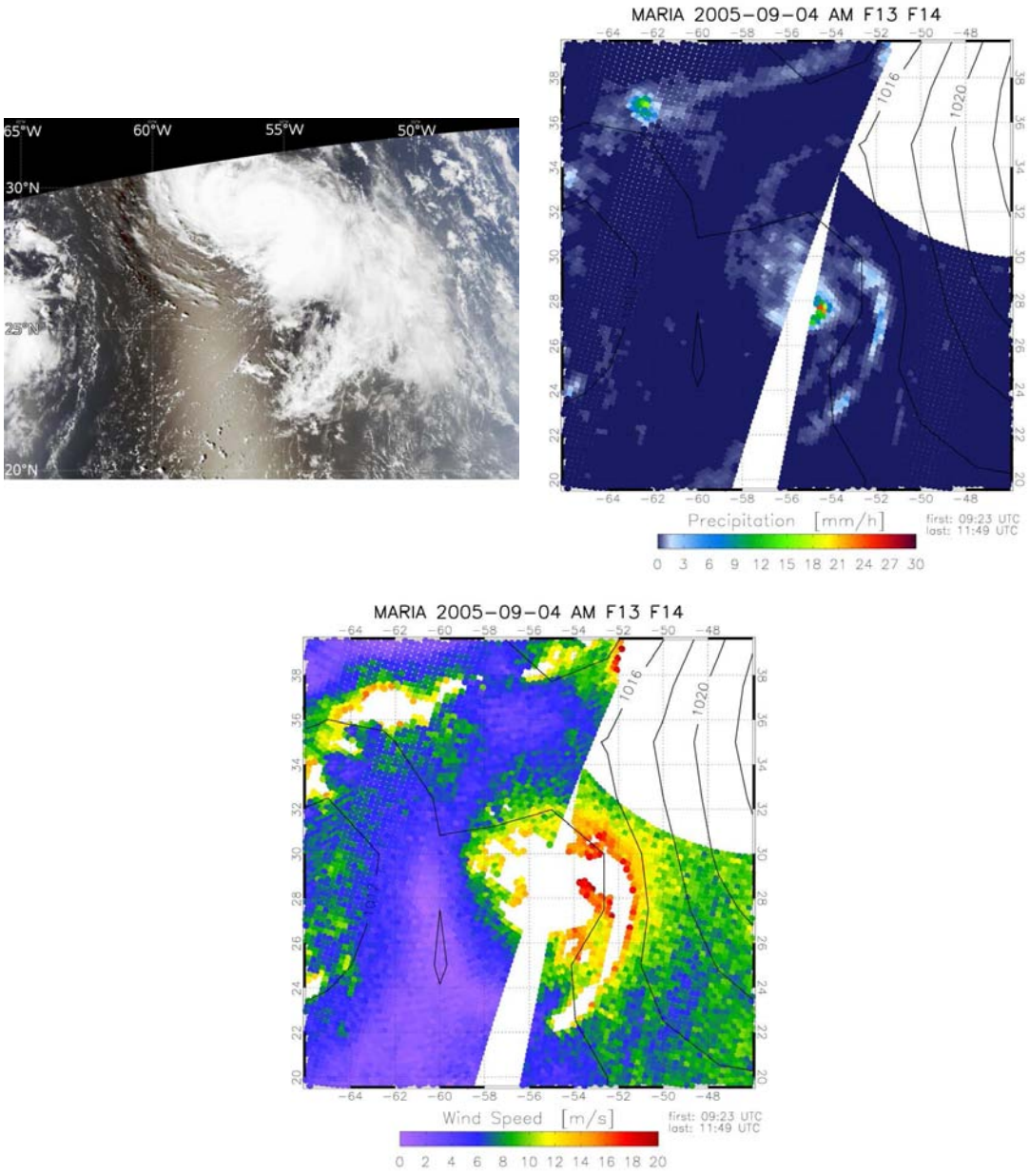

Figure 5.5: Maria on 4 September at the stage of a category 1 hurricane. The Aqua MODIS VIS image (top left) was recorded at 17:00 UTC. HOAPS-3 data for precipitation (top right) and wind (bottom) is composed from overflights between 9:23 UTC and 11:49 UTC. Isolines in the HOAPS-3 precipitation and wind fields, show the NCEP-R2 MSLP [hPa] field for 12:00 UTC.

associated with strong wind and precipitation, as is evident from the HOAPS-3 data. Heavy precipitation occurs with rates over 20 mm/h at the core and up to 6 mm/h in the spiral arms. The wind field exhibits some gaps in regions where the surface signal is shielded by heavy rain. However, a mostly symmetric appearance around the core is recognizable. The eastern quadrant with the pronounced spiral arm exhibits slightly higher wind speeds than the region west of the storm. This is in accordance with the MODIS image, where convection is also evident to the east of the system, but not in the regions west of the storm.

Fig. 5.6 shows Maria shortly after the hurricane reached its peak intensity (category 3) on 6 September. The center of Maria exhibits circular cloud patterns with a broad tail extending from the southeastern quadrant to the south of the storm. Another convective cloud band is located north of the hurricane and at the western boundary of the image a second hurricane, Nate, is visible.

In the HOAPS-3 precipitation data (Fig. 5.6, top right panel), which is from about 6 hours prior to the MODIS image, the heavy precipitating core is clearly discernible with rates up to 30 mm/h. In the inner core, the values are likely to be even higher, but are masked out by the retrieval. The tail of clouds extending to the south is also represented in the HOAPS-3 data. In the cloud band north of the hurricane, strong precipitation is found collocated with the brightest clouds (and hence thickest) on the MODIS image. The core of hurricane Nate is also partly visible in the HOAPS-3 precipitation data at the southwestern edge of the image.

The lower panels in Fig. 5.6 show two wind fields from QuikSCAT (bottom left) and HOAPS-3 (bottom right). The HOAPS-3 image is composited from two overflights at 9:36 UTC and 10:36 UTC, from which the latter overpass covers the center of the storm. The QuikSCAT image was recorded just a short time earlier at 9:14 UTC, hence allowing a good comparison of the two data sources. Although the values in the QuikSCAT image are given in knots, the color scale is roughly comparable to the one given for the HOAPS-3 image, as 1 knot equals about 0.5 m/s.

Since the accuracy of the SSM/I based wind retrievals is influenced by precipitation, the corresponding values are flagged out in HOAPS-3 (see chapter 3.2.1). The scatterometer signal is influenced by precipitation as well. Absorption and/or scattering at hydrometeors in the signal pathway and changes of the ocean surface roughness impair the wind retrieval and hence the accuracy of the derived values (*JPL*, 2006). However, in the QuikSCAT image (Fig. 5.6, bottom left panel) the corresponding regions are not completely flagged out, but marked by white wind barbs, indicating unreliable values. The dashed white line in the QuikSCAT image of Fig. 5.6 makes the affected regions clearer. The main areas where this is the case are the core of the cyclone and the cloud band north of the storm. These

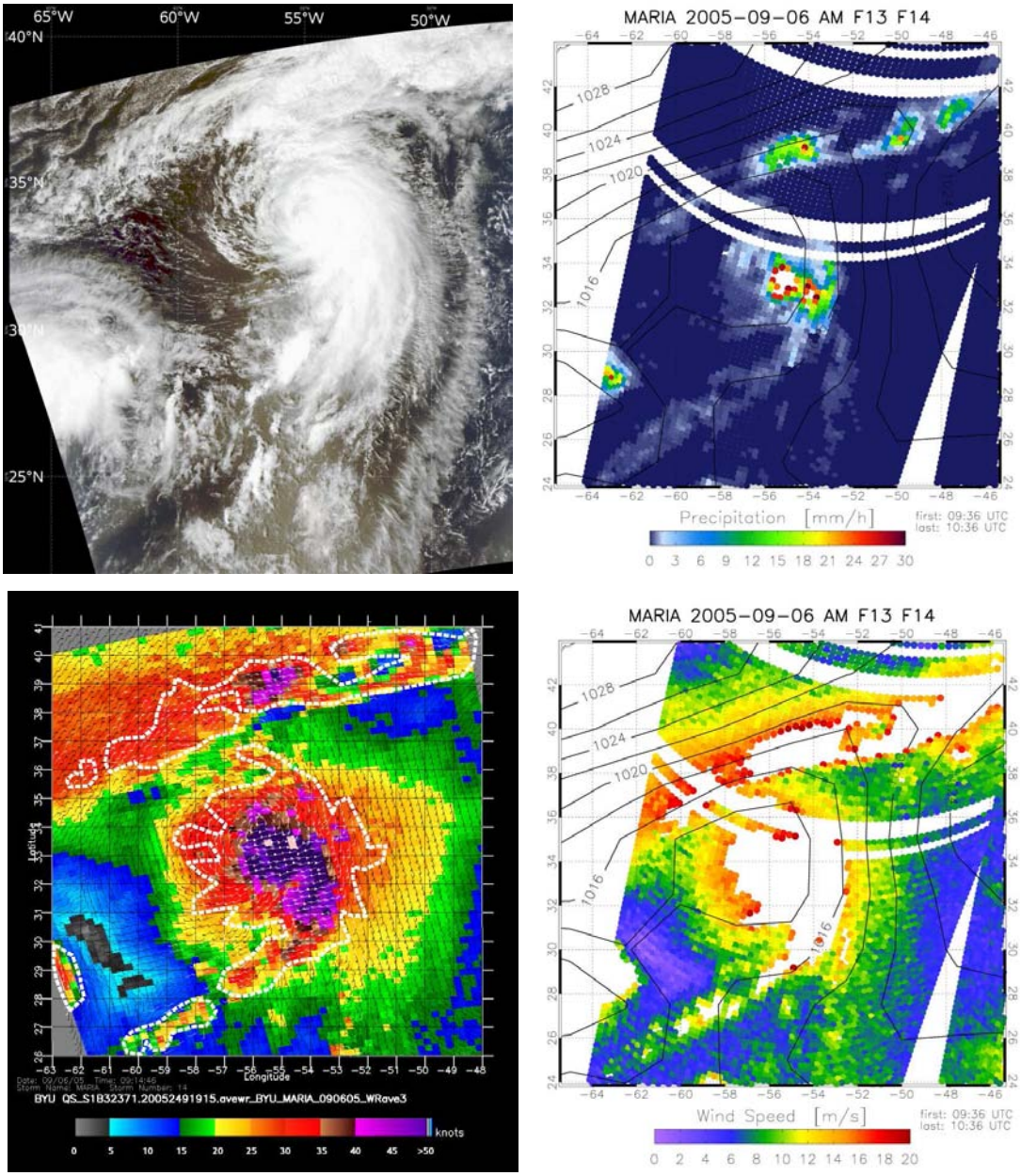

Figure 5.6: Maria on 6 September at peak intensity (category 3). The Aqua MODIS VIS image (top left) was recorded at 16:50 UTC. HOAPS-3 data for precipitation (top right) and wind (bottom right) is composed from overflights between 9:36 UTC and 10:38 UTC. Isolines in the HOAPS-3 precipitation and wind fields, show the NCEP-R2 MSLP [hPa] field for 12:00 UTC. The bottom left panel shows a QuikSCAT wind field from an overpass at 9:14 UTC. Regions where rain contamination was detected in the QuikSCAT retrieval are marked by a white dashed line.

regions in the QuikSCAT image are in good agreement with the precipitation patterns detected in HOAPS-3 and hence where the HOAPS-3 wind data is masked out.

In the center of the hurricane, where most of the wind values are flagged in the HOAPS-3 and QuikSCAT data. In this comma shaped region strong precipitation is detected by HOAPS-3. The flagged QuikSCAT wind speeds are around 25 m/s (50 knots) in this region. The corresponding maximum values from the NHC best track data set are higher as these are between 50 m/s at 0 UTC and 40 m/s at 12 UTC. The circular wind barbs in the QuikSCAT image indicate the position of the hurricane's eye near 34° N at the northern tip of the comma shaped region of maximum wind and precipitation.

Just outside the masked area in the core of the cyclone, wind speeds of 15 m/s to 20 m/s are found HOAPS-3. This agrees with the values from QuikSCAT that reach up to 35 knots (18 m/s).

In the cloud band north of the storm, a second region with very high QuikSCAT wind speeds and strong precipitation in HOAPS-3 is found. Where available, HOAPS-3 and QuikSCAT wind speeds exhibit comparable values in this region.

In the cloud-free area west of the storm, HOAPS-3 and QuikSCAT both consistently show wind speeds below 7 m/s.

The NCEP-R2 MSLP field also captures a pressure minimum near the core. However, with more than 1000 hPa, this core pressure is much higher than that given by the NHC best track data set. Also, a slight displacement of the storm center to the west compared to the satellite is evident in the NCEP-R2. The reasons for these deviations is most likely the coarse spatial resolution of the NCEP-R2 data, as the temporal mismatch is small and the storm moved in northern direction at that time.

5.6 Extratropical Transition

As Maria moved further northward it began to lose strength. On 9 September Maria had weakened to a tropical storm while it approached the midlatitude baroclinic environment.

Fig. 5.7 shows MODIS and HOAPS-3 data of Maria on the afternoon of 9 September. The MODIS cloud patterns (Fig. 5.7, top left panel) exhibit a decrease of deep convection in the southwestern quadrant, but still a mostly symmetric cloud structure of the TC. In the northeastern quadrant, centers of deep convection persist, leading to heavy precipitation as it is evident from the HOAPS-3 precipitation in the top right panel of Fig. 5.7. Near the center of the storm, precipitation rates of up to 30 mm/h occur. A second patch of intense precipitation

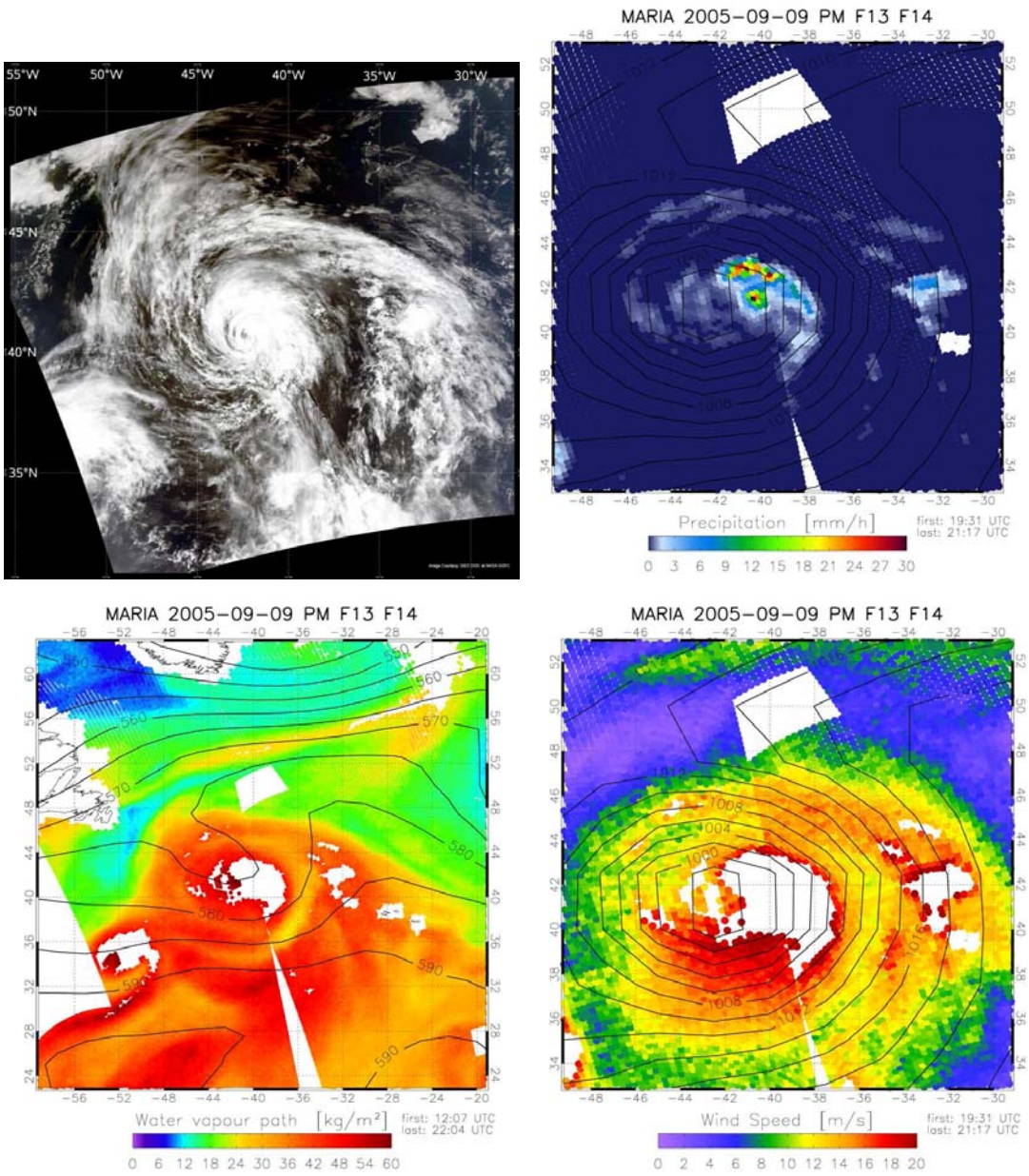

Figure 5.7: Maria on 9 September. The Aqua MODIS VIS image (top left) was recorded at 15:45 UTC. HOAPS-3 data for precipitation (top right) and wind (bottom right) is composed from overflights between 19:31 UTC and 21:17 UTC. The HOAPS-3 water vapor image (bottom left) is composed from overflights between 12:07 UTC and 22:04 UTC. Note the different spatial scale of the water vapor image. Isolines in the HOAPS-3 precipitation and wind fields, show the NCEP-R2 MSLP [hPa] field for 18:00 UTC and the 500 hPa geopotential height [gpdm] field in the water vapor image.

is located to the east of the center at 32° W with rates of more than 6 mm/h. The MODIS cloud image shows a convective system at the same position.

The HOAPS-3 wind field (Fig. 5.7, bottom right panel) exhibits wind speeds of more than 20 m/s just outside the masked areas near the center of precipitation. Also in the area south of the core of the TC wind speeds of up to 20 m/s occur, while to the northwest of the core the wind speeds are substantially lower with 10 m/s to 15 m/s.

Some of the structural changes in the storm, such as the modification of the precipitation field, indicate the onset of ET according to the conceptual model of *Klein et al.* (2000) (section 5.2). However, from the HOAPS-3 water vapor image (Fig. 5.7, bottom left panel) it is evident that the cyclone is still embedded in moist tropical air masses. Moreover, the western sector does not yet show a substantial advection of cool, dry air into the TC from the north.

The 500 hPa geopotential height field (Fig. 5.7, lower left panel) shows a disturbance extending to the northwest from the center of the storm. The interaction of a TC with an upper level trough during the process of ET is an important factor for a possible re-intensification of the system in the extratropical stage. For example *Harr and Elsberry* (2000) and *Ritchie and Elsberry* (2003) showed that the further development during ET is very sensitive to the existence and position of an upper level disturbance relative to the transforming TC. A trough located to the northwest of the storm is favorable for the development of an extratropical cyclone with distinct frontal structures. The upper tropospheric potential vorticity maximum and increased baroclinity in the lower troposphere associated with the trough leads to an intensification of the cyclone during the ET process (*Klein et al.*, 2000).

On the next day, 10 September, Maria was declared extratropical according to the NHC best track data set. The cyclone had moved into a region with strong SST gradients (see Fig. 5.3) and the cloud pattern has lost its circular shape. The southwestern sector is now mostly free of clouds as shown by the dark area on the AVHRR IR image (Fig. 5.8, top left panel). The influx of dry air masses into this region is clearly evident from the HOAPS-3 water vapor image (Fig. 5.8, bottom left panel). These air masses form a dry slot and are wrapping around the core from the southwestern sector. Such a dry slot is associated with the transport of upper level potential vorticity down to the troposphere and can lead to a rapid cyclogenesis (*Browning*, 1997). In the ET process dry slots are regularly observed as shown in the scheme of Klein (section 5.2).

East of the cyclone, tropical air masses are advected northward, leading to a maximum of precipitation north of the core and frontal structures and multi-layer clouds begin to evolve as described in the second step of the Klein ET scheme. In the AVHRR image (Fig. 5.8, top left panel) deep convection (associated with

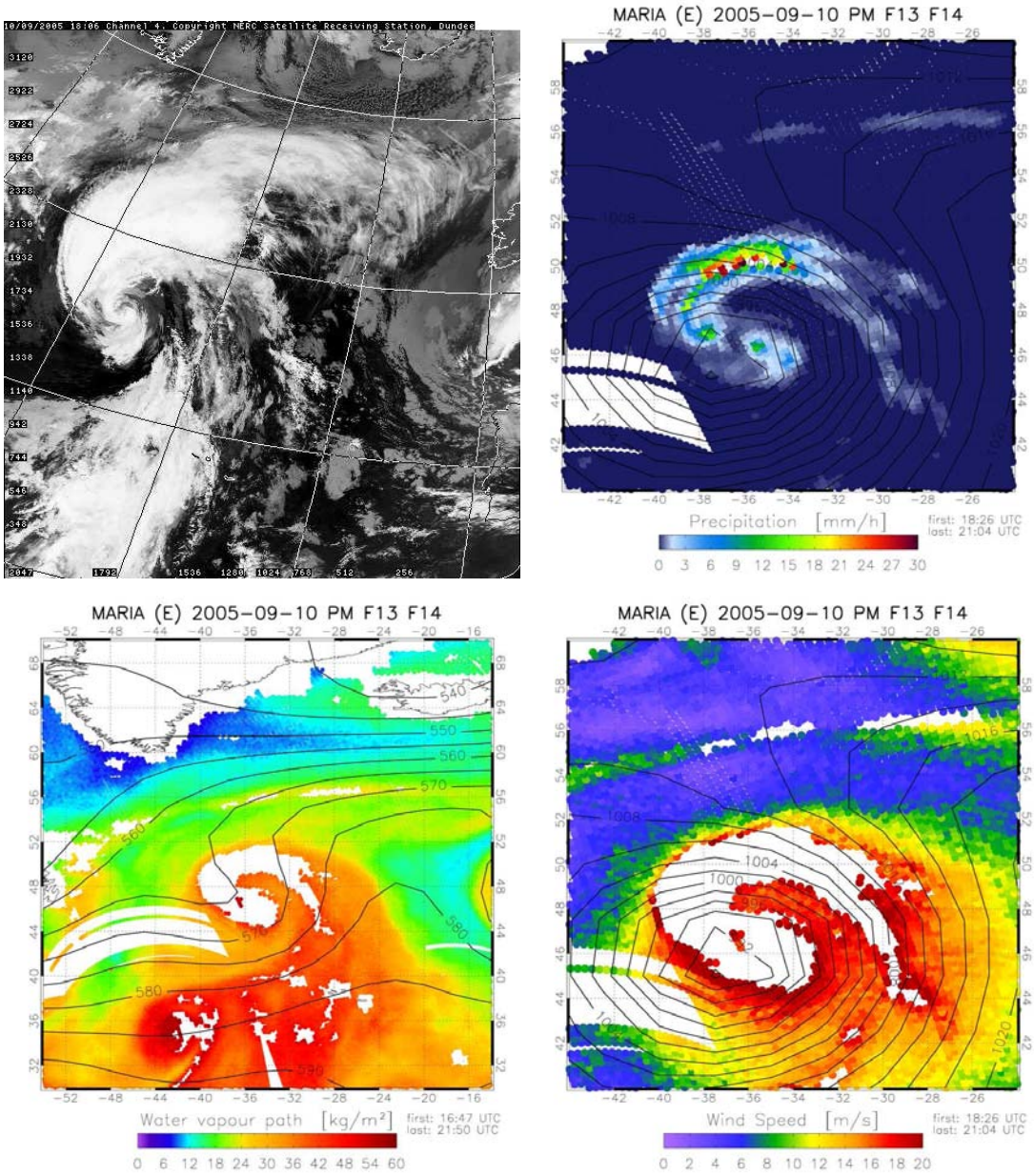

Figure 5.8: Maria on 10 September. The AVHRR quicklook IR image (top left) was recorded at 18:06 UTC. HOAPS-3 data for precipitation (top right) and wind (bottom right) is composed from overflights between 18:26 UTC and 21:04 UTC. The HOAPS-3 water vapor image (bottom left) is composed from overflights between 16:47 UTC and 21:50 UTC. Note the different spatial scale of the water vapor image. Isolines in the HOAPS-3 precipitation and wind fields, show the NCEP-R2 MSLP [hPa] field for 18:00 UTC and the 500 hPa geopotential height [gpdm] field in the water vapor image.

bright, cool pixels) is found now north of the core and wrapping in a hook like structure counter-clockwise around the core. The HOAPS-3 precipitation patterns (Fig. 5.8, top right panel) agree remarkably well with the cloud structures in the AVHRR image.

Further to the north, cirrus from the remnants of the TC outflow extends eastward. Dark and bright clouds on the AVHRR image indicate a mixture of high and low-level clouds in the cyclone.

The wind field (Fig. 5.8, bottom right panel) is becoming increasingly asymmetric and shifted northeastward of the core. High wind speeds of more than 20 m/s are evident around the core and along the evolving fronts in the southeastern sector.

On 11 September, the ET of Maria is nearly completed. The deep convection around the core is eroded and low-level clouds appear on the AVHRR image (Fig. 5.9, top left panel). In the north of the cyclone, the remnants of the cirrus shield from the TC outflow are still visible. A distinct warm front has developed to the east of the cyclone center. The HOAPS-3 water vapor image (Fig. 5.9, bottom left panel) shows that the front is still in contact with tropical air masses which are advected northward along the front. Strong precipitation occurs north of the cyclone's center where these air masses ascent in the baroclinic environment and along the bent back front that is wrapping cyclonically around the center of the system.

Directly to the south of the circulation center a sharp edged cloud structure is observed in the AVHRR image. HOAPS-3 data exhibits strong precipitation and winds in this region. This feature is a so called "sting jet"and regularly occurs in rapidly deepening cyclones, where a seclusion of warm air is encircled in the center of the cyclone. The jet is located at the head of the bent back front along with the dry slot and is associated with strong winds due to diabatic cooling and hence downward transport of momentum (*Browning and Field*, 2004).

Subsequently, Maria underwent a rapid deepening from 11 September to 12 September and reached its maximum extratropical intensity with a core pressure of 962 hPa. Fig. 5.10 shows Maria as a mature extratropical cyclone on 12 September. During the rapid intensification, a warm core seclusion has developed. From the water vapor image, the warm core seclusion is evident by the moist air which is trapped in the center of the cyclone as it was quickly surrounded by cool, dry air and the bent back front (*Shapiro and Keyser*, 1990; *Hart*, 2003).

The air in the core is unstable and convection around the core has developed again, as shown by the AVHRR image (Fig. 5.10, top left panel). The radius of strong winds around the center has increased as has the overall size of system. In the region around the core, wind speeds of 25 m/s and precipitation rates

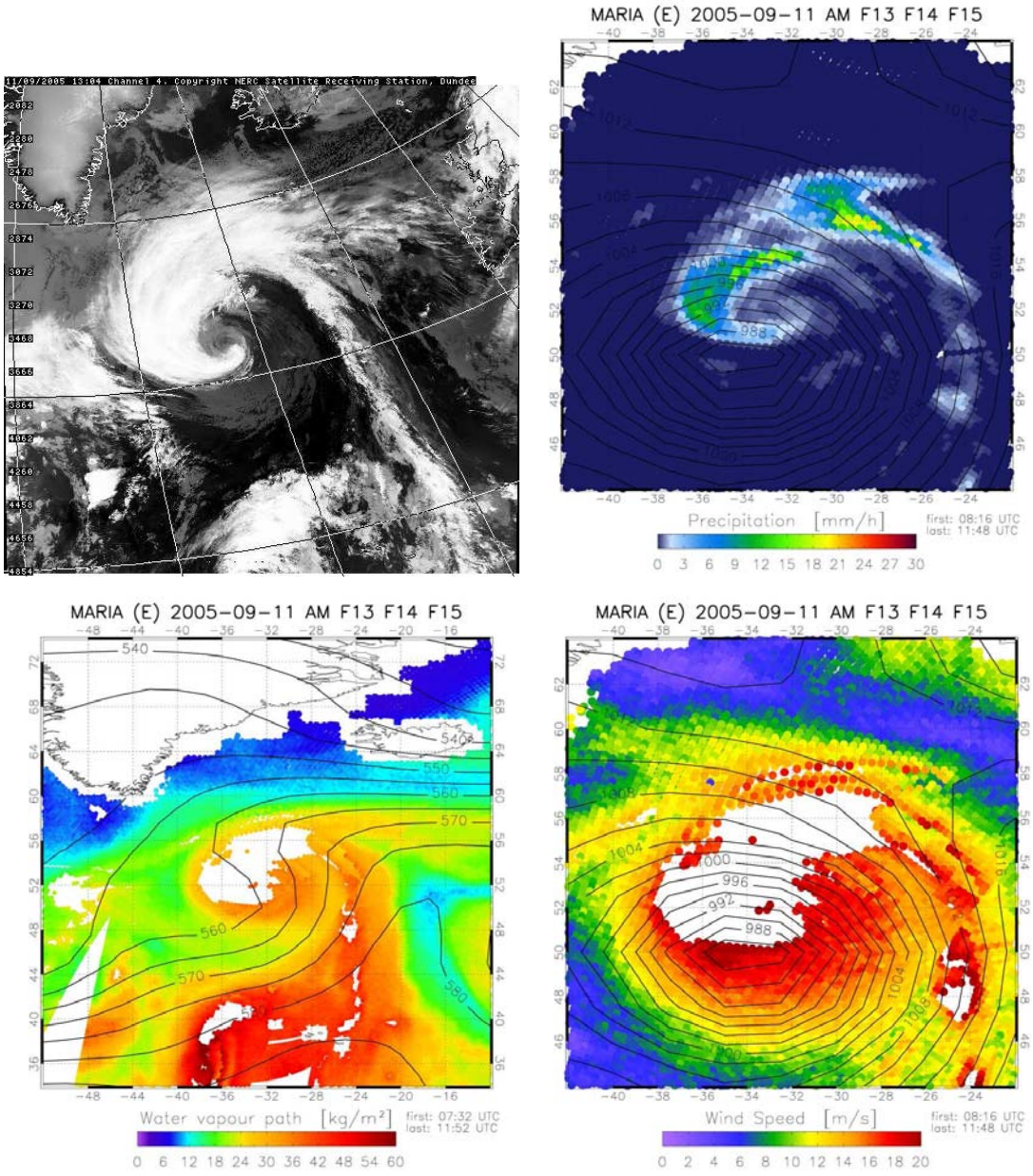

Figure 5.9: Maria on 11 September. The AVHRR quicklook IR image (top left) was recorded at 13:04 UTC. HOAPS-3 data for precipitation (top right) and wind (bottom right) is composed from overflights between 08:16 UTC and 11:48 UTC. The HOAPS-3 water vapor image (bottom left) is composed from overflights between 07:32 UTC and 11:52 UTC. Note the different spatial scale of the water vapor image. Isolines in the HOAPS-3 precipitation and wind fields, show the NCEP-R2 MSLP [hPa] field for 12:00 UTC and the geopotential height [gpdm] field in the water vapor image (unit is gpm).

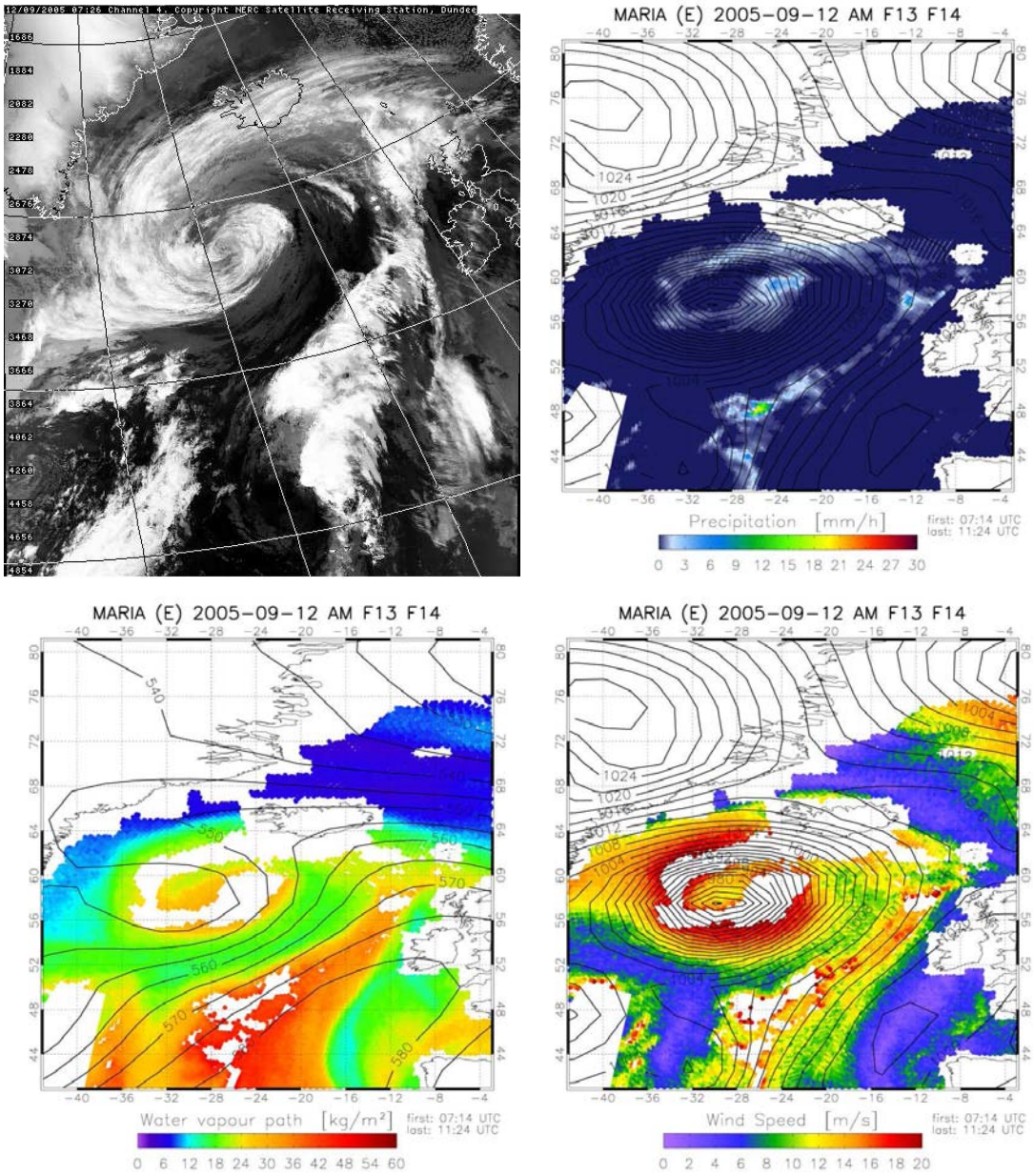

Figure 5.10: Maria on 10 September. The AVHRR quicklook IR image (top left) was recorded at 07:26 UTC. HOAPS-3 data for precipitation (top right), water vapor image (bottom left), and wind (bottom right) is composed from overflights between 07:14 UTC and 11:24 UTC. The spatial scale of the precipitation and wind images differs from the previous figures. Isolines in the HOAPS-3 precipitation and wind fields, show the NCEP-R2 MSLP [hPa] field for 12:00 UTC and the 500 hPa geopotential height [gpdm] field in the water vapor image.

of 8 mm/h are detected by HOAPS-3. The frontal convection centers contain precipitation of up to 20 mm/d.

In the following days, Maria caused hurricane force winds over Iceland and brought massive precipitation to the Norwegian coast, while moving on eastward.

5.7 Conclusions

The development of the hurricane Maria has been examined using HOAPS-3 and additional satellite data. Through the synergetic use of different data sources, a detailed view on the structure of the storm was achieved, documenting the different stages of its evolution. With the use of HOAPS data for this study, a nearly complete twice daily coverage of the storm development from the storm's genesis in the tropics until its decay at high latitudes is achieved. The use of information from the SSM/I microwave radiometer, allows the derivation of geophysical parameters such as wind and precipitation, which cannot be reliably measured using IR instruments.

For the hurricane phase, precipitation patterns exhibit the characteristic structures of a hurricane with a heavy precipitating core and rain bands that are extending to the outer circulation of the hurricane. The precipitation intensity agrees qualitatively well with the observed cloud pattern and shows reasonable relative magnitudes. Using additional information from the liquid water path for the cases, where the HOAPS-3 precipitation retrieval is not defined, a total precipitation flux of 0.4 Sv for the peak intensity phase as well as during ET could be estimated.

The retrieval of wind speed under extreme conditions, especially in connection with heavy rain, remains a common problem of satellite based retrieval methods. Nevertheless, with the limitation of being available for rain-free regions only, HOAPS-3 and QuikSCAT retrievals were in good agreement for coincident overflights at the date of peak intensity of Maria.

From 10 to 12 September Maria transformed from a tropical cyclone into a strong warm core seclusion extratropical cyclone. The structural changes such as the displacement of the precipitation to the north of the core, an asymmetric wind field and the advection of air masses into the cyclone, are captured using HOAPS-3 and VIS/IR data. The independent SSM/I and VIS/IR observations agree remarkably well for large and small scale features.

Overall, the use of HOAPS-3 data allowed an improved frequent and continuous coverage of a tropical cyclone and its ET in a case study, resulting in the retrieval of valuable geophysical parameters from satellite data for an ET as demanded by *Jones et al.* (2003). Due to the successful application of HOAPS-3

data in this case study, a further climatological assessment of ET appears to be possible including additional parameters from HOAPS-3. Also, a detailed comparison study with a model simulation is desirable, which may add additional information on the atmospheric dynamics within the transforming cyclone. Another important factor in the development is the exchange of latent and sensible heat at the atmosphere-ocean interface. The impact of surface fluxes on the development of an extratropical cyclone is not as clear as for a TC (*Jones et al.*, 2003). In principle, this could be studied using HOAPS-3 data, but due to the limitation of the retrieval to rain-free regions only very fragmented data is available for one case. Here, a composite study using a number of cases could give more meaningful results.

6

HOAPS and GPCC Combined Precipitation Analysis of North Atlantic Variability

In this chapter the precipitation and freshwater flux from HOAPS-3 is assessed with respect to its variability associated with the *North Atlantic Oscillation* (NAO). The NAO is one of the most prominent atmospheric teleconnection patterns of the Northern Hemisphere with distinct impacts for the whole oceanic and continental North Atlantic region. Especially for the European winter, the climatic conditions are to a great extent determined by the NAO. The strong signal of this phenomenon makes it a source of validation for the HOAPS-3 data set on climatological scale. Therefore, the response of HOAPS-3 parameters to the atmospheric variations related to the NAO will be investigated. While the focus of this study is on precipitation, the freshwater flux and related parameters will also be examined.

Since HOAPS-3 does not include any over-land precipitation retrievals, it was complemented with the "Full Data Reanalysis Product Version 4" (*Schneider et al.*, 2008), which is provided by the *Global Precipitation Climatology Centre* (GPCC) . This product is solely based on rain gauge measurements and provides global land surface precipitation. The combination of both data sets yields unique high-resolution, quasi-global precipitation fields compiled from two independent data sources.

Other satellite climatologies, such as the Global Precipitation Climatology

Project (GPCP, *Adler et al.*, 2003), NOAA's Climate Prediction Center (CPC) Merged Analysis of Precipitation (CMAP, *Xie and Arkin*, 1997), or products from the Tropical Rainfall Measuring Mission (TRMM, *Adler et al.*, 2000) provide over land retrieved precipitation data. However, these satellite based estimates are constrained or complemented with precipitation estimates based on rain gauge measurements to correct deficiencies in the satellite retrievals. The CMAP enhanced data set (Xie, 1997) additionally uses reanalysis data.

Next to precipitation, the ocean surface freshwater flux plays an important role for the North Atlantic climate system. Variations of this parameter over the ocean are considered large enough to influence surface salinity with the potential to effect the thermohaline circulation in the ocean (*Marshall et al.*, 2001; *Hurrell et al.*, 2003).

A previous analysis based on the first version of HOAPS was carried out by *Bakan et al.* (2000) including the two winter seasons of 1994/95 and 1995/96, which represented a pronounced high and low NAO state. This study already indicated the potential of satellite derived data to assess the over ocean freshwater flux components precipitation and evaporation with respect to North Atlantic variability. However, this analysis lacked a sound statistical basis. Recently *Mariotti and Arkin* (2007) assessed the long-term sensitivity of precipitation to the NAO using reanalysis data and the satellite based CMAP and GPCP products. Many other studies featured either only land based precipitation, used ship based measurements or were exclusively based on model and reanalysis data (*Cayan*, 1992; *Hurrell*, 1995; *Walsh and Portis*, 1999; *Bojariu and Reverdin*, 2002). Furthermore, *Wanner et al.* (2001) review previous studies concerning the North Atlantic Oscillation.

The present study follows a new approach by combining over-ocean satellite retrievals with a purely rain gauge based land data set. Apart from the agreement of the climatological mean fields, the evaluation of the response of the combined data set to atmospheric fluctuations related to the NAO will prove the validity of the merged HOAPS-3/GPCC data set and hereby also of the individual source products.

At first an introduction to the data used along with an overview of the NAO is given in section 6.1 and section 6.2. Regional impacts of the NAO on the precipitation will be inspected in section 6.3, followed by the evaluation of composite patterns in section 6.4, and an *empirical orthogonal function* (EOF) analysis in section 6.5. Finally correlation patterns for the North Atlantic and on the global scale are investigated in section 6.6. This includes a comparison with other precipitation data and the assessment of oceanic freshwater flux components from HOAPS-3.

6.1 The HOAPS-3/GPCC Data Set

For this study, a combined data set of satellite retrieved precipitation from the HOAPS-3 climatology and rain gauge based data from the GPCC was compiled. Both data sets stem from completely independent data sources and the combined HOAPS-3/GPCC product contains no adjustments between the data sets.

The HOAPS-3 over ocean precipitation data set is the HOAPS-G monthly mean gridded product described in chapter 3 (*Andersson et al.*, 2007a). In addition to the publicly available data for the time period mid 1987 to end of 2005, the record for the precipitation parameter has been extended to April 2007. It now includes nineteen December to March winter seasons from December 1988 to March 2007. Data from winter 1987/88 are not used due to a defective satellite (see chapter 3).

Over land, rain gauge based data from GPCC is used, which are created from various sources of rain gauge raw data from international weather services. All data that are processed at the GPCC undergo various quality-checks, a harmonization procedure, and are finally resampled as spatial means on a regular grid. As rain gauges are not distributed uniformly over the land surface, interpolation methods are used to fill data void regions and gauge over-population. GPCC uses an empirical interpolation method after *Willmott et al.* (1985) which is a spherical adaption of an inverse distance-weighting scheme by *Shepard* (1968) (*Rudolf et al.*, 1994). According to *Rudolf and Schneider* (2005) the scheme takes into account:
(a) the distances of the stations to the gridpoint (for a limited number of nearest stations),
(b) the directional distribution of stations versus the gridpoint (in order to avoid an overweight of clustered stations), and
(c) the gradients of the data field in the gridpoint environment.

Here, the "Full Data Reanalysis Product Version 4" (*Schneider et al.*, 2008) with a grid resolution of 0.5° is used, which was obtained from the GPCC's website (`http://gpcc.dwd.de`). The time series starts at 1901 and is regularly updated with recent data. The Full Data Reanalysis Product uses all station data available in the GPCC data base to provide high spatial accuracy. A drawback of this procedure is that the number of stations per gridbox can vary, depending on the existing input data.

GPCC provides another long-term climatological data set, the "VASClimO" product, which is optimized to maintain a spatial and temporally homogeneous time series. However, at present, the VASClimO product covers the time period from 1951 until 2000. This would limit the overlapping time frame with HOAPS-3 to 13 years only. Hence, the Full Data Reanalysis Product is used here as it

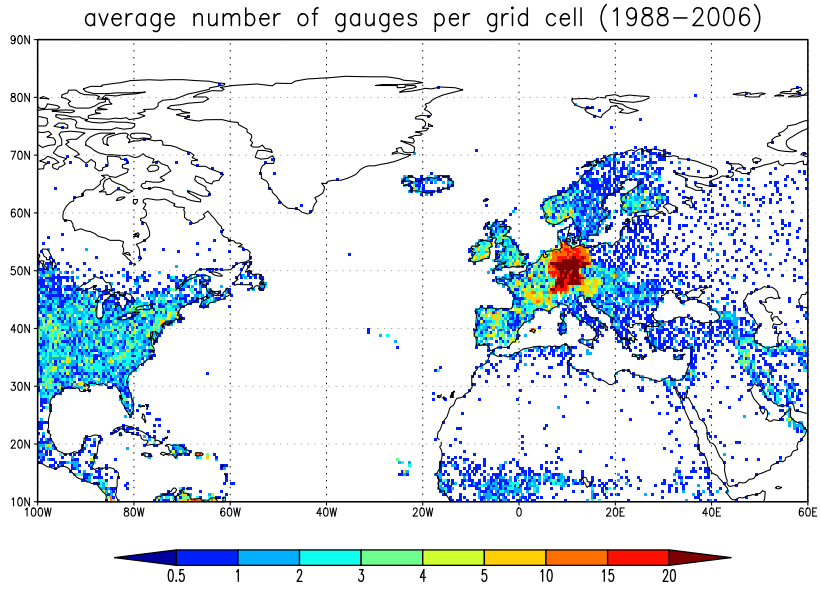

Figure 6.1: Mean number of gauges per grid box in the GPCC Full Data Reanalysis Product V4 product.

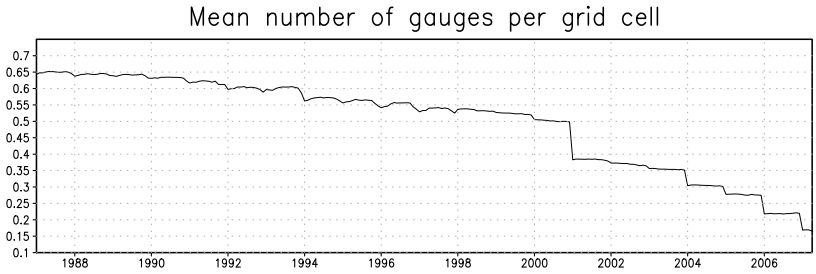

Figure 6.2: Average number of gauges for the North Atlantic region (100° W – 60° E, 10° N – 90° N) in the GPCC Full Data Reanalysis Product V4 product.

contains data until the present date, allowing an analysis based on a nearly 20 year time record including nineteen winter seasons.

Moreover, for the North Atlantic region, the Full Data Reanalysis Product provides a sufficient coverage throughout the overlapping time period with HOAPS-3. As depicted in Fig. 6.1, a dense coverage of stations is achieved, except for Russia, the almost data void Arctic, and desert regions in Africa and Arabia. However, as mentioned above, the temporal coverage is not constant. Fig. 6.2 shows a continuous decline in the mean number of gauges per grid cell with a pronounced step at the end of 2001. This step is mainly caused by a decrease in the number of station from central Europe and the United States. Since the number of stations in these regions is generally very dense, this decrease should not affect the quality of the product. The density of stations is considered to be sufficient to provide a homogeneous record for the North Atlantic region and the whole time period

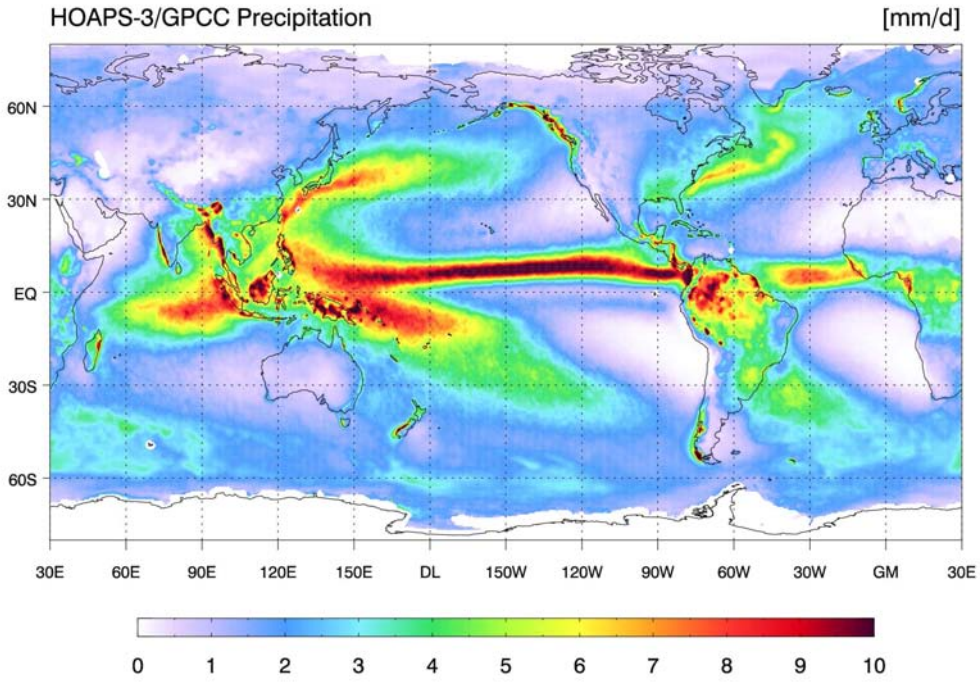

Figure 6.3: Global climate mean precipitation in mm/d for the years 1988–2006 of the combined HOAPS-3/GPCC product.

relevant for this study.

The GPCC Full Data Reanalysis Product and the HOAPS-3 monthly mean gridded data set are combined into a product with a grid resolution of 0.5°, which is natively available from both sources. Coastal pixels are not included in either of the data sets. Therefore, an interpolation routine was implemented to fill these gaps. The method involves a distance weighted mean of the 8 pixels surrounding the missing data point, while a minimum of 5 valid data points is the threshold for which the interpolation is performed. This procedure is repeated recursively until all gridboxes, that fulfill the criterion for interpolation, are filled.

Overall, this yields a high-resolution data set which is capable of resolving variability on fine spatial scales. Fig. 6.3 shows the climatological mean of the combined HOAPS-3/GPCC data set. Except for regions permanently covered by sea ice, the data void Antarctica and some smaller spots at islands or regions with very uneven coast lines, a quasi-global coverage is achieved. The resulting merged field is consistent and exhibits an apparently globally homogeneous precipitation structures. The transition of large scale precipitation patterns from sea to land regions is reasonably resembled in magnitude and location. The following analyses will be limited to the land regions and the ice-free ocean, since no precipitation data over sea ice is available from either of the input data sets. This concerns

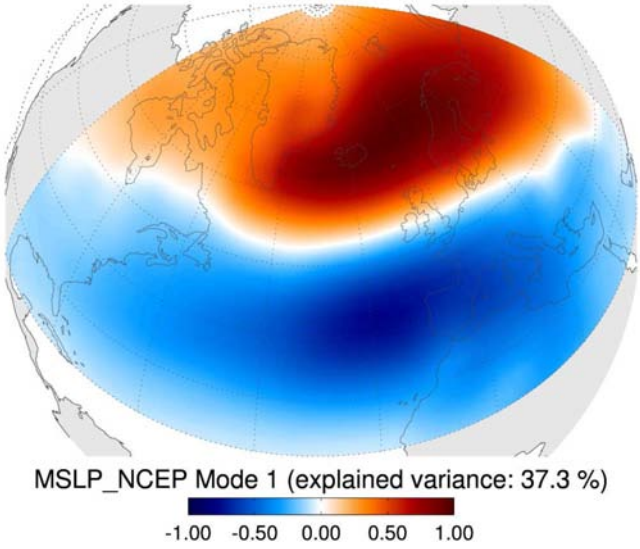

Figure 6.4: First normalized EOF of North Atlantic mean sea level pressure from NCEP-2 data based on December to March monthly means of the years 1988 to 2006.

mainly the Arctic Ocean, Nordic Seas, and the Labrador Sea region. For the EOF analysis in section 6.5 and the correlation analysis in section 6.6 the data is locally deseasonalized and detrended for each grid box in order to focus on the monthly variation of the data.

6.2 The North Atlantic Oscillation (NAO)

Records of the phenomenon that is nowadays named the "North Atlantic Oscillation" date back to the 18th century, when the missionary Hans Egede Saabye wrote: "*In Greenland all winters are severe yet they are not all alike. The Danes have noticed that when the winter in Denmark was severe, as we perceive it, the winter in Greenland in its manner was mild, and conversely*" (*van Loon and Rogers*, 1978). At present day it is known, that this apparently contradictory behavior of the weather is associated with the meridional oscillation of air masses in the North Atlantic region.

Especially during the cold season, a pressure dipole associated with the Icelandic low and the Azores high is the dominant mode of weather and climate variability in the North Atlantic region. During this season, more than one third of the *sea level pressure* (SLP) variance over the North Atlantic can be attributed to the NAO (*Barnston and Livezey*, 1987; *Hurrell and van Loon*, 1997). Fig. 6.4 shows the first normalized EOF of the North Atlantic mean SLP computed for the winter months from NCEP-R2 reanalysis data. A distinct dipole pattern with

maxima at the locations of the Icelandic low and Azores high is evident. The pattern explains 37.3 % of the winter SLP variance in the North Atlantic region for the time period 1988-2006.

Because of the well defined regional signature of the NAO, it can be described by the difference of the SLP at two stations near the centers of action. The first definition of such a "North Atlantic Oscillation Index" originates from Sir Gilbert Walker (*Walker*, 1923; *Walker and Bliss*, 1932). Later, several commonly used station based NAO indices were defined by *Rogers* (1984), *Hurrell* (1995), and *Jones et al.* (1997). These indices are computed from the normalized SLP difference between the Icelandic stations and Ponta Delgada on the Azores, Lisbon or Gibraltar. Another way of defining a NAO index is based on a *Rotated Principal Component Analysis* (RPCA) as proposed by *Barnston and Livezey* (1987).

In this study, the station based NAO index after *Jones et al.* (1997) is used, which is computed from the difference between the normalized SLP over Gibraltar and the normalized SLP over southwest Iceland (Reykjavik). The normalization is done on a monthly basis with long term means and standard deviations derived from the period 1951-1980. For the winter seasons, an index based on stations from the Iberian peninsula yields a slightly higher signal-to-noise ratio (*Hurrell and van Loon*, 1997; *Jones et al.*, 1997) compared to an index based on the Azores-Iceland relationship.

The NAO index defines "high" (positive) and "low" (negative) states of the NAO depending on the meridional pressure gradient between the Azores high and the Icelandic low. The variations of this dipole pressure system causes impacts throughout the whole North Atlantic region. Fig. 6.5 schematically illustrates the effect for both NAO regimes. During positive NAO conditions (NAO+) the Icelandic low and Azores high are strengthened, creating an increased pressure gradient over the North Atlantic. As a consequence, the Westerlies are stronger and advect relatively mild and moist air to northern Europe while the eastern Canadian Arctic and the Mediterranean region experience dryer and colder conditions. Also the subtropical Easterlies are enhanced by the Azores high and cause mild to warm conditions in the southeastern United States (US).

Phases in which the NAO index is negative (NAO–) are characterized by a weak Icelandic low and Azores high, which results in a decreased pressure gradient and the Westerlies slacken. The storm activity over the North Atlantic is decreased and the storm track is shifted southward, advecting more moist air to the Mediterranean region. Greenland also experiences mild weather, while northern Europe and the eastern US face cold conditions.

Fig. 6.6 shows the NAO index for the period 1988 to 2007. During the first half of the 1990s the NAO index was mostly positive. Especially the cold seasons were characterized by strong positive values. The winter 1989/90 had the highest

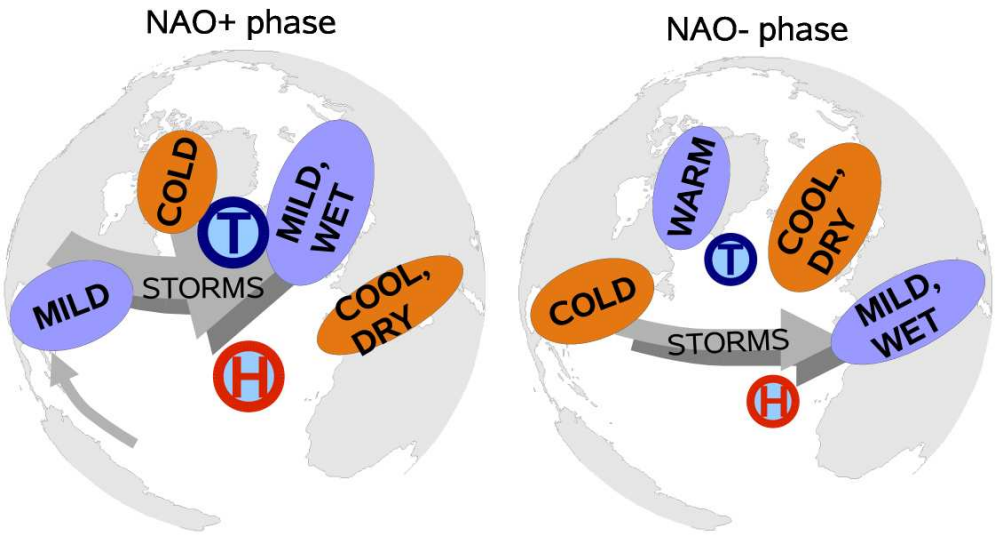

Figure 6.5: Schematic illustration of the effects related to positive and negative phases of the NAO.

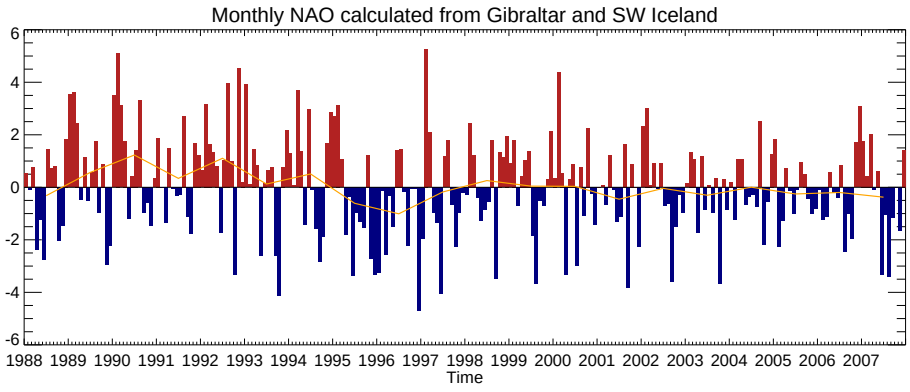

Figure 6.6: Monthly NAO index values based on normalized SLP anomalies from southwest Iceland and Gibraltar after *Jones et al.* (1997). The orange line represents the annual mean NAO index for the corresponding years.

mean NAO index recorded until now. From 1995 until 1997 NAO– conditions predominated. Since the late 1990 until present date, there is no clear tendency discernible in the NAO index.

6.2.1 The Arctic Oscillation (AO)

The strong signal of the NAO is not only affecting the North Atlantic ocean and its directly adjacent regions, but also exerts its influence to distant regions from North America to Siberia and the Middle East. The overarching reason is the close connection to a Northern Hemisphere mode, called *Arctic Oscillation* (AO), which is highly correlated to the NAO in spatial and temporal structure. Usually, the AO is defined as the first EOF of the MSLP of the Northern Hemisphere. The associated signal can be detected on timescales from days to multiple years. It extends from the troposphere into the stratosphere and is associated with the transfer of air masses in and out of the circumpolar vortex (*Thompson and Wallace*, 1998; *Greatbatch*, 2000). Especially in wintertime the AO and NAO variability are very similar and nearly indistinguishable. The underlying physical mechanisms and the connection of the NAO to the AO are still debated and it is not fully understood if they are manifestations of the same mode or independent fluctuations (*Thompson and Wallace*, 1998; *Wallace*, 2000; *Ambaum et al.*, 2001; *Wang et al.*, 2005)

6.3 Regional Statistics

As described in chapter 6.2, some regions are distinctly impacted by the effects of the NAO. In the following, the precipitation time series for the entire North Atlantic and for four selected regions as shown in Fig. 6.7 are assessed. The selected regions are representative for northern Europe (Box 1), the Mediterranean region (Box 2), the southeastern US including the Gulf Stream (Box 3), and the storm track region of the central North Atlantic (Box 4). Fig. 6.8 shows the time series of the monthly mean precipitation and the corresponding climatological annual cycle for the whole North Atlantic domain and for each of the subregions. The time series for spatial averages of the complete box, the land portion, and the oceanic part are depicted separately. Coastline pixels are treated as sea pixels. In Box 4 the small land part is neglected, and only the oceanic time series is shown. A three month running mean has been applied to the data, in order to filter high frequency fluctuations. Fig. 6.9 shows the corresponding anomalies for each region relative to the climatological annual cycle for the period 1988-2006. The correlation coefficients of precipitation and the NAO index for each Box are depicted in Tab. 6.1. The table shows the correlation of annual mean precipitation

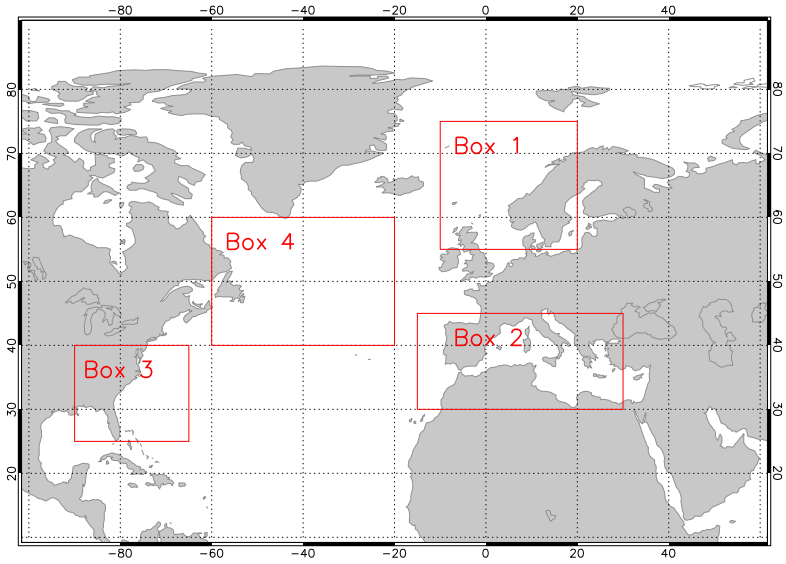

Figure 6.7: Box areas for which spatial mean time series have been computed.

with the annual mean NAO index and the correlation of monthly values for the December to March winter season.

Common to the entire North Atlantic and all subregions is a more pronounced annual cycle of the over-ocean precipitation compared to the over-land values. The peak in the seasonal cycle of oceanic precipitation is in the wintermonths December and January, while the minimum is in May to July. The largest amplitude of 3.5 mm/d is found in the storm track region of the central North Atlantic with values ranging from 2.3 mm/d in the summer months up to 5.8 mm/d in January. For the other regions, the amplitude of oceanic precipitation ranges from 1.5 mm/d to 2.5 mm/d. The eastern US (Box 3) exhibits a secondary maximum in September which is coincident with the peak of the hurricane season (see chapter 5). Also, the signal in Box 3 appears comparably noisy due to high variability over the Gulf Stream.

As the annual cycle of over-land precipitation differs in the individual regions, it is very weak for the entire North Atlantic with hardly discernible maxima in June/July and November/December (Fig. 6.8 a). For two regions, northern Europe and the eastern US (Fig. 6.8 b,d), the peak of over-land precipitation is found in July and June and is out of phase with the oceanic precipitation. In Box 1, the lowest values are found from January to May with the minimum in March. For Box 3 the minimum occurs in October and a secondary minimum is found in December. In the Mediterranean region oceanic and land precipitation are in phase (Fig. 6.8 c) with the maximum occurring in December and the minimum in July. The amplitudes of the annual cycle over land are smaller compared to the oceanic part in all subregions. The highest amplitude is found for Box 3 with

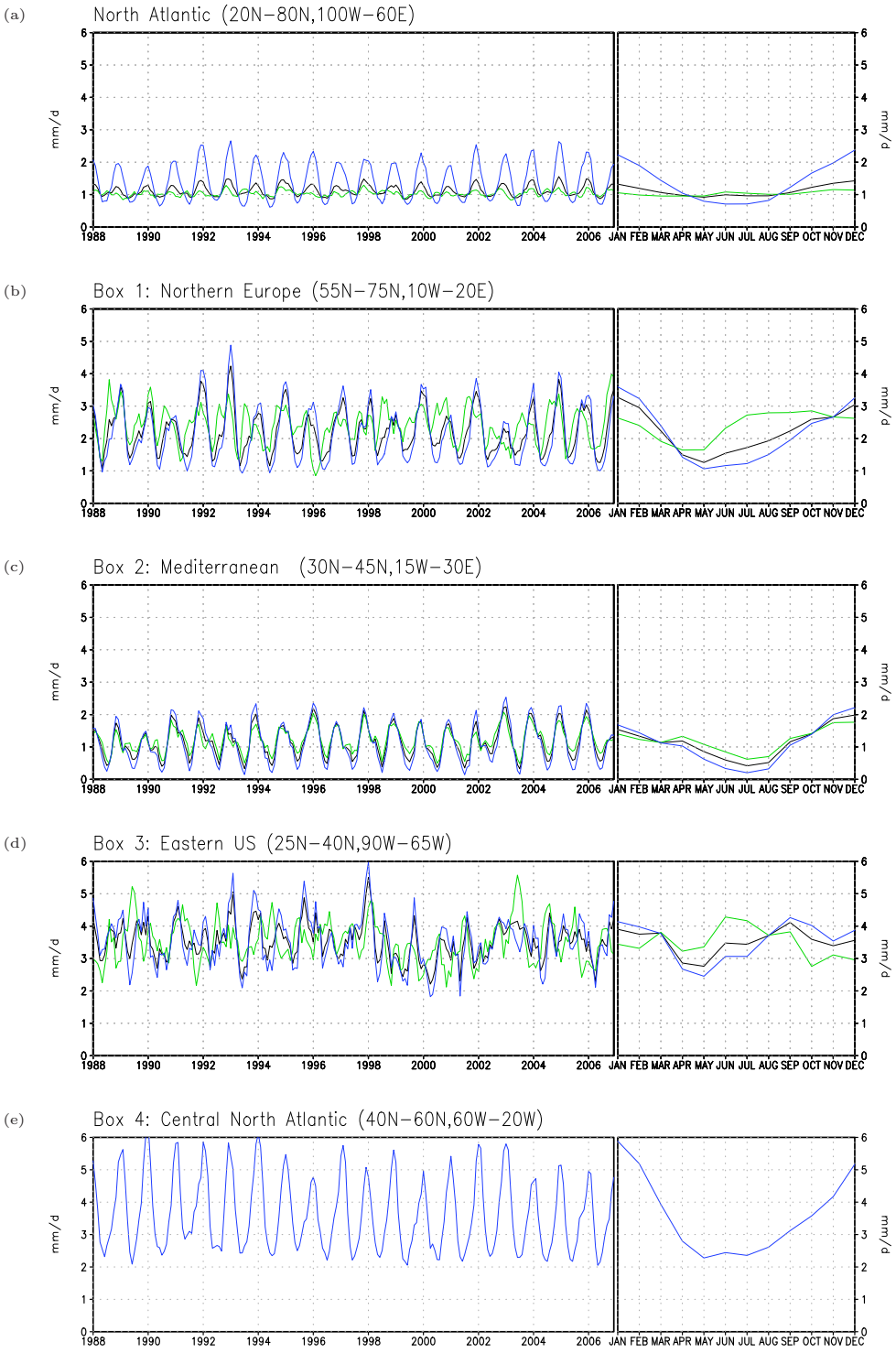

Figure 6.8: Precipitation time series of monthly spatial means and the corresponding mean annual cycle for boxes depicted in Fig. 6.7. A 3-month running mean filter has been applied to the data in order to filter high frequency fluctuations. Blue lines represent the mean for the oceanic part, green lines the mean for land part, and black lines the mean for the whole box. The small land part of Newfoundland contained in Box 4 is neglected, hence only the ocean part is plotted.

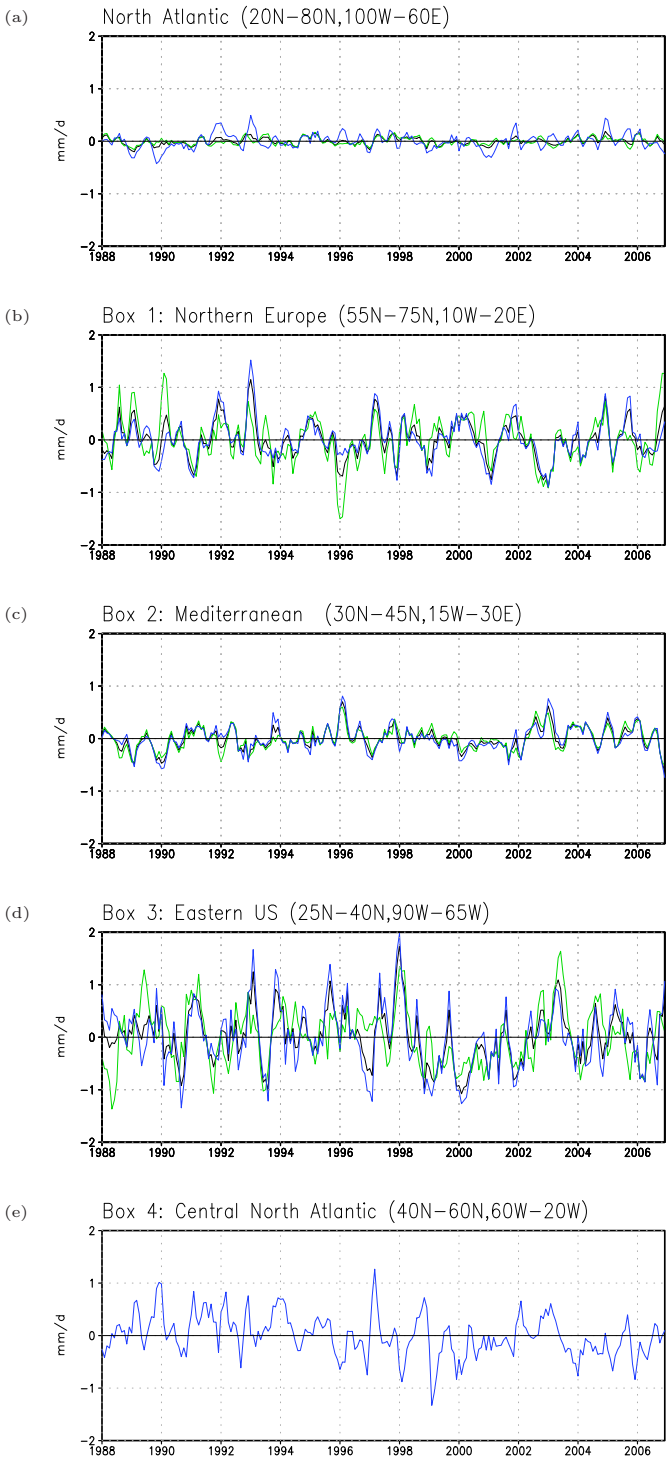

Figure 6.9: Same as Fig. 6.8, but the time series is deseasonalized by subtracting the climate mean annual cycle for the years 1988-2006.

Table 6.1: Correlation coefficients of mean annual and mean winter (December-March) precipitation and the corresponding NAO index for the entire North Atlantic region and the subregions depicted in Fig. 6.8. The last three rows depict the correlations between the precipitation in Box 1 and Box 2.

Region	r annual	r DJFM
North Atlantic	-0,18	-0,17
Land	-0.03	-0.04
Sea	-0.31	-0.25
Box 1	0.46	0.62
Land	0.51	0.84
Sea	0.29	0.38
Box 2	-0.48	-0.73
Land	-0.46	-0.74
Sea	-0.44	-0.68
Box 3	-0.06	-0.07
Land	0.13	0.12
Sea	-0.16	0.04
Box 4 Sea	0.47	0.47
Box 1/Box 2	-0,53	-0.68
Land	-0.60	-0.84
Sea	-0.23	-0.36

approximately 1.5 mm/d. For Box 1 and Box 2 the amplitudes are below 1 mm/d.

The time series for the whole North Atlantic region (Fig. 6.8 a) shows little variation with time for the mean precipitation and the land part. For the oceanic part, particularly the wintertime maxima exhibit a high interannual variability. This is also evident from the anomaly time series in Fig. 6.9 a, where much higher values up to 0.5 mm/d are found for the ocean compared to 0.2 mm/d for the land. During the period of persisting high values of the NAO index in the early 1990's, a positive anomaly is found for the oceanic precipitation in the winter seasons 1991/92 and 1992/93. In the years 1988 to 1990, when periods of strong NAO+, but also NAO– occurred, the precipitation is mostly below average. During the years with a prevailing negative NAO index, 1995 to 1997, the precipitation does not shows a uniform response. The correlations from Tab. 6.1 suggest a weak anticorrelation of oceanic precipitation and the NAO index for the North Atlantic region while the precipitation over land is not correlated with the NAO index. This suggests, rather a regional redistribution of precipitation depending on the state of the NAO than a variation of the total mean North Atlantic precipitation.

A more pronounced dependence of precipitation on the NAO is found for Box 1 and Box 2. The northern European precipitation in Box 1 shows large variability for the oceanic and land precipitation. Distinct peaks in oceanic precipitation coincide with the winters 1991/92 and 1992/93 during the long NAO+ phase with anomalies of 1 mm/d and 1.5 mm/d, respectively. The over-land precipitation exhibits a strong positive anomaly coinciding with NAO+ conditions for January to March 1990 and by the end of 2006 and a minimum in the low NAO index winter season of 1995/96. Both, land and ocean precipitation are positively correlated with the NAO index. During the winter months, the precipitation over land is highly correlated to the NAO index with r=0.84 (Tab. 6.1) while the correlation for precipitation over the ocean is weaker with r=0.38.

In the Mediterranean region (Box 2) an opposite response of precipitation to the NAO occurs, albeit the anomalies are weaker and mostly of the same magnitude for land and ocean as shown in Fig. 6.9 c. Distinct positive anomalies appear for the strong negative phase of 1995/96 and from 2002 to 2006 when the NAO index was generally slightly negative. The precipitation in Box 2 is negatively correlated with the NAO index, as it is suggested from Fig. 6.5. Moreover, an inverse response of precipitation in northern Europe and the Mediterranean region is expected from Fig. 6.5. From Tab. 6.1 this relation is evident as the correlation of precipitation in Box 1 and Box 2 is negative with r=-0.68 for the winter season and r=-0.53 for the annual mean. Over land the anticorrelation is even higher with r=-0.84, while it is lower over the ocean with r=-0.36 during the winter season.

In contrast to the European sector, the precipitation in Box 3, which was selected to be representative for the eastern US is not correlated with the NAO index. The time series is very noisy and the signal in precipitation is not dominated by the NAO in this region. Singular events such as the 1992/93 El Niño which was followed by a severe drought in the southeastern US (*Lott*, 1994) are clearly visible in the anomaly time series in Fig. 6.9 d. Also the strong El Niño event of 1997/98 causes a positive precipitation anomaly.

As in the other subregions, the inter-annual variability of wintertime precipitation is higher than for the summer season in the storm track regions of the central North Atlantic (Box 4, Fig. 6.8 e). Annual mean and monthly wintertime precipitation are equally correlated with the NAO index for this Box with r=0.47. The anomaly time series in Fig. 6.9 e reflects the long-term fluctuations of the NAO index with more positive values from the beginning of the record until the middle of the 1990's followed by mostly negative values until 1998. The peak positive anomaly in February 1997 concurs with the highest value of the NAO index for the investigated time series.

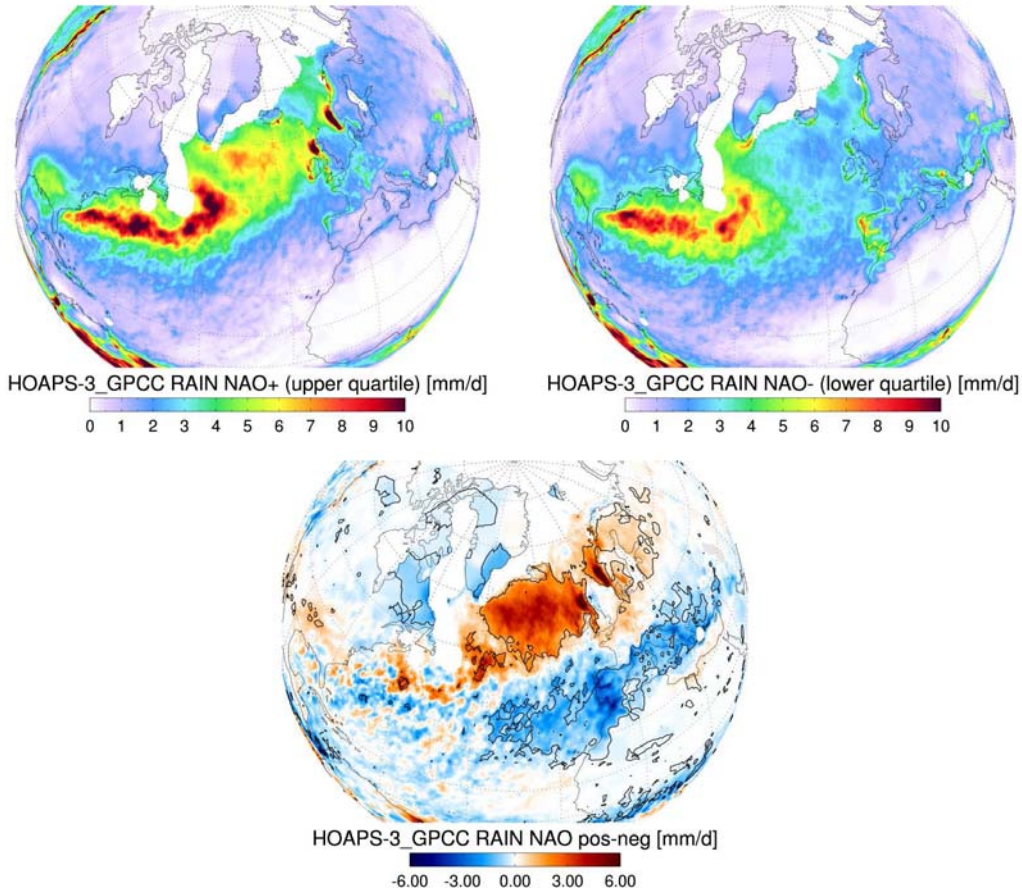

Figure 6.10: Composite fields of precipitation from the corresponding timesteps for the upper quartile of NAO index values (top left), the lower quartile of NAO index values (top right) and the difference of both composites. The black line in the difference plot indicates where both samples differ on the 99 % significantly level of a Mann-Whitney U test.

6.4 Composites

From the nineteen winter periods (December to March) of the years 1988-2007, composites for NAO+ and NAO– conditions have been constructed by selecting the months corresponding to the upper/lower quartile of the NAO index values. Thus these composite fields represent the mean precipitation for pronounced high/low NAO states and should reveal systematic regional differences between the NAO+ and NAO– states. Fig. 6.10 shows the resulting fields for the NAO+ (top left), the NAO– (top right) phase, and the difference map of the NAO+ and NAO– composite (bottom). Whether the samples corresponding to the NAO+ and NAO– composites do not stem from the same distribution, i.e. differ significantly, has been tested with a non-parametric Mann-Whitney U test (*Mann and Whitney*, 1947).

For the NAO+ composite shown in Fig. 6.10, top left panel, the pronounced storm track during this conditions is clearly evident by a band of strong precipitation extending from the Gulf Stream along the North American east coast and over the central North Atlantic between Newfoundland and the British Isles. Maximum precipitation occurs in the cyclogenesis regions over the Gulf Stream offshore the North American east coast and in the Labrador outflow region with values of more than 10 mm/d.

Two other distinct maxima at the western coasts of Scotland and Norway result from the interaction of the enhanced storm track with orography. At the mountain ranges of the Scottish Highlands and the Norwegian coast, orographic rainfall is induced through the uplifting of air masses. In the leeward regions of the mountains significantly lower rain rates are found in the Baltic and North Sea. Precipitation rates in the southeastern US are up to 6 mm/d, whereas most of southern Europe, northern Africa, and the Mediterranean Sea suffer from very low precipitation of about 1 mm/d during NAO+ phases.

For NAO– phases (Fig. 6.10 top right panel), precipitation in the Mediterranean region exhibits distinctly higher values. In the western part of the Iberian peninsula and along the northern coasts of the Mediterranean values up to 6 mm/d are found. Local maxima exist at the east coast of the Adriatic Sea and at the Atlantic coast of the Iberian peninsula. The northern European west coasts still exhibit relatively high rain rates up to 6 mm/d, while the precipitation maximum that is located over the high latitude North Atlantic in the region between the southeastern coast of Greenland and the British Isles during the NAO+ phase has vanished in the NAO– composite and rain rates of 2 to 3 mm/d are evident in this region. In the southeastern US, the precipitation still exhibits values up to 6 mm/d, but the local maximum is smaller for NAO–. The band of strong precipitation over the Gulf Stream is slightly extended to the south compared to NAO+ conditions, but weaker in its center. However, in the oceanic region between the Azores and western Europe a southward shift of the precipitation patterns is evident and the precipitation rates increase up to 4 mm/d.

The difference map of the composites for NAO+ and NAO– shown in the bottom panel of Fig. 6.10 illustrates the systematic deviations in the precipitation pattern for the two NAO states. Positive values (red) correspond to more precipitation during NAO+, negative values (blue) indicate higher precipitation during NAO– phases. The region, where the samples corresponding to the NAO+ and NAO– composites differ significantly on the 99 % level from each other is denoted by a black line in the difference map (Fig. 6.10, bottom). The characteristic quadrupole pattern as illustrated in Fig. 6.5 is resembled over land and in coastal regions by positive precipitation values in the southeastern US and northern Europe and negative precipitation values in northeastern Canada and

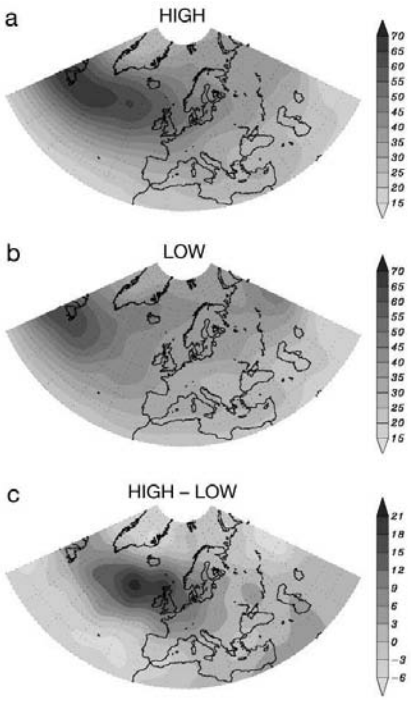

Figure 6.11: Composites of synoptic activity (gpm) for the winter months (DJFM) of the 1958 to 1997 period: (a) NAO index >1.0, (b) NAO index <-1.0, and (c) their difference. (from *Trigo et al.*, 2002)

the Mediterranean region, respectively. Except for the southeastern US, the difference NAO+ and NAO– patterns is mostly significant in these regions. Over the ocean, distinct anomalies are found over the Gulf Stream and in the storm track regions of the North Atlantic. In the western North Atlantic Gulf Stream region the patterns are mostly not significant. However, the meridional shift of the storm track depending on the NAO phase is evident by the significant dipole precipitation pattern over the central and eastern North Atlantic. Associated with this shift is a change in the moist air masses, which are conveyed by the Westerlies to the coastal regions of Europe that are directly exposed to the storm track, where they lead to enhanced precipitation depending on the state of the NAO. Hence, the strongest positive signals are found at the Scottish and Norwegian coast for NAO+ and the strongest negative signal is located at the Iberian peninsula for NAO–. over the ocean, the positive signal over the North Atlantic is more pronounced as the negative anomaly, indicating a stronger response of the storm track during NAO+ phases.

The HOAPS-3 ocean and GPCC land patterns are regionally consistent and agree qualitatively with previous findings. Both show the close connection of the meridional shift in precipitation and of the North Atlantic storm track with the NAO phase (*Carleton*, 1988; *Hurrell and van Loon*, 1997; *Rogers*, 1997; *Dickson et al.*, 2000; *Mariotti and Arkin*, 2007). Studies detecting regional synoptic activ-

ity by cyclone tracking algorithms (e.g. *Serreze et al.*, 1997; *Sickmöller et al.*, 2000) indicate a decrease in the absolute number of cyclone activity for the NAO– phase and a southward shift of the storm track. During NAO+ phases, an increase in the number of storm systems along the storm track together with a slightly higher intensity as compared to the climatological mean is identified as the dominant signal. Fig. 6.11 from *Trigo et al.* (2002, their Fig. 2) shows composites of synoptic activity derived from the root mean square of 2 to 8 day periodicity band-pass-filtered 500 hPa geopotential height data, which provides a proxy for the synoptic variability. The synoptic activity is connected to the cyclone tracks and hence is reflected in the HOAPS-3/GPCC precipitation patterns. For NAO+ conditions a strong storm track extends from Newfoundland eastwards to Iceland and the British Isles. A local maximum southeast of Greenland is evident in the synoptic activity analog to the NAO+ precipitation composite (Fig. 6.10, top left). For the NAO– phase (Fig. 6.11 b) the storm track appears much weaker and shifted southward as it was also evident in the precipitation composite. Fig. 6.11 c shows the difference in synoptic activity during NAO+ and NAO– conditions. As indicated by the precipitation patterns, the response of cyclonic activity to NAO+ is stronger than to NAO–. The pattern exhibits reasonable agreement with the patterns of the difference map shown in the lower panel of Fig. 6.10.

6.5 Empirical Orthogonal Functions (EOF)

Empirical orthogonal functions determine a set of functions, which characterize the covariability of a specified number of values at different measurement points (i.e. time series of spatial patterns in a gridded data set). EOFs can be regarded as eigenvectors, which are aligned such that the first EOF describes a spatially coherent pattern which explains most of the temporal variance in the data set. The succeeding EOFs are mutually orthogonal in space and time and consecutively explain less variance. The EOF patterns are time-independent, their temporal evolution is described by the associated *principal component* (PC) time series. However, it has to be kept in mind that EOFs are just a statistical representation of the data, which is not necessarily connected to physical processes that create the variability.

An EOF analysis has been applied to the HOAPS-3/GPCC precipitation data as proposed by *Wilks* (2006), using the singular value decomposition method to calculate eigenfunctions of the covariance matrix (*Bjornsson and Venegas*, 1997). As before, only the winter seasons from December 1988 to March 2007 are used. The seasonal cycle was removed from the data as well as local linear trends, as much of the variability would be assigned to these signals in the EOFs. Furthermore, a latitudinal weighting was applied in order to preserve the influence of

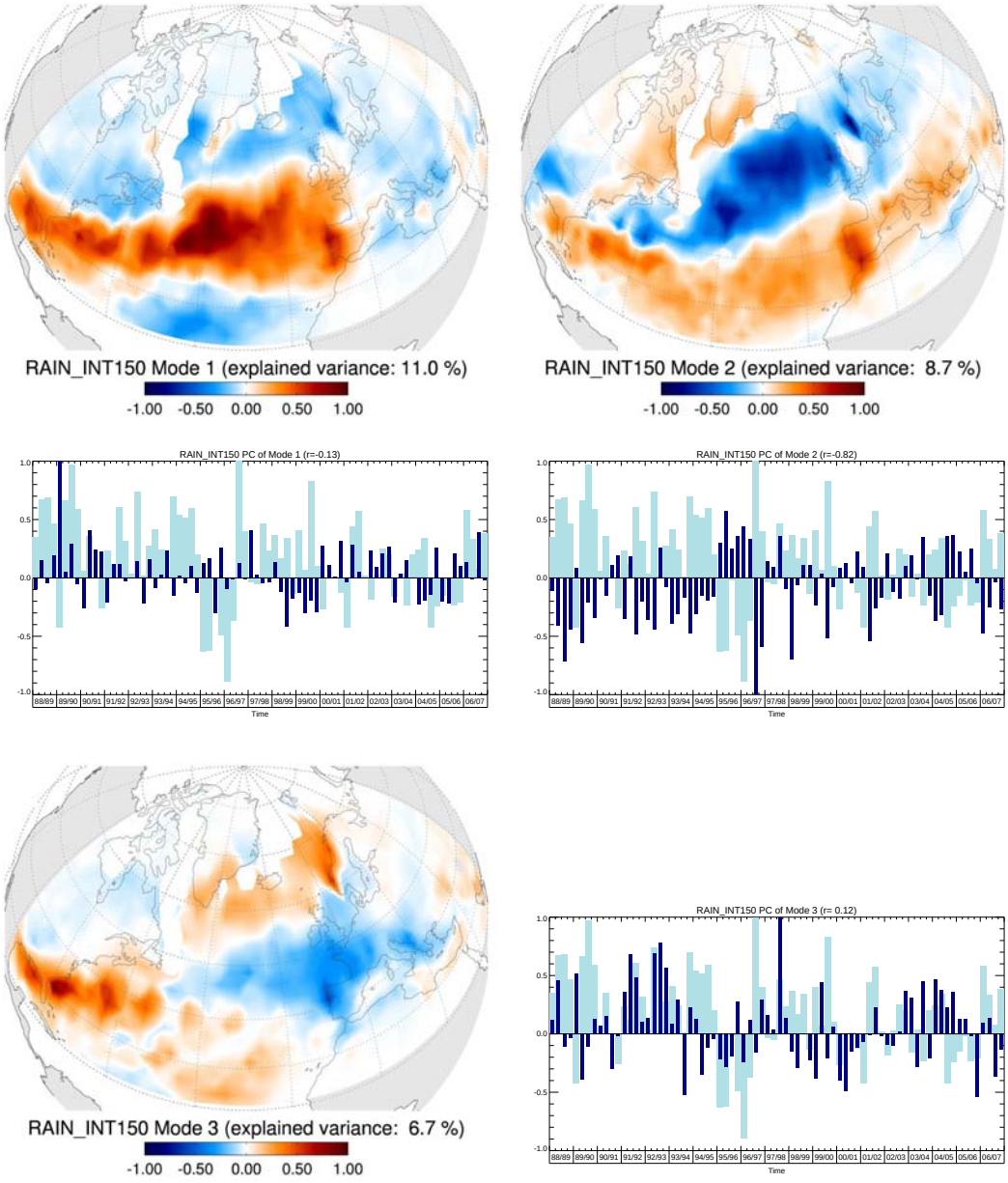

Figure 6.12: First three EOF modes of the combined HOAPS-3 and GPCC Full Data Reanalysis Product V4 product with a resolution of 2.5°computed from the winter seasons 1988/89-2004/5. Map projections show the EOF patterns, the bar plots show the PCs (dark blue) and the corresponding values of the monthly NAO index (light blue). All data are normalized to unity.

the grid point size. The EOFs were calculated for the area 20° N – 90° N and 100° W – 60° E. Studies based on a different region may not give the same results as the EOFs are sensitive to the selected domain. Furthermore, a version of the HOAPS-3/GPCC data set with a reduced resolution of 2.5° is used, which favors large scale patterns over small scale variability.

Fig. 6.12 shows the first three modes of the resulting EOF patterns together with the time series of the related principal components. The explained variability of the EOF patterns is 11 % for the first mode, 8.7 % for the second, and 6.7 % for the third mode. Due to these rather small values, none of the individual patterns can alone explain the major fluctuations in winter precipitation over the whole North Atlantic region. The reason for this is the more indirect relation of precipitation and pressure patterns and the high temporal and spatial variability of precipitation, due to its intermittent character. Wind, in contrast, can be directly linked to the pressure field with the assumption of geostrophy. Hence, the first mode of HOAPS-3 oceanic wind speeds explains already 22 % of the variance (see Appendix B). The explained variability of the leading EOF of sea level pressure itself is much larger, and accounts for more than one third of the variability (see Fig. 6.4).

But nevertheless, the EOFs reveal valuable information about the North Atlantic precipitation variability. The pattern of the first mode shows a maximum variability in the region extending from the southeastern US along the storm track region in the western North Atlantic and then continuing to the European westcoast. It reveals some similarities with the composite patterns shown in section 6.4 in the western Atlantic, but in the eastern Atlantic the pattern resembles more a tripole pattern instead of the dipole pattern found in the composite analysis. Also, the response for continental Europe does not match the characteristic NAO pattern which consists of opposed patterns for northern and southern Europe. Hence, a direct connection of the first mode with the NAO cannot be deduced. Looking at the corresponding PCs (Fig. 6.12 center left panel) confirms this assumption, as they are only weakly correlated (r=0.13) with the NAO index.

If the first EOF mode is compared with the East Atlantic Pattern defined by *Barnston and Livezey* (1987), a better accordance is found. The East Atlantic Pattern emerges as a prominent mode from a RPCA of North Atlantic pressure fields. It is shifted slightly southward compared to the NAO pattern and is strongly linked to the subtropics. A corresponding index for the East Atlantic Pattern is defined by the NOAA National Weather Service, *Climate Prediction Center* (CPC) (c.f. `http://www.cpc.noaa.gov/data/teledoc/ea.shtml`). The correlation of this index with the PC time series is r=0.57, which is much higher compared to correlation with the NAO index.

Moreover, the PCs for mode 1 (Fig. 6.12, center left) are dominated by a single

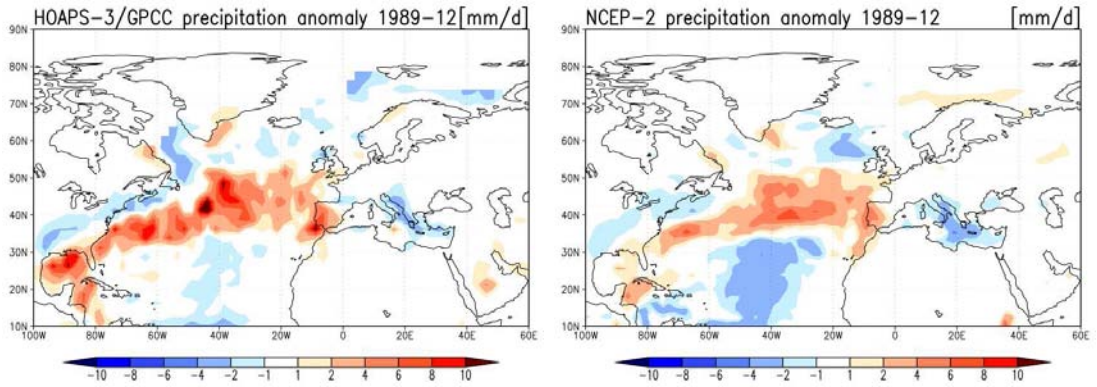

Figure 6.13: Precipitation anomaly for December 1989 relative to the 1988-2006 period from HOAPS-3/GPCC and NCEP-R2.

event in December 1989 which gives by far the highest value in the PC time series. This may be explained by a "flip-flop" of the NAO during the 1989/90 winter season. In November and December 1989 strong NAO– conditions prevailed and by the end of the year 1989, a sudden switch to strong and persisting NAO+ occurred, leading to the highest mean winter season NAO index and one of the mildest winters in Europe in the record. During December 1989 western Europe experienced a series of storm events. E.g. a strong gale hit southern England, France, Spain, and Portugal on 16-17 December, while on the other side of the Atlantic in the eastern US severe cold weather with heavy snowfall occurred. The precipitation anomalies for December 1989 of HOAPS-3/GPCC and NCEP-R2 are shown in Fig. 6.13. Both data sets reveal a strong positive anomaly matching the EOF mode 1 pattern. The positive anomaly in the HOAPS-3/GPCC data is higher than in NCEP-R2. However, the patterns of the continental (GPCC) and ocean (HOAPS-3) precipitation anomalies agree, in particular for the Iberian peninsula.

The pattern of the second mode (Fig. 6.12, top right panel) can be almost identically identified with the composite difference map in Fig. 6.10. Thus it could be associated with the NAO as it reflects the precipitation variability associated with difference of the high and low NAO states. Moreover, a high correlation of r=0.81 is found between the PC time series and the NAO index. The highest variability is located at the Gulf Stream and the storm track region, the Norwegian and Scottish west coast, at the Iberian peninsula, Morocco, and at the Mediterranean coasts. The peak in the PCs occurs in February 1997, coinciding with the highest value for the NAO index during the investigated time range.

The EOF pattern of the third mode shows a maximum in the Gulf of Mexico and along the Gulf Stream. Over Europe a dipole can be recognized with maxima at the Norwegian coast and the northwestern tip of the Iberian peninsula. The associated PCs exhibit a weak correlation of r=0.12 with the NAO index. For

the winters 1990/91 to 93/94 some similarities of the PC time series with the NAO index exist, albeit the highest value in the PCs is found in February 1998. The latter can be related to the extremely strong *El Niño / Southern Oscillation* (ENSO) event of 1997/98, which significantly influenced the precipitation in the subtropical regions of the North Atlantic (*Ropelewski and Halpert*, 1987).

The comparison with the EOFs from additional satellite-based and reanalysis data sets (GPCP-V2, CMAP, NCEP-R2, and ERA interim; see Appendix B) which cover the same time period as HOAPS-3/GPCC, reveals comparable values for the explained variance. Due to the low explained variance of the EOF patterns, a comparison of the patterns has limited validity as no explicitly dominating mode exists. However, the patterns show some similarities, while the satellite based products and reanalysis data sets each agree better. Note for the comparison of the EOFs, that the EOF patterns and PCs may have reversed signs since just the sign of the product of both is determined. For all data sets, the PC time series of the first two modes exhibit correlations with the NAO index of r=0.43 to r=0.76, and the values for third mode are very small, except for NCEP-R2 for which the PC of all modes are correlated with the NAO index. The December 1989 maximum in the PCs of mode 1 is contained in all of the data sets, but not as dominating as for HOAPS-3/GPCC. A peak in the PCs of the third EOF mode for the winter 1997/98 that may correspond to the El Niño is found for all data sets, except NCEP-R2.

6.6 Correlation Patterns

In the following the local temporal correlation of HOAPS-3 parameters with the NAO index will be investigated. At first, correlation patterns of HOAPS-3/GPCC precipitation in the North Atlantic sector are considered, followed by global fields and possible teleconnections of the NAO along with a comparison to several other data products. Finally, the implications of the NAO on the ocean surface freshwater flux and the related parameters, as they are derived in HOAPS-3, will be evaluated.

All correlations were calculated using the non-parametric Spearman's rank correlation method. The significance of the resulting correlation patterns is determined with a two sided t-test (*Wilks*, 2006). As for the EOFs, the precipitation data was locally deseasonalized and detrended prior to the calculation of the correlations.

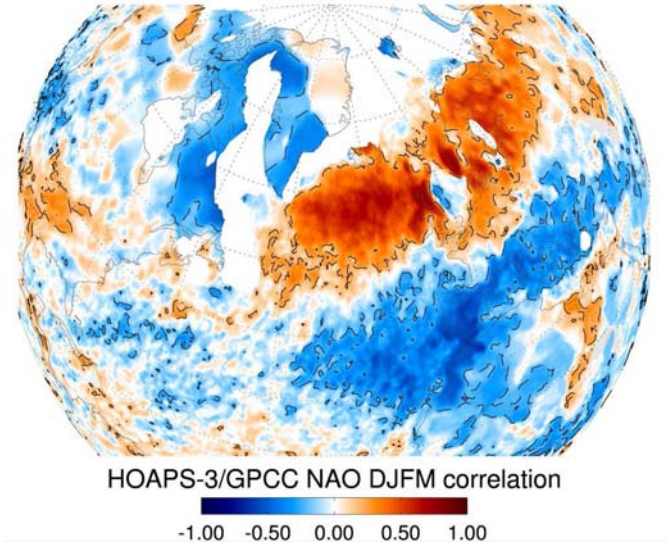

Figure 6.14: Local correlations of HOAPS-3/GPCC precipitation with the NAO index. The dashed line indicates the 95 % significance level of the t-test.

6.6.1 North Atlantic Precipitation

Fig. 6.14 shows the correlation of each grid point of the HOAPS-3/GPCC data set with the NAO index for the North Atlantic region. The pattern reasonably shows the impact of NAO+ and NAO– phases on the precipitation, and agrees well with the difference map of the NAO+/– composites (Fig. 6.10) and the second mode of the EOF analysis (Fig. 6.12). In accordance with the expected quadrupole pattern from Fig. 6.5, several consecutive regions of significant correlations can be identified which are mainly located in the Labrador region, the eastern Atlantic, and Europe. In the western Atlantic and over the eastern continental US the correlations are mostly weak and not significant.

A large pattern of significant positive correlation extends from the northeast Atlantic over northern Europe to Siberia. The highest correlations occur at the northwestern European coasts and at the storm track between Newfoundland and the British Isles. The high resolution of the data set additionally reveals some small scale features such as the negative correlation of precipitation and the NAO index over the North Sea and Baltic, which are caused by mountain lee effects (*Uvo*, 2003). For the southeastern US mainly positive correlations are found, which are mostly not significant, except for the southern part.

Significant negative correlations with the NAO index, i.e. precipitation increase during NAO– phases, are located in the region extending from the Azores in the Atlantic over the Mediterranean into the Middle East, and the land area adjacent to the Baffin Bay and Labrador Sea. Correlations over the ocean could not be calculated for the latter region and most of the Arctic Ocean due to the

lack of a retrieval over sea-ice covered regions. Precipitation in northwest Africa, the Iberian peninsula, and the northern Mediterranean region exhibits the highest correlation with NAO– conditions, as they are directly impacted by the southward shift of the storm track and the associated moisture transport into these regions. Over the Gulf Stream region, smaller patches of significant negative correlations with the NAO index can be associated with the southward broadening of the precipitation pattern during NAO– conditions as it is found in the composite analysis (chapter 6.4). As in the composite and EOF analysis, the pattern consistency between the HOAPS-3 and the GPCC data set is convincing.

6.6.2 Global Precipitation

In this section the influence of the NAO on global precipitation beyond the North Atlantic region is investigated. Moreover the correlation patterns of several data sets are evaluated and compared with HOAPS-3/GPCC.

The compared data sets are the satellite based GPCP V2 (*Adler et al.*, 2003) and CMAP enhanced (version 809) (*Xie and Arkin*, 1997) products and the NCEP-R2 (*Kanamitsu et al.*, 2002) and ERA interim (*Simmons et al.*, 2007) reanalysis data sets. The CMAP enhanced product is not purely satellite based, as it is complemented with reanalysis data in data void regions. Also GPCP and CMAP are not completely independent from GPCC over the continents as they use rain gauge data to constrain their retrievals over land. While the HOAPS-3/GPCC product has a grid of 0.5°, the resolution for the other data sets is 1.5° (ERA interim) and 2.5° (GPCP, CMAP, NCEP-R2), respectively. Hence, some finer structures present in HOAPS-3/GPCC may not be resolved by the latter data sets.

Fig. 6.15 shows the global correlation of monthly mean precipitation and the NAO index for HOAPS-3/GPCC and the compared data sets. Additionally, the correlation of HOAPS-3/GPCC with an alternative NAO index from CPC, the AO index, and the ENSO related *Southern Oscillation* (SO) index are depicted in Figs. 6.15 b,g and h. Correlations, that are not significant above the 95 % level have been masked out. Thus only robust correlation patterns are shown.

The CPC NAO index is calculated from the leading mode of monthly mean standardized 500 hPa height anomalies using a RPCA technique (c.f. `http://www.cpc.noaa.gov/products/monitoring_and_data/oadata.shtml`), the AO index is constructed by projecting monthly mean 1000 hPa height anomalies onto the leading EOF mode (c.f. `http://www.cpc.ncep.noaa.gov/products/precip/CWlink/daily_ao_index/ao.shtml`), and the SO index is based on the Standardized Tahiti – Darwin pressure difference (c.f. *Trenberth* (1984), `http://www.cgd.ucar.edu/cas/catalog/climind/soi.html`).

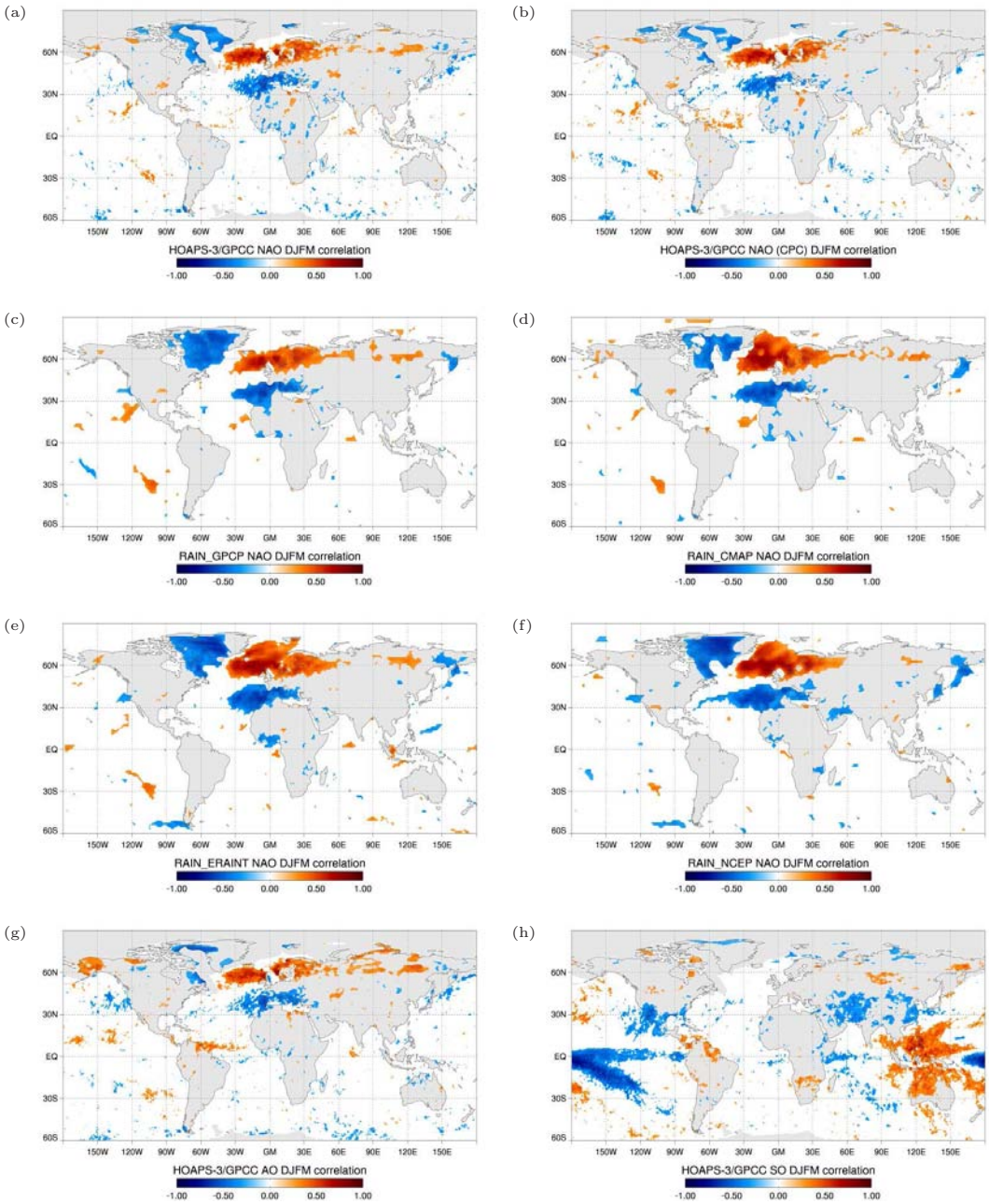

Figure 6.15: Correlation patterns of monthly mean precipitation from HOAPS-3 (a,b,g,h), GPCP V2 (c), CMAP (d), ERA interim (e), and NCEP-R2 (f) with the station based NAO index (a,c-f), CPC NAO index (b), AO index (g), and SO index (h). Only data with correlations above the 95 % significance level are shown. The time period is 1988-2005 (1989-2005 for ERA interim). Grey shaded ocean regions indicate domains excluded in HOAPS-3 due to the presence of sea ice (a,b,g,h).

Correlation features of the HOAPS-3/GPCC product over the North Atlantic have been described in the previous section. The characteristic pattern of significant correlations is basically resolved in all data sets and is also evident for the CPC NAO index. However, some differences remain for the North Atlantic and for global teleconnections.

In the subpolar regions, differences occur in the Nordic Seas and the Labrador Sea, where HOAPS-3/GPCC data is not available due to the presence of sea ice. The reanalysis products and CMAP exhibit a high positive correlation with the NAO index over the Nordic Seas north of 60° N, which is not present in the GPCP data. Also, the extent of the significant pattern over the Labrador Sea and western Greenland varies between the data sets. The patterns over northeastern Canada agree quite well, including HOAPS-3/GPCC, while the patterns for Greenland differ. The reason for the inconsistencies at high latitudes are due to deficiencies of satellite retrievals, that often lack skill to detect frozen precipitation properly and the generally poor data coverage of other input data for the reanalyses (*Adler et al.*, 2001). Common to all data sets is the extension of positive correlation from northern Europe over almost entire Eurasia and a patch of negative correlation over northern Japan and Kamchatka.

At North Atlantic midlatitudes, the negative correlation pattern extend from the central North Atlantic eastward over the Mediterranean region as represented in all data sets. In the NCEP-R2 data, a narrow band of significant negative correlation extends this pattern to the Gulf Stream region in the western Atlantic. In the HOAPS-3/GPCC precipitation a weak similar pattern is evident over the western Atlantic that is related to the southward broadening of the precipitation over the Gulf Stream patterns during NAO– phases.

At the northeastern African Mediterranean coast, precipitation is positively correlated with the NAO index in all data sets. This pattern extends to central northern Africa in HOAPS-3/GPCC. As this is not the case for the compared data sets, this might be an artifact due to inconsistent data sampling of the GPCC product (see chapter 6.1).

Some differences between the data sets occur in the Middle East and the Arabian peninsula. Except for ERA interim, all data sets exhibit at least a small patch of negative correlation at the Turkish/Syrian border adjacent to the eastern tip of the Mediterranean Sea. NCEP-R2 is also significantly correlated with the NAO index in the Persian Gulf region. This feature is much weaker in the other data sets.

For the equatorial Indian Ocean, a small patch of positive correlation of precipitation and the NAO index is found southwest of the tip of the Indian subcontinent for all data sets, but NCEP-R2. Positive NAO phases are known to be correlated with warm SST anomalies in the Indian Ocean (*Hoerling et al.*, 2001;

Bader and Latif, 2005). These SST anomalies are associated with enhanced tropical convection and hence more precipitation. Such a relationship of significantly increased monthly convection in the Indian Ocean and positive NAO phases has also been shown by *Miller et al.* (2003) using *outgoing longwave radiation* (OLR) from NCEP reanalysis and satellite observations of the NASA *Earth Radiation Budget Experiment* (ERBE).

Another tropical feature is evident in all data sets over western central Africa, where the precipitation is negatively correlated with the NAO index. Several studies suggest a feedback of tropical SST variations and the NAO (e.g. *Marshall et al.*, 2001; *Hurrell et al.*, 2003, and references therein). The tropical circulation is influenced by the modulation of the trade winds through the NAO. On the other hand, the position and strength of the *Inter-Tropical Convergence Zone* (ITCZ), but also the extratropical circulation show a response to the cross equatorial meridional SST gradient. Hence the precipitation and surface fluxes in the tropical Atlantic and adjacent continental regions are modulated by this tropical NAO feedback. A coherent response of oceanic wind speed and evaporation along the tropical west African coast is evident from HOAPS-3 data (not shown).

Moreover, the statistical response of tropical Atlantic precipitation to the NAO is sensitive to the NAO index chosen as a reference. When the principal component based CPC NAO index is used (Fig. 6.15 b), a positive correlation pattern in the western tropical Atlantic emerges. This pattern is present for the correlation with the AO index (Fig. 6.15 g) as well.

More NAO related teleconnections are indicated by correlation patterns in the Pacific. Over the eastern Pacific and North America a dipole structure extending from the subtropics to the midlatitudes is evident in HOAPS-3/GPCC and to some extent in the other data sets as well. This pattern may be associated with a teleconnection of the NAO to the *Pacific North American* (PNA) pattern. Furthermore, positive correlations of precipitation and the NAO index are found in Alaska at the position of the Aleutian low. An even stronger link of North Atlantic to Pacific patterns is found for the correlation with the AO index, which is strongly correlated with the NAO in wintertime. As shown in Fig. 6.15 g, the patterns in the Pacific region and over Siberia are stronger while the Atlantic correlations are similar to those for the NAO index. A direct link of atmospheric variability in the North Atlantic and Pacific is still debated. *Ambaum et al.* (2001) suggests a weak anticorrelated relationship between the average zonal flow in the Atlantic and Pacific which would explain the inverted structure compared to the NAO pattern in the North Atlantic, while *Wallace and Thompson* (2002) argue that the PNA could also be represented by a second mode of 500 hPa height EOFs which is out of phase with the AO.

In the southeastern Pacific, all data sets exhibit a patch of positive correla-

tion, which may be related to ENSO. ENSO is the most prominent atmospheric oscillation pattern on the globe, accounts by far for most of the variability in the Pacific, and has significant impact on distant regions. Fig. 6.15 h shows the correlation of HOAPS-3/GPCC precipitation with the SO index. Negative values of the SO index are associated with El Niño events and positive values indicate a La Niña phase. Thus negative (positive) correlations can be regarded as a positive (negative) precipitation anomaly for an El Niño event and vice versa for La Niña. Except for the characteristic precipitation anomalies in the tropical Pacific, distinct effects on the precipitation are evident throughout Asia and Africa. In the Atlantic sector, especially for the southern US and central America significant correlations are found. Large scale atmospheric circulations such as the PNA, and the NAO are influenced by the ENSO as shown by *Huang et al.* (1998) who found significant modes of coherent variability between ENSO and the NAO for about 70 % of warm ENSO events. A signature of the strong 1997/98 event was also evident in the EOFs of HOAPS-3/GPCC (section 6.5).

6.6.3 North Atlantic Freshwater Budget

While the main focus of this chapter lies on the analysis of precipitation, another important factor is the heat and moisture exchange of the atmosphere with the underlying ocean. As the ocean freshwater flux, i.e. the difference of evaporation and precipitation (E-P), is available from HOAPS-3, the relation of these fields to the NAO index is investigated in the following. HOAPS-3 latent and sensible heat fluxes are estimated using a bulk approach which is based on the wind speed, the near surface humidity difference, and air temperature differences as input parameters (see chapter 3.2.3). The sea surface humidity and temperature difference are directly derived from the SST.

The freshwater input into the ocean affects the surface salinity and hence the density and stratification of the upper ocean layers. Consequently, surface freshwater variations have the potential to influence the ocean circulation. *Dickson et al.* (2000) showed that the NAO has a significant impact on the ice and freshwater export from the Arctic. *Walsh and Portis* (1999) and *Bojariu and Reverdin* (2002) investigated the freshwater balance of oceanic evaporation and precipitation for the North Atlantic using NCEP and ERA reanalysis data. At least, longer periods of NAO anomalies are found to have a significant effect on the surface salinity by changes in the regional freshwater flux. Although this link could be established, it is not sure, whether the effect is strong enough to influence the deepwater formation and therefore the strength of the *thermohaline circulation* (THC) (*Hurrell*, 1995; *Greatbatch*, 2000).

Fig. 6.16 shows the local correlation of HOAPS-3 freshwater flux and re-

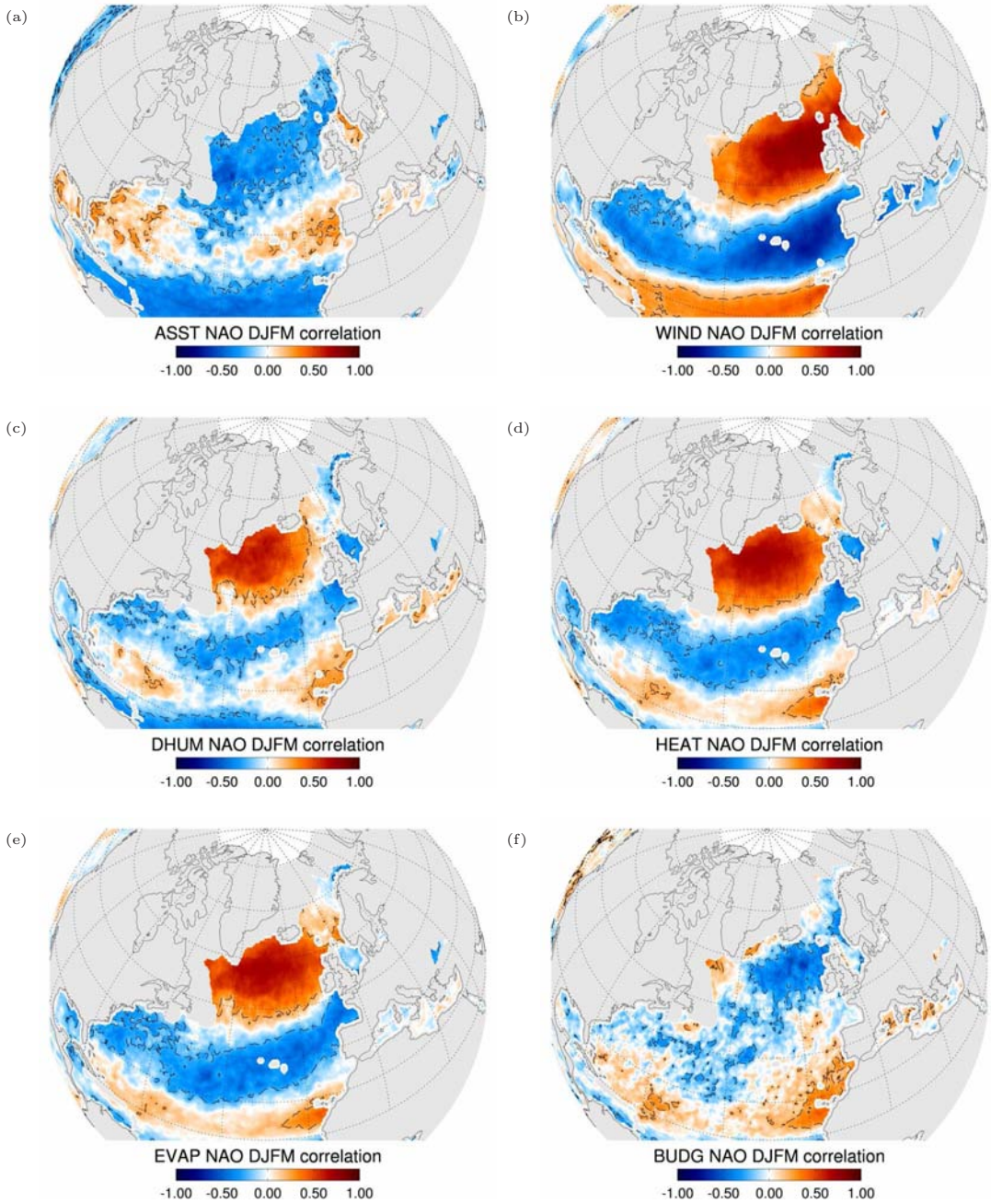

Figure 6.16: Local correlations of HOAPS-3 freshwater flux related parameters with the NAO index for the months December to March. The dashed line indicates the 95 % significance level of the t-test. Grey shaded ocean regions indicate domains excluded in HOAPS-3 due to the presence of sea ice.

lated bulk parameters with the NAO index. The correlation of the wind speed (Fig. 6.16 b) with the NAO index reflects the direct response of the wind field to the strengthened meridional pressure gradient in the NAO+ phase. The positive correlation patterns are associated with the northward shift and strengthening of the Westerlies and enhanced trade winds in the tropical regions, while the negative correlations indicate the stronger winds at the mid latitudes during NAO– phases.

During NAO+ phases, the stronger winds north of 50° N in the central Atlantic are related with advection of cold, dry Arctic air masses into the southwest sector of the Icelandic low, which leads to an increase in the humidity difference (Fig. 6.16 c). Together with the enhanced wind speed, this results in a positive response of evaporation and sensible heat flux in this region, which in turn leads to a cooling of the underlying ocean surface. An opposite effect can be observed in the southeastern sector of the Icelandic low around the British Isles and the North Sea, where warm, moist air is advected in NAO+ conditions, causing a decrease in the humidity difference. Hence the heat fluxes are reduced and negatively correlated with the NAO index, while the SST of the North Sea is positively correlated. During NAO– phases the response of the North Sea region is negative as the advection of cold and dry air masses from the Arctic leads to enhanced heat exchange and cooling of the sea surface.

The feedback of the sensible heat flux and hence evaporation (Fig. 6.16 d,e) on the wind is most pronounced at the mid to high latitudes over the North Atlantic, where both are significantly correlated with the NAO index. At high latitudes the humidity difference appears as a strong driver for the surface flux response as it is highly correlated with the NAO index. At the midlatitudes and subtropics the correlations are lower because the horizontal humidity gradients over the ocean decrease towards the tropical regions, and advection of air masses has a less pronounced effect on the near surface humidity difference. In the central North Atlantic the humidity difference is significantly correlated with the NAO index, but in the subtropics the response of the heat fluxes is mainly triggered by the modulation of the windspeed through the NAO as correlations for humidity difference are rather low and mostly not significant. However, in the region around the Canary islands, where dry continental air masses from the Sahara are advected over the ocean within the trades, a significant positive correlation of the humidity difference and heat fluxes is evident. A similar effect is evident at the North American east coast, where more cold air outbreaks reach the Gulf Stream region during NAO– conditions.

The correlations of the SST (Fig. 6.16 a) with the NAO index exhibit a well-known largely significant correlated tripole structure (e.g. *Cayan*, 1992; *Visbeck et al.*, 1998) with negative values in the subpolar and the subtropical North At-

lantic and mostly positive correlations at the midlatitudes. This pattern appears inverted to the correlation patterns of wind speed and the evaporation and sensible heat fluxes, which suggests a direct response of the SST field to the fluxes depending on the state of the NAO. The wind driven surface fluxes cause a cooling of the sea surface, imprinting the signature on the SST. Moreover, the wind induced mechanical mixing contributes to the cooling upper-ocean temperature field, albeit the effect it less pronounced compared to the heat exchange by sensible heat and evaporation (*Cayan*, 1992). The heat extraction from the ocean is of great importance for the moderate climate in northwestern Europe. When the NAO index is high, the stronger westerly winds lead to an amplification of the heat release from the North Atlantic into the atmosphere, which is then advected over the continent. Apart from the direct effects of the atmosphere on the SST, long term SST variations on decadal timescales have been identified that may be part of a dynamically coupled ocean-atmosphere feedback affecting the NAO variability (*Deser and Blackmon*, 1993; *Visbeck et al.*, 1998; *Czaja and Marshall*, 2001). On shorter timescales, SST anomalies preceding NAO phases by some months might imply some forecast potential for the NAO (*Czaja and Frankignoul*, 1999; *Hurrell et al.*, 2003).

The correlation for the freshwater flux from HOAPS-3 with the NAO index is shown in Fig. 6.16 f. Since both components, the precipitation (Fig. 6.14) as well as the evaporation (Fig. 6.16 e) exhibit distinct correlation patterns with the NAO index, these are reflected in the correlation of the freshwater flux with the NAO index.

In the northeast Atlantic at latitudes north of 50°, the correlation of E-P with the NAO index is negative. Here both parameters, the precipitation and evaporation are positively correlated with the NAO index. The resulting negative correlation of E-P with the NAO index, implies that the positive precipitation anomalies exceed the increase in evaporation during NAO+ phases. Hence the precipitation dominates the variability of the freshwater flux in this region.

For the midlatitudes, the E-P correlations in the Gulf Stream region, the eastern Atlantic and the Mediterranean are mostly inverse to the precipitation patterns indicating a stronger influence of the precipitation on the freshwater flux compared to the evaporation, likewise to the high latitudes. However, the correlations of the freshwater flux with the NAO are often not significant. In the central midlatitude Atlantic and the subtropics, the evaporation signal mostly determines the correlations patterns. A region of significant positive E-P correlation with the NAO index is found extending from the Iberian peninsula over Canary islands to the southwest. Here, the opposite correlations of precipitation and evaporation result in an amplification of the freshwater flux into the atmosphere during NAO+ phases.

The correlation patterns agree qualitatively with previous findings of *Walsh and Portis* (1999), *Bojariu and Reverdin* (2002), and *Hurrell et al.* (2003)/*Hurrell* (1995) which are based on reanalysis data and ship observations. However due to large uncertainties in the tropical freshwater balance of the reanalysis products larger differences between the data sets for these regions occur (*Walsh and Portis*, 1999). *Hurrell* (1995) found only a weak correlation of E-P and the NAO index in the northeastern subtropical Atlantic by using ECMWF data to infer the vertically integrated moisture transport. This was not in conformity with station based data from this region. However, this disagreement is not evident in the HOAPS-3 freshwater flux, where a significant positive response to the NAO is clearly proven.

6.7 Conclusions

A combined precipitation data set consisting of the HOAPS-3 satellite derived product and the rain gauge based GPCC Full Data Reanalysis Product Version 4 has been compiled and analyzed regarding its response to the NAO during the December to March winter season. Variability on regional scale is realistically reproduced as well as on the large scale. Composites and correlation patterns agree well and show a remarkably detailed and homogeneous response to the variability related to the NAO. A significant impact of the NAO on the corresponding precipitation patterns is evident. The strongest influence occurs in the northeastern Atlantic and Europe as well as in the regions adjacent to the Baffin Bay and Labrador Sea.

With a record of nineteen winter seasons and thus 76 months of data, an EOF analysis of North Atlantic precipitation became possible. Albeit no clearly dominating EOF pattern could be identified due to the strong inherent intra-monthly variability, the EOFs reveal coherent response and no land-sea difference or effect of changing station density was detected. Moreover, the first EOF revealed similarities and a better correlation with the East Atlantic Pattern defined by *Barnston and Livezey* (1987) than with the NAO index. It was also shown that singular events such as a strong NAO+ or NAO– have a significant impact on the EOF patterns. The subtropical variability is also governed to some extent by ENSO events. In particular the 1997/98 El Niño had strong influence on the precipitation.

More teleconnections were revealed by global correlation patterns. Especially in the Pacific, significant correlations of the precipitation with the NAO index were found. In the correlation patterns of the precipitation and the Northern Hemisphere mode of the AO index, this relationship is even more evident.

The comparison of global correlation patterns of the NAO index and precipi-

tation with other data sets shows an overall good agreement for the large scale patterns, but regional differences remain, especially at high latitudes. Although, the data coverage over the continents in the GPCC product varies in some regions, the global correlations do not exhibit obviously spurious patterns.

It has been shown that the HOAPS-3/GPCC data set, consisting of two completely independent data sources, is valuable for the investigation of regional and large scale precipitation related processes in the North Atlantic region. However, for further global studies, a more homogeneous GPCC data set, such as the VASClimO product may be more appropriate, when a time series covering the full HOAPS-3 record is available. On the other hand, the global correlation analyses in this study did not reveal major conspicuous patterns in the GPCC Full Data Reanalysis Product.

The investigation of the North Atlantic oceanic freshwater flux agreed with previous studies. In particular for the tropical regions HOAPS-3 has the potential to improve the understanding of the related processes compared to reanalysis data.

7

Concluding Remarks and Outlook

HOAPS-3, the latest version of the SSM/I based satellite climatology "Hamburg Ocean Atmosphere Parameters and Fluxes from Satellite Data" provides various data products of turbulent heat fluxes, evaporation, precipitation, freshwater flux and related atmospheric variables. A sophisticated processing chain, including all available SSM/I instruments and inter-sensor calibration, ensures a homogeneous time-series with dense data sampling and hence detailed information of the underlying weather situations. Within this work, the HOAPS-3 data set was completely reprocessed and now contains a continuous time series from 1987 to 2005. Additionally, new NODC/RSMAS AVHRR Pathfinder V5 SST fields and a new 85 GHz synthesis procedure for the faulty SSM/I on DMSP F08 have been implemented into the HOAPS-3 processing chain.

Apart from the methodological description in chapter 3, three evaluation and application studies have been presented. Therefore, this thesis work provides a comprehensive validation of the HOAPS-3 climatology. The studies encompassed the high temporal and spatial resolution with instantaneous data in a case study, a regionally limited analysis of North Atlantic climate variability, and the global evaluation on climatological scale.

In chapter 4 the HOAPS-3 parameters wind speed, precipitation, SST, evaporation, and the freshwater flux were evaluated on climatological scale. All of the examined parameters exhibit reasonable global patterns. The evaluations against other data sets revealed some systematic regional differences as well as convincing consistency with the HOAPS-3 retrievals. Regarding the validity of the temporal development of the global ocean freshwater flux and its components, a consistent

answer could not be given using other available data sets. However, the imbalance in the global ocean freshwater flux compared to global river runoff data is approximately 10 % of the HOAPS-3 global mean precipitation and evaporation. This value appears to be within the accuracy found in the comparison of HOAPS-3 parameters with other data sets. Overall, this value is a great improvement compared to earlier versions of HOAPS and points out the ability of HOAPS to derive the global ocean freshwater balance from satellite data consistently in one data set.

In chapter 5 the development of the hurricane Maria has been examined using HOAPS-3 and additional satellite data in a case study. Through the synergetic use of different data sources, a detailed view on the structure of the storm was achieved, documenting the different stages of its evolution including the transition process to an extratropical cyclone. Compared to previous studies, the use of HOAPS-3 data allowed an improved continuous and frequent coverage with satellite derived geophysical parameters from the storm's genesis in the tropics until its decay at high latitudes. The high resolution pixel level HOAPS precipitation, wind and water vapor data showed a consistent agreement with VIS and IR cloud images. Furthermore, HOAPS-3 and QuikSCAT retrievals were in good agreement for coincident overflights at the date of peak intensity of Maria, although with the limitation to the rainfree areas. Due to the successful application of HOAPS-3 data in this case study, a further climatological assessment of ET appears to be possible as well as a detailed comparison study with a model simulation, which may add additional information on the atmospheric dynamics within the transforming cyclone.

A novel approach was chosen to asses the precipitation variability of the North Atlantic region with respect to the NAO in chapter 6. For this study, the HOAPS-3 oceanic precipitation was combined with the GPCC Full Data Reanalysis Product Version 4. In the combined HOAPS-3/GPCC product, both data sets exhibit a remarkable consistency without the need of a bias adjustment or the like. It has been shown that this data set, consisting of two completely independent data sources, is valuable for the investigation of regional and large scale precipitation related processes in the North Atlantic region. Composites and correlation patterns agree well and show a detailed and homogeneous response of the precipitation variability related to the NAO. A significant impact of the NAO on the corresponding patterns is evident for the precipitation as well as for the freshwater flux and related parameters.

The Evaluation and application of HOAPS-3 data on different temporal and spatial scales presented in this work indicates a consistent and homogeneous time series, which is valuable for regional and case studies as well as for climatological investigations. However, some limitations regarding trend analyses of the

freshwater flux parameters remain.

Outlook

Future tasks will have to involve the further systematic quantification of uncertainties of the HOAPS retrievals. Especially promising results in high latitude cold season precipitation motivate further in situ validation efforts (*Klepp*, 2007). Also a comprehensive assessment of the long term stability of satellite based climatologies is still a barely touched issue which is important for applications regarding local and global trend analyses. Some of these matters are already investigated in cooperation with the IPWG and the SEAFLUX project. Furthermore, knowledge of the error propagation within the retrievals is important for the use of HOAPS data in applications which require an error estimate, such as input data sources for a model.

The NODC/RSMAS AVHRR Pathfinder data sets revealed some deficits in situations of high aerosol load in the atmosphere. Hence a substitution of this data set may improve the retrieval of the quantities depending on the SST. A climatological data set with a comparable temporal coverage to the Pathfinder data set is based on *(Advanced) Along-Track Scanning Radiometer* ((A)ATSR) measurements and is currently reprocessed by the ARC (ATSR Reprocessing for Climate) project (*Llewellyn-Jones et al.*, 2007) and will be available in the near future. Due to the dual viewing radiometer, (A)ATSR measurements are less affected from aerosol contamination in the atmosphere. However the data record starts in 1992 and hence will not cover the period from 1987 until the eruption of Mt. Pinatubo in 1991.

As no new SSM/I instruments following the DMSP F15 will be launched and no reliable measuring SSM/I is in space anymore by the end of 2008, a continuation of HOAPS will only be possible by the introduction of new sensors. This will be preferably the SSM/I successor series, the *Special Sensor Microwave Imager/Sounder* (SSMIS), which was launched first in 2003 and became operational in November 2005. The SSMIS essentially maintains the configuration of the SSM/I surface viewing channels but has a 91 GHz channel instead of the 85 GHz channel and additional temperature and sounding channels. Hence additional efforts regarding radiance conversions and the intercalibration with the SSM/I instruments are necessary. From 2013 on the *Global Precipitation Measurement* (GPM) mission will be available, which will be a constellation of nine satellites carrying microwave radiometers, including one core satellite that additionally carries a dual-frequency precipitation radar. Apart from the precipitation measurement, the retrieval of turbulent fluxes will also be possible by using the radiometer data from the GPM satellites. Another future satellite mission of interest is the *Soil Moisture and Ocean Salinity* (SMOS) mission, which will observe soil moisture

over the Earth's landmasses and the salinity over the oceans. Thus this instrument will give the opportunity to validate the ocean freshwater flux through the response of the surface salinity to evaporation and precipitation processes.

Finally, the development of satellite based retrievals to extend HOAPS over land for some parameters, i.e. precipitation and evapotranspiration, is one of the goals for the near future. This challenging tasks will require the incorporation of different additional satellite data sources.

Currently, the routine operation of HOAPS is transferred to the EUMETSAT *Climate Monitoring Satellite Application Facility* (CM-SAF) of the *Deutscher Wetterdienst* (DWD), which opens a long term perspective for the further development of HOAPS.

Cookies!
Give me some cookies!
Cookie Monster, Sesame Street

8 Danksagung/Acknowledgments

Neben vielen Freunden und Mitmenschen, die alle auf ihre Art Anteil am Gelingen dieser Arbeit haben, möchte ich einigen besonders danken:

Mein Dank gilt Herrn Prof. Dr. Hartmut Graßl, für die sehr gute Betreuung, bei der er mir viel Freiheit in der Ausgestaltung der Arbeit ließ. Stete Gesprächsbereitschaft und seine Anregungen waren ein verlässlicher Kompass im Verlauf dieser Arbeit.

Herrn Dr. Stephan Bakan möchte ich an dieser Stelle besonders herzlich für die fortlaufende Unterstützung und den Einsatz bei der Betreuung dieser Arbeit danken. Sein Wirken im Hintergrund, viele Diskussionen und gute Hinweise, waren für den Fortgang dieser Arbeit außerordentlich hilfreich.

Ein weiterer Dank geht an Christian Klepp. Seine große Begeisterung und sein Wissenshunger sind mir ein steter Antrieb. Die vielen Gespräche und Diskussionen mit ihm waren ein Schlüssel zum Gelingen dieser Arbeit. Während einiger Konferenzen und Tagungen konnte ich zudem zusammen mit ihm die (wissenschaftliche) Welt erkunden.

Ebenfalls an dieser Stelle zu erwähnen ist Karsten Fennig. Seiner Arbeit ist ein Großteil der hohen technischen und methodischen Qualität der HOAPS-Klimatologie zu verdanken. Mit der Neuimplementierung von HOAPS II, sowie dem neuen Niederschlagsalgorithmus hat er den wesentlichen Grundstein für die während dieser Arbeit entstandene Version HOAPS-3 gelegt. Auch vom Met Office in Exeter aus hatte er weiterhin stets ein offenes Ohr für Fragen und Diskussionen.

Meinen Kollegen aus dem 17. und jetzt 14. Stock des Geomatikums danke ich für eine immer freundliche und konstruktive Arbeitsatmosphäre. Besonders meinen ehemaligen Zimmergenossen Anne Blechschmidt und Marin Tomašić danke ich für viele heitere Stunden.

Das regelmäßige Essen in der Mensa wäre nicht ohne gegenseitige geistig-moralische Unterstützung einiger Leute, insbesondere Gunnar Spreen, sowie Stefan Kuck und Focko Meier aus der Physik an der Jungiusstraße, durchzuhalten gewesen.

Vielen Dank auch an die Korrekturleser Karen Anderßen, Anne Blechschmidt, Christian Klepp, Magnus Kutz und Gunnar Spreen.

Ein sehr herzlicher Dank gilt meinen Eltern und meiner Schwester, die mich stets unterstützt und bestärkt haben und so auf vielerlei Weise zum Gelingen dieser Arbeit beigetragen haben.

Zum Schluss sei ganz besonders Karen Anderßen für ihre Geduld, Unterstützung und Aufmunterung gedankt. Ihr starker Rückhalt während aller Höhen und Tiefen in den letzten Jahren hat vieles leichter gemacht.

Diese Arbeit wurde im Rahmen des Virtuellen Instituts “EXTROP” durch die Helmholtz-Gemeinschaft finanziert.

Nomenclature

(A)ATSR	(Advanced) Along-Track Scanning Radiometer
AMSR-E	Advanced Microwave Scanning Radiometer for Earth Observing System
AMSU-B	Advanced Microwave Sounding Unit-B
AO	Arctic Oscillation
ATT	Antenna Temperature Tapes
AVHRR	Advanced Very High Resolution Radiometer
CGMS	Coordination Group for Meteorological Satellites
CM-SAF	Climate Monitoring Satellite Application Facility
CMAP	CPC Merged Analysis of Precipitation
CMORPH	CPC Morphing Technique
COARE	Coupled Ocean-Atmosphere Response Experiment
CPC	Climate Prediction Center
DMSP	Defense Meteorological Satellites Program
DOE	Department of Energy
DOISST	Daily Optimum Interpolation (Daily OI) SST
DWD	Deutscher Wetterdienst
ECHAM5	European Centre Hamburg Model V5
ECMWF	European Centre for Medium-Range Weather Forecast
ENSO	El Niño / Southern Oscillation
EOF	empirical orthogonal function
ERA	ECMWF Re-Analysis
ERAint	ERA interim

ERBE	Earth Radiation Budget Experiment
ET	extratropical transition
FOV	field of view
GEWEX	Global Energy and Water Cycle Experiment
GPCC	Global Precipitation Climatology Center
GPCP	Global Precipitation Climatology Project
GPM	Global Precipitation Measurement
GRDC	Global Runoff Data Center
GSMaP	Global Satellite Mapping of Precipitation
GSSTF2	Goddard Satellite based Surface Turbulent Fluxes version 2
HOAPS	Hamburg Ocean Atmosphere Parameters and Fluxes from Satellite Data
ICOADS	International Comprehensive Ocean-Atmosphere Data Set
IFREMER	Institut Français de Recherche pour l'Exploration de la Mer
IPWG	International Precipitation Working Group
IR	infrared
ISCCP	International Satellite Cloud Climatology
ITCZ	Inter-Tropical Convergence Zone
J-OFURO 2	Japanese Ocean Flux data sets with the Use of Remote sensing Observations
JAXA	Japan Aerospace Exploration Agency
JCDAS	JMA Climate Data Assimilation System
JRA-25	Japanese 25-year ReAnalysis
MODIS	Moderate Resolution Imaging Spectroradiometer
MSLP	mean sea level pressure
NAO	North Atlantic Oscillation
NASA	National Aeronautics and Space Administration
NCAR	National Center for Atmospheric Research
NCEP	National Centers for Environmental Prediction

NDBC	National Data Buoy Center
NESDIS	National Environmental Satellite, Data, and Information System
NHC	National Hurricane Center
NOAA	National Oceanic and Atmospheric Administration
NOCS	National Oceanographic Centre Southampton
NODC	NOAA National Oceanographic Data Center
OAFLUX	Objectively Analyzed air-sea FLUXes
OLR	outgoing longwave radiation
PC	principal component
PERSIANN	Precipitation Estimation from Remotely Sensed Information using Artificial Neural Networks
PFSST	NODC/RSMAS Pathfinder V5 SST
PNA	Pacific North American
PR	Precipitation Radar
RPCA	Rotated Principal Component Analysis
RSMAS	Miami's Rosenstiel School of Marine and Atmospheric Science
RSS	Remote Sensing Systems
SLP	sea level pressure
SMOS	Soil Moisture and Ocean Salinity
SO	Southern Oscillation
SPCZ	South Pacific conversion zone
SSM/I	Special Sensor Microwave Imager
SSMIS	Special Sensor Microwave Imager/Sounder
SST	sea surface temperature
TAO	Tropical Atmosphere/Ocean
TB	brightness temperature
TC	tropical cyclone
TDR	Temperature Data Records
THC	thermohaline circulation

TIROS	Television and InfraRed Observation Satellite
TMI	TRMM Microwave Imager
TMPA	TRMM multisatellite precipitation analysis
TOVS	TIROS Operational Vertical Sounder
TRMM	Tropical Rainfall Measuring Mission
UMORA	Unified Microwave Ocean Retrieval Algorithm
VIS	visible
VOS	Voluntary Observing Ships
WCRP	World Climate Research Programme

Bibliography

Adler, R., C. Kidd, G. Petty, M. Morissey, and H. Goodman (2001), Intercomparison of global precipitation products: The third Precipitation Intercomparison Project (PIP-3), *Bull. Amer. Meteor. Soc.*, *82*(7), 1377–1396.

Adler, R. F., G. J. Huffman, D. T. Bolvin, S. Curtis, and E. J. Nelkin (2000), Tropical rainfall distributions determined using TRMM combined with other satellite and rain gauge information, *J. Appl. Meteor.*, *39*(12), 2007–2023.

Adler, R. F., G. J. Huffman, A. Chang, R. Ferraro, P. Xie, J. Janowiak, B. Rudolf, U. Schneider, S. Curtis, D. Bolvin, A. Gruber, J. Susskind, P. Arkin, and E. Nelkin (2003), The version-2 Global Precipitation Climatology Project (GPCP) monthly precipitation analysis (1979-present), *J. Hydrometeor.*, *4*(6), 1147–1167.

Agusti-Panareda, A., C. D. Thorncroft, G. C. Craig, and S. L. Gray (2004), The extratropical transition of hurricane Irene (1999): A potential-vorticity perspective, *Quart. J. Roy. Meteor. Soc.*, *130*(598), 1047–1074.

Ambaum, M. H. P., B. J. Hoskins, and D. B. Stephenson (2001), Arctic Oscillation or North Atlantic Oscillation?, *J. Climate*, *14*, 3495–3507.

Andersson, A., S. Bakan, K. Fennig, H. Graßl, C. Klepp, and J. Schulz (2007a), Hamburg Ocean Atmosphere Parameters and Fluxes from Satellite Data - HOAPS-3 - monthly mean, *World Data Center for Climate*, doi:10.1594/WDCC/HOAPS3_MONTHLY, electronic publication.

Andersson, A., S. Bakan, K. Fennig, H. Graßl, C. Klepp, and J. Schulz (2007b), Hamburg Ocean Atmosphere Parameters and Fluxes from Satellite Data - HOAPS-3 - twice daily composite, *World Data Center for Climate*, doi:10.1594/WDCC/HOAPS3_DAILY, electronic publication.

Andersson, A., S. Bakan, K. Fennig, H. Graßl, C. Klepp, and J. Schulz (2007c), Hamburg Ocean Atmosphere Parameters and Fluxes from Satellite Data - HOAPS-3 - 5-days mean, *World Data Center for Climate*, doi:10.1594/WDCC/HOAPS3_PENTAD, electronic publication.

Andersson, A., S. Bakan, K. Fennig, H. Graßl, and C. Klepp (2007d), The HOAPS-3 climatology, in *Proceedings of the 3rd International Precipitation Working Group Workshop (IPWG), Melbourne, 23-27 October, 2006*.

Andersson, A., C. P. Klepp, H. Graßl, S. Bakan, K. Fennig, and J. Schulz (2007e), HOAPS-3: Improved climatology of the global ocean water cycle parameters derived from SSM/I satellite data, in *Proceedings of the Joint 2007 EUMETSAT Meteorological Satellite Conference and the 15th Satellite Meteorology and Oceanography Conference of the American Meteorological Society, Amsterdam, The Netherlands, 24-28 September*, ISSN 1011-3932.

Bader, J., and M. Latif (2005), North Atlantic Oscillation response to anomalous Indian Ocean SST in a coupled GCM, *J. Climate*, *18*(24), 5382–5389.

Bakan, S., V. Jost, and K. Fennig (2000), Satellite derived water balance climatology for the North Atlantic: First results, *Phys. Chem. Earth Part B*, *25*(2), 121–128.

Barnston, A. G., and R. E. Livezey (1987), Classification, seasonality and persistence of low-frequency atmospheric circulation patterns, *Mon. Wea. Rev.*, *115*(6), 1083–1126.

Bauer, P. (1992), Wasserdampf, Gesamtwasser und Niederschlagsrate aus Daten passiver Mikrowellenradiometer über dem Ozean, *Forschungsbericht*, DLR, Köln, Germany, ISSN 0939-2963.

Bauer, P. (2001), Over-ocean rainfall retrieval from multisensor data of the Tropical Rainfall Measuring Mission. Part I: Design and evaluation of inversion databases, *J. Atmos. Oceanic Technol.*, *18*(8), 1315–1330.

Bauer, P., and P. Schlüssel (1993), Rainfall, total water, ice water, and water-vapor over sea from polarized microwave simulations and special sensor microwave imager data, *J. Geophys. Res.-Atmos.*, *98*(D11), 20,737–20,759.

Bauer, P., P. Lopez, A. Benedetti, D. Salmond, and E. Moreau (2006a), Implementation of 1D+4D-Var assimilation of precipitation-affected microwave radiances at ECMWF. I: 1D-Var, *Quart. J. Roy. Meteor. Soc.*, *132*(620), 2277–2306.

Bauer, P., E. Moreau, F. Chevallier, and U. O'Keeffe (2006b), Multiple-scattering microwave radiative transfer for data assimilation applications, *Quart. J. Roy. Meteor. Soc.*, *132*(617), 1259–1281.

Bentamy, A., K. B. Katsaros, A. M. Mestas-Nunez, W. M. Drennan, E. B. Forde, and H. Roquet (2003), Satellite estimates of wind speed and latent heat flux over the global oceans, *J. Climate*, *16*(4), 637–656.

Berry, D. I., and E. C. Kent (2008), A new air-sea interaction gridded dataset from ICOADS with uncertainty estimates., submitted to BAMS.

Bjornsson, H., and S. Venegas (1997), A manual for EOF and SVD analyses of climatic data, *CCGCR Report No. 97-1*, Centre for climate and Global Change Research, McGill University, Montréal, Québec.

Blechschmidt, A. M. (2008), A 2-year climatology of polar low events over the Nordic Seas from satellite remote sensing, *Geophys. Res. Lett.*, *35*, L09,815.

Bojariu, R., and G. Reverdin (2002), Large-scale variability modes of freshwater flux and precipitation over the Atlantic, *Clim. Dynam.*, *18*(5), 369–381.

Bourras, D. (2006), Comparison of five satellite-derived latent heat flux products to moored buoy data, *J. Climate*, *19*(24), 6291–6313.

Bradley, E. F., C. W. Fairall, J. E. Hare, and A. A. Grachev (2000), An old and improved bulk algorithm for air-sea fluxes: COARE 2.6 a, in *Preprints, 14th Symp. on Boundary Layers and Turbulence, Aspen, CO*, pp. 294–296, Amer. Meteor. Soc.

Browning, K., and M. Field (2004), Evidence from meteosat imagery of the interaction of sting jets with the boundary layer, *Meteor. Appl.*, *11*(4), 277–289.

Browning, K. A. (1997), The dry intrusion perspective of extra-tropical cyclone development, *Meteor. Appl.*, *4*(4), 317–324.

Burnett, W. C., M. Taniguchi, and J. Oberdorfer (2001), Measurement and significance of the direct discharge of groundwater into the coastal zone, *J. Sea Res.*, *46*(2), 109–116.

Carleton, A. M. (1988), Meridional transport of eddy sensible heat in winters marked by extremes of the North Atlantic Oscillation, 1948/49-1979/80, *J. Climate*, *1*(2), 212–223.

Cayan, D. R. (1992), Latent and Sensible Heat Flux Anomalies over the Northern Oceans: The Connection to Monthly Atmospheric Circulation., *J. Climate*, *5*, 354–370.

Cayan, D. R. (1992), Latent and sensible heat flux anomalies over the northern oceans: Driving the sea surface temperature, *J. Phys. Oceanogr.*, *22*(8), 859–881.

Chou, S. H., E. Nelkin, J. Ardizzone, R. M. Atlas, and C. L. Shie (2003), Surface turbulent heat and momentum fluxes over global oceans based on the goddard satellite retrievals, version 2 (GSSTF2), *J. Climate*, *16*(20), 3256–3273.

Chou, S. H., E. Nelkin, J. Ardizzone, and R. M. Atlas (2004), A comparison of latent heat fluxes over global oceans for four flux products, *J. Climate*, *17*(20), 3973–3989.

Clayson, C. A., J. Roberts, A. Bentamy, M. A. Bourassa, J. A. Curry, D. Jackson, C. Klepp, A. Andersson, M. Kubota, W. B. Rossow, J. Schulz, S. Smith, M. Tomita, and G. Wick (2009), Results of the seaflux intercomarison project, in prep.

Colton, M. C., and G. A. Poe (1999), Intersensor calibration of DMSP SSM/I's: F-8 to F-14, 1987-1997, *IEEE Trans. Geosci. Remote Sens.*, *37*(1), 418–439.

Curry, J. A., A. Bentamy, M. A. Bourassa, D. Bourras, E. F. Bradley, M. Brunke, S. Castro, S. H. Chou, C. A. Clayson, W. J. Emery, L. Eymard, C. W. Fairall, M. Kubota, B. Lin, W. Perrie, R. A. Reeder, I. A. Renfrew, W. B. Rossow, J. Schulz, S. R. Smith, P. J. Webster, G. A. Wick, and X. Zeng (2004), Seaflux, *Bull. Amer. Meteor. Soc.*, *85*(3), 409–424.

Czaja, A., and C. Frankignoul (1999), Influence of the North Atlantic SST on the atmospheric circulation, *Geophys. Res. Lett.*, *26*(19), 2969–2972.

Czaja, A., and J. Marshall (2001), Observations of atmosphere-ocean coupling in the North Atlantic, *Quart. J. Roy. Meteor. Soc.*, *127*(576), 1893–1916.

Dai, A., I. Fung, and A. DelGenio (1997), Surface observed global land precipitation variations during 1900-88, *J. Climate*, *10*(11), 2943–2962.

Deser, C., and M. L. Blackmon (1993), Surface climate variations over the North Atlantic Ocean during winter: 1900-1989., *J. Climate*, *6*(9), 1743–1753.

Dickson, R., T. Osborn, J. Hurrell, J. Meincke, J. Blindheim, B. Adlandsvik, T. Vinje, G. Alekseev, and W. Maslowski (2000), The Arctic Ocean response to the North Atlantic Oscillation, *J. Climate*, *13*(15), 2671–2696.

Evans, M. S., D. Keyser, L. F. Bosart, and G. M. Lackmann (1994), A satellite-derived classification scheme for rapid maritime cyclogenesis, *Mon. Wea. Rev.*, *122*, 1381–1416.

Fairall, C., E. Bradley, J. Godfrey, G. Wick, J. Edson, and G. Young (1996a), Cool-skin and warm-layer effects on sea surface temperature, *J. Geophys. Res.-Oceans*, *101(C1)*, 1295–1308.

Fairall, C. W., E. F. Bradley, D. P. Rogers, J. B. Edson, and G. S. Young (1996b), Bulk parameterization of air-sea fluxes for Tropical Ocean-Global Atmosphere Coupled-Ocean Atmosphere Response Experiment, *J. Geophys. Res.-Oceans*, *101*, 3747–3764.

Fairall, C. W., E. F. Bradley, J. E. Hare, A. A. Grachev, and J. B. Edson (2003), Bulk parameterization of air-sea fluxes: Updates and verification for the COARE algorithm, *J. Climate*, *16*(4), 571–591.

Fennig, K., S. Bakan, H. Graßl, C. Klepp, and J. Schulz (2006a), Hamburg Ocean Atmosphere Parameters and Fluxes from Satellite Data - HOAPS II - monthly mean, *World Data Center for Climate*, doi:10.1594/WDCC/HOAPS2_MONTHLY, electronic publication.

Fennig, K., S. Bakan, H. Graßl, C. Klepp, and J. Schulz (2006b), Hamburg Ocean Atmosphere Parameters and Fluxes from Satellite Data - HOAPS II - pentad mean, *World Data Center for Climate*, doi:10.1594/WDCC/HOAPS2_PENTAD, electronic publication.

Fuhrhop, R., and C. Simmer (1996), SSM/I brightness temperature corrections for incidence angle variations, *J. Atmos. Oceanic Technol.*, *13*(1), 246–254.

Gardashov, R. G., K. S. Shifrin, and J. K. Zolotova (1988), Emissivity, thermal albedo and effective emissivity of the sea at different wind speeds, *Oceanol. Acta*, *11*(2), 121–124.

GLOBE Task Team (1999), The global land one-kilometer base elevation (GLOBE) digital elevation model, version 1.0., *Tech. rep.*, National Oceanic and Atmospheric Administration, National Geophysical Data Center, 325 Broadway, Boulder, Colorado 80303, U.S.A.

Graßl, H. (1976), The dependence of the measured cool skin of the ocean on wind stress and total heat flux, *Bound.-Lay. Meteoro.*, *10*(4), 465–474.

Graßl, H., V. Jost, J. Schulz, R. Kumar, P. Bauer, and P. Schlussel (2000), The Hamburg Ocean-Atmosphere Parameters and Fluxes from Satellite Data (HOAPS): A climatological atlas of satellite-derived air-sea-interaction parameters over the oceans, *Max-Planck Report 312*, Max-Planck Institute for Meteorology, Bundesstr. 53, 20146 Hamburg, Germany.

GRDC (2009), Surface freshwater fluxes into the world oceans / global runoff data centre: Comparisons of GRDC freshwater flux estimate with literature, *Tech. rep.*, Federal Institute of Hydrology (BfG), Koblenz, Germany, `http://grdc.bafg.de/`.

Greatbatch, R. (2000), The North Atlantic Oscillation, *Stoch. Env. Res. Risk A.*, *14*(4), 213–242.

GSFC (2007), *Algorithm 3B43 - TRMM and Other Data Precipitation*, Goddard Space Flight Center, `http://trmm.gsfc.nasa.gov/3b43.html`.

Harr, P., and R. Elsberry (2000), Extratropical transition of tropical cyclones over the western North Pacific. Part I: Evolution of structural characteristics during the transition process, *Mon. Wea. Rev.*, *128*(8), 2613–2633.

Hart, R., and J. Evans (2001), A climatology of the extratropical transition of Atlantic tropical cyclones, *J. Climate*, *14*(4), 546–564.

Hart, R., J. Evans, and C. Evans (2006), Synoptic composites of the extratropical transition life cycle of north Atlantic tropical cyclones: Factors determining posttransition evolution, *Mon. Wea. Rev.*, *134*(2), 553–578.

Hart, R. E. (2003), A cyclone phase space derived from thermal wind and thermal asymmetry, *Mon. Wea. Rev.*, *131*(4), 585–616.

Hilburn, K. A., and F. J. Wentz (2008), Intercalibrated passive microwave rain products from the Unified Microwave Ocean Retrieval Algorithm (UMORA), *J. Appl. Meteor. Climatol.*, *47*(3), 778–794.

Hoerling, M. P., J. W. Hurrell, and T. Xu (2001), Tropical origins for recent North Atlantic climate change, *Science*, *292*(5514), 90–92.

Hollinger, J. P., J. L. Peirce, and G. A. Poe (1990), SSM/I instrument evaluation, *IEEE Trans. Geosci. Remote Sens.*, *28*(5), 781–790.

Hsu, K., X. Gao, S. Sorooshian, and H. Gupta (1997), Precipitation estimation from remotely sensed information using artificial neural networks, *J. Appl. Meteor.*, *36*(9), 1176–1190.

Huang, J., K. Higuchi, and A. Shabbar (1998), The relationship between the North Atlantic Oscillation and El Niño Southern Oscillation, *Geophys. Res. Lett.*, *25*(14), 2707–2710.

Huffman, G., R. Adler, D. Bolvin, G. Gu, E. Nelkin, K. Bowman, Y. Hong, E. Stocker, and D. Wolff (2007), The TRMM Multisatellite Precipitation Analysis (TMPA): Quasi-global, multiyear, combined-sensor precipitation estimates at fine scales, *J. Hydrometeor.*, *8*(1), 38–55.

Huffman, G. J., R. F. Adler, P. Arkin, A. Chang, R. Ferraro, A. Gruber, J. Janowiak, A. McNab, B. Rudolf, and U. Schneider (1997), The Global Precipitation Climatology Project (GPCP) combined precipitation dataset, *Bull. Amer. Meteor. Soc.*, *78*(1), 5–20.

Huntington, T. (2006), Evidence for intensification of the global water cycle: Review and synthesis, *J. Hydrol.*, *319*(1-4), 83–95.

Hurrell, J., and H. van Loon (1997), Decadal variations in climate associated with the North Atlantic Oscillation, *Climatic Change*, *36*(3), 301–326.

Hurrell, J. W. (1995), Decadal trends in the North Atlantic Oscillation: Regional temperatures and precipitation, *Science*, *269*(5224), 676–679.

Hurrell, J. W. (1995), Transient eddy forcing of the rotational flow during northern winter, *J. Atmos. Sci.*, *52*(12), 2286–2301.

Hurrell, J. W., Y. Kushnir, M. Visbeck, and G. Ottersen (2003), An overview of the North Atlantic Oscillation, in *The North Atlantic Oscillation: Climate Significance and Environmental Impact*, *Geophysical Monograph Series*, vol. 134, edited by J. W. Hurrell, Y. Kushnir, G. Ottersen, and M. Visbeck, pp. 1–35.

IFREMER/CERSAT (2002), *Mean Wind Fields (MWF product) - User Manual - Volume 2 : QuikSCAT*, `ftp://ftp.ifremer.fr/ifremer/cersat/products/gridded/mwf-quikscat/documentation/mutwqscat.pdf`.

Jarvinen, B., C. Neumann, and M. Davis (1984), A tropical cyclone data tape for the North Atlantic basin, 1886-1983: Contents, limitations, and uses., *NOAA Technical Memorandum NWS NHC 22*, NOAA/National Hurricane Center, Miami, FL.

Jones, P., T. Jonsson, and D. Wheeler (1997), Extension to the North Atlantic Oscillation using early instrumental pressure observations from Gibraltar and south-west Iceland, *Int. J. Climatol.*, *17*(13), 1433–1450.

Jones, S., P. Harr, J. Abraham, L. Bosart, P. Bowyer, J. Evans, D. Hanley, B. Hanstrum, R. Hart, F. Lalaurette, M. Sinclair, R. Smith, and C. Thorncroft (2003), The extratropical transition of tropical cyclones: Forecast challenges, current understanding, and future directions, *Wea. Forecasting*, *18*(6), 1052–1092.

Jost, V. (2000), Eine neue Klimatologie des Süßwasserflusses an der Meeresoberfläche abgeleitet aus Satellitendaten, Ph.D. thesis, Max Planck Institute for Meteorology, Bundesstr. 53, 20146 Hamburg, Germany, ISSN 0938-5177.

Jost, V., S. Bakan, and K. Fennig (2002), HOAPS - a new satellite-derived freshwater flux climatology, *Meteor. Z.*, *11*(1), 61–70.

Joyce, R., J. Janowiak, P. Arkin, and P. Xie (2004), CMORPH: A method that produces global precipitation estimates from passive microwave and infrared data at high spatial and temporal resolution, *J. Hydrometeor.*, *5*(3), 487–503.

JPL (2006), *QuikScat Science data product, Users Manual, Overview and Geophysical Data Products, Version 3.0*, Jet Propulsion Laboratory, California Inst. Of Tech., `ftp://podaac.jpl.nasa.gov/ocean_wind/quikscat/L2B/doc/QSUG_v3.pdf`.

Kalnay, E., M. Kanamitsu, R. Kistler, W. Collins, D. Deaven, L. Gandin, M. Iredell, S. Saha, G. White, J. Woollen, et al. (1996), The NCEP/NCAR 40-Year Reanalysis Project., *Bull. Amer. Meteor. Soc.*, *77*(3), 437–472.

Kanamitsu, M., W. Ebisuzaki, J. Woollen, S. Yang, J. Hnilo, M. Fiorino, and G. Potter (2002), NCEP-DOE AMIP-II Reanalysis (R-2), *Bull. Amer. Meteor. Soc.*, *83*(11), 1631–1643.

Kelly, K. A., S. Dickinson, M. J. McPhaden, and G. C. Johnson (2001), Ocean currents evident in satellite wind data, *Geophys. Res. Lett.*, *28*(12), 2469–2472.

Kenneth, S. C. (2004), Global AVHRR 4 km SST for 1985-2001, Pathfinder V5.0, NODC/RSMAS, *Tech. rep.*, NOAA National Oceanographic Data Center, Silver Spring, Maryland, NODC Accession Numbers 0001763-0001864: Pathfinder AVHRR Version 5.0.

Kilpatrick, K. A., G. P. Podesta, and R. Evans (2001), Overview of the NOAA/NASA advanced very high resolution radiometer Pathfinder algorithm for sea surface temperature and associated matchup database, *J. Geophys. Res.-Oceans*, *106*(C5), 9179–9197.

Kitabatake, N. (2008), Extratropical transition of tropical cyclones in the western north pacific: Their frontal evolution, *Mon. Wea. Rev.*, *136*, 2066–2090.

Klein, P. M., P. A. Harr, and R. L. Elsberry (2000), Extratropical transition of western North Pacific tropical cyclones: An overview and conceptual model of the transformation stage, *Wea. Forecasting*, *15*(4), 373–395.

Klepp, C. P. (2005), HOAPS II global ocean precipitation data base, in *Eumetsat Proceedings, P.44, Second International Precipitation Working Group Workshop*, pp. 169–176, ISBN 92-9110-070-6.

Klepp, C. P. (2007), An over ocean snowfall validation data set for satellite retrievals, in *Proceedings of the 3rd International Precipitation Working Group Workshop (IPWG), Melbourne, 23-27 October, 2006*.

Klepp, C. P., S. Bakan, and H. Graßl (2003), Improvements of satellite-derived cyclonic rainfall over the North Atlantic, *J. Climate*, *16*(4), 657–669.

Klepp, C. P., S. Bakan, and H. Graßl (2005), Missing North Atlantic cyclonic precipitation in ECMWF numerical weather prediction and ERA-40 data detected through the satellite climatology HOAPS II, *Meteor. Z.*, *14*(6), 809–821.

Klocke, D. (2008), Vergleichende Analyse des globalen Wasserhaushalts aus HOAPS-3 mit ERA40 und ECHAM5/IPCC, Diplomarbeit, University of Hamburg, Germany.

Krasnopolsky, V. M., L. C. Breaker, and W. H. Gemmil (1995), A neural network as a nonlinear transfer function model for retrieving surface wind speeds from the Special Sensor Microwave Imager, *J. Geophys. Res.-Oceans*, *100*(C6), 11,033–11,045.

Kronberg, P. (1985), *Fernerkundung der Erde*, 394 pp., Ferdinand Enke Verlag, Stuttgart.

Kubota, M., and H. Tomita (2007), Introduction of J-OFURO latent heat flux version 2, in *Proceedings of the Joint 2007 EUMETSAT Meteorological Satellite Conference and the 15th Satellite Meteorology and Oceanography Conference of the American Meteorological Society, Amsterdam, The Netherlands, 24-28 September*, ISSN 1011-3932.

Kubota, M., A. Kano, H. Muramatsu, and H. Tomita (2003), Intercomparison of various surface latent heat flux fields, *J. Climate*, *16*(4), 670–678.

Kubota, T., S. Shige, H. Hashizurne, K. Aonashi, N. Takahashi, S. Seto, M. Hirose, Y. Takayabu, T. Ushio, K. Nakagawa, K. Wanami, M. Kachi, and K. Okamoto (2007), Global precipitation map using satellite-borne microwave radiometers by the GSMaP project: Production and validation, *IEEE Trans. Geosci. Remote Sens.*, *45*(7), 2259–2275.

Labat, D., Y. Godderis, J. Probst, and J. Guyot (2004), Evidence for global runoff increase related to climate warming, *Adv. Water Resour.*, *27*(6), 631–642.

Lawrence, S. P., D. T. Llewellyn-Jones, and S. J. Smith (2004), The measurement of climate change using data from the Advanced Very High Resolution and Along Track Scanning Radiometers, *J. Geophys. Res.*, *109*, 8017–8017.

Legates, D., H. Lins, and G. McCabe (2005), Comments on"Evidence for global runoff increase related to climate warming"by Labat et al., *Adv. Water Resour.*, *28*(12), 1310–1315.

Levizzani, V., P. Bauer, and F. Turk (2007), *Measuring Precipitation from Space: EURAINSAT and the Future*, *Advances in Global Change Research*, vol. 28, 722 pp., Springer Verlag.

Liu, J. P., and J. A. Curry (2006), Variability of the tropical and subtropical ocean surface latent heat flux during 1989-2000, *Geophys. Res. Lett.*, *33*(5), L05,706.

Llewellyn-Jones, D., G. Corlett, and C. Mutlow (2007), AATSR - completing the first 15 years global SST for climate, in *Proceedings of the Envisat Symposium 2007*, ESA SP 636, European Space Agency.

Lott, J. N. (1994), The US summer of 1993: A sharp contrast in weather extremes, *Weather*, *49*(11), 370–383.

Mann, H., and D. Whitney (1947), On a test of whether one of two random variables is stochastically larger than the other, *Ann. Math. Stat.*, *18*(1), 50–60.

Mariotti, A., and P. Arkin (2007), The North Atlantic Oscillation and oceanic precipitation variability, *Clim. Dynam.*, *28*(1), 35–51.

Marshall, J., Y. Kushner, D. Battisti, P. Chang, A. Czaja, R. Dickson, J. Hurrell, M. McCartney, R. Saravanan, and M. Visbeck (2001), North Atlantic climate variability: Phenomena, impacts and mechanisms, *Int. J. Climatol.*, *21*(15), 1863–1898.

Meissner, T., D. Smith, and F. Wentz (2001), A 10 year intercomparison between collocated Special Sensor Microwave Imager oceanic surface wind speed retrievals and global analyses, *J. Geophys. Res.*, *106*, 11,731–11,742.

Miller, A. J., S. Zhou, and S. K. Yang (2003), Relationship of the Arctic and Antarctic Oscillations to the outgoing longwave radiation, *J. Climate*, *16*(10), 1583–1592.

Monahan, A. H. (2006), The probability distribution of sea surface wind speeds. Part II: Dataset intercomparison and seasonal variability, *J. Climate*, *19*(4), 521–534.

NODC (2008), *4 km Pathfinder Version 5.0 User Guide*, National Oceanographic Data Center, Silver Spring, Maryland, `http://www.nodc.noaa.gov/sog/pathfinder4km/userguide.html`.

Onogi, K., J. Tsutsui, H. Koide, M. Sakamoto, S. Kobayashi, H. Hatsushika, T. Matsumoto, N. Yamazaki, H. Kamahori, K. Takahashi, et al. (2007), The JRA-25 Reanalysis, *J. Meteor. Soc. Japan*, *85*(3), 369–432.

Parker, D., H. Wilson, P. Jones, J. Christy, and C. Folland (1996), The impact of Mount Pinatubo on world-wide temperatures, *Int. J. Climatol.*, *16*(5), 487–497.

Pasch, R. J., and E. S. Blake (2006), Hurricane Maria, 1-10 September 2005, *Tropical Cyclone Report*, National Hurricane Center, Miami, FL.

Rasmusson, E. M., and P. A. Arkin (1993), A global view of large-scale precipitation variability, *J. Climate*, *6*(8), 1495–1522.

Reynolds, R. W. (1993), Impact of Mount Pinatubo aerosols on satellite-derived sea surface temperatures, *J. Climate*, *6*(4), 768–774.

Reynolds, R. W., N. A. Rayner, T. M. Smith, D. C. Stokes, and W. Wang (2002), An improved in situ and satellite SST analysis for climate, *J. Climate*, *15*(13), 1609–1625.

Reynolds, R. W., T. M. Smith, C. Liu, D. B. Chelton, K. S. Casey, and M. G. Schlax (2007), Daily high-resolution-blended analyses for sea surface temperature, *J. Climate*, *20*(22), 5473–5496.

Ritchie, A. A., M. R. Smith, H. M. Goodman, R. L. Schudalla, D. K. Conway, F. J. LaFontaine, D. Moss, and B. Motta (1998), Critical analyses of data differences between FNMOC and AFGWC spawned SSM/I datasets, *J. Atmos. Sci.*, *55*(9), 1601–1612.

Ritchie, E. A., and R. L. Elsberry (2003), Simulations of the extratropical transition of tropical cyclones: Contributions by the midlatitude upper-level trough to reintensification, *Mon. Wea. Rev.*, *131*(9), 2112–2128.

Robock, A. (2002), Pinatubo eruption: The climatic aftermath, *Science*, *295*(5558), 1242–1244.

Rogers, J. (1997), North Atlantic storm track variability and its association to the North Atlantic Oscillation and climate variability of northern Europe, *J. Climate*, *10*(7), 1635–1647.

Rogers, J. C. (1984), The Association between the North Atlantic Oscillation and the Southern Oscillation in the Northern Hemisphere, *Mon. Wea. Rev.*, *112*(10), 1999–2015.

Romanova, V., A. Köhl, D. Stammer, C. Klepp, A. Andersson, and S. Bakan (2009), Intercomparison of GECCO, HOAPS and NCEP net sea surface freshwater flux fields, submitted to J. Climate.

Ropelewski, C., and M. Halpert (1987), Global and regional scale precipitation patterns associated with the El Niño/Southern Oscillation, *Mon. Wea. Rev.*, *115*(8), 1606–1626.

Rossow, W. B., and R. A. Schiffer (1991), ISCCP cloud data products, *Bull. Amer. Meteor. Soc.*, *72*(1), 2–20.

Rudolf, B., and U. Schneider (2005), Calculation of gridded precipitation data for the global land-surface using in-situ gauge observations, in *Proceedings of the 2nd Workshop of the International Precipitation Working Group IPWG, Monterey October 2004*.

Rudolf, B., H. Hauschild, W. Rueth, and U. Schneider (1994), Terrestrial precipitation analysis: Operational method and required density of point measurements. Global Precipitations and Climate Change, M. Desbois and F. Desalmond, Eds., NATO ASI Series I, 26.

Schlosser, C. A., and P. R. Houser (2007), Assessing a satellite-era perspective of the global water cycle, *J. Climate*, *20*(7), 1316–1338.

Schluessel, P., W. J. Emery, H. Grassl, and T. Mammen (1990), On the bulk-skin temperature difference and its impact on satellite remote sensing of sea surface temperature, *J. Geophys. Res.*, *95(C8)*, 13,341–13,356.

Schlüssel, P. (1995), *Passive Fernerkundung der unteren Atmosphäre und der Meeresoberfläche aus dem Weltraum*, *Berichte aus dem Zentrum für Meeres- und Klimaforschung, Reihe A: Meteorologie*, vol. 20, 175 pp., Max Planck Institute for Meteorology, Bundesstr. 55, 20146 Hamburg, Germany, ISSN 0947-7128.

Schlüssel, P. (1996), *Radiation and water in the climate system: Remote measurements*, *NATO ASI Series*, vol. 145, chap. Satellite remote sensing of evaporation over sea, pp. 431–459, Springer-Verlag, Berlin , Germany.

Schlüssel, P., and W. J. Emery (1990), Atmospheric water-vapor over oceans from SSM/I measurements, *Int. J. Remote Sens.*, *11*(5), 753–766.

Schneider, U., T. Fuchs, A. Meyer-Christoffer, and B. Rudolf (2008), Global precipitation analysis products of the GPCC, *Internet publication*, Global Precipitation Climatology Centre (GPCC), DWD, `ftp://ftp.dwd.de/pub/data/gpcc/PDF/GPCC_intro_products_2008.pdf`.

Schulz, J., P. Schlüssel, and H. Graßl (1993), Water-vapor in the atmospheric boundary layer over oceans from SSM/I measurements, *Int. J. Remote Sens.*, *14*(15), 2773–2789.

Schulz, J., V. Jost, and S. Bakan (1998), A new satellite-derived freshwater flux climatology (Hamburg Ocean Atmosphere Parameters and Fluxes from Satellite Data), *International WOCE Newsletter*, *32*, 20 and 25–26.

Serreze, M., F. Carse, R. Barry, and J. Rogers (1997), Icelandic low cyclone activity: Climatological features, linkages with the NAG, and relationships with recent changes in the Northern Hemisphere circulation, *J. Climate*, *10*(3), 453–464.

Shapiro, M., and D. Keyser (1990), *Extratropical Cyclones: The Erik Palmen Memorial Volume*, chap. Fronts, jet streams and the tropopause, pp. 167–191, American Meteorological Society.

Shepard, D. (1968), A two-dimensional interpolation function for irregularly-spaced data, in *Proceedings of the 1968 23rd ACM national conference*, pp. 517–524, ACM, New York, NY, USA.

Sickmöller, M., R. Blender, and K. Fraedrich (2000), Observed winter cyclone tracks in the Northern Hemisphere in re-analysed ECMWF data, *Quart. J. Roy. Meteor. Soc.*, *126*, 591–620.

Simmons, A., S. Uppala, D. Dee, and S. Kobayashi (2007), ERA–Interim: New ECMWF reanalysis products from 1989 onwards, *ECMWF Newsletter*, *110*, 25–35.

Simpson, R. (1974), The hurricane disaster potential scale, *Weatherwise*, *27*(169), 323–333.

Slutz, R., S. Lubker, J. Hiscox, S. Woodruff, R. Jenne, D. Joseph, P. Steurer, and J. Elms (1985), *Comprehensive Ocean-Atmosphere Data Set; Release 1*, NOAA Environmental Research Laboratories, Climate Research Program, Boulder, Colo., (NTIS PB86-105723).

Stenchikov, G., A. Robock, V. Ramaswamy, M. D. Schwarzkopf, K. Hamilton, and S. Ramachandran (2002), Arctic Oscillation response to the 1991 Mount Pinatubo eruption: Effects of volcanic aerosols and ozone depletion, *J. Geophys. Res.*, *107*(D24), 4803.

Swift, C. T., L. S. Fedor, and R. O. Ramseier (1985), An algorithm to measure sea ice concentration with microwave radiometers, *J. Geophys. Res.-Oceans*, *90*, 1087–1099.

Thompson, D. W. J., and J. M. Wallace (1998), The Arctic Oscillation signature in the wintertime geopotential height and temperature fields, *Geophys. Res. Lett.*, *25*(9), 1297–1300.

Thorncroft, C., and S. C. Jones (2000), The extratropical transitions of hurricanes Felix and Iris in 1995, *Mon. Wea. Rev.*, *128*(4), 947–972.

Trenberth, K. E. (1984), Signal versus noise in the Southern Oscillation, *Mon. Wea. Rev.*, *112*(2), 326–332.

Trenberth, K. E., and D. P. Stepaniak (2004), The flow of energy through the Earth's climate system, *Quart. J. Roy. Meteor. Soc.*, *130*(603), 2677–2701, Symons Lecture 2004.

Trigo, R., T. Osborn, and J. Corte-Real (2002), The North Atlantic Oscillation influence on Europe: climate impacts and associated physical mechanisms, *Climate Res.*, *20*(1), 9–17.

Uppala, S., P. Kllberg, A. Simmons, U. Andrae, V. da Costa Bechtold, M. Fiorino, J. Gibson, J. Haseler, A. Hernandez, G. Kelly, X. Li, K. Onogi, S. Saarinen, N. Sokka, R. Allan, E. Andersson, K. Arpe, M. Balmaseda, A. Beljaars, L. van de Berg, J. Bidlot, N. Bormann, S. Caires, F. Chevallier, A. Dethof, M. Dragosavac, M. Fisher, M. Fuentes, S. Hagemann, E. Hlm, B. Hoskins, L. Isaksen, P. Janssen, R. Jenne, A. McNally, J.-F. Mahfouf, J.-J. Morcrette, N. Rayner, R. Saunders, P. Simon, A. Sterl, K. Trenberth, A. Untch, D. Vasiljevic, P. Viterbo, and J. Woollen (2005), The ERA-40 re-analysis., *Quart. J. Roy. Meteor. Soc.*, *131*(612), 2961–3012.

Uvo, C. (2003), Analysis and regionalization of northern European winter precipitation based on its relationship with the North Atlantic Oscillation, *Int. J. Climatol.*, *23*(10), 1185–1194.

van Loon, H., and J. Rogers (1978), The seesaw in winter temperatures between Greenland and Northern Europe. Part I: General description, *Mon. Wea. Rev.*, *106*(3), 296–310.

Visbeck, M., H. Cullen, G. Krahmann, and N. Naik (1998), An ocean model's response to North Atlantic Oscillation-like wind forcing, *Geophys. Res. Lett.*, *25*(24), 4521–4524.

Walker, G. (1923), Correlation in seasonal variations of weather. IX. A further study of world weather., *Mem. Indian Meteorol. Dept.*, *24 (Part 9)*, 275–332.

Walker, G., and E. Bliss (1932), World weather. Part V, *Mem. Roy. Meteor. Soc.*, *4*, 53–84.

Wallace, J. (2000), North Atlantic Oscillation/annular mode: Two paradigms - one phenomenon, *Quart. J. Roy. Meteor. Soc.*, *126*(564), 791–805.

Wallace, J., and D. Thompson (2002), The Pacific center of action of the Northern Hemisphere annular mode: real or artifact?, *J. Climate*, *15*(14), 1987–1991.

Walsh, J., and D. Portis (1999), Variations of precipitation and evaporation over the North Atlantic Ocean, 1958-1997, *J. Geophys. Res.-Atmos.*, *104*, 16,613–16,631.

Wang, D., C. Wang, X. Yang, and J. Lu (2005), Winter Northern Hemisphere surface air temperature variability associated with the Arctic Oscillation and North Atlantic Oscillation, *Geophys. Res. Lett.*, *32*(16), 16,706–16,706.

Wang, Y., and C. Wu (2004), Current understanding of tropical cyclone structure and intensity changes - a review, *Meteor. Atmos. Phys.*, *87*(4), 257–278.

Wanner, H., S. Bronnimann, C. Casty, D. Gyalistras, J. Luterbacher, C. Schmutz, D. Stephenson, and E. Xoplaki (2001), North Atlantic Oscillation - concepts and studies, *Surveys in Geophys.*, *22*(4), 321–382.

Wentz, F. J. (1991), User's manual for SSM/I antenna temperature tapes revision 1, *Technical Report 120191*, Remote Sensing Systems, Santa Rosa, California.

Wentz, F. J. (1992), Production of SSM/I data sets, *Technical Report 90192*, Remote Sensing Systems, Huntsville, Alabama.

Wentz, F. J. (1997), A well-calibrated ocean algorithm for Special Sensor Microwave/Imager, *J. Geophys. Res.-Oceans*, *102*(C4), 8703–8718.

Wentz, F. J., and R. W. Spencer (1998), SSM/I rain retrievals within a unified all-weather ocean algorithm, *J. Atmos. Sci.*, *55*(9), 1613–1627.

Wentz, F. J., L. Ricciardulli, K. Hilburn, and C. Mears (2007), How much more rain will global warming bring?, *Science*, *317*(5835), 233–235.

Wick, G. A., W. J. Emery, L. H. Kantha, and P. Schlüssel (1996), The behavior of the bulk – skin sea surface temperature difference under varying wind speed and heat flux, *J. Phys. Oceanogr.*, *26*(10), 1969–1988.

Wick, G. A., J. J. Bates, and D. J. Scott (2002), Satellite and skin-layer effects on the accuracy of sea surface temperature measurements from the GOES satellites, *J. Atmos. Oceanic Technol.*, *19*(11), 1834–1848.

Wilks, D. (2006), *Statistical Methods in the Atmospheric Sciences*, *International Geophysics Series*, vol. 91, second ed., Academic Press LTD.

Willmott, C. J., C. M. Rowe, and W. D. Philpot (1985), Small-scale climate maps: A sensitivity analysis of some common assumptions associated with grid-point interpolation and contouring, *Cartography and Geographic Information Science*, *12*(1), 5–16.

Winterfeldt, J., A. Andersson, C. P. Klepp, S. Bakan, and R. Weisse (2009), Comparison of HOAPS, QuikSCAT and buoy wind speed in the eastern North Atlantic and the North Sea, submitted to IEEE Trans. Geosci. Remote Sens.

Xie, P., and P. Arkin (1997), Global precipitation: A 17-year monthly analysis based on gauge observations, satellite estimates, and numerical model outputs, *Bull. Amer. Meteor. Soc.*, *78*(11), 2539–2558.

Yu, L. S., and R. A. Weller (2007), Objectively analyzed air-sea heat fluxes for the global ice-free oceans (1981-2005), *Bull. Amer. Meteor. Soc.*, *88*(4), 527–539.

Yu, L. S., X. Jin, and R. A. Weller (2008), Multidecade global flux datasets from the objectively analyzed air-sea fluxes (OAFlux) project: Latent and sensible heat fluxes, ocean evaporation, and related surface meteorological variables, *Technical Report. OA-2008-01*, Woods Hole Oceanographic Institution, OAFlux Project, Woods Hole. MA.

Zahn, M., H. von Storch, and S. Bakan (2008), Climate mode simulation of North Atlantic polar lows in a limited area model, *Tellus A*, *60*(4), 620–631.

A

HOAPS Data Processing Chain

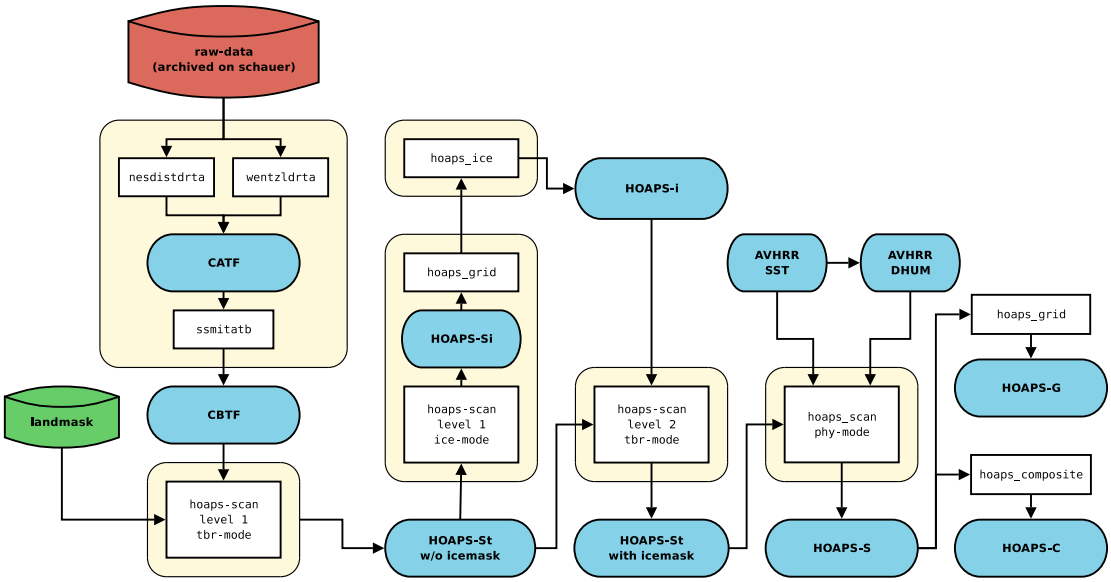

Figure A.1: Flow chart of the HOAPS data processing chain.

B

EOF Patterns of the North Atlantic

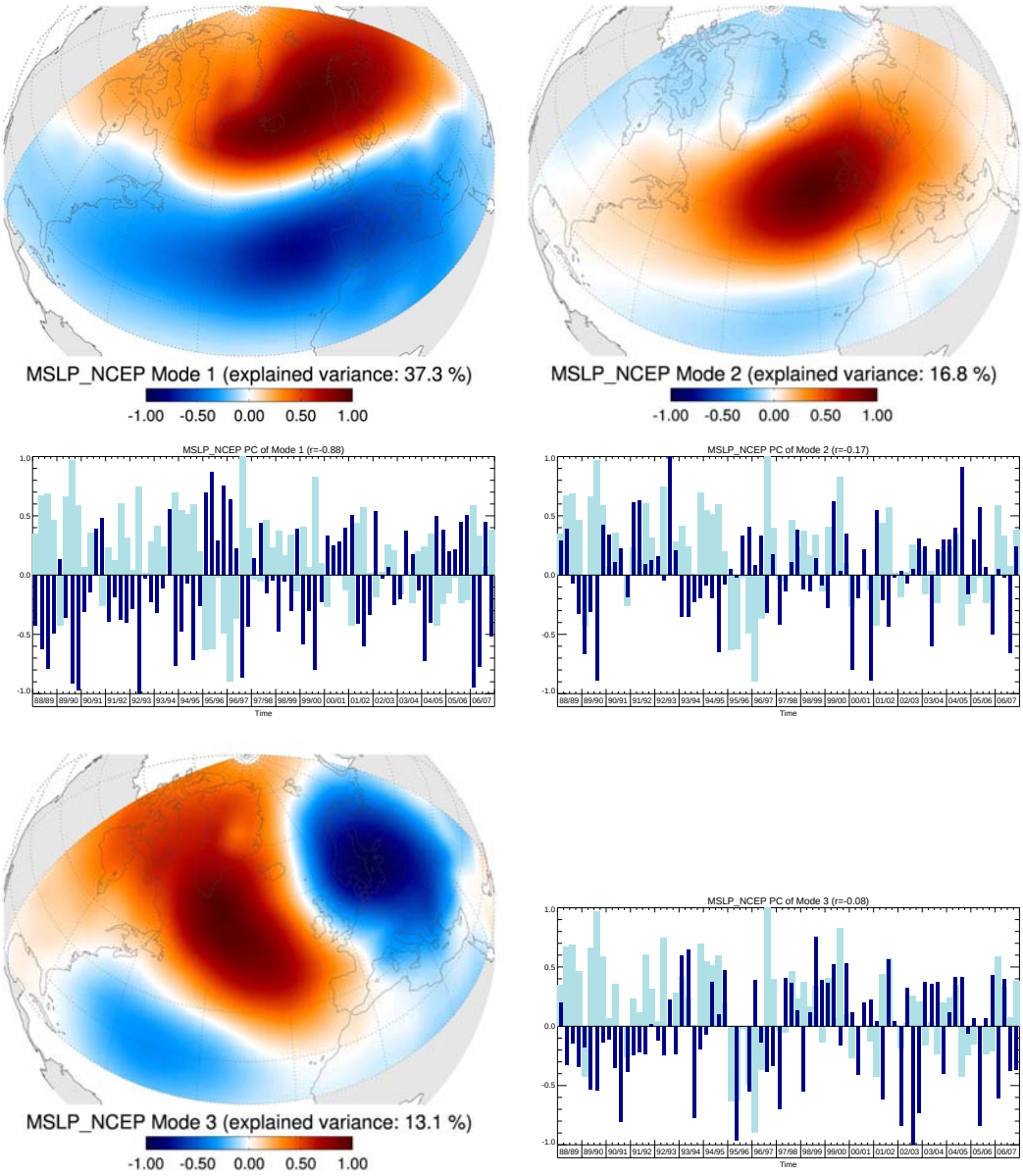

Figure B.1: First three EOF modes of NCEP-R2 mean sea level pressure computed from the winter seasons 1988/89-2006/7. Bar plots show the PCs (dark blue) and the corresponding values of the monthly NAO index (light blue). All data are normalized to unity.

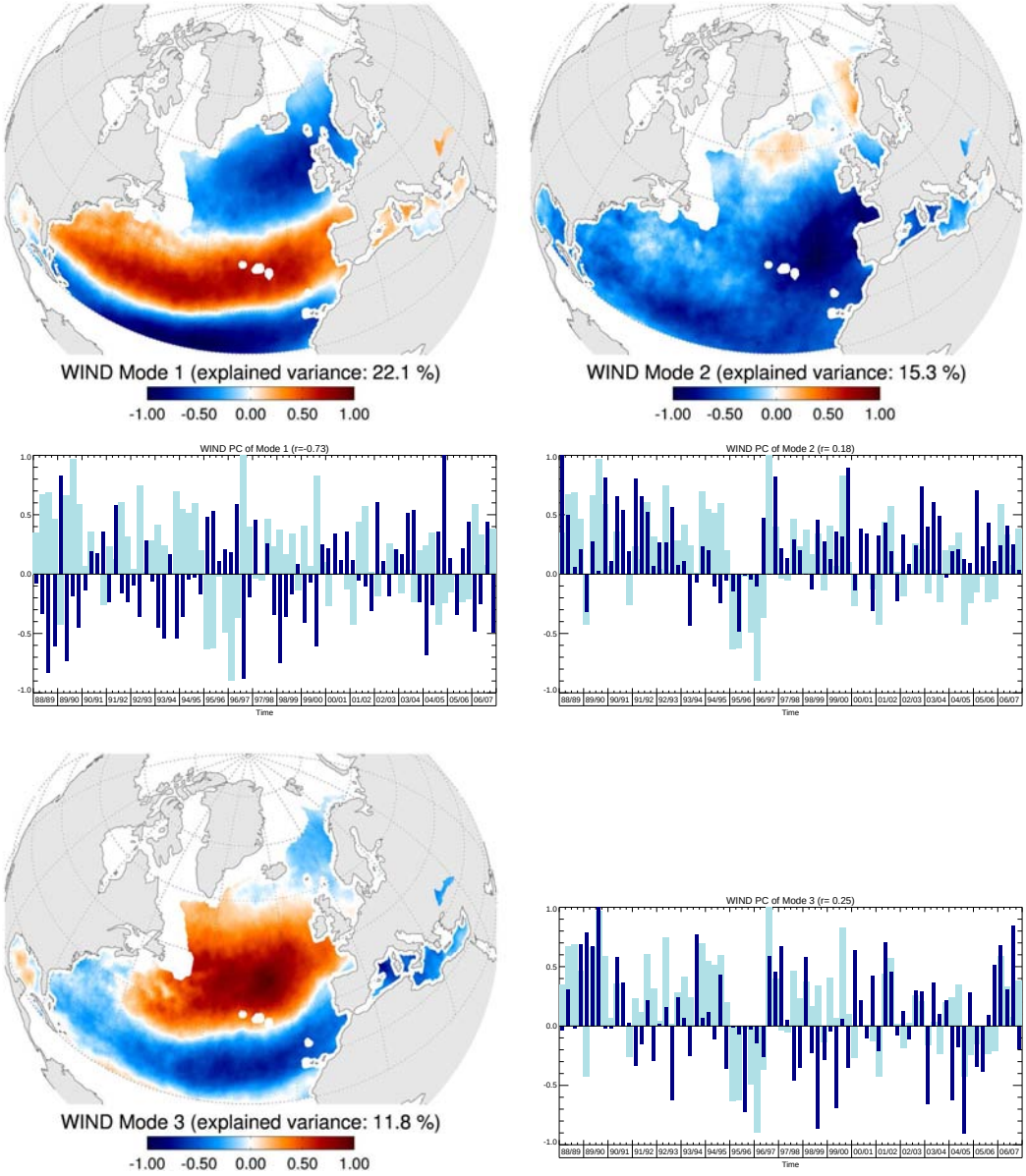

Figure B.2: First three EOF modes of HOAPS-3 windspeed computed from the winter seasons 1988/89-2006/7. Bar plots show the PCs (dark blue) and the corresponding values of the monthly NAO index (light blue). All data are normalized to unity.

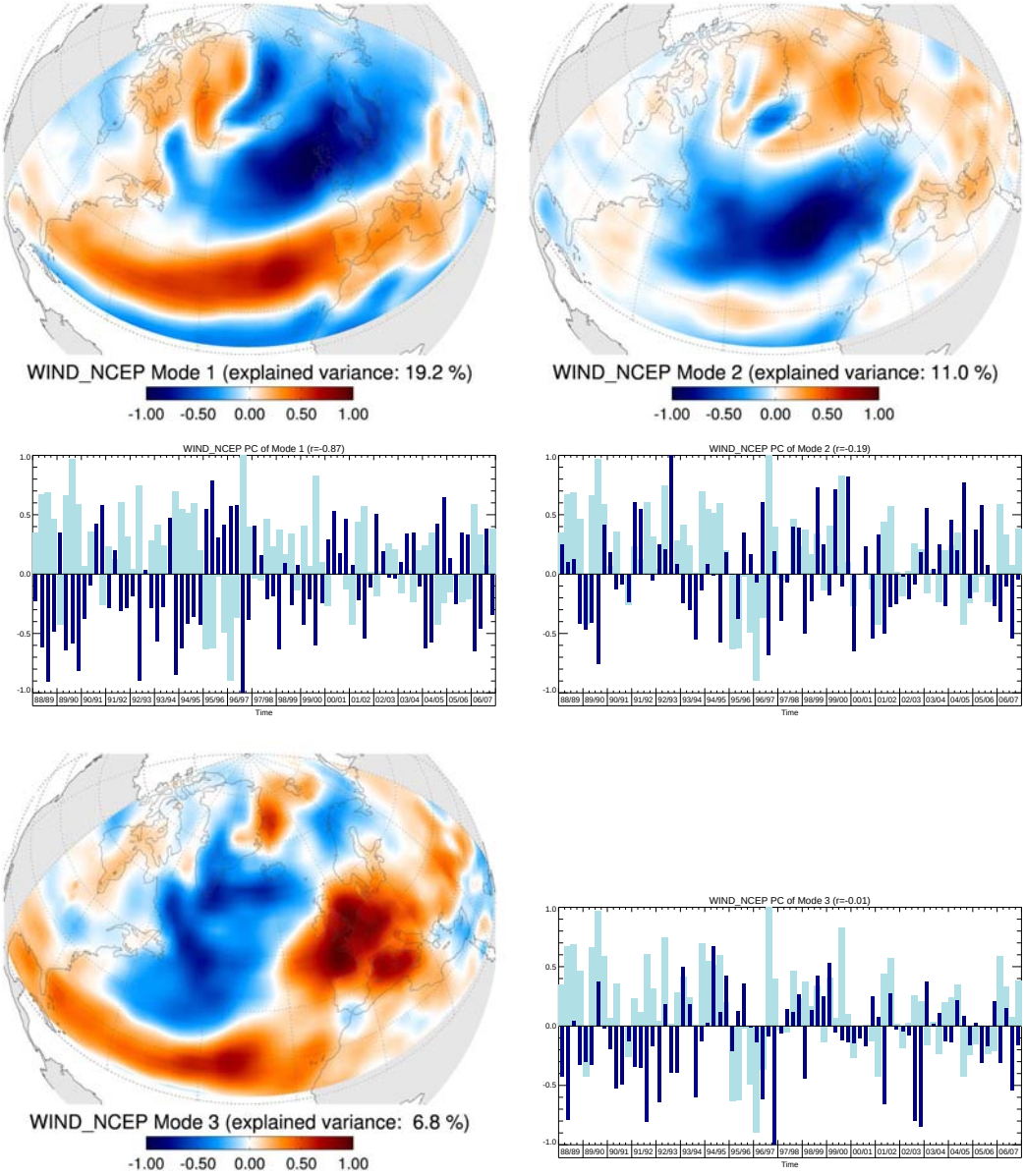

Figure B.3: First three EOF modes of NCEP-R2 windspeed computed from the winter seasons 1988/89-2006/7. Bar plots show the PCs (dark blue) and the corresponding values of the monthly NAO index (light blue). All data are normalized to unity.

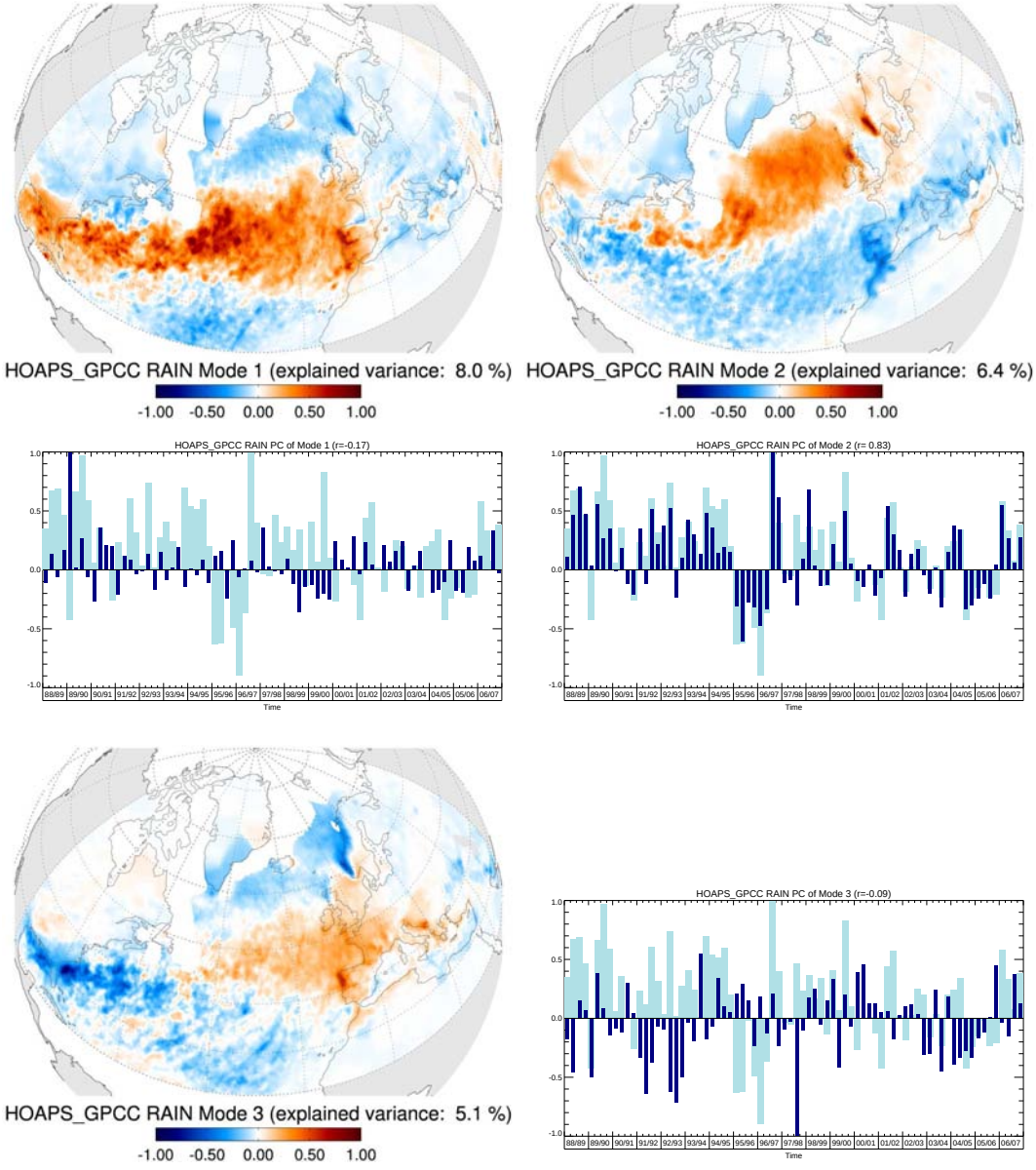

Figure B.4: Same as Fig. 6.12, but with a spatial resolution of 0.5°.

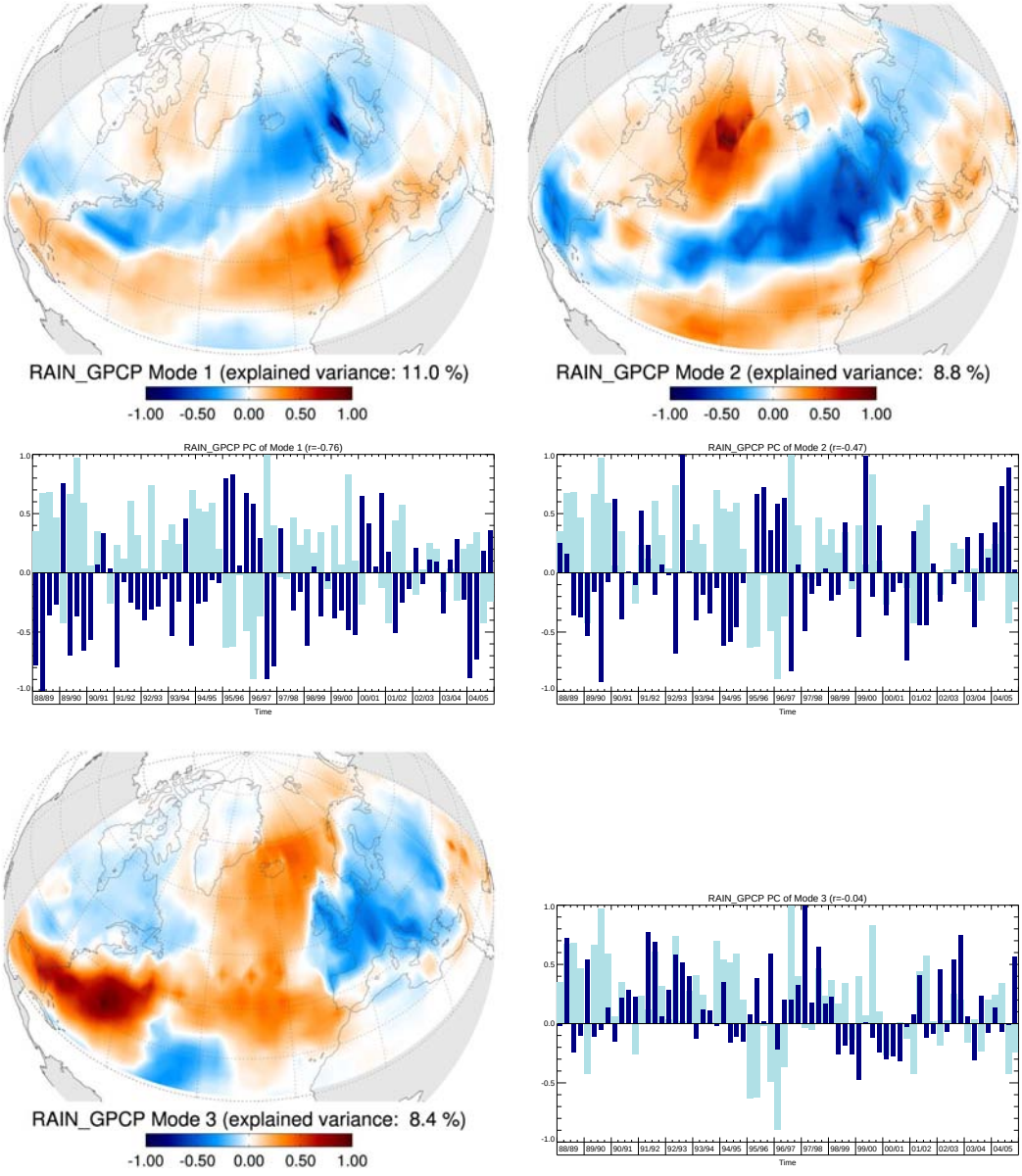

Figure B.5: Same as Fig. 6.12, but for GPCP-V2 precipitation and computed from the winter seasons 1988/89-2004/5.

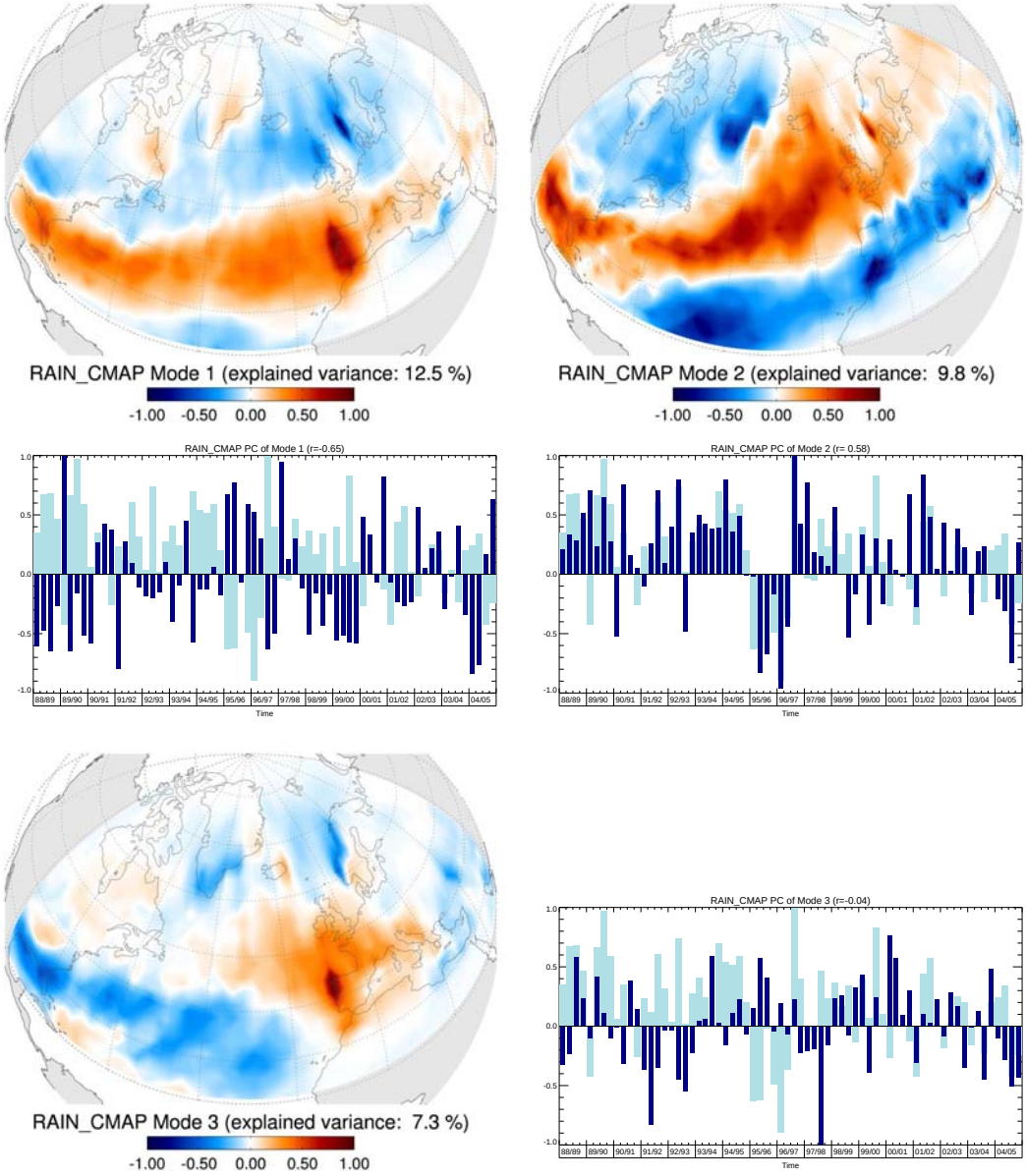

Figure B.6: Same as Fig. 6.12, but for CMAP precipitation and computed from the winter seasons 1988/89-2004/5.

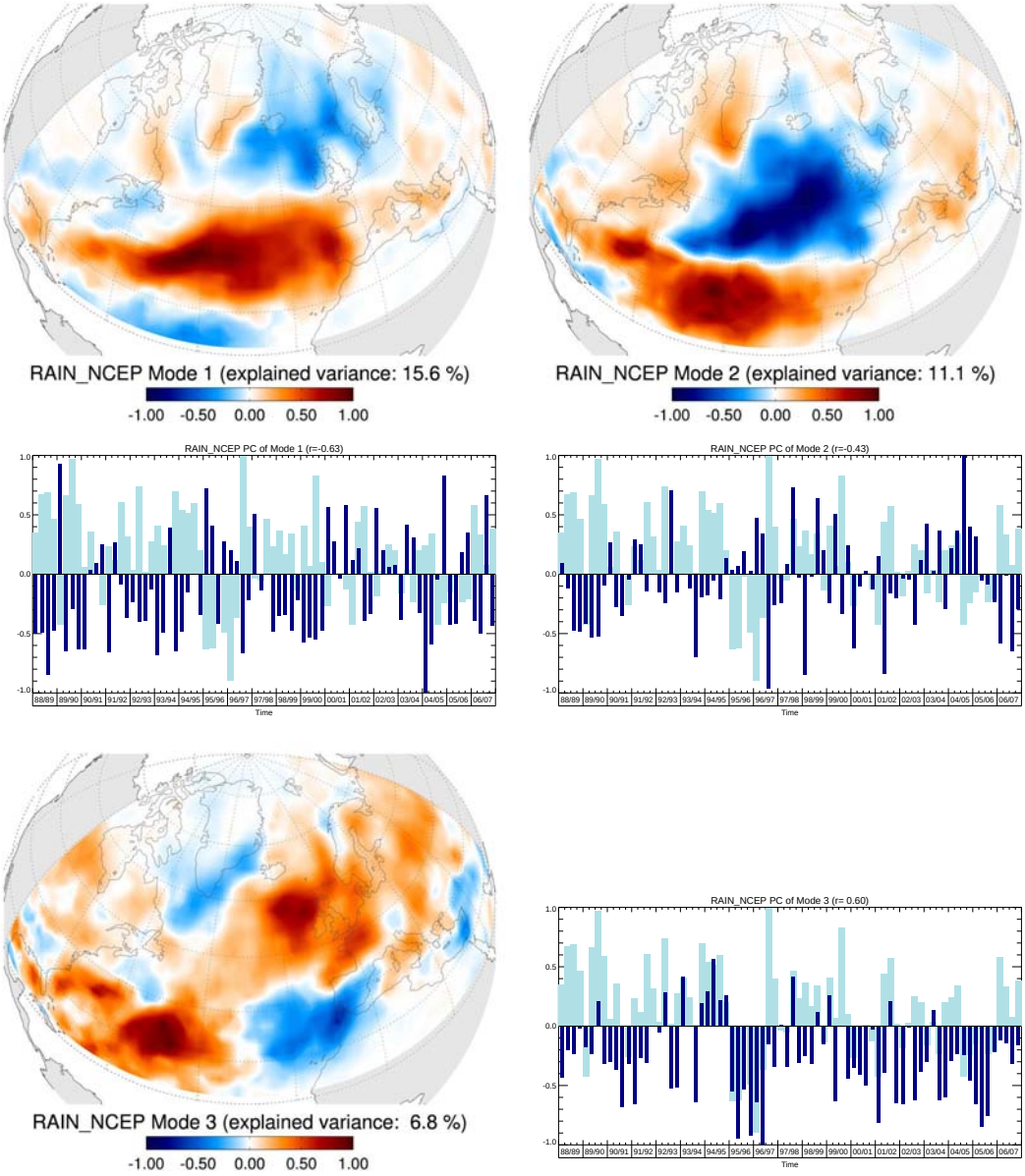

Figure B.7: Same as Fig. 6.12, but for NCEP-R2 precipitation.

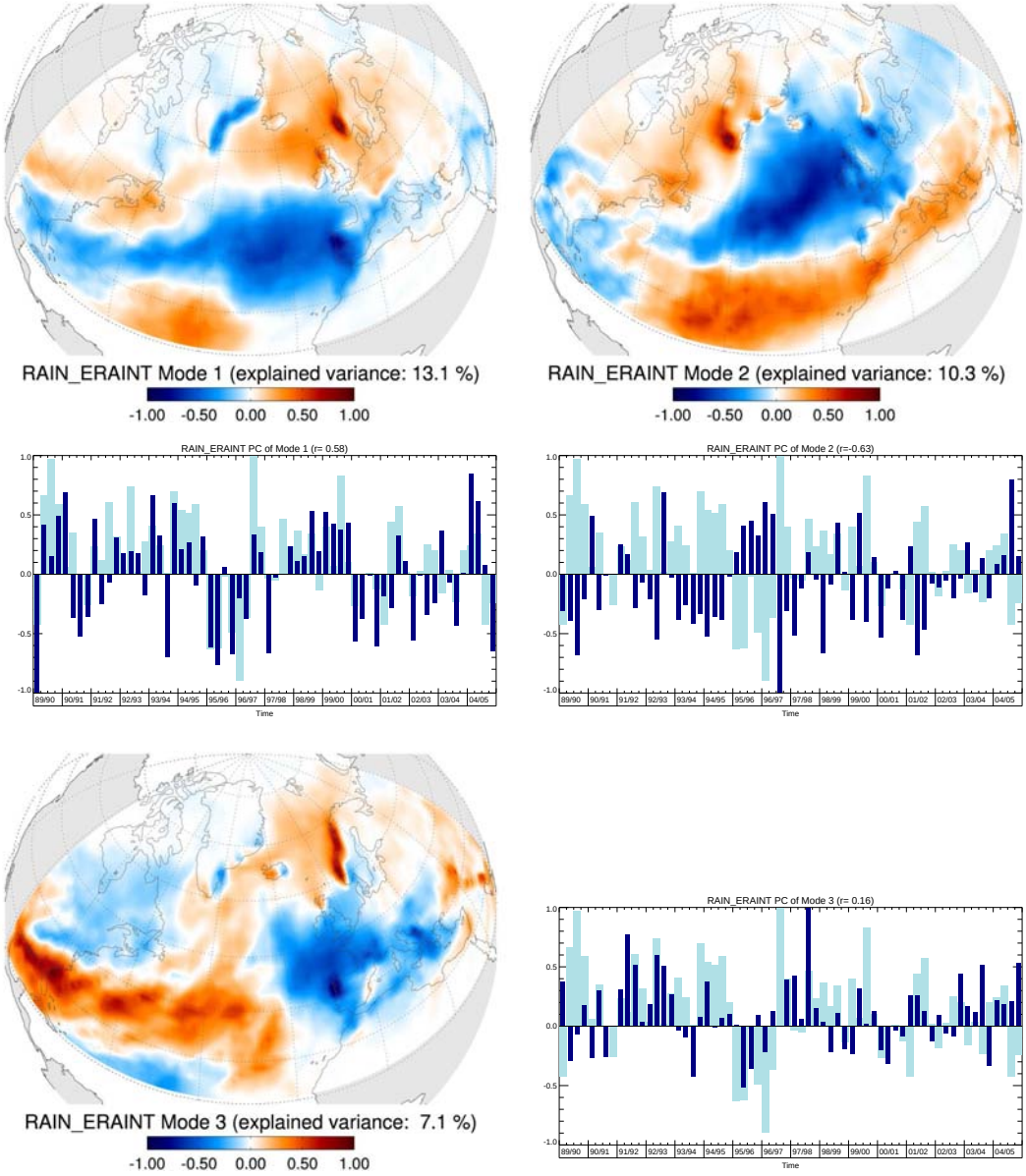

Figure B.8: Same as Fig. 6.12, but for ERA interim precipitation and computed from the winter seasons 1989/90-2004/5.

C

HOAPS-3 Climatological Mean Fields

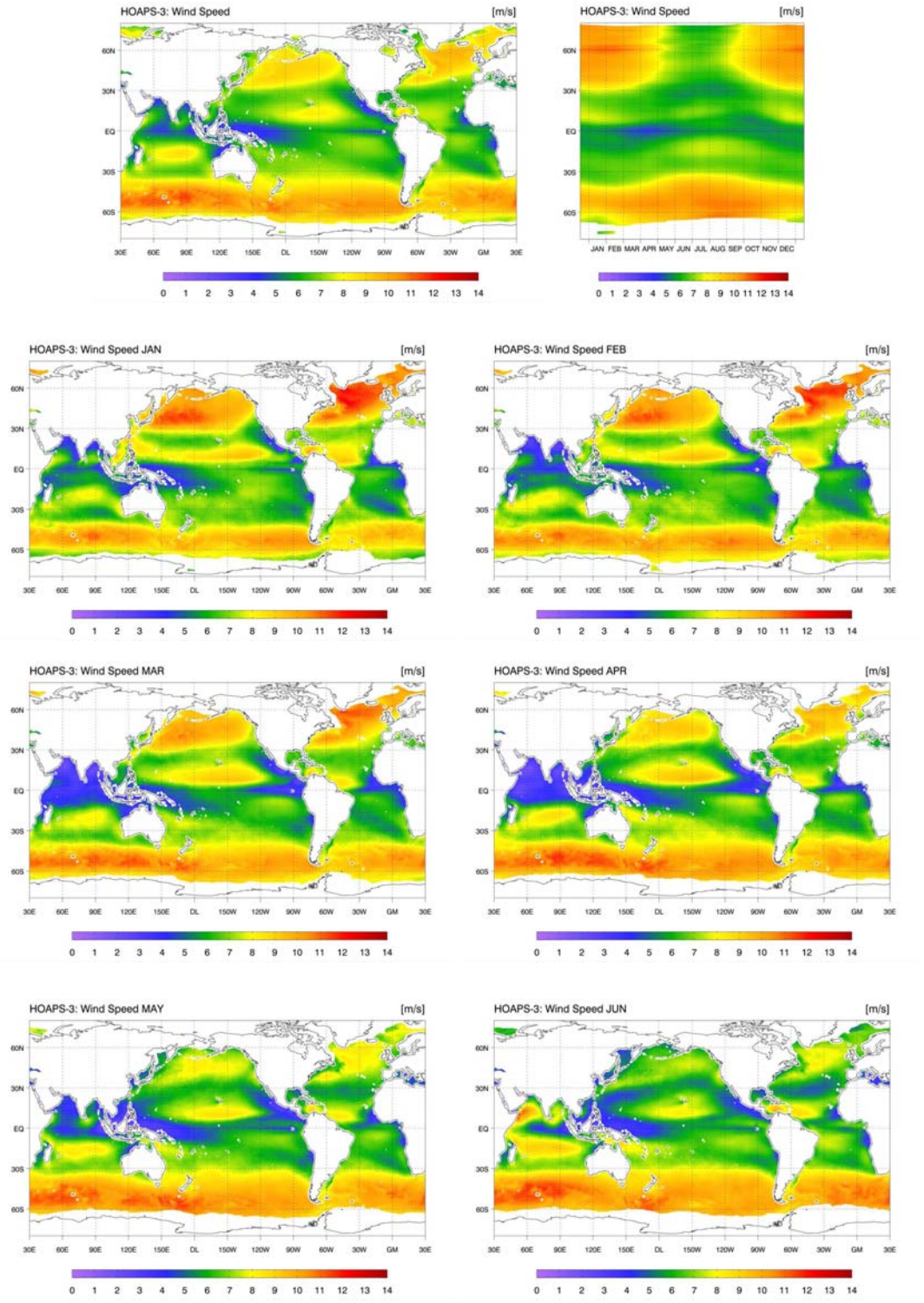

Figure C.1: Climate mean fields of HOAPS-3 wind speed for the years 1988-2005. Upper panel shows the climatological mean (left) and the annual cycle of zonal mean values (right). The lower panels show the climatological monthly mean values for January to June.

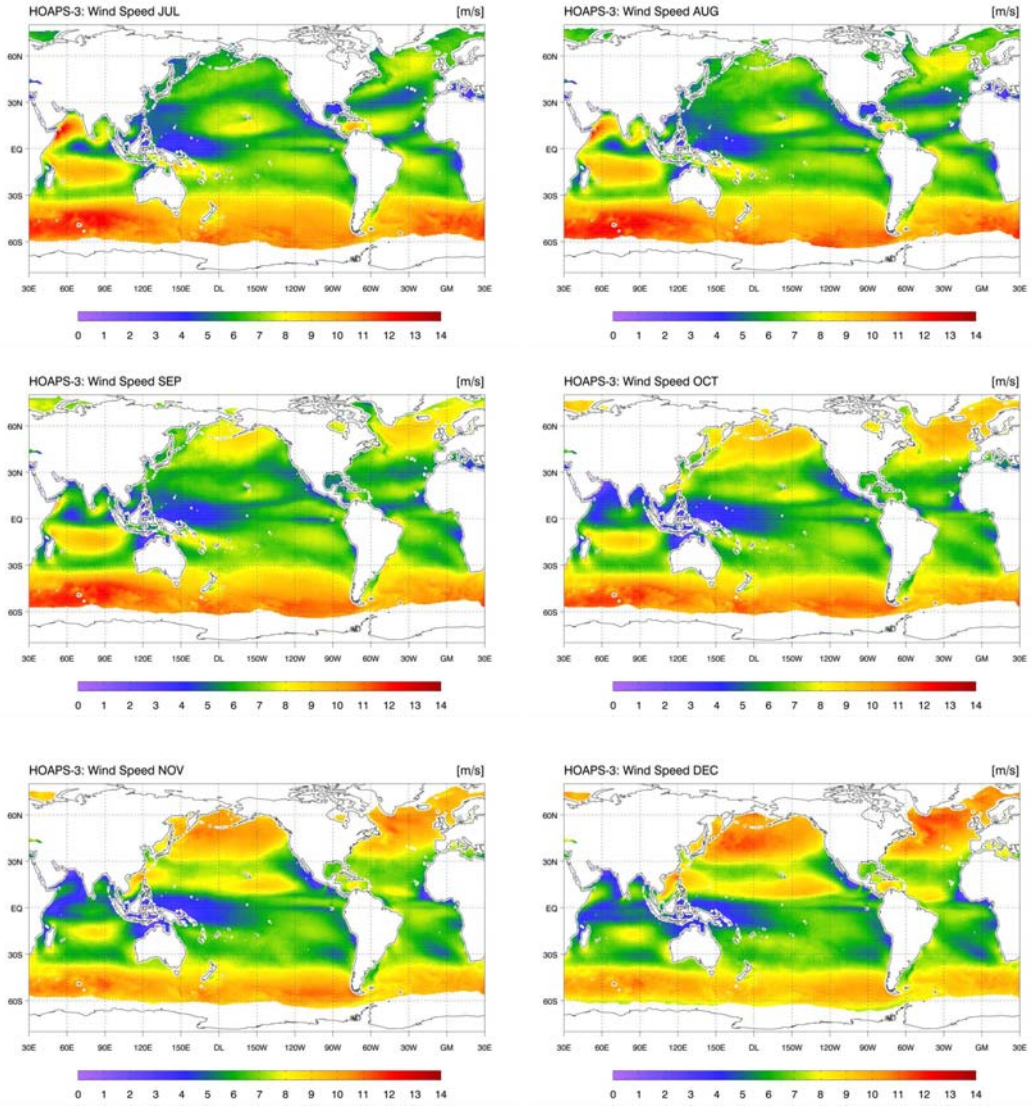

Figure C.2: HOAPS-3 wind speed climatological monthly mean values for July to December.

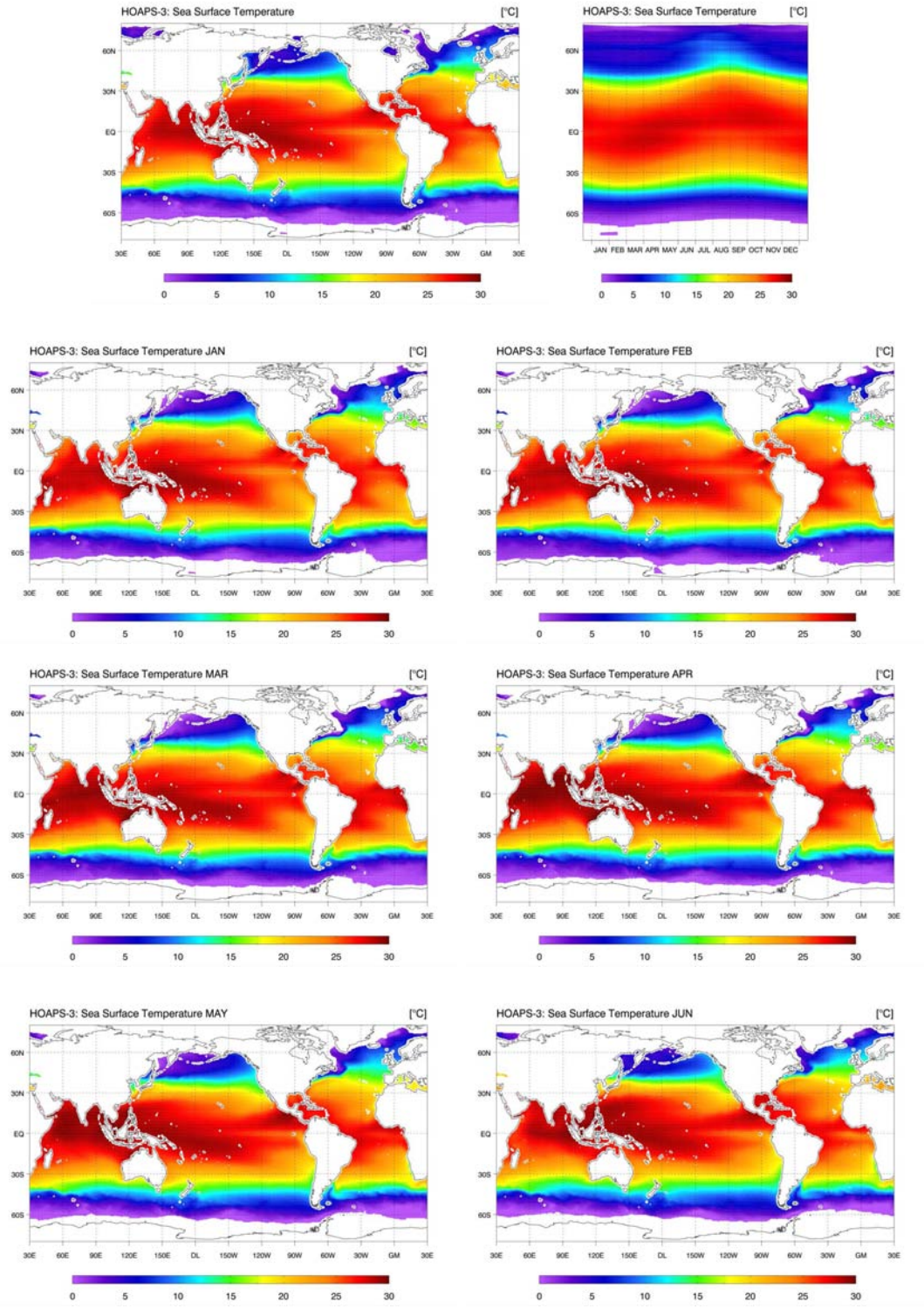

Figure C.3: Climate mean fields of HOAPS-3 sea surface temperature for the years 1988-2005. Upper panel shows the climatological mean (left) and the annual cycle of zonal mean values (right). The lower panels show the climatological monthly mean values for January to June.

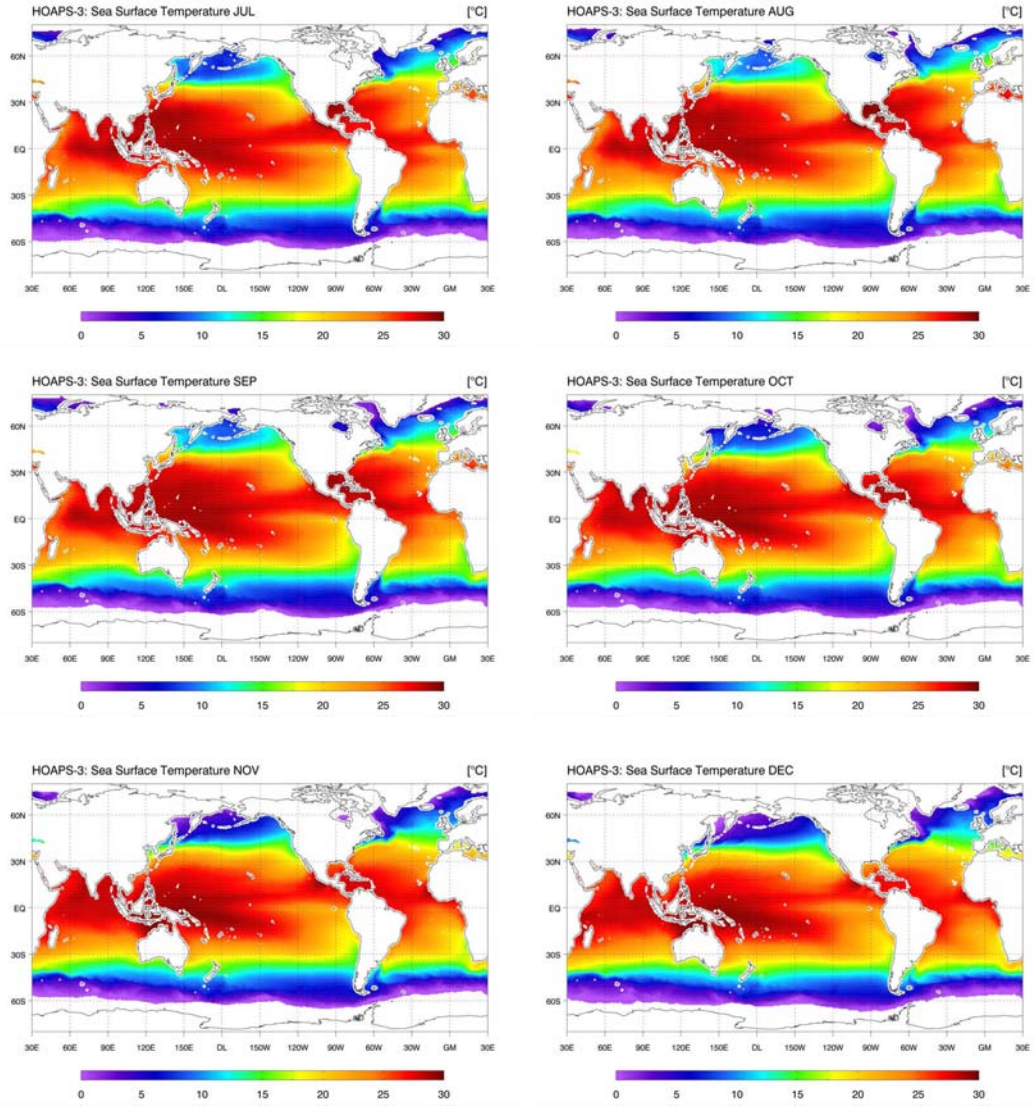

Figure C.4: HOAPS-3 sea surface temperature climatological monthly mean values for July to December.

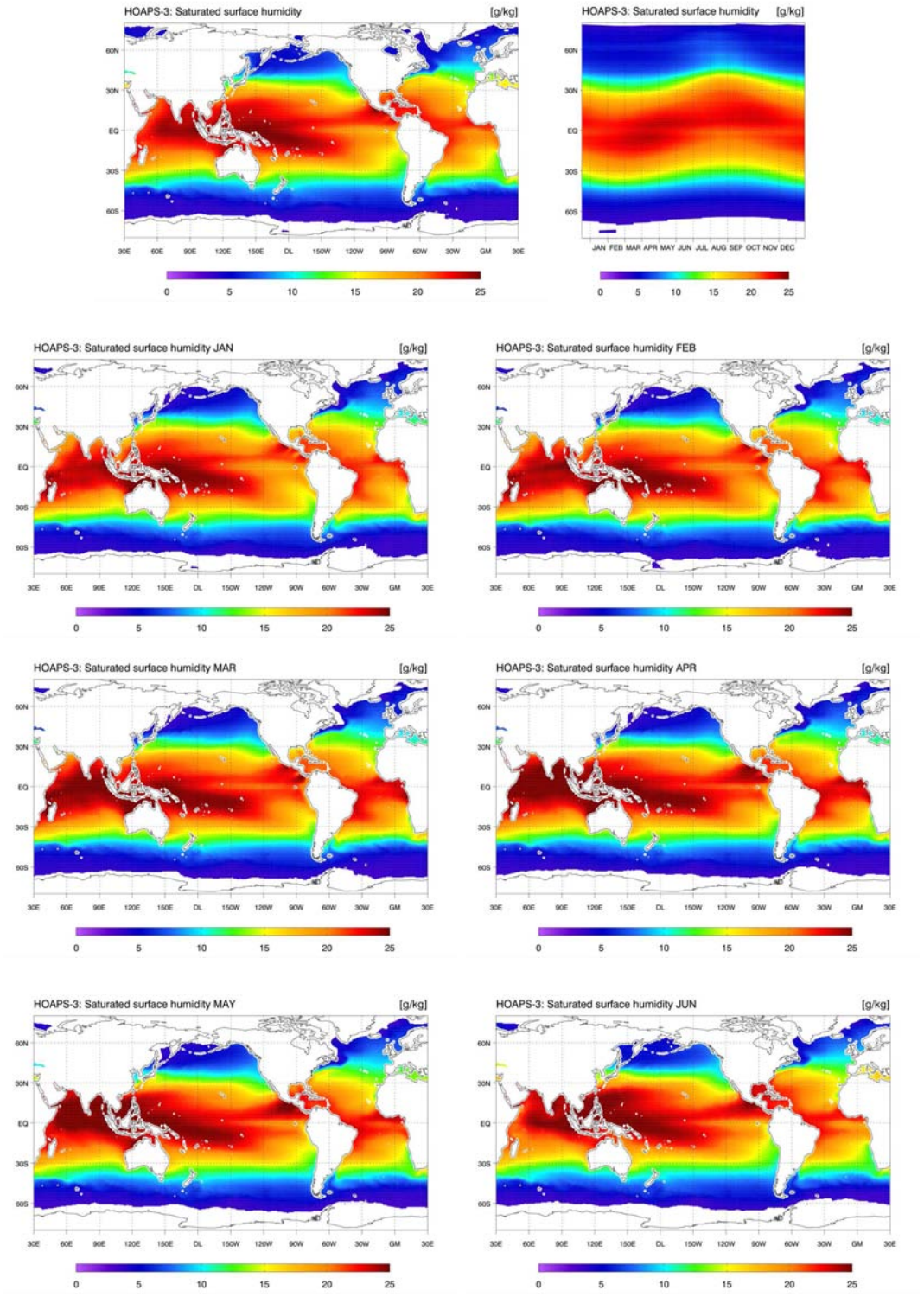

Figure C.5: Climate mean fields of HOAPS-3 sea surface saturated specific humidity for the years 1988-2005. Upper panel shows the climatological mean (left) and the annual cycle of zonal mean values (right). The lower panels show the climatological monthly mean values for January to June.

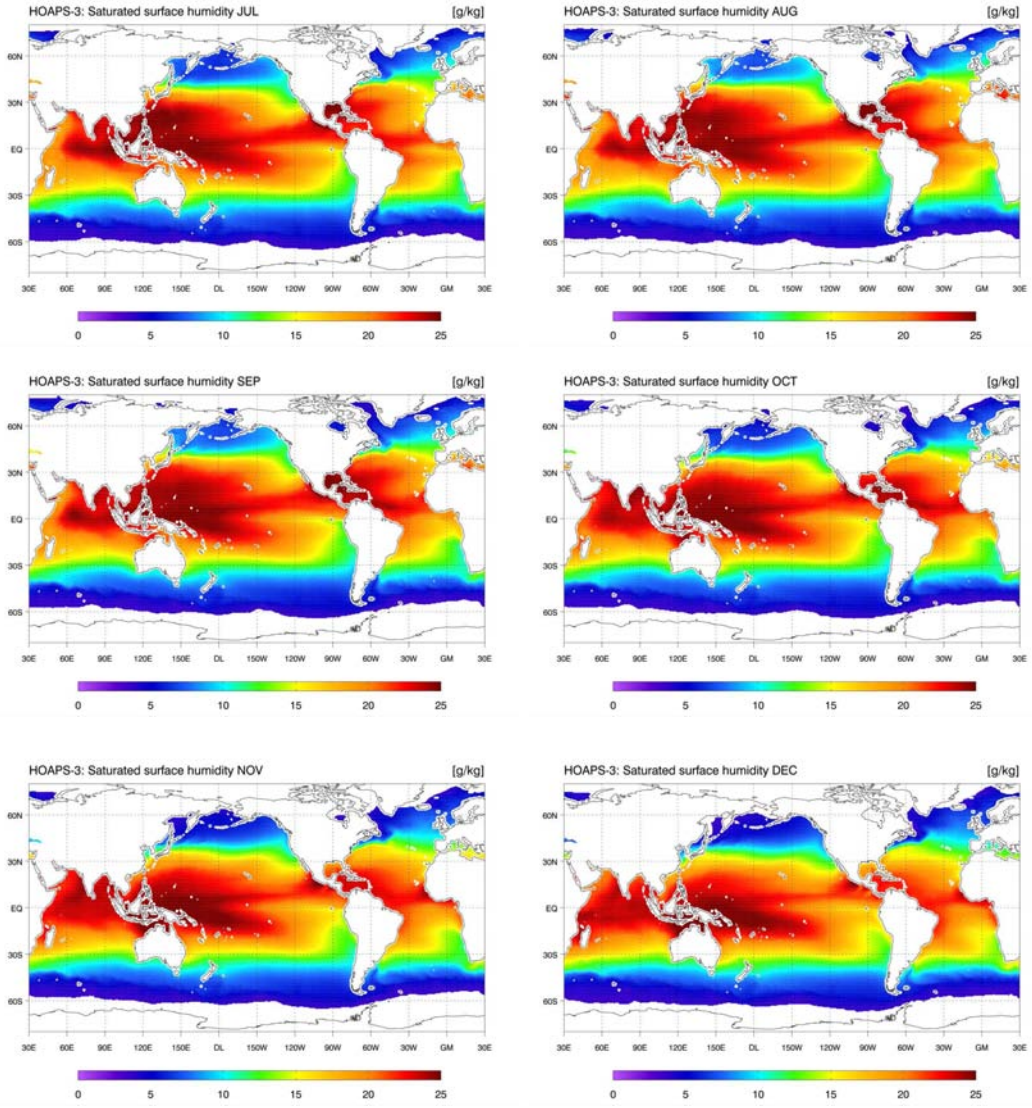

Figure C.6: HOAPS-3 sea surface saturated specific humidity climatological monthly mean values for July to December.

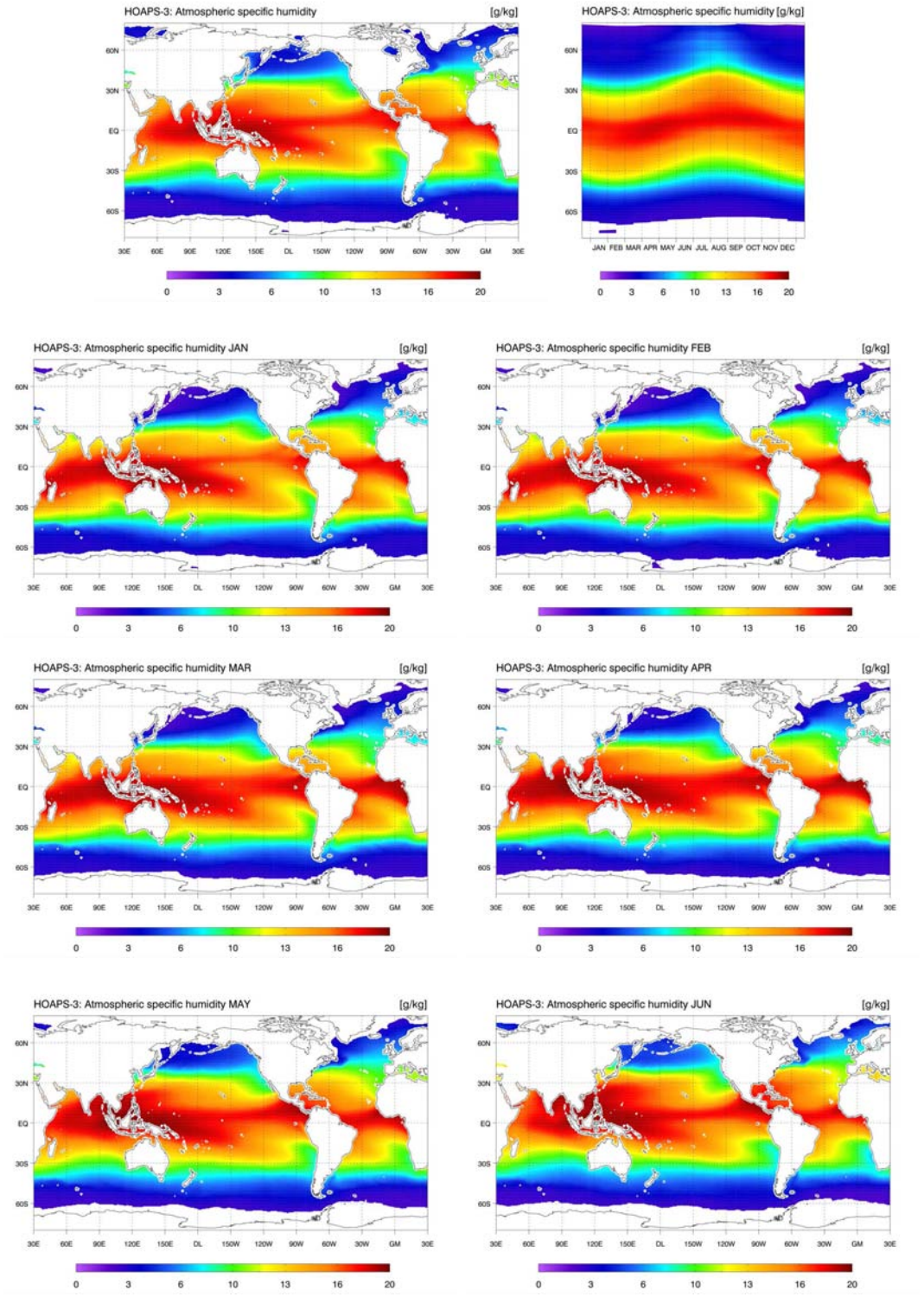

Figure C.7: Climate mean fields of HOAPS-3 atmospheric near surface specific humidity for the years 1988-2005. Upper panel shows the climatological mean (left) and the annual cycle of zonal mean values (right). The lower panels show the climatological monthly mean values for January to June.

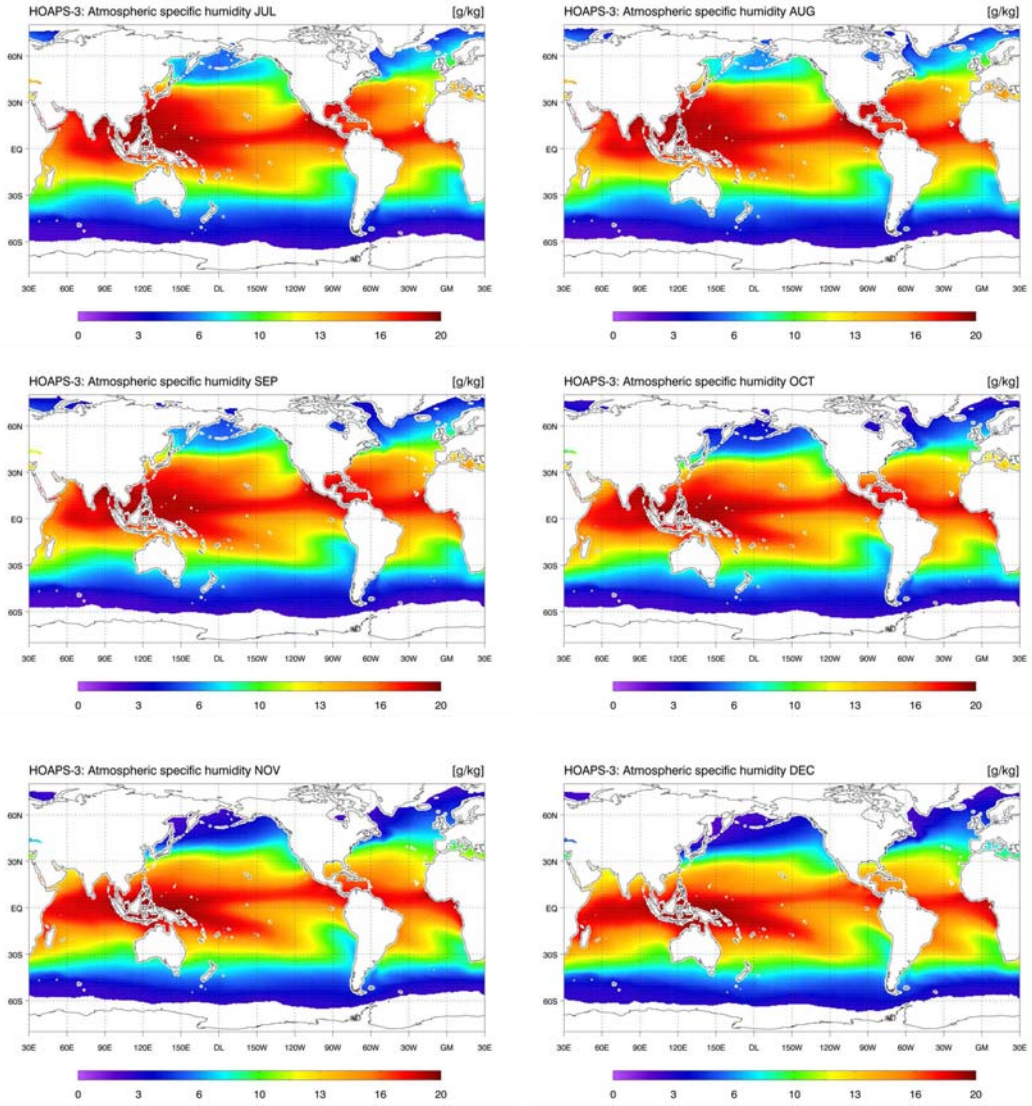

Figure C.8: HOAPS-3 atmospheric near surface specific humidity climatological monthly mean values for July to December.

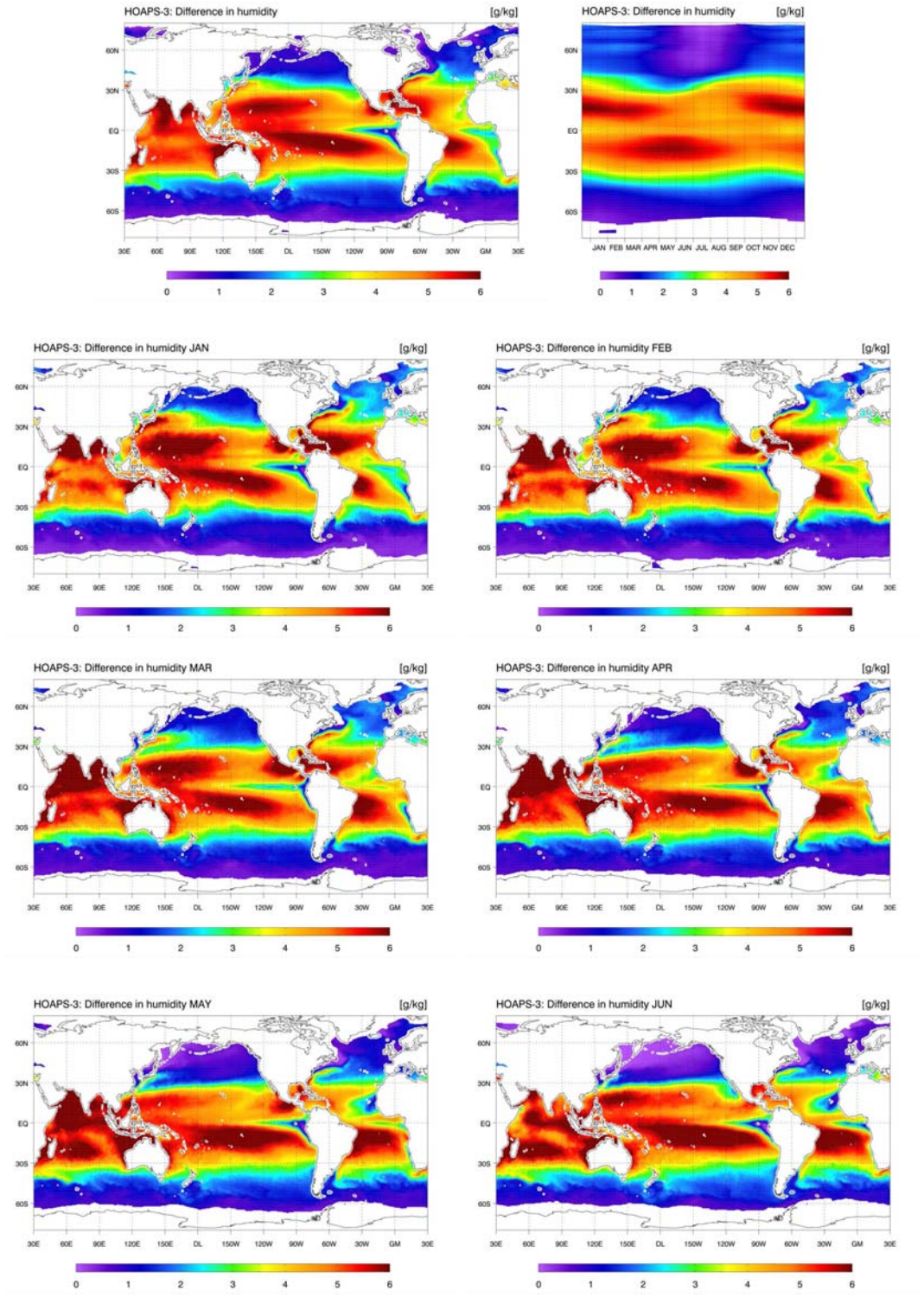

Figure C.9: Climate mean fields of HOAPS-3 difference in humidity for the years 1988-2005. Upper panel shows the climatological mean (left) and the annual cycle of zonal mean values (right). The lower panels show the climatological monthly mean values for January to June.

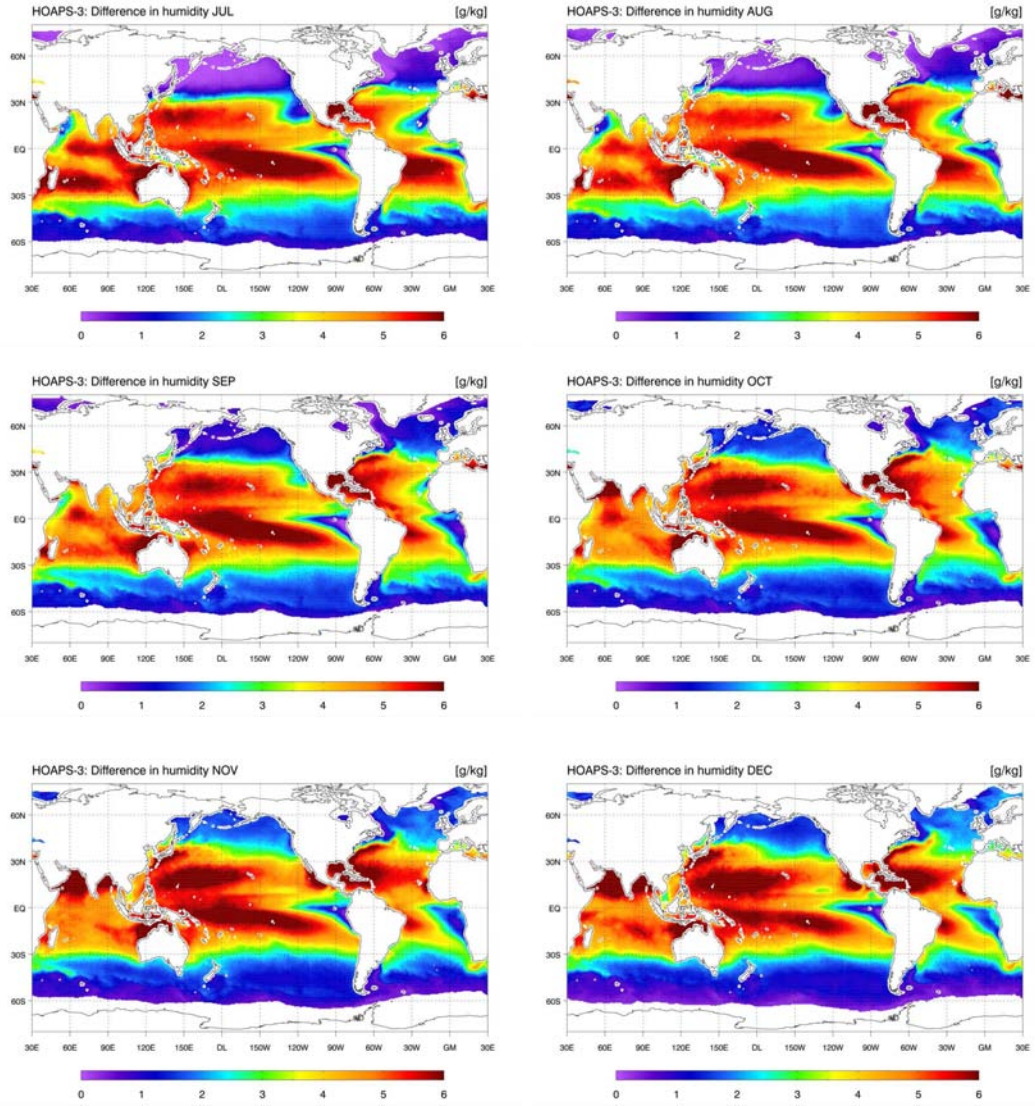

Figure C.10: HOAPS-3 difference in humidity climatological monthly mean values for July to December.

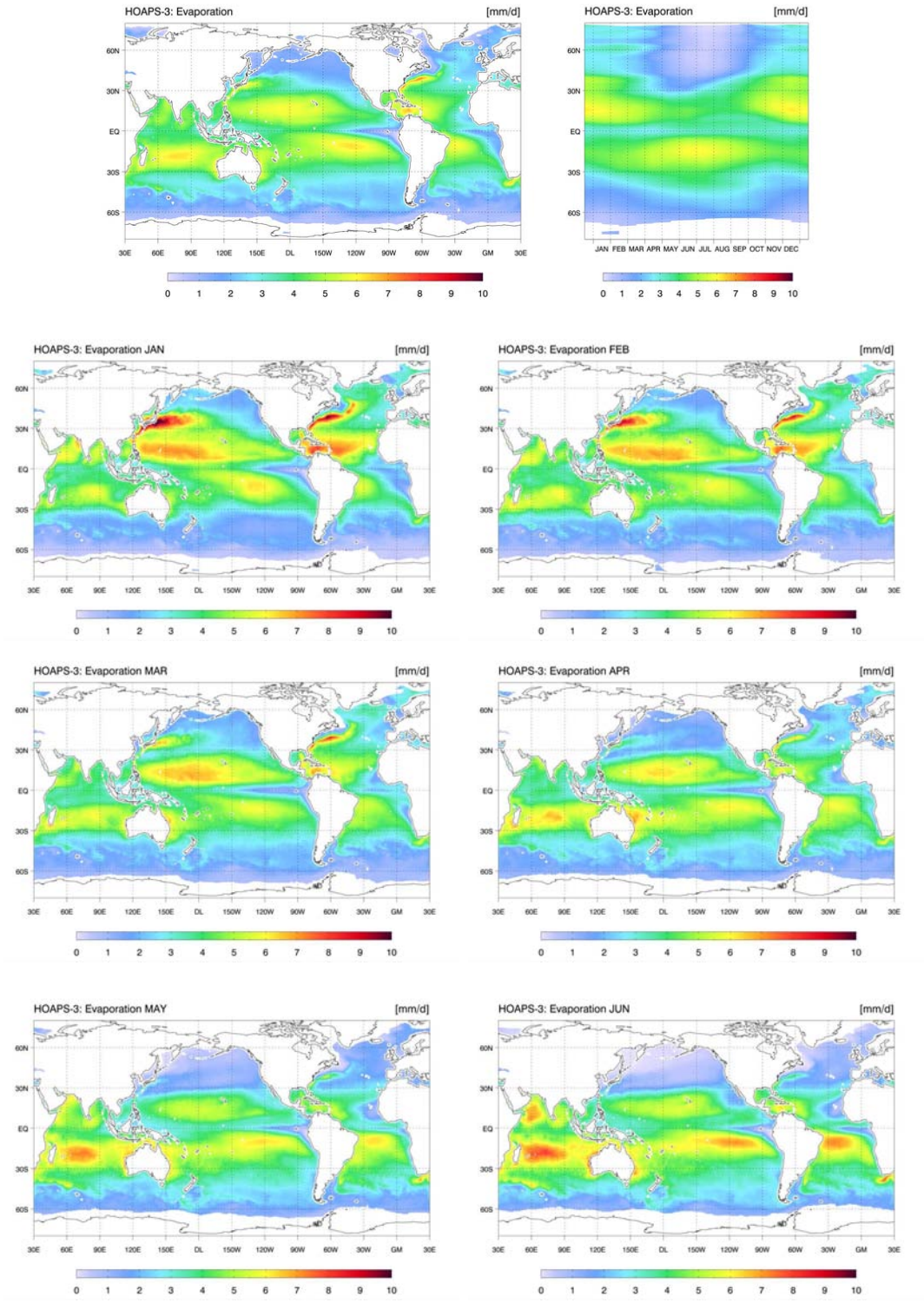

Figure C.11: Climate mean fields of HOAPS-3 evaporation for the years 1988-2005. Upper panel shows the climatological mean (left) and the annual cycle of zonal mean values (right). The lower panels show the climatological monthly mean values for January to June.

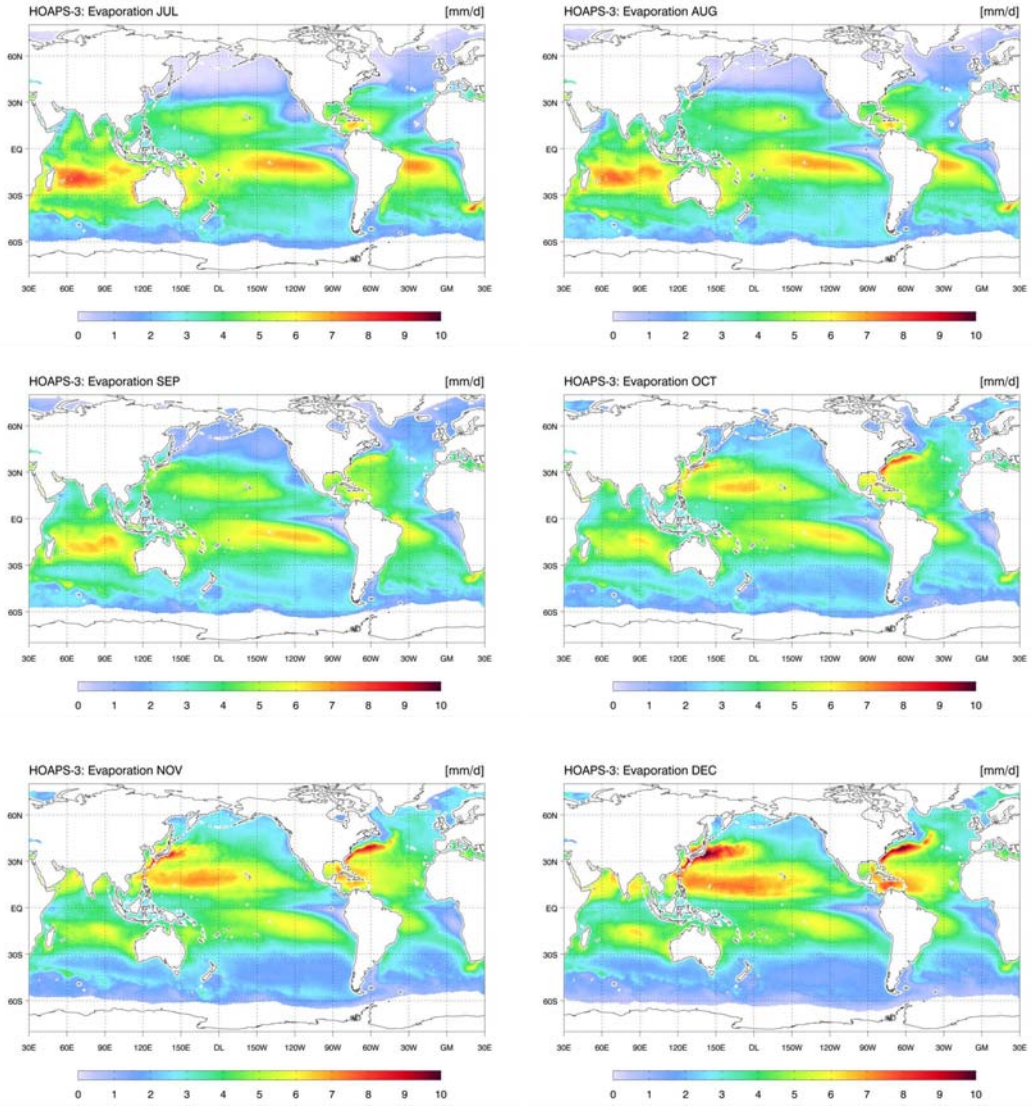

Figure C.12: HOAPS-3 evaporation climatological monthly mean values for July to December.

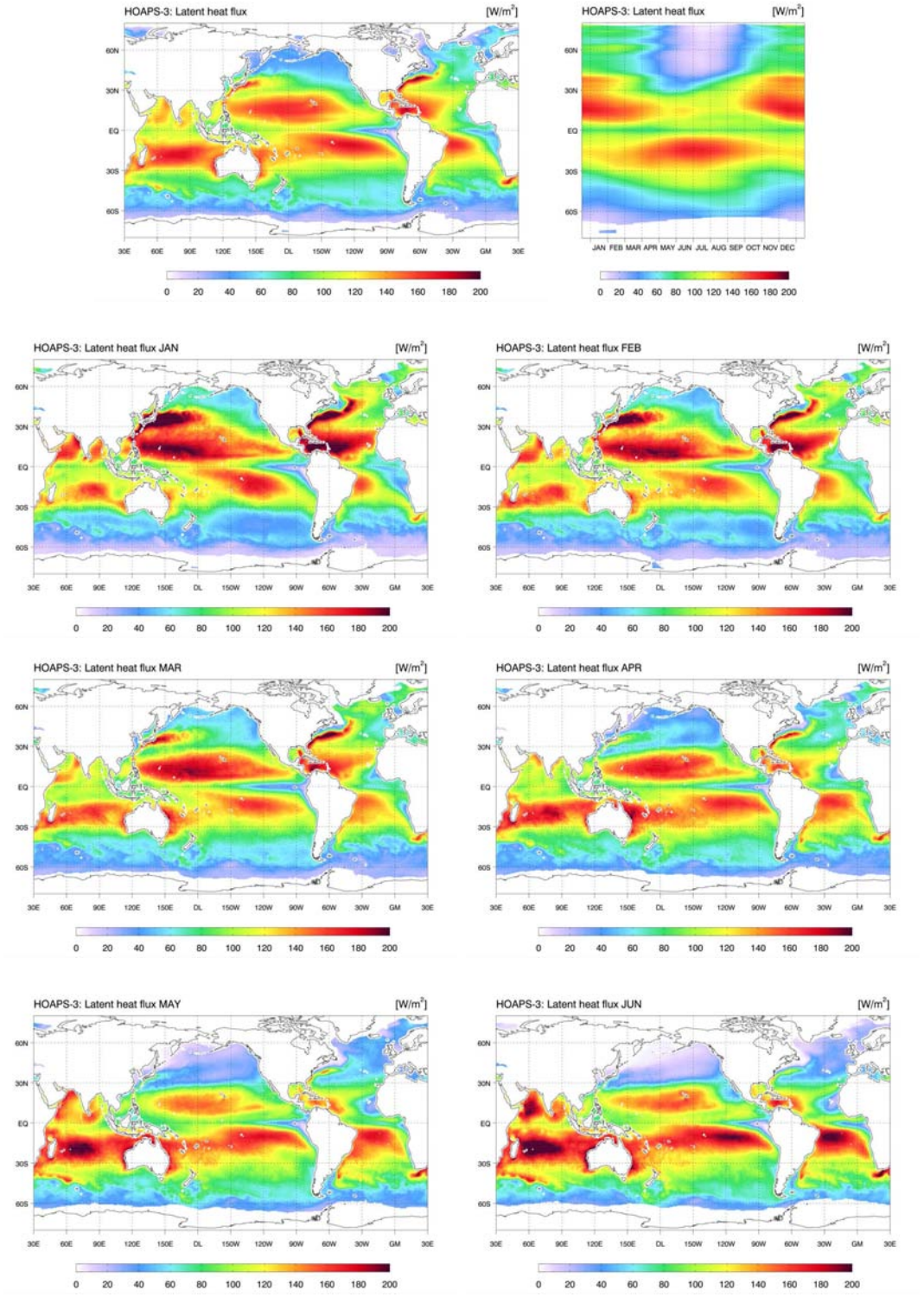

Figure C.13: Climate mean fields of HOAPS-3 latent heat flux at sea surface for the years 1988-2005. Upper panel shows the climatological mean (left) and the annual cycle of zonal mean values (right). The lower panels show the climatological monthly mean values for January to June.

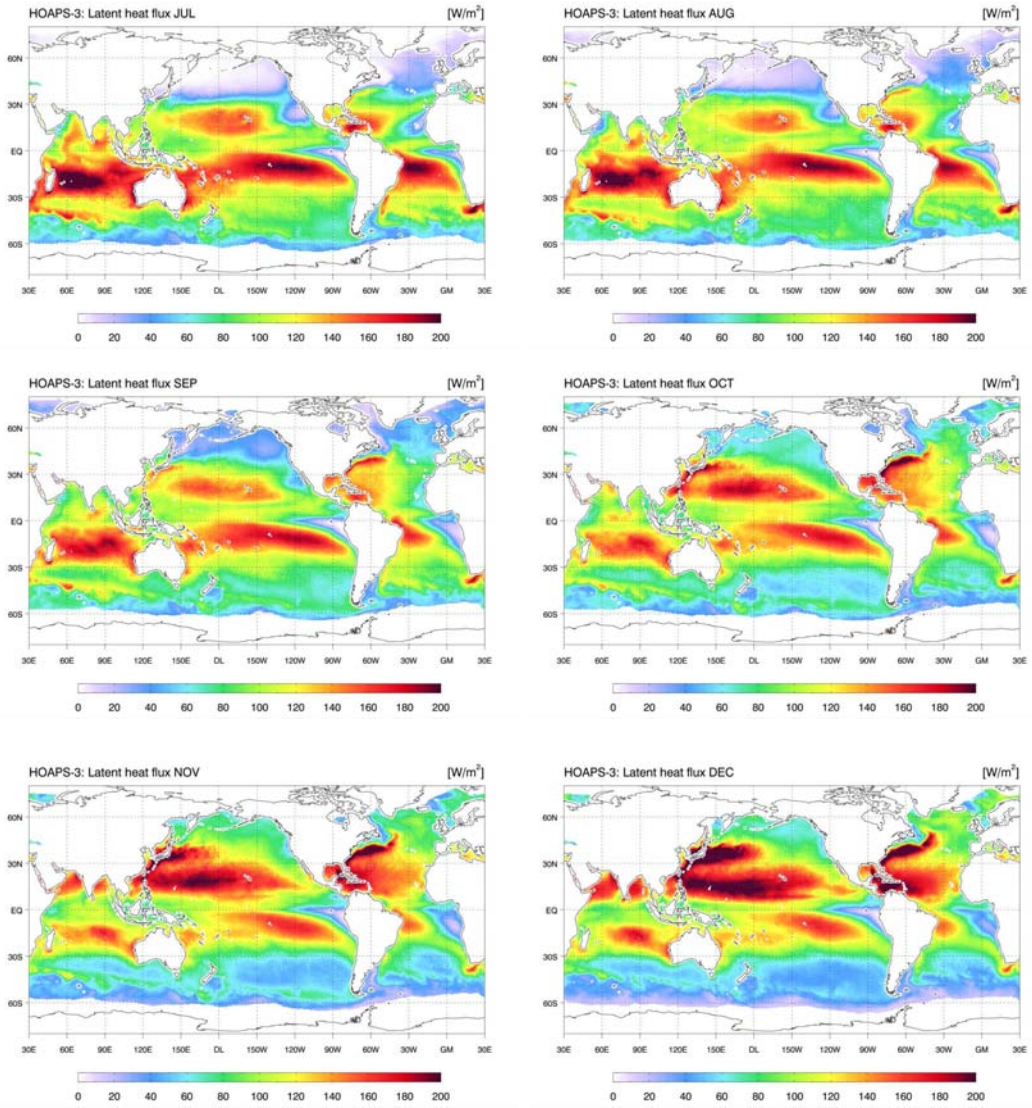

Figure C.14: HOAPS-3 latent heat flux at sea surface climatological monthly mean values for July to December.

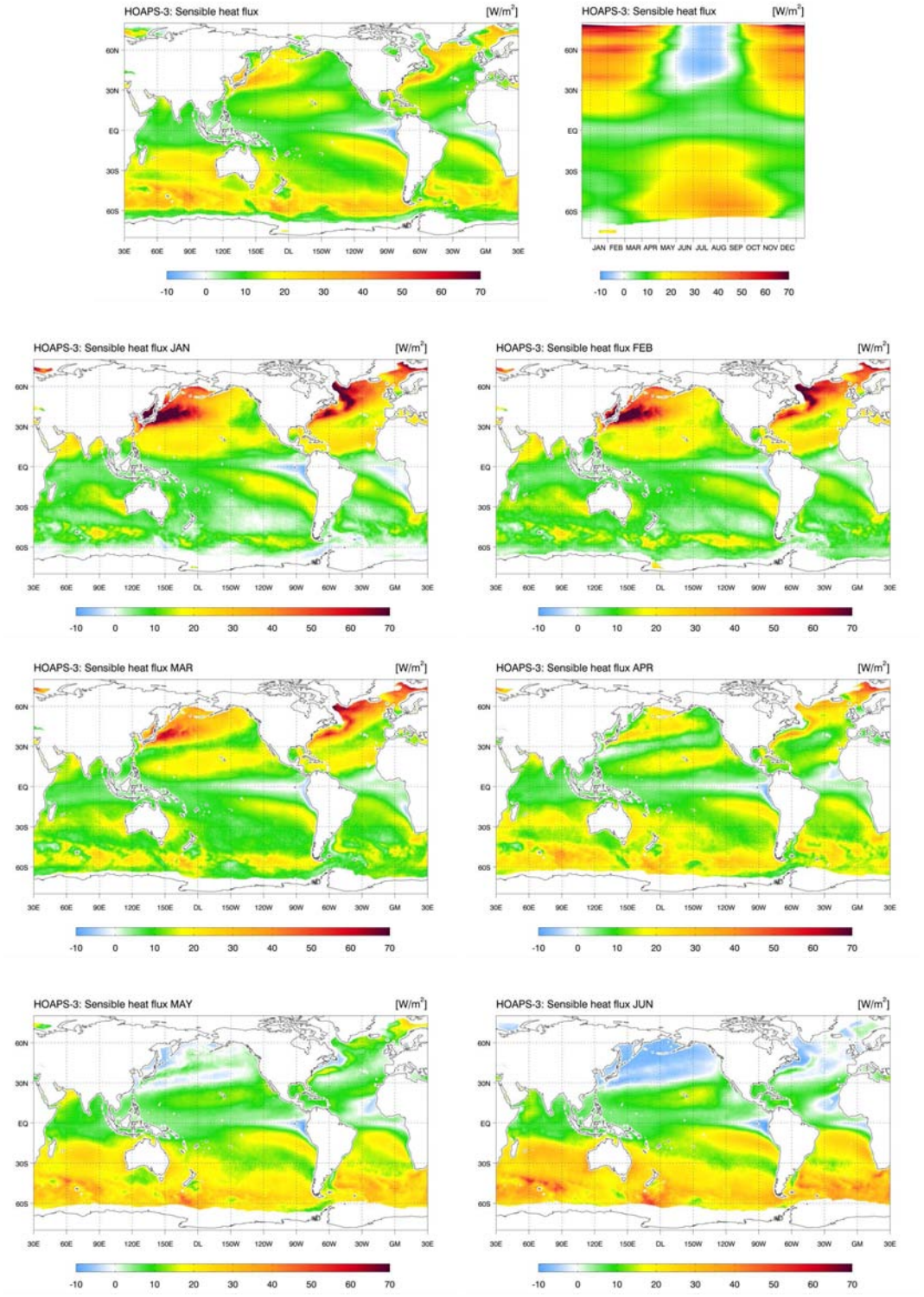

Figure C.15: Climate mean fields of HOAPS-3 sensible heat flux at sea surface for the years 1988-2005. Upper panel shows the climatological mean (left) and the annual cycle of zonal mean values (right). The lower panels show the climatological monthly mean values for January to June.

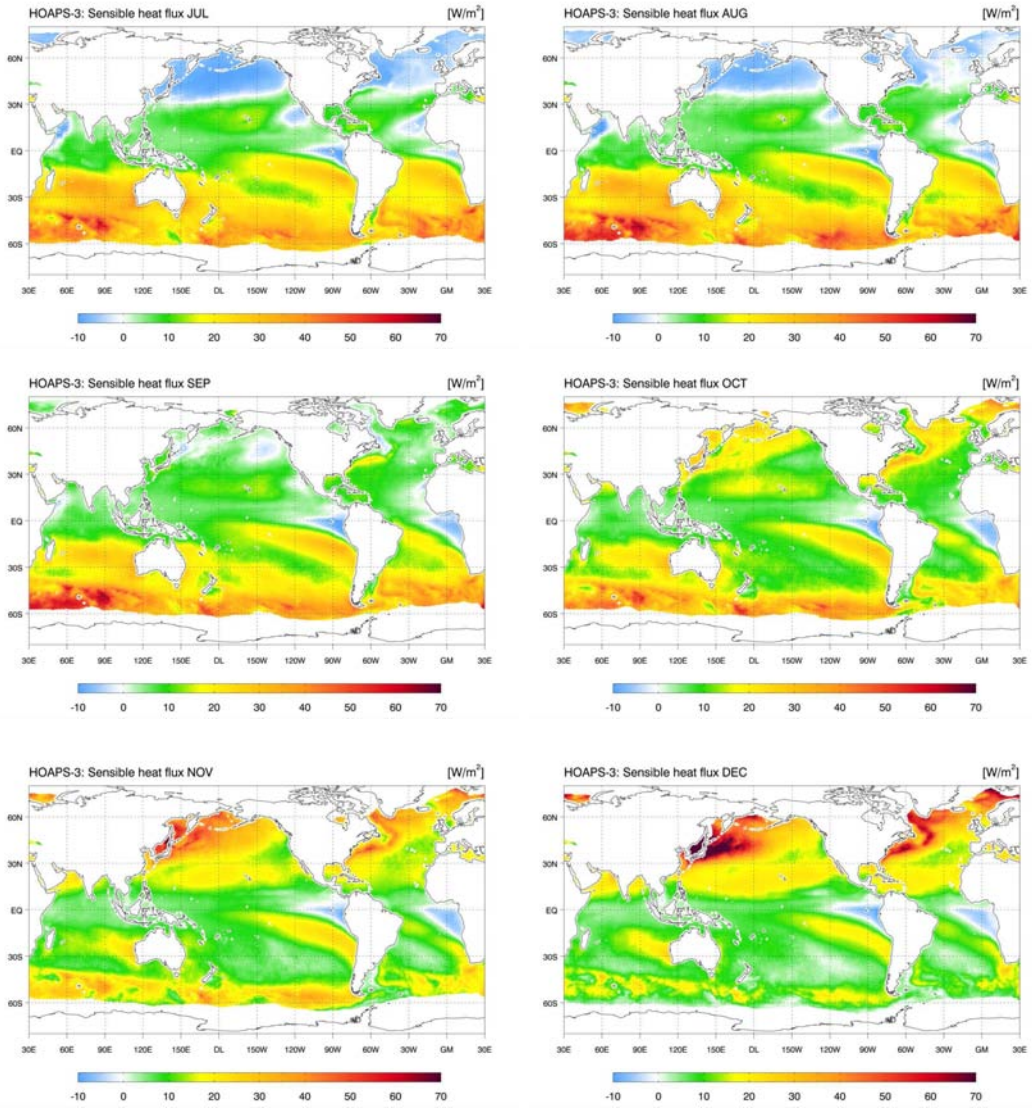

Figure C.16: HOAPS-3 sensible heat flux at sea surface climatological monthly mean values for July to December.

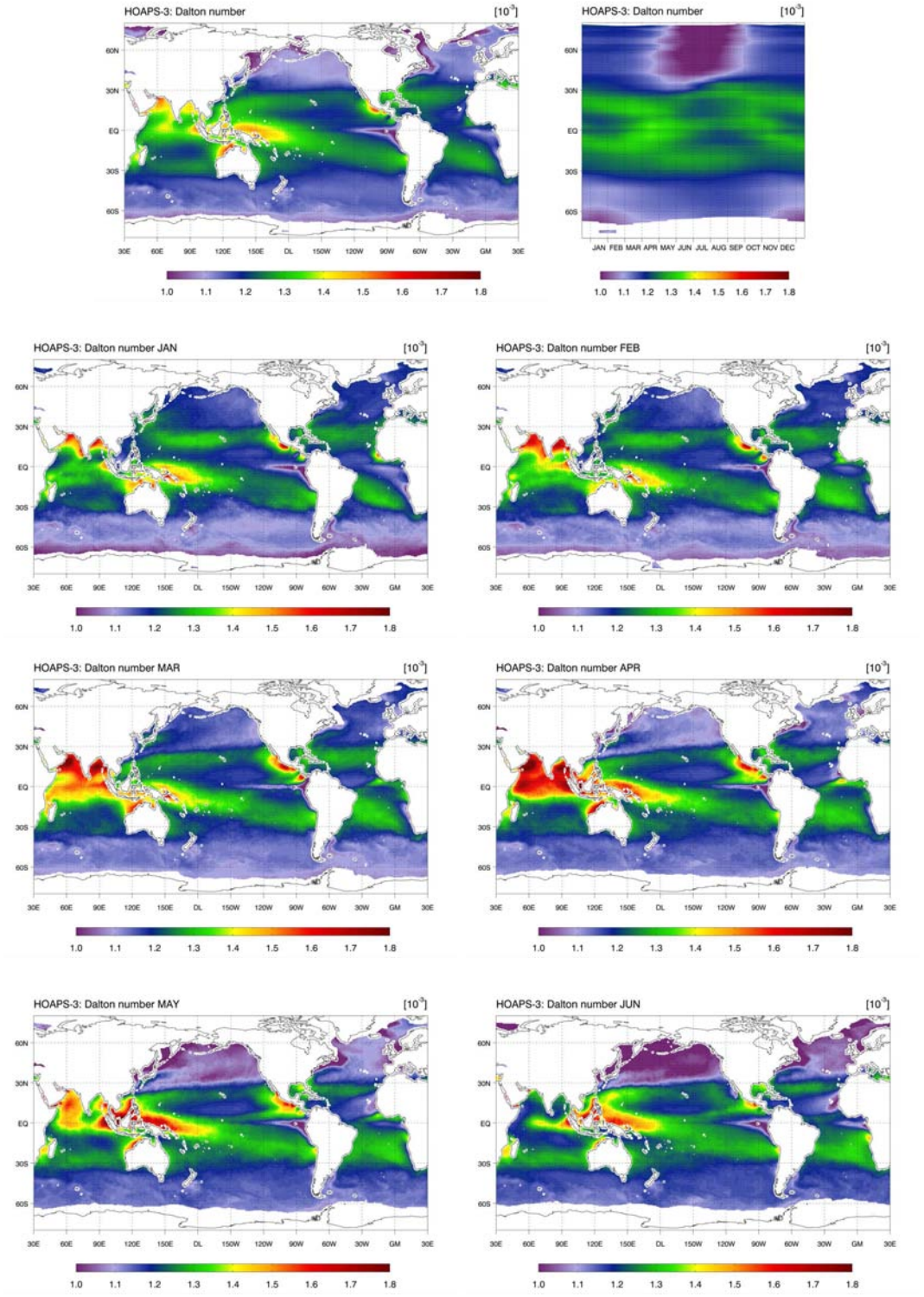

Figure C.17: Climate mean fields of HOAPS-3 latent heat transfer coefficient (Dalton number) for the years 1988-2005. Upper panel shows the climatological mean (left) and the annual cycle of zonal mean values (right). The lower panels show the climatological monthly mean values for January to June.

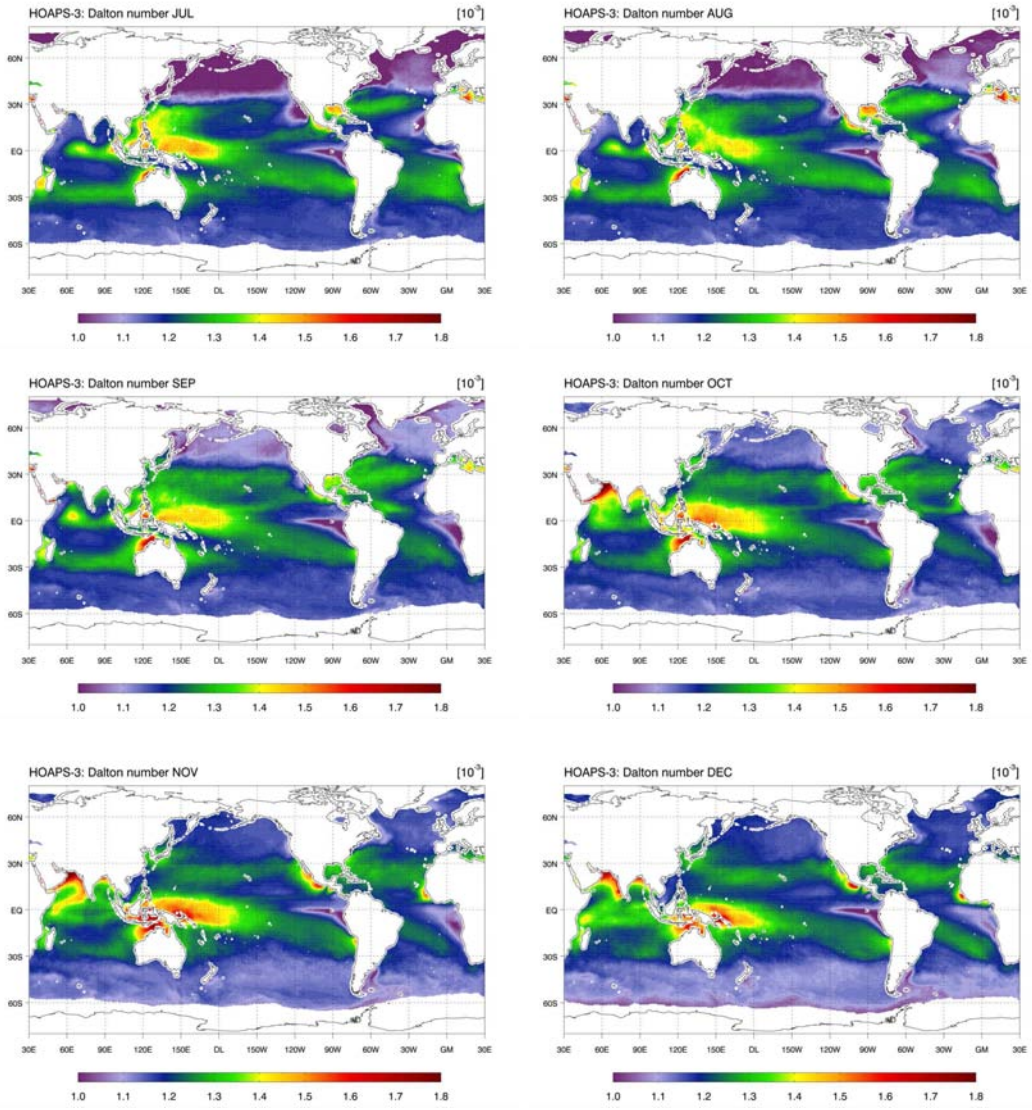

Figure C.18: HOAPS-3 latent heat transfer coefficient (Dalton number) climatological monthly mean values for July to December.

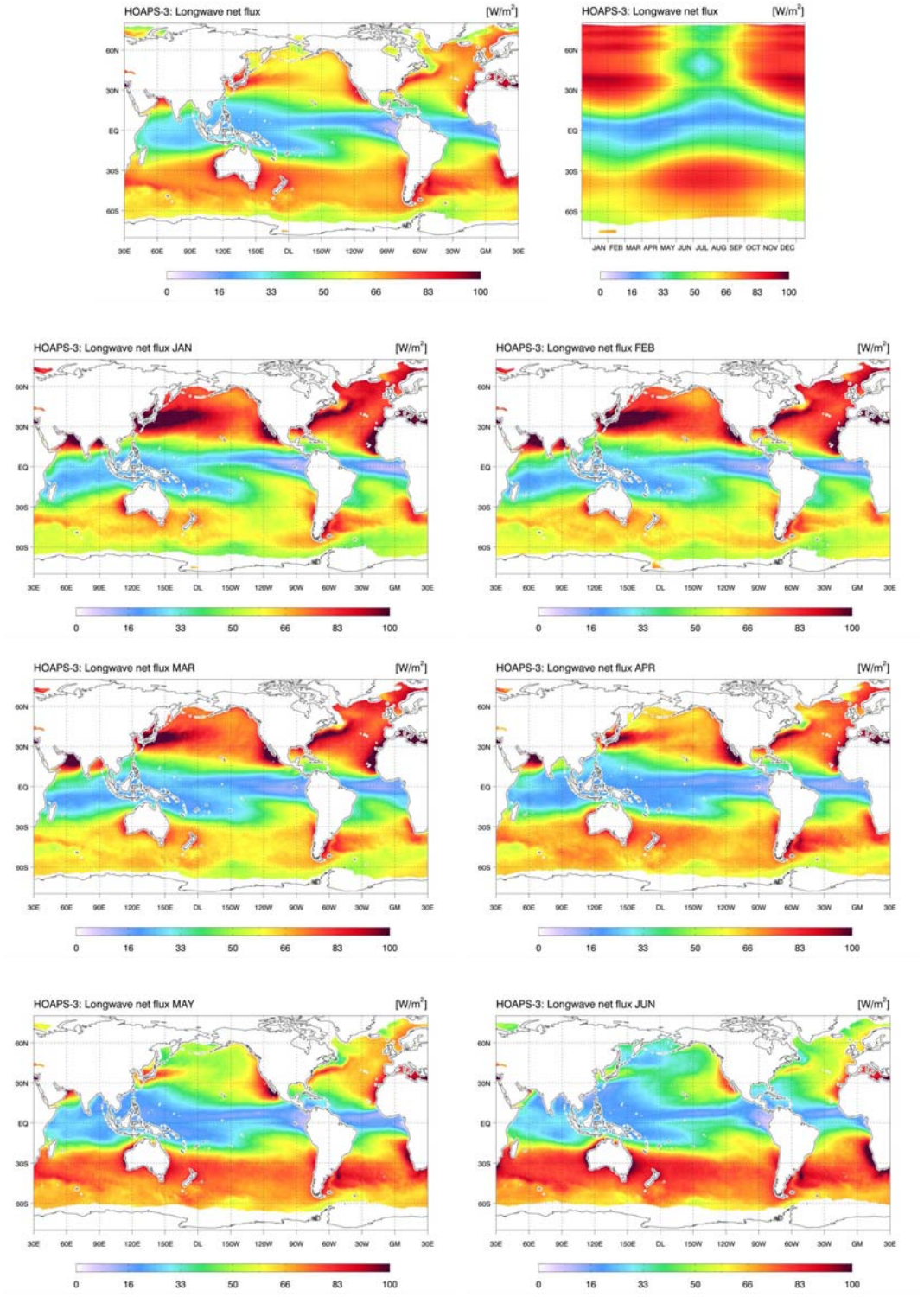

Figure C.19: Climate mean fields of HOAPS-3 longwave net flux at sea surface for the years 1988-2005. Upper panel shows the climatological mean (left) and the annual cycle of zonal mean values (right). The lower panels show the climatological monthly mean values for January to June.

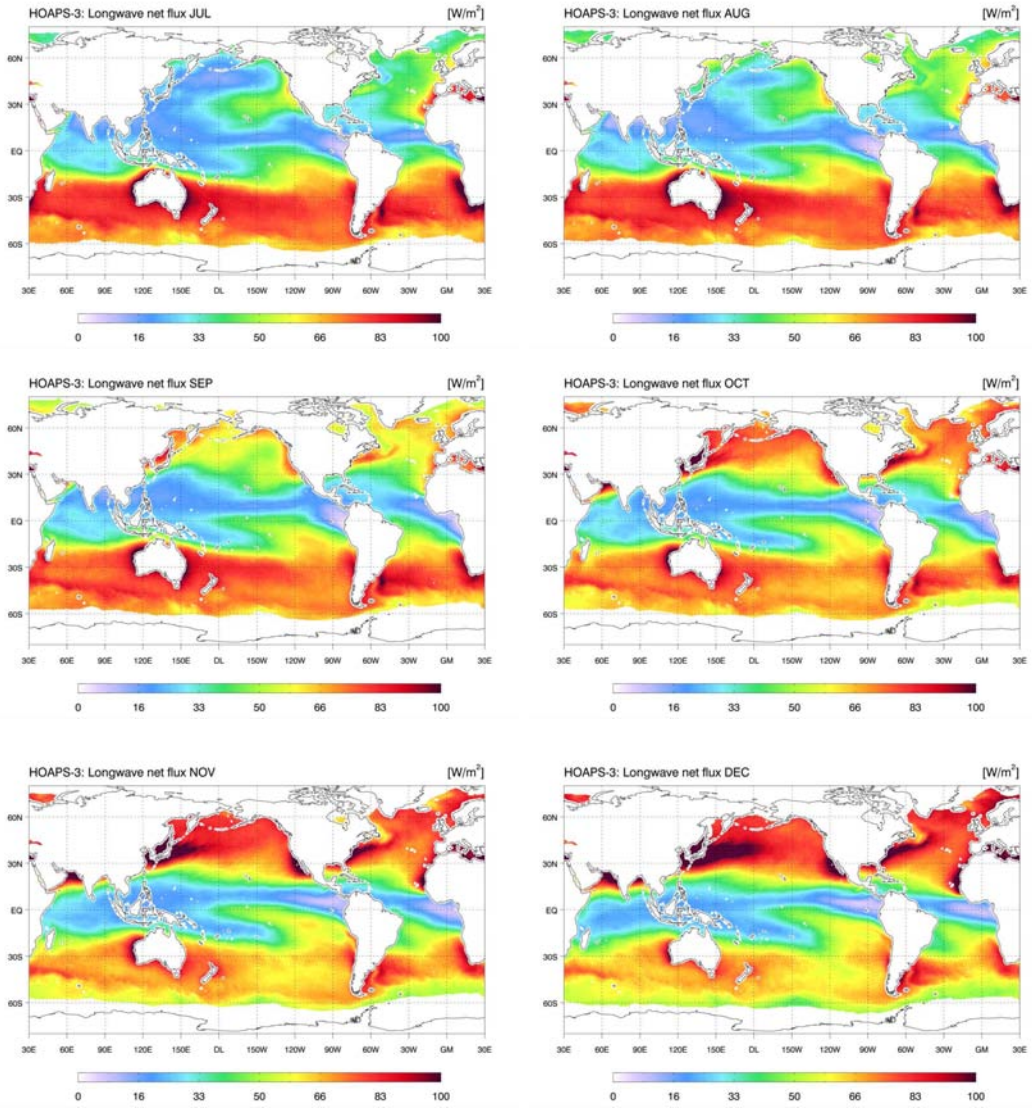

Figure C.20: HOAPS-3 longwave net flux at sea surface climatological monthly mean values for July to December.

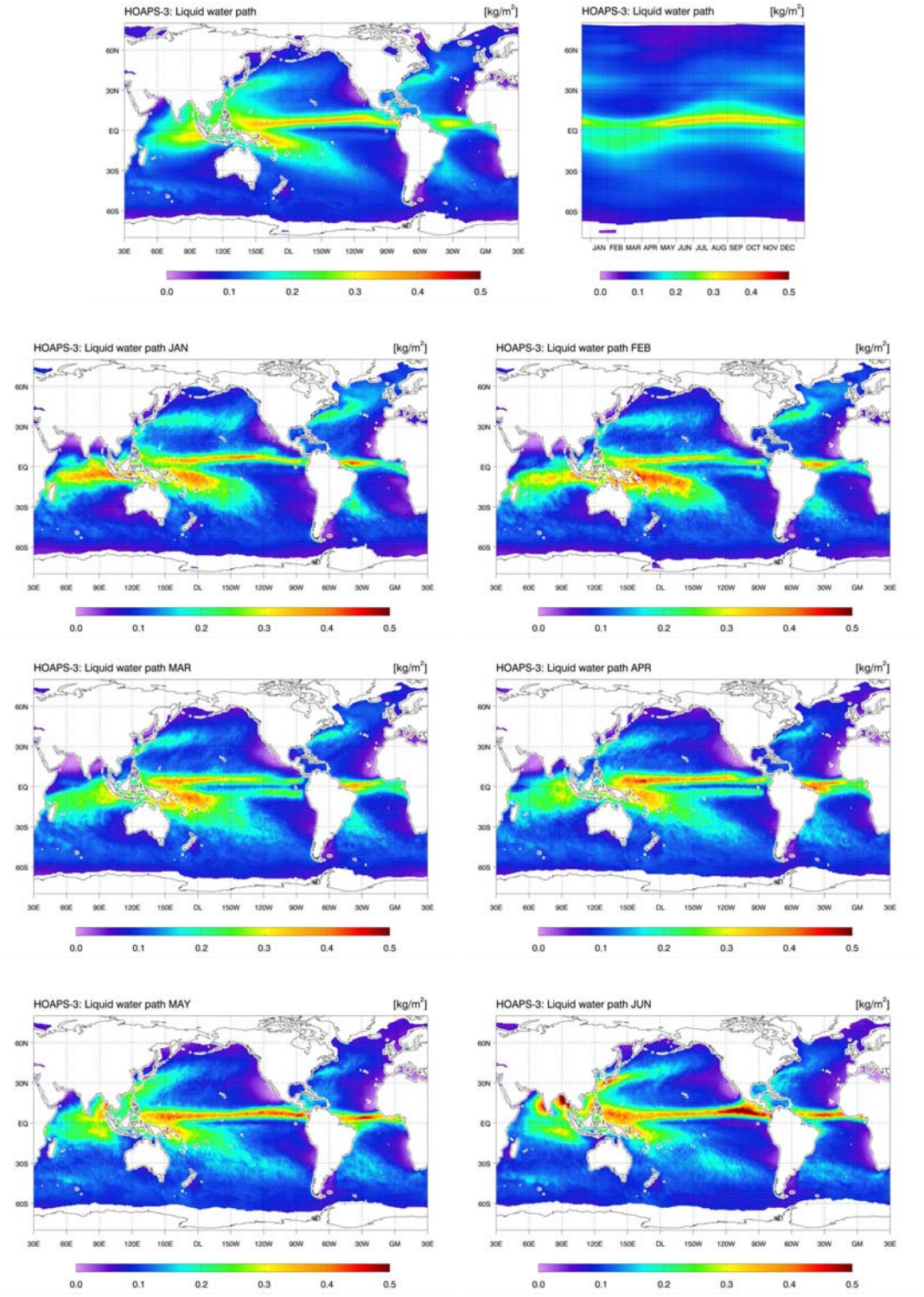

Figure C.21: Climate mean fields of HOAPS-3 vertically integrated liquid water for the years 1988-2005. Upper panel shows the climatological mean (left) and the annual cycle of zonal mean values (right). The lower panels show the climatological monthly mean values for January to June.

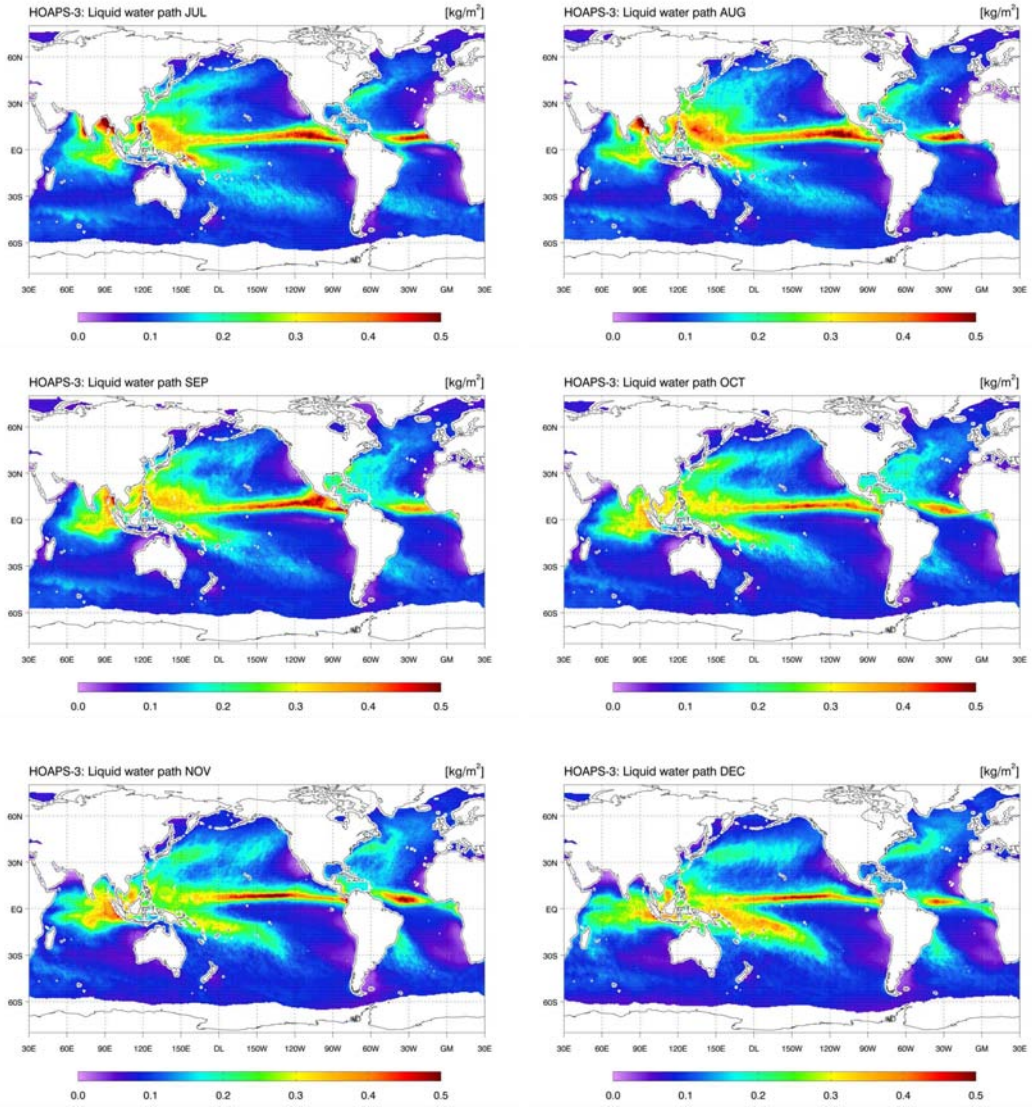

Figure C.22: HOAPS-3 vertically integrated liquid water climatological monthly mean values for July to December.

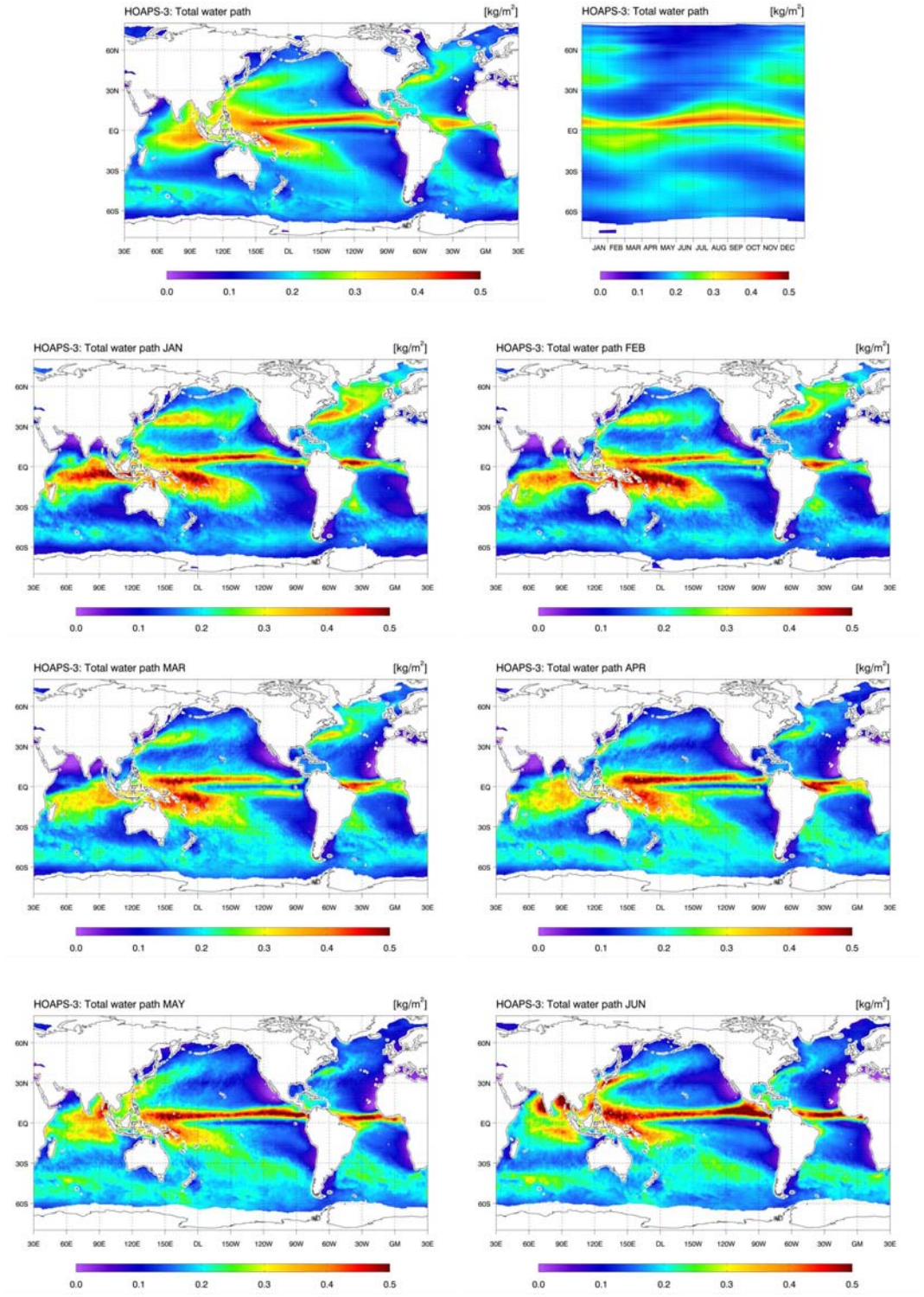

Figure C.23: Climate mean fields of HOAPS-3 vertically integrated total water for the years 1988-2005. Upper panel shows the climatological mean (left) and the annual cycle of zonal mean values (right). The lower panels show the climatological monthly mean values for January to June.

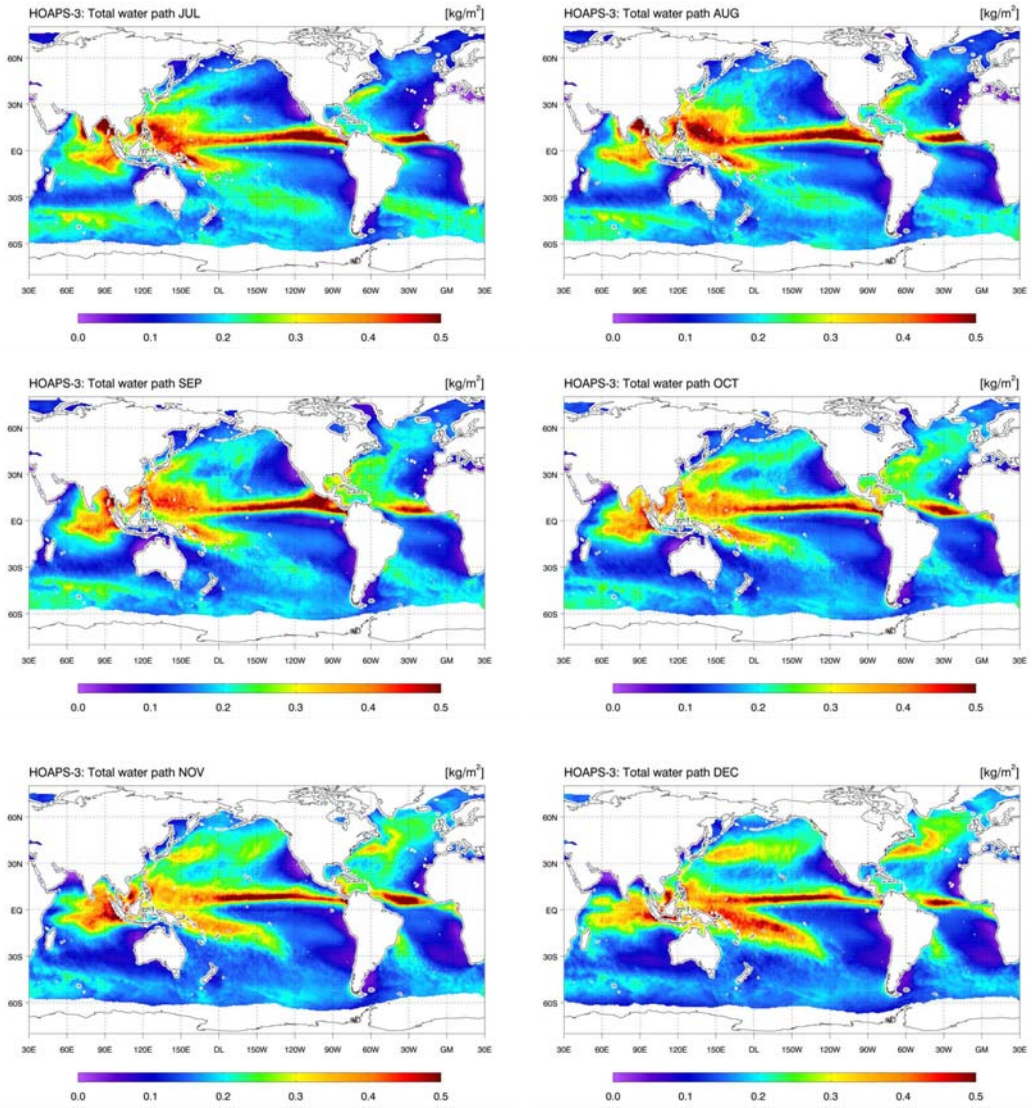

Figure C.24: HOAPS-3 vertically integrated total water climatological monthly mean values for July to December.

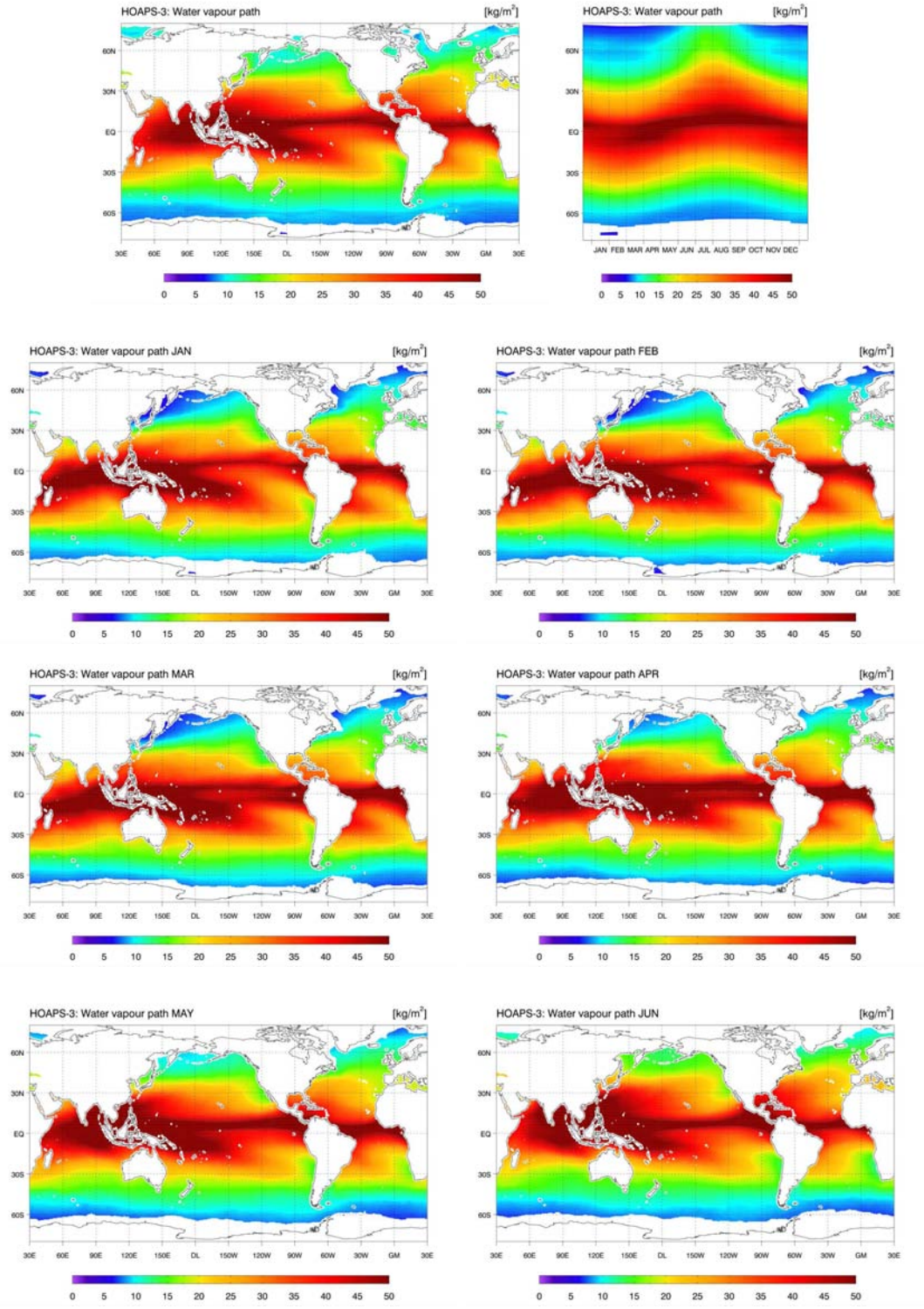

Figure C.25: Climate mean fields of HOAPS-3 vertically integrated water vapor for the years 1988-2005. Upper panel shows the climatological mean (left) and the annual cycle of zonal mean values (right). The lower panels show the climatological monthly mean values for January to June.

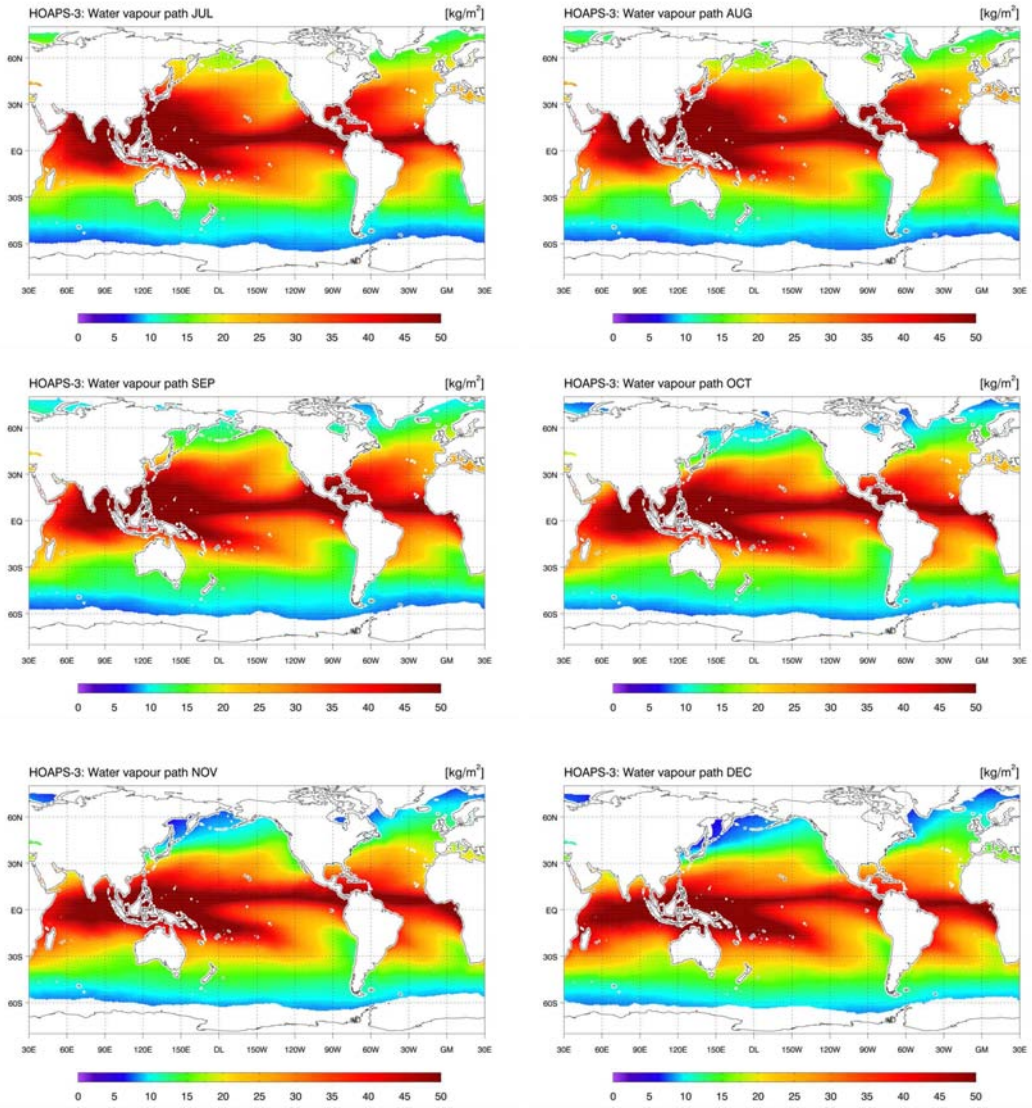

Figure C.26: HOAPS-3 vertically integrated water vapor climatological monthly mean values for July to December.

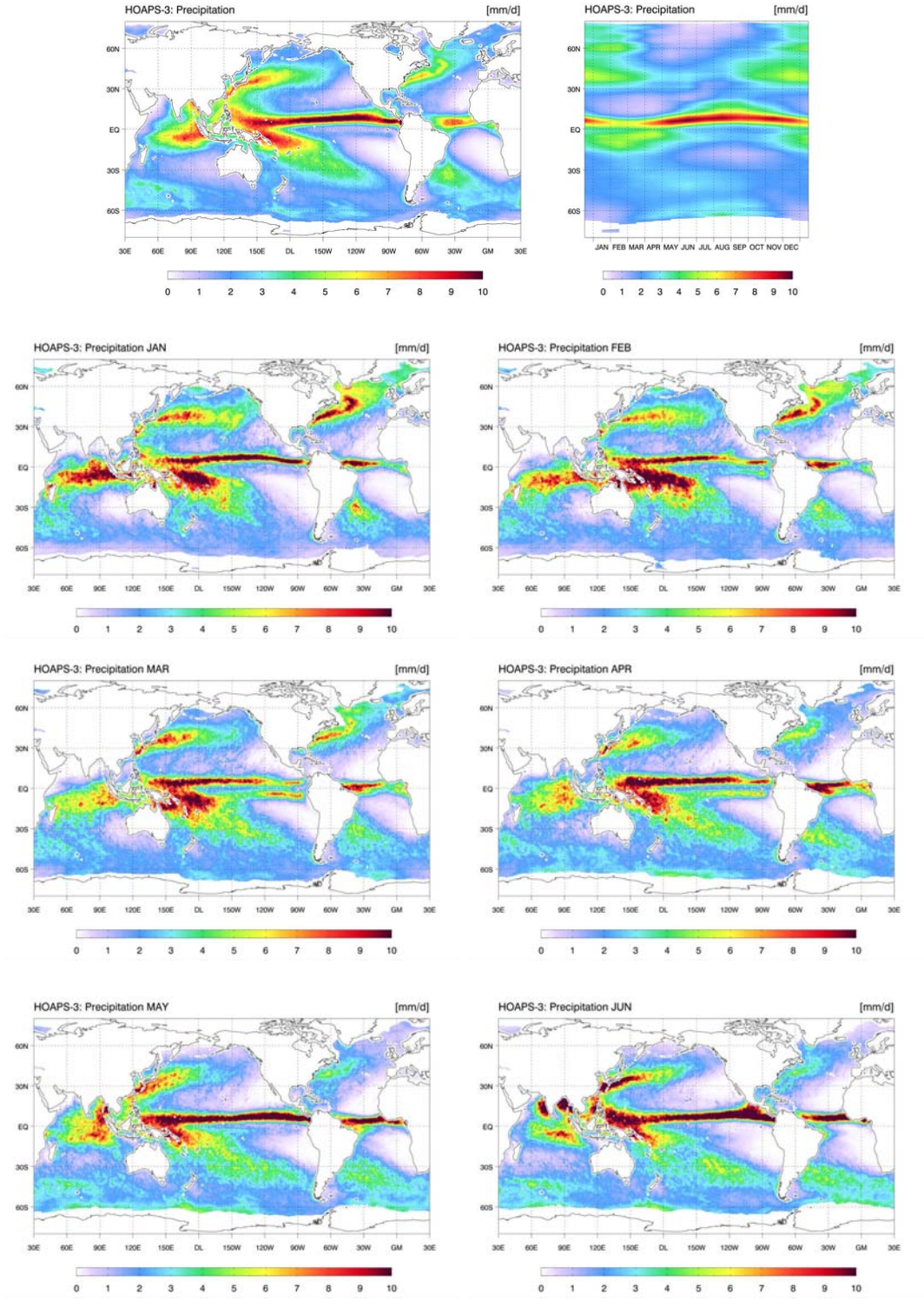

Figure C.27: Climate mean fields of HOAPS-3 precipitation for the years 1988-2005. Upper panel shows the climatological mean (left) and the annual cycle of zonal mean values (right). The lower panels show the climatological monthly mean values for January to June.

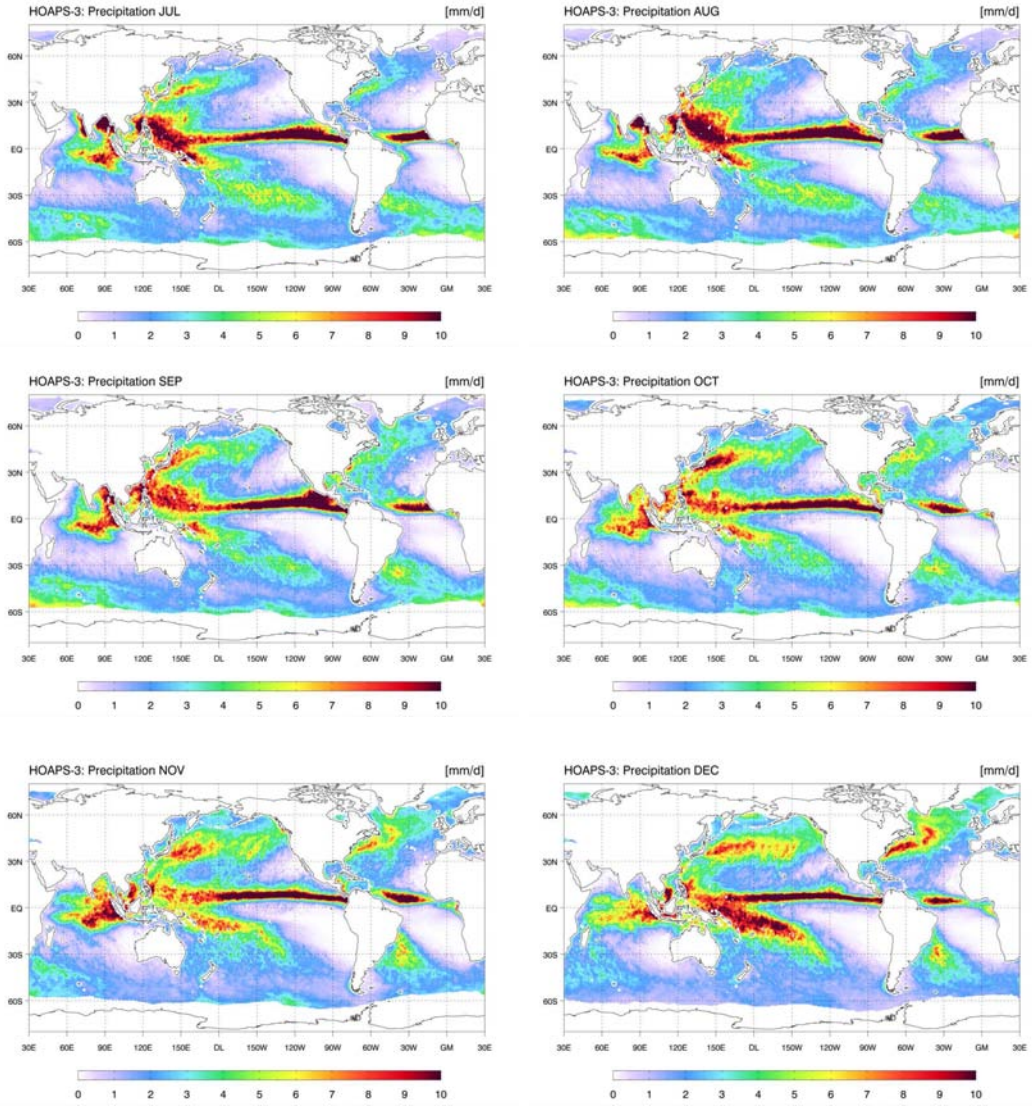

Figure C.28: HOAPS-3 precipitation climatological monthly mean values for July to December.

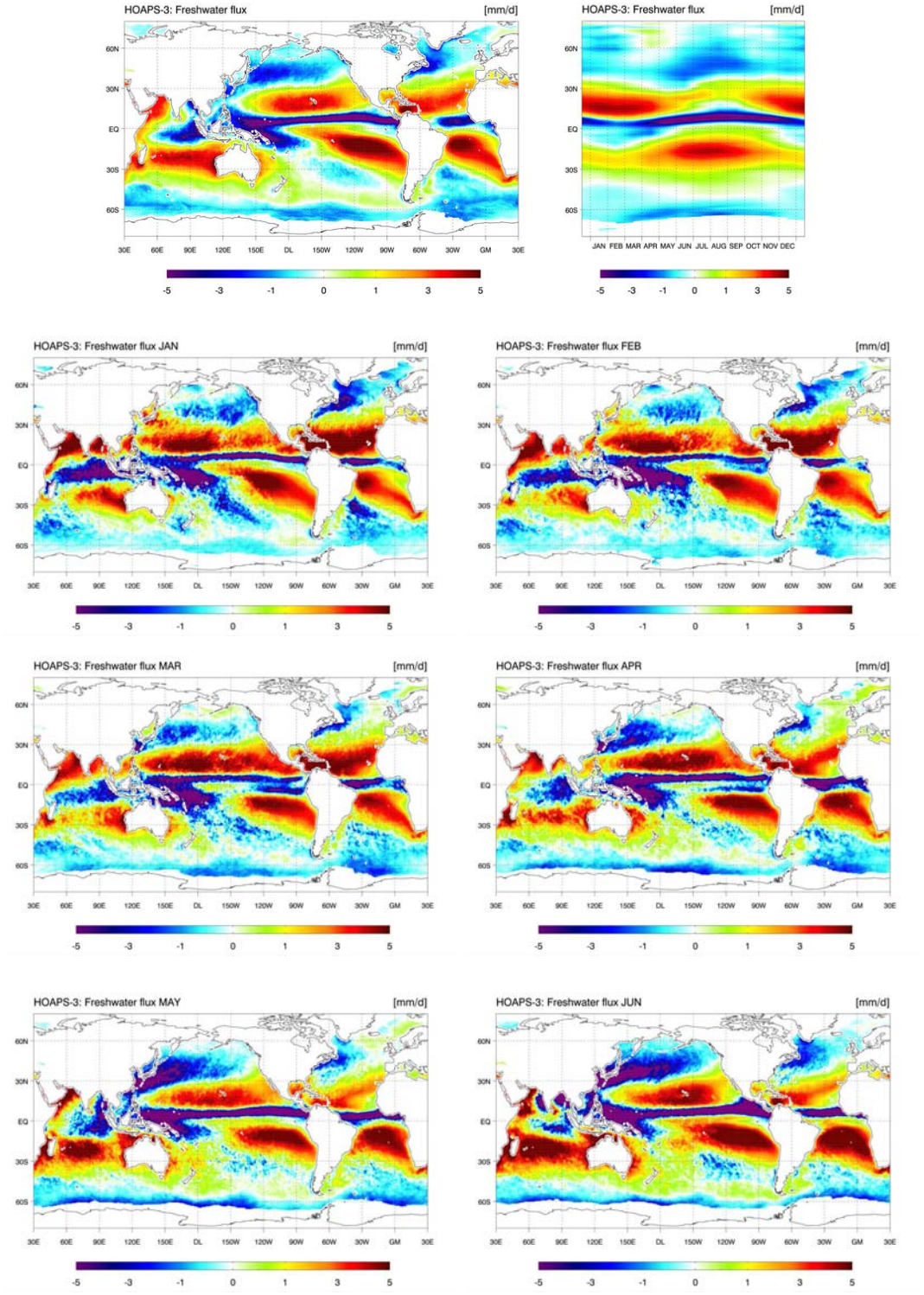

Figure C.29: Climate mean fields of HOAPS-3 freshwater flux (evaporation minus precipitation) for the years 1988-2005. Upper panel shows the climatological mean (left) and the annual cycle of zonal mean values (right). The lower panels show the climatological monthly mean values for January to June.

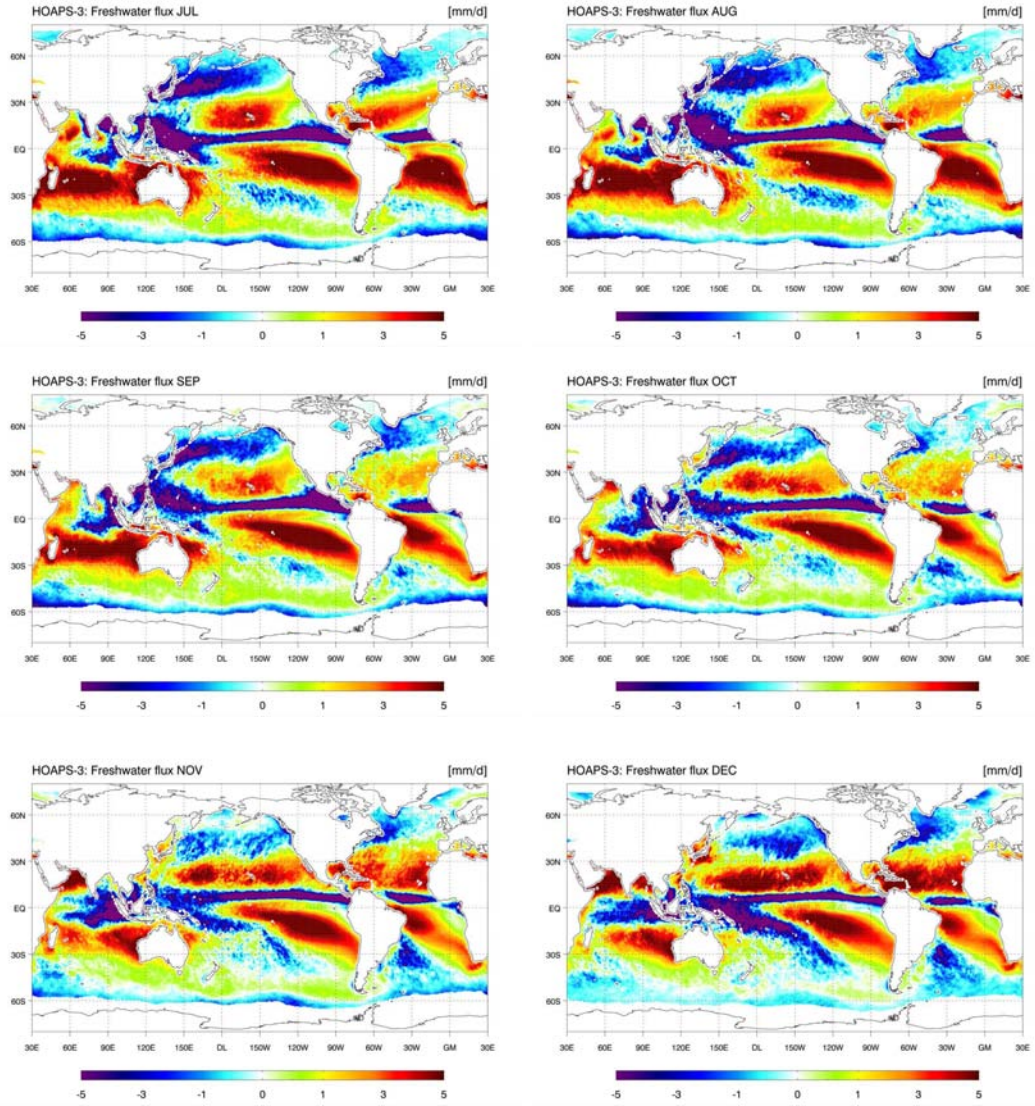

Figure C.30: HOAPS-3 freshwater flux (evaporation minus precipitation) climatological monthly mean values for July to December.

Die gesamten Veröffentlichungen in der Publikationsreihe des MPI-M
„Berichte zur Erdsystemforschung“,
„Reports on Earth System Science“,
ISSN 1614-1199

sind über die Internetseiten des Max-Planck-Instituts für Meteorologie erhältlich:

http://www.mpimet.mpg.de/wissenschaft/publikationen.html



ISSN 1614-1199